Fully Integrated CMOS-Compatible Mode-Locked Lasers

by

Katia Shtyrkova
B.S., Optical Sciences and Engineering
University of Arizona (2009)

S.M., Electrical Engineering
Massachusetts Institute of Technology (2013)

Submitted to the Department of
Electrical Engineering and Computer Science
in partial fulfillment of the requirements for the degree of
Doctor of Philosophy
at the
MASSACHUSETTS INSTITUTE OF TECHNOLOGY
February 2018

Author .....
Department of
Electrical Engineering and Computer Science
October 19, 2017

Certified by .....
Erich P. Ippen
Elihu Thomson Professor of Electrical Engineering
Professor of Physics
Thesis Supervisor

Accepted by .....
Leslie A. Kolodziejski
Professor of Electrical Engineering and Computer Science
Chair, Department Committee on Graduate Students

Fully Integrated CMOS-Compatible Mode-Locked Lasers

by

Katia Shtyrkova

Submitted to the Department of
Electrical Engineering and Computer Science
on October 19, 2017, in partial fulfillment of the
requirements for the degree of
Doctor of Philosophy

Abstract

The field of integrated photonics has already revolutionized optical communications and is making rapid advances in signal processing, light detection and ranging, optical sensing, bio-medical diagnostics and imaging, and military-related applications. Large and complex radio-frequency and optical systems could be potentially replaced with compact, power-efficient, alignment-free, cost-effectively mass-produced integrated photonics components. An on-chip high repetition-rate mode-locked laser is a key enabler of many integrated photonics applications, such as all-optical sampling, on-chip frequency combs, low phase noise microwave oscillators, photonic ADCs and others. First-ever fully-integrated on-chip mode-locked lasers are demonstrated in this work, fabricated using a CMOS-compatible process. The lasers have no off-chip elements other than the pump laser, which could be easily co-packaged. 1900nm and 1550nm lasers are designed, fabricated and characterized. For 1900nm central wavelength lasers, several different laser configurations are demonstrated, with repetition rates of 690MHz and 1.2GHz. Q-switched, Q-switch-mode-locked, and CW mode-locked laser operation was demonstrated, with the shortest pulse durations of 250fs. The smallest foot-print of one laser is 23.6mm $\times$0.78mm$\times$0.6mm. In addition, first-ever fully-on-chip CMOS-compatible mode-locking element based on Kerr nonlinearity is demonstrated for 1550nm and 1900nm laser wavelengths. Demonstrated modulation depths for 1900nm and 1550nm mode-locking devices are 9% and 2.5% respectively. The work in this thesis presents the first-ever demonstration of fully-on-chip CMOS compatible mode-locking device, as well as first-ever CMOS-compatible mode-locked lasers with no off-chip components.

Thesis Supervisor: Erich P. Ippen
Title: Elihu Thomson Professor of Electrical Engineering
Professor of Physics

To Daniel, with Love.

To Erich P. Ippen, and Robert A. Norwood, with gratitude.

Acknowledgments

"I started my life with a single absolute: that the world was mine to shape in the image of my highest values and never to be given up to a lesser standard, no matter how long or hard the struggle" - this quote from Ayn Rand's book has been my guiding principle for many years. However, this principle has never been more tested than during my years at MIT. The quote still stands, and I stand with it, but the ride has been anything but smooth. It had its ups and the downs, but whatever it was in between the ups and the downs could not be accurately described by mathematical functions... unless we (maybe?) use chaos theory. Yet through this chaos I learned, grew and developed as a person, as a scientist, and as a leader.

No one has helped more through this process than my PhD advisor, Professor Erich Ippen. Professor Ippen frequently says "Sometimes you need to work hard, sometimes you need to get lucky. But it's good to have both". I had both, in that I worked hard, but I got exceptionally lucky to have him as my PhD advisor, in fact, this was the best choice I ever made during my years at MIT. Professor Ippen is always available to have a scientific conversation, he has deep scientific insight, his office door is always open, we can always walk in and talk to him. His mind works like that of a true scientist, in that with every experiment or result he always finds more questions to ask, more things to learn, more experiments to do. Professor Ippen has given me a lot of flexibility in terms of when I worked, how I worked, and what I chose to work on. Whenever I didn't quite deliver, he responded by backing me up, giving me more time, confidence, and resources. Through everything that I did Professor Ippen has always backed me up. He went out of his way to help me, every time. I echo the phrase repeated by many of his former students: "There never was, and never will be, another Erich Ippen". I am grateful, and lucky, and fortunate for having a chance to work with him. To Professor Ippen - thank you, from the bottom of my heart, for all your help, time, advice, guidance, trust, support, understanding, and thank you for always having my back. I have learned so much from you, as a person and as a scientist, and I look forward to learning more.

Professor Franz Kärtner has been like a second adviser to me. Although he took an appointment at DESY, Germany, shortly after I started at MIT, it never felt like he was away. He manages to respond to all his emails within 24 hours, and he has been available for video calls the same day or next day at the latest, whenever I had a question. Many times I was stuck on a particular calculation, and I knew that we would clear it out "by tomorrow the latest", because Professor Kärtner would find time to talk with me, and we would work it out. He has shown me how to be an outstanding adviser, how to give students all the support and resources necessary to push them forward, how to efficiently and effectively run a research group, and how to be leader in one's field. Together with Professor Ippen, they are some of the world's best experts on mode-locked laser. I look forward to collaborating with him in the future and to finishing up some of our still-in-progress mode-locked laser work.

Professor Michael Watts has also been like a second advisor to me. In fact, I was cross-listed as a group member with the three professors - Erich Ippen, Franz Kärtner,

and Michael Watts, and I worked very closely with the three of them. Professor Watts is one of the world's experts in silicon photonics, and he has made tremendous contributions to the development of this field in the US. He has a few very unique talents that few people have, pulling together large DARPA efforts, getting the funding, and running them efficiently is one of them. Few students have an opportunity to work with integrated photonics on a wafer-scale platform. Having this opportunity, being able to complete several tape-outs per year filled with our devices and made at a professional fabrication facility, and having all the necessary equipment to characterize those devices is a rare treat. We were able to do this thanks to Professor Watts' leadership and group structure. I have seen him rigorously defend the group, the approach, and individual students to senior DARPA management, with firmness, confidence, and absolute expertise. Professor Watts has also given me a leadership opportunity to run and manage DARPA DODOS program in the group, and it has been an outstanding experience. I am thankful for being a part of his group, for all the leadership opportunities, and for being a part of a large scale silicon photonics effort.

None of this work would have been possible without the funding agencies that sponsor our research and our students. I would like to acknowledge Air Force Office of Scientific Research (AFOSR), DARPA's EPHI Program, DARPA'S DODOS program, and NDSEG fellowship program that supported me for three years.

Throughout my years at MIT, I have been fortunate to work with fantastic colleagues. First, I would like to thank former students from Professor Ippen's group who trained me in the lab and taught me most of what they know when I was a first year student. For this, I am very thankful to Marcus Dahlem and Ali Motamedi. I am also thankful to Michelle Sander, David Chao and Jonathan Morse, for all the intellectual discussions during my first three years at MIT. Next, I would like to thank the 2016/2017 MIT DODOS Team - Patrick Callahan, Nanxi Li, Salih Magden, Neetesh Singh, Alfonso Ruocco, Ming Xing, and our newer members Manal Raval and Jelena Notaros. It has been really wonderful working with all of them as a team, and together we made tremendous progress on DODOS project. I am also grateful to all the former members of the PMG group for their friendship, advice, scientific insight, and contributions to the group - Jonathan Bradley, Anna Baldycheva, Chris Poulton, David Cole, Erman Timurdogan, Zhan Su, Ehsan Hosseini, Diedrik Vermeulen, Matthew Byrd, Ami Yacoobi, and all other former group members. I am thankful to Peter Krogen from Professor 's group, who always had a unique experimental insight, and could trouble-shoot almost anything. I am thankful to numerous former members of Professor Kärtner's and Professor Ippen's groups for their friendships and advice.

A special thank you goes out to Kenaish Al Qubaisi for the one summer we worked together, for his continuous friendship, and for all that chocolate. Kenaish, I have learned as much from you as you have learned from me, and I am exceedingly proud of you, every day. I look forward to all the advances you'll make in the field of silicon photonics during your time in graduate school and for the years to come, and I also look forward to our continuous friendship. Also, good luck avoiding bears on BU campus.

At MIT, we have the best people. I have worked with many faculty and staff

members who have been invaluable in the smooth operation of the institute, and in moving our research programs forwards. Thank you to Dorothy Fleischer from OQE group for helping the group run smoothly, thank you to Donna Gale for being an invaluable part of Ippen group for thirty years, thank you to Melissa Sheehan and Maxine Samuels from RLE headquarters for helping us with all the purchase orders and contract-related work, thank you to Al McGurl and Bill Gibbs for doing our building maintenance and for always fixing everything we needed on a short notice, thank you to David Foss for helping me trouble-shoot my numerous IT issues over the years. A special BIG thank you to Bill Adams, who has helped me with even more IT-related issues, who has fixed my personal computer, twice, and recovered a lot of lost data. Bill, I really appreciate your time, help, and work ethics. Thank you to Professor Yoel Fink for his help on numerous unique occasions, and for always having my back in those. Thank you to Janet Fischer and Professor Leslie Kolodziejski for running the EECS graduate student office smoothly, and for supporting GW6 group over many years.

Some of our work on EPHI and DODOS programs would not have been possible without MIT's Microsystems' Technology Laboratories (MTL). I would like to thank Dr. Vicky Diadiuk from MTL for her impeccable and outstanding leadership of the laboratories. No one could run MIT fabrication facilities better than her, and I have seen few leaders so capable and determined. Thank you to Gary Riggott from MTL for doing numerous active depositions for us over several years, for helping us trouble-shoot the issues, for working many hours for Watts' group and then working many hours all over again. Our results wouldn't have been possible without Gary's help. I would like to thank Dave Terry and Dennis Ward from MTL's TRL laboratories for their help, time, knowledge, competence, and expertise in nano-fabrication. What took me over a year at EML with no results in sight, took a day and a half on a first try at TRL labs, due to Dave's and Dennis' expertise and help.

While at MIT, I have had a few successful collaborations with other institutions. In particular, my Masters' thesis work on Titanium Dioxide was done in collaboration with Professor Mazur's group at Harvard. Together, we have published many papers and made interesting advances in TiO_2-based nonlinear optics. I am thankful for the opportunity to work with Mazur group, and for several friendships I made due to that collaboration (in particular, a special thank you to Chris Evans and Orad Reshef).

During my last two years at MIT, I have had a wonderful collaboration with MEEI's Boston Keratoprosthesis Laboratory. I am particularly thankful to Dr. Eleftherios Paschalis from KPro group - he is one of the brightest, most fascinating people I ever met, and I truly enjoyed working together. I look forward to our continuous friendship and potential future collaborations.

In addition to academic research, I have been engaged in numerous non-academic activities on MIT campus, and had a chance to work with many wonderful people. I am thankful to the EECS' Visiting Committee 2013, 2015, and 2017 graduate students members, to the GSC 2013, 2014, and 2015, and to all Directors of MIT Fall Career Fair 2014 (especially to Bianca Homberg and Sven Schlumpberger). A special thank you to MIT-Tohoku University Research Collaboration, with Professor Ippen, Professor del Alamo, and Professor Nakazawa, for allowing me to lead a Japan-MIT student

symposium at MIT, and to visit Japan with a group of fellow graduate students. A warm thank you to Jessica Landry from ODGE office - it has been wonderful working together on Graduate Student Life Grants program over several years. A spent three years chairing MIT's GradRat Committee and designing the new official MIT graduate ring. I am thankful to all members of the MIT GradRat from 2011/2012, 2012/2013, and 2013/2014 academic years, and particularly to Ahmed Helal and Peg Mead. Thank you to Matt Haberland for your collaborations with the GradRat program, for all our runs around the Charles River, for your friendship, and for running the Green Building stairs, up and down many times, "just for the fun of exercise". Finally, I would like to thank Matt McCutchen for running MIT's DDR club.

While MIT has so far been the most defining part of my career, there have been people before MIT who have helped me succeed academically and who made me fall in love with physics and scientific research. I would like to thank Jerry Long from Pima Community College who taught physics with the most clarity and insight. I would like to thank Shawn Jackson from the University of Arizona for his outstanding, unique, insightful, and absolutely captivating physics lectures. I would like to thank Professor Franko Kueppers, who taught the introduction to laser physics and photonics, and who spent a lot of time with me during office hours answering my never-ending questions. I would like to thank all my former faculty from College of Optical Sciences. Finally, I would like to thank Professor Robert Norwood (College of Optical Sciences) for taking me in as a part time research student and allowing me to do real research throughout my undergraduate years. Professor Norwood is wonderful to work with - he has never-ending positive energy, just as never-ending research ideas, and he goes out of his way to help his students succeed. Thank you, Dr. Norwood, for helping to jump-start my career, and for making me fall in love with scientific research, and for encouraging me to apply for graduate school at MIT.

I want to also thank my wonderful family for their love and support over the years - my sisters Tania, Sasha, and Anastasia, my brother Evan, and my little niece Ashley. I would like to thank my dad, Dmitriy, for his help and support through the years. No matter what, where, and how, he always stood and stands behind his family, and he always has our backs. I have yet to meet another man like him.

Finally, I would like to thank my personal friends. To Apu Bhopale - you have been a friend like no other, thank you for all the nature trips, all the 80s music, all the laughter, the best in the world green tea chocolate... looking forward to much more of all of the above :-) I am lucky to have you in my life. To Ahmed Helal - you have been an amazing friend to me. Thank you for always listening, for giving me space when I needed it, for giving me *four* volumes of Calvin and Hobbes comics... the ride isn't over, I am just hopping on a different train :-) To Patrick Callahan - thank you for all the work-related and work-unrelated conversations, thank you for our occasional beers after work, thank you for being my close and much needed friend at MIT. I have really enjoyed working with you, and "thinking" with you. I shall miss you every day. Thank you to Chris Evans for your friendship and numerous scientific discussions. Looking forward to many more :) Thank you to Matthew Schwab, Mirna Slim, Katie Hall, and Mike Oliker for your friendships. A very warm thank you to Peg Mead and John Kokot, who have been absolutely fantastic friends to Daniel and me. We are

so very fortunate to know you guys, and we look forward to being in touch. Always. Thank you to Matthias and Megan Whitney, and their Oliver, Camilla, Lilian and Nolan. We are truly blessed to have you in our lives.

Last and not least, I would like to thank my son Daniel - the boy who makes the sun shine for me, who showers me every day with love and happiness, who stood by me for the last 13+ years, and who always has been, and will always be the number one person in my life. MIT has been an experience, but it has been wonderful because he was part of it. To Daniel: thank you for being so wonderful, and thank you for all your love and kindness. I'll love you forever. You are my sunshine, today and always.

Contents

List of Figures

List of Tables

Chapter 1

Introduction

This thesis focuses on the design and development of integrated mode-locked lasers centered at 1550nm, and 1900nm and fabricated using a CMOS-compatible process. It therefore combines two major photonic fields of study - a mature field of ultrafast mode-locked lasers and the relatively new field of integrated photonics. There are specific and well-known challenges associated with the mode-locked lasers design and development and very different challenges associated with the integrated photonics components. Yet, the development of on-chip high repetition rate mode-locked lasers bring its own, new and unique set of challenges, which we carefully address in this work.

This thesis is organized as follows: first, we introduce high repetition rate mode-locked lasers and their applications. Next, we discuss integrated silicon photonics, with its advantages, recent innovations, and potential applications. In Sections 1.3 and 1.4 we introduce two major DARPA programs that have motivated and sponsored the work on developing integrated mode-locked lasers presented in this thesis; we present relevant goals, possible applications, and the unique approach adopted by the MIT team to address silicon photonics tasks in those programs. Chapter 2 provides detailed design of the first on-chip CMOS-compatible saturable absorber - the key missing element in many integrated approaches to mode-locked laser implementation. Chapter 3 details the development of the on-chip mode-locked laser at 1900nm, including component and system design, numerical pulse propagation simulations,

and characterization results. Chapter 4 provides development and characterization of the on-chip mode-locked laser at 1550nm.

1.1 High repetition rate mode-locked lasers

Mode-locked (or short-pulse operation) lasers have revolutionized the fields of frequency and time-resolved spectroscopy and metrology, medical diagnostics, optical communications, material processing, and many others. The theory and physics behind mode-locked lasers is well established, and has been presented, with elaborating details, elsewhere [7, 8, 9]. The work in this thesis, however, focuses on high repetition rate mode-locked lasers, where the radio frequency (RF) repetition rate ranges from 200MHz to 10 or more GHz. Such high repetition rate mode-locked lasers are more challenging to design, but they offer unique advantages to the series of applications such as photonic Analog-to-Digital Converters, astro-combs, optical arbitrary waveform generation, and low noise microwave synthesis. Those applications are briefly described below.

Photonic Analog-to-Digital Converters(ADC) rely on high repetition rate short pulse duration mode-locked lasers, with subsequent optical sampling of a voltage signal to be digitized. Aperture jitter in electronic ADCs remains the main limitation of going to higher effective number of bits at high frequencies [10]. Photonic ADCs offer a solution to this aperture jitter bottleneck, by taking advantage of the low timing jitter of a mode-locked laser pulse train. Timing jitter of the mode-locked lasers is proportional to the pulse duration, and inversely proportional to the square root of the pulse energy. Therefore, high power and short pulse duration mode-locked lasers (MLLs) could have extremely low timing jitter (on the order a few femtoseconds [11]). Together with high frequency operation, this provides several orders of magnitude improvement over equivalent frequency electronic ADCs [12].

Optical arbitrary waveform generation (OAWG) promises a number of interesting applications, such as coherent control over quantum mechanical processes, communications at terabit-per-second using a single light source, and Light, Detection and

Ranging (LIDAR) systems with under 5nm ranging precision, with a significantly improved resolution and faster update compared with CW-laser-based frequency-swept LIDAR[13, 14, 15]. Because in true OAWG system the spectrum must be manipulated with a resolution equal to the pulsed source laser repetition frequency, higher repetition rates are much more practical to work with (1-10GHz) [16]. Therefore, high repetition rate mode-locked lasers are excellent choices for robust OAWG systems.

Astro-combs are another application of high repetition rate MLLs. In this case, a stable laser frequency comb is used as a precise frequency reference to calibrate a high resolution astrophysical spectrograph. The spectrograph helps detect Earth-like exoplanets, by measuring exoplanet-induced Doppler shift on stellar radial velocity, which must be done with a precision of 2cm s^{-1} [17]. The comb spacing must correspond to the resolving power of the spectrograph, which typically maps to a $\sim$10GHz comb repetition rate. Such repetition rates are usually hard to achieve for MLLs; therefore, a source-comb at about 1GHz is used, and its repetition rate is multiplied by, for example, an external Fabry-Perot etalon, to a required 10GHz optical mode spacing [18].

Finally, high repetition rate mode-locked lasers could be used for low noise microwave and optical signals synthesis, which implies numerous applications. Very stable microwave and optical signals could be created by stabilizing and referencing an optical comb to an external stable oscillator. While a stabilized comb already has low timing jitter, locking it to a separate ultra-stable reference produces an ultra-low-noise signal. Separately, an optical signal could have extremely low noise **relative** to a given RF oscillator source. The applications of such stabilized RF and optical sources include ultra-high-speed communications, high resolution signal processing applications such as radar, and many other RF applications requiring a stable clock or a local reference. Sections 1.3 and 1.4 explore those applications in details, and motivate the mode-locked laser developments presented in this thesis.

1.2 CMOS-Compatible Silicon Photonics

Integrated photonics is a field of engineering optical/photonic devices on a small substrate, with feature dimensions usually on the order of microns. With integrated photonics, it is possible to shrink otherwise large optical components to the ones with very small shape factors, similarly to replacing vacuum tube transistors with printed p-n junction ones on a silicon chip. The field is thus well-positioned to revolutionize RF and optical systems, by replacing large systems with very compact, low power consumption equivalents.

1.2.1 Advantages/challenges of using silicon

Silicon photonics refers to fabricating optical devices on silicon chips, usually using silicon-on-insulator (SOI) wafers as a starting point [19, 20]. Such devices frequently operate around the optical communications C-band wavelength range (1530-1565nm, corresponding to the lowest point of silica fiber absorption), in order to be compatible with telecommunication standards. Using SOI wafers for integrated devices has many unique challenges and advantages. Silicon has a high linear refractive index (≈3.5 at 1550nm), compared with a low index of surrounding SiO_2(≈1.45 at 1550nm). This allows for high-index-contrast devices, which allow very compact size waveguides and waveguide bends. In addition, silicon has very high nonlinear refractive index ($\approx 5 \times 10^{-14}$ cm^2/W at 1550nm [21]). This, coupled with highly confined small dimension waveguides allows for effective nonlinearities to be very large, thus enabling numerous nonlinear optical applications (for example, frequency conversion and supercontinuum generation). Strong free-carrier absorption in silicon inhibits certain optical devices, but allows the implementation of plasma-dispersion-based modulators. One of the main drawbacks of using silicon for integrated photonics is the challenge of making a silicon laser. Many semiconductor laser diodes use traditional direct bandgap materials, while silicon has an indirect electronic bandgap. Together with a strong free-carrier absorption, this makes using silicon itself as a primary lasing material very challenging. While a few approaches have been tried to

make a laser directly using silicon (such as using quantum confinement in order to relax momentum conservation requirement, silicon Raman gain, and Erbium doping), other hybrid approaches, which rely on heterogeneous integration of a different gain material on SOI wafers, are becoming much more popular. A major, key advantage of using silicon photonics over other integrated photonics platforms is being able to use semiconductor foundries to mass-produce the devices.

1.2.2 Advantages of a CMOS-compatible process

The complimentary metal-oxide-semiconductor (CMOS) process is used for integrated circuits fabrication for most microprocessors, microcontrollers, and many RF devices employed by the electronics industry [22, 23, 24]. Consequently, this technology is very mature, and numerous resources have been invested to make the process reliable, scalable, and very cost-effective. Being able to leverage this mature process for integrated photonics devices is an instant advantage for mass-producible, repeatable, and cost-effective silicon photonics devices. Alternative approaches include layer-by-layer integrated device fabrication in small individual research facilities, or using other integrated photonics platforms, such as, for example, Indium-Phosphide(InP) or Gallium-Arsenide(GaAs)-based photonics [25]. Although in-house fabrication of integrated photonic devices offers a great research tool for a proof-of-concept phenomena and novel materials investigation [26, 27, 28], and InP-based devices offer direct laser integration, they do not offer existing scalable mass-production pathways of electronics and photonics integrated together. Therefore, CMOS-compatible silicon photonics are uniquely positioned for potential commercial applications. Moreover, one can combine CMOS electronics, such as logic, imaging, RF components and others, directly with silicon photonics fabricated using a CMOS-compatible process, using one of many wafer-bonding techniques (or using a so-called "zero change" approach, where no 3D integration is needed [29]). This allows for numerous fully integrated electronic-photonic systems and allows for potentially miniaturizing a vast variety of devices for applications such as radar, LIDAR, optical imaging systems (for example, Optical Coherence Tomography(OCT)), ADCs, and many others.

The unique challenges in designing photonic components for a CMOS-compatible process include restrictions on layer dimensions, fixed and fabrication-specific tolerances, fixed set of materials available (with corresponding optical losses and refractive indices), required pattern densities, constrained layer placements, and numerous other integration restrictions. Therefore, for all the benefits of the state-of-the-art fabrication process, one gives up design flexibility.

1.2.3 Recent Advances in Silicon Photonics

Over the last decade, numerous silicon photonics integrated devices have been demonstrated. This include low loss optical waveguides, high-Q resonator filters, modulators, detectors, photonic transmitters and receivers [30, 31, 32, 33, 34, 35]. Traditional applications are transceivers for optical communications and optical interconnects - integrated sub-systems that focus on on-chip photonic communication between the cores of a multi-core processors, and chip-to-chip processor-to-memory links [36, 37, 38]. Recent advances include a path towards many-core processor-to-DRAM networks, where optical transceivers are used for cross-chip communication between the cores and dynamic random access memory(DRAM) modules through an on-chip global switch network [39]. This allows a large number of processor cores to communicate and access DRAM modules with sufficient bandwidth and power consumption, because photonic channels in this case are much more energy-efficient than electric ones. Another team has demonstrated an actual chip, fabricated using commercial 45nm CMOS process, that combines electronics and photonics in one seamless platform [29]. The chip includes an electronic micro-processor and a 1 MB memory bank that communicate with each other and with other components directly using silicon photonics fabricated on the same chip/platform. The chip contains over 70 million transistors and over 850 photonic components and employs a design where photonic devices are fabricated in a silicon layer that is a part of a standard CMOS process (therefore, no need for 3D electronic-photonic integration).

A new, recent, demonstration of a novel silicon photonics sub-system is a two-dimensional nanophotonic phased array. The team at MIT has demonstrated an

array of 64x64 nanoantennas, with the ability to balance power and phase of each element, in order to precisely manipulate the far field pattern. The phased array has a footprint of 576μm x 576μm, and operates at 1550nm [40]. In a separate work, the team has also demonstrated dynamic far-field beam shaping and steering [41]. Such a device has numerous potential applications, such as LIDAR, biomedical devices, and 3D holography.

1.2.4 US Government Silicon Photonics Strategic Initiatives

In the United States, the Defense Advanced Research Project Agency(DARPA) has been supporting integrated silicon photonics efforts with strategic programs aimed at gradually maturing this technology platform [42]. In 2005, the Electronic-Photonic Integrated Circuits (EPIC) program was launched to demonstrate a suite of high performance individual integrated components such as detectors, modulators, high-Q wavelength division multiplexing filters, and efficient on/off chip couplers [43, 44]. The EPIC effort also went beyond from individual high performance components to demonstrate integrated photonic sub-systems such as on-chip analog-to-digital converters (ADC) and fast photonic transceivers. The program was able to successfully mature several silicon photonics technologies in both academic and industrial settings. Next, DARPA's Photonically Optimized Embedded Microprocessors(POEM) program was launched to push towards photonic microprocessor-to-memory communication [45] and has so far resulted in two successful demonstrations, both fabricated using 45nm CMOS platforms. In the first demonstration, the Oracle team has produced a 6-channel link with a bit rate of 48 Gb/s which ran at 1.95pJ/bit [46]. In the second demonstration, a multi-university team has demonstrated a link with 5 Gb/s bandwidth at 1.3pJ/bit (described in the previous subsection) [29]. Commercial photonic transceivers became a realistic application that was further picked up and funded by the industry [34].

The next strategic DARPA move was to fund further silicon photonics sub-systems that were not picked up by the industry yet but could have large potential impact in both defense and non-defense-related applications. The agency focused on the re-

maining problems of heterogenous integration of a light source onto a photonic chip, 3D integration of electronic CMOS with CMOS-compatible silicon photonics, and applications that center around mode-locked lasers and their stabilization, to enable an on-chip low-noise microwave oscillator. The Electronic-Photonic Heterogeneous Integration(EPHI) program, and a subsequent Direct-On-chip Digital Optical Synthesizer (DODOS) program were launched in order to facilitate this effort. These two programs funded and motivated most of the work presented in this thesis, therefore, we describe them in more detail in Sections 1.3 and 1.4.

Building on the continuing success of DARPA-funded advances in integrated photonics, the US Department of Defence announced a competition for over $100 million in federal funding, to create a new Integrated Photonics Institute for Manufacturing Innovation(IP-IMI) [47]. The institute's goal is to create an end-to-end photonic ecosystem in the US, in order to lower the cost of entry barrier to integrated silicon photonics for US-based companies. The State University of New York (SUNY), partnering with numerous other institutions (including MIT), submitted a proposal called American Institute for Manufacturing(AIM) Photonics that was selected to receive the funding and to run IP-IMI. AIM Photonics currently has over 70 members, and has a goal of streamlining the entire integrated photonics process - the steps and services provided include design, layout, fabrication, packaging, and testing/characterization, all assuming multi-project wafer(MPW) service, and multiple options for each service provided [48]. The benefit of multi-project wafer service is splitting a large silicon wafer between the customers, so that each customer gets some fraction of the wafer. This significantly reduces the barrier to silicon photonics business entry and should allow numerous companies to launch their silicon photonics projects. A complete process design kit has been created for numerous multi-layer active and passive components that are now standardized and well-characterized. This allows the users to quickly create desired sub-systems in a plug-and-play type environment. AIM Photonics should revolutionize and catalyze integrated photonics industry in the US by reducing numerous entry barriers and therefore enable many US companies to enter integrated photonic business in the US using US facilities.

1.3 Electronic-Photonic Heterogeneous Integration Program

Numerous integrated photonics components have been fabricated using several existing fabrication platforms over the last decade. Such components include low loss waveguides, high speed modulators, splitters, filters, detectors, interferometers, light sources, and many more complicated optical sub-systems. SOI wafers were able to deliver many of those components but were unable to also have an integrated light source as an integral part of such sub-circuits. Having a light source integrated on a silicon chip, and the ability to co-integrate photonics and electronics, opens the door to many larger, new integrated photonic sub-systems. In particular, on-chip mode-locked lasers could be developed and on-chip control loops with nanosecond response time could be used to stabilize such on-chip MLLs, enabling the integrated optics version of a low noise microwave oscillator.

A low noise RF oscillator, a system of a particular interest to DARPA for numerous applications such as high speed communications, imaging, clocks, remote sensing, and many others has been demonstrated by, among other methods, extracting an RF signal from an optical comb laser source [49, 50, 51]. Various laser comb sources (more recently fiber-based) and various feedback/stabilization techniques have been demonstrated. However, most such low-noise microwave oscillators have been done using a scheme that included a separate optical frequency comb source (fiber or solid-state based) with conventional optomechanical/fiber components and all the stabilization/control loops implemented using traditional microwave components. Such systems are bulky, expensive, and alignment sensitive.

1.3.1 EPHI: Goals/Objectives

DARPA's Electronic-Photonic Heterogeneous Integration (EPHI) program was initiated to come up with a reliable process to heterogeneously integrate the light source directly on SOI chip [4], to develop a platform for 3D CMOS electronic-photonic

integration scheme, and to develop a fully-on-chip low noise microwave oscillator [42].

Key deliverables of the EPHI program are the overall integration scheme and the three demonstrations of fully-on-chip microsystems/components:

1. Continuous Wave Laser Source
2. Pulsed Laser Source
3. Low Noise RF Source

Required specifications of those components are listed in Table 1.1. The ideal outcome of the program would be a realization of all three demonstrations with electronics and photonics 3D-integrated on one chip, all the light sources integrated directly on the same chip, and a full system having low footprint and low electric power consumption.

Component	Specification Type	Specification Value
CW Laser Source	Wavelength range	1-2μm
	Output power	> 20mW
	RIN	< -165dB/Hz @ 10kHz
	Frequency noise	<100 Hz^2/Hz @ 100Hz offset <10 Hz^2/Hz @ 1kHz offset <1 Hz^2/Hz @ 10kHz offset
Pulsed Laser Source	Wavelength range	1-2μm
	Peak power	>200mW
	Repetition rate	20 GHz
	Absolute jitter	< 10 fs (integrated 1 Hz to 10GHz)
RF Oscillator	Output frequency	20 GHz
	RF output power	> 20mW
	Phase noise	-104dBc/Hz @ 1 Hz offset -124dBc/Hz @ 10 Hz offset -144dBc/Hz @ 100 Hz offset -161dBc/Hz @ 1 kHz offset -161dBc/Hz @ 10 kHz offset

Table 1.1: DARPA EPHI program specifications. Full list of specifications can be found in [4].

A straightforward (though challenging to implement in practice) solution to the light source integration is some form of III-V source bonding to SOI chip. Such an ap-

proach has been pursued, with various degrees of success, by several large institutions and companies, with detailed results discussed in [52, 53, 54].

3D Electronic-Photonic integration has several potential approaches. While direct co-fabrication of CMOS electronics and photonics is possible, it presents certain difficulties and limitations because an optimized electronics CMOS process is not always best for integrated photonics requirements. A better approach is to wafer-bond CMOS wafers, which are optimized for CMOS electronics, with CMOS-compatible photonics wafers optimized for photonics. Previously proposed approaches for wafer-bonding include the so-called flip-chip technology based on either microbumps or through-Silicon vias (TSVs). Both techniques have been successfully demonstrated, but they are currently limited by large parasitic capacitance [55, 56].

1.3.2 EPHI: MIT Approach

MIT's EPHI approach relies on a silicon photonics fabrication platform using back-end-deposited rare-earth-doped glass as a gain material, with 3D integration using through-oxide vias to connect CMOS and photonic layers. Low noise microwave signal generation would be demonstrated using optical frequency division by locking an on-chip mode-locked laser at 1550nm to a stabilized CW laser fabricated on the same chip.

For this program, MIT has partnered with College of Nanoscale Science and Engineering (CNSE) in Albany, for CMOS electronics/photonics fabrication and with UC Berkeley for CMOS development.

MIT's RF oscillator approach is based on RF signal extraction from an integrated mode-locked laser, where the output of the mode-locked laser is locked to a separate CW laser, fabricated on the same platform. Because a major part of this thesis focuses on mode-locked laser development for this EPHI RF oscillator, we describe this approach in details. Low phase noise and low timing jitter microwave signals have been extracted from MLLs in the past, with solid state or fiber-based lasers used as a comb source; frequently, an ultra-stable oscillator was used as a reference for the system [49, 50]. MIT's approach allows to significantly reduce the footprint,

eliminate alignment issues and reduce power requirements to the system by making all components fully integrated on chip. Full architecture of our oscillator is shown in Figure 1-1.

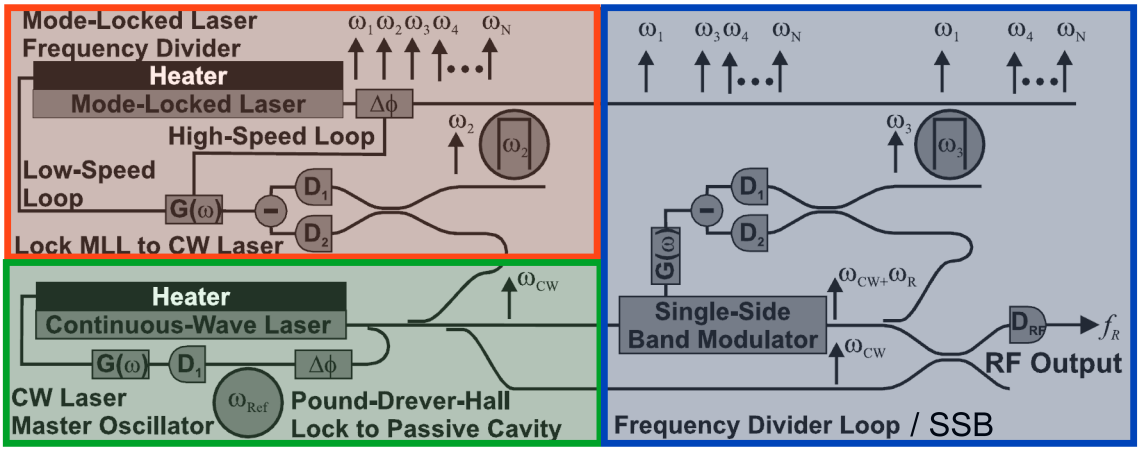

Figure 1-1: MIT EPHI RF oscillator architecture.

The oscillator consists of the three main sub-systems that have been proposed to meet the goals stated in the DARPA EPHI BAA as presented in Table 1.1. Each component, with designed specifications as proposed by MIT team, is illustrated in Figure 1-1, and described below:

1. **Erbium-ytterbium integrated CW laser**. Fiber-based Erbium-ytterbium lasers have been demonstrated with exceptional linewidths [57], and thus with relatively low frequency noise. Theoretically, the frequency noise of a narrow linewidth CW laser should be limited by the Schawlow-Townes limit [58]. However, in practice, thermal and spontaneous emission-based noise sources make it difficult to directly achieve the Schawlow-Townes limit. Locking a CW laser master oscillator to a thermally stable passive cavity (for example, an integrated athermal microring resonator) using a standard Pound-Drever-Hall(PDH) [59, 60] loop allows to correct for most of the noise sources and to significantly reduce the phase noise [61]. Therefore, a PDH-stabilized Erbium-Ytterbium-based integrated CW laser on chip can serve as a master oscillator for the final EPHI synthesizer.

2. **Erbium-based integrated mode-locked laser**. To do optical frequency division, we propose an integrated on-chip Erbium-based mode-locked laser, stabilized to the CW Master Oscillator described above. Detailed design and development of this laser are presented in Chapter 4. Timing jitter, and thus corresponding phase noise, of the free-running mode-locked laser are proportional to the pulse duration, and inversely proportional to the pulse energy. Thus, the shorter the pulses the lower the timing jitter. For free running MLLs, the typical measured timing jitter is on the order of a few picoseconds. To significantly reduce this number, the MLL is locked to the stabilized CW laser. This allows to transfer the low phase noise of the CW laser directly to the MLL lines. The locking is accomplished by beating the CW laser and one line of the MLL on a balanced photodiode, and using the output to control the repetition rate of the laser (with either the piezo that holds saturable absorber or integrated heater within the laser cavity). At this point, the stabilized mode-locked laser should have a phase noise that exceeds specifications in Table 1.1.

3. **Integrated Single-Sideband Modulator (SSB) (optional)**. The final, optional, step in the oscillator demonstration has been proposed in order to potentially increase the microwave output of the stabilized MLL in step 2). The idea is to use the MLL for its low noise and high repetition rate specifications but to also utilize the remaining power in our integrated CW laser to increase the magnitude of the resulting RF signal. This is accomplished by using an integrated SSB with which the CW laser is frequency-shifted by the value specified by a selected MLL line (for example, for a 1GHz MLL, the 20GHz RF beat would be fed to the SSB, to frequency-shift the CW laser by 20GHz). This frequency-shifted output of the SSB (at f_{cw}+20GHz) is combined with the original CW laser (at f_{cw}) on a balanced photodetector. The output of this photodetector is the difference between the two incident frequencies: f_{output}=f_{cw} + 20GHz - f_{cw}=20GHz. Thus, the final microwave output would be at 20GHz (used here as an example - this could be any desired harmonic of

MLL repetition rate). The heterodyne gain of the balanced detector, provided by CW laser, allows for higher amplitude final RF output, preserving the low phase noise obtained from locking the MLL to a stabilized CW laser.

1.3.3 EPHI: Photonics Integration Approach

Fabrication for the EPHI program is done at the College of Nanoscale Science and Engineering (CNSE) in Albany, NY, on a 65nm CMOS-compatible 300mm wafer platform. CMOS and Photonics wafers are optimized individually, and 3D-integrated as a last fabrication step. The photonics layer stack is shown in Figure 1-2, and includes two silicon nitride layers, a silicon waveguide layer with optional ridge (with dopants where necessary), germanium photodetectors, a metal layer, and metal pads. Active devices, such as modulators, are done in silicon, while passive waveguides for the MLL and most CW lasers are fabricated using silicon nitride layers. A 70μm-wide trench is etched over the mode-locked laser gain region (labeled as "TR" in Figure 1-2), in order to confine the gain material close to the FN layer and thus confine the optical mode in Al_2O_3:Er^{3+}, but have it be "anchored" to the structure by silicon nitride. The thicknesses of each Si_3N_4 layer are 200nm, and the thickness of silicon is 220nm, as provided by standard SOI wafers, with an optional 100nm ridge.

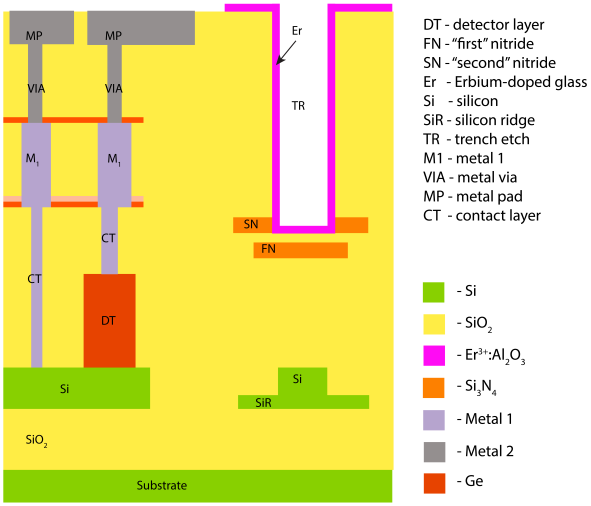

Figure 1-2: MIT EPHI photonics layer stack (not to scale).

MIT's proposed 3D integration scheme, illustrated in Figure 1-3, relies on through-oxide vias (TOVs), where the photonic and CMOS wafers are bonded prior to dicing, using an intermediate oxide layer. The silicon handle of the photonics wafer is then removed, and vias are drilled through the oxide layers only. This approach has resulted in parasitic capacitance of 1.45 fF, an over of magnitude improvement over the TSV process [62, 63]. Moreover, the process is wafer-scale, and has an almost 100% yield.

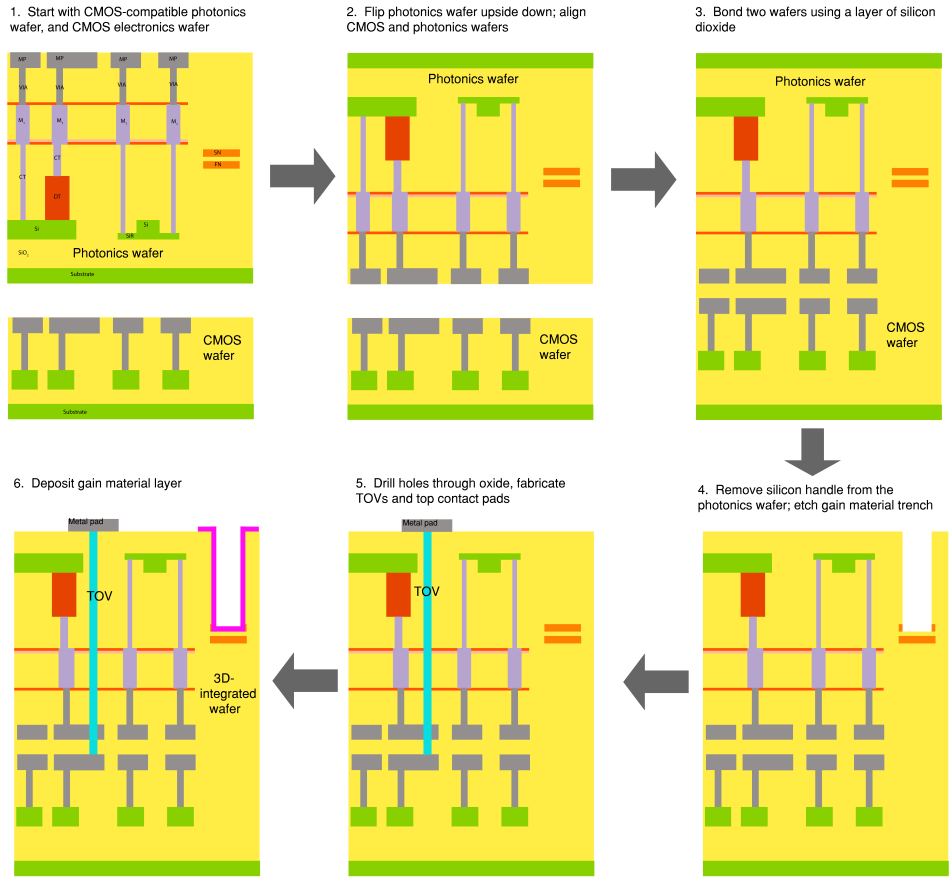

Figure 1-3: MIT/CNSE 3D integration approach, developed during EPHI program.

The photonics layout is done in Cadence Virtuoso using the SKILL Code interface, where components are laid out using in-house developed parametrized cells (p-cells). Smaller p-cells are combined into p-cells for larger sub-systems, which allows for efficient layout manipulation. Moreover, CMOS and photonics layers use the same Cadence environment, allowing one a complete flexibility to design 3D-integrated structures. Design-rule-checking (DRC) for each layer and structure are implemented.

Together, photonic simulations, layout p-cells, and corresponding DRCs constitute the so-called Process-Design Kit (PDK), which allows for a plug-and-play photonics design environment.

The MIT gain material for the 1550nm CW and MLL lasing wavelength is rare-earth-doped Aluminum Oxide Glass (Al_2O_3), that has been previously demonstrated as an excellent platform for low-loss optical gain media [64, 65]. For optical C-band lasing, Erbium ions are used as dopants in Al_2O_3, producing a material with up to 1dB/cm small signal optical gain. Al_2O_3:$Er^{3+}$is deposited in one step using back-end-of-the line RF sputtering process, over the entire chip. The depositions are done at MIT's Microsystems Technology Laboratories(MTL) using commercial sputterer system. The gain material is currently pumped optically, but the pump diode could be eventually co-integrated on the same chip. This approach allows for both CW laser source and mode-locked laser to be implemented using the same gain platform and in fact the same gain film, because the film is deposited as a blanket over the entire chip. For the 3D integration scheme, once photonics and electronics are bonded, depositing gain material is the last step; however, care should be taken in order to use deposition process where the temperature in sputtering chamber does not melt underlying metals in CMOS and photonics parts of the wafer. To this end, MIT has demonstrated a low temperature and high optical quality Al_2O_3:Er^{3+}process [66]. Further specific details on gain material fabrication, spectroscopic parameters, and performance in integrated lasers can be found in Chapter 4, and also in [67, 68].

1.3.4 EPHI: Progress/Outcomes To-Date

As of Spring 2017, the EPHI effort has been in full implementation at MIT for over 4 years. The program has produced many novel break-through demonstrations, both in integration/fabrication techniques and in novel silicon photonics devices/systems demonstrations. We highlight a few of those accomplishments here.

3D CMOS/photonics wafer-scale integration [62], discussed in Section 1.3.3, is a major accomplishment with large implications for integrated photonics industry. Other fabrication platform accomplishments include CW DFB and DBR lasers, based

on a segmented Si_3N_4 waveguide architecture. Low temperature(250°C) deposition of high optical quality Al_2O_3:Er^{3+} was demonstrated for the first time, allowing for safe co-integration of Al_2O_3-based gain media devices (CW and MLL lasers, amplifiers) with CMOS and metal layers [69]. Zero thermo-optic shift resonators have been demonstrated on the EPHI platform by using negative thermo-optic coefficient amorphous TiO_2 as a cladding for positive thermo-optic coefficient Si_3N_4 [70].

Integrated mode-locked lasers have been developed and Q-switched and Q-switch-mode-locked operation has been demonstrated at 1550nm [71], with over 10mW of CW power on-chip and with Q-switching rates from 200kHz to 2MHz (see Chapter 4 for detailed development).

For the final oscillator demonstration, an extensive fiber-based oscillator testbed has been implemented with commercial-off-the-shelf components as well as home-built fiber lasers, to mimic our future integrated oscillator and to model and study the phase noise in such systems [72]. The main difficulty was the inability to implement the 1f-2f interferometry for f_{ceo} stabilization using the SOI platform. Therefore, a synchronous pump modulation scheme was implemented to stabilize f_{ceo} instead, in experimental testbed. This scheme was successful in achieving very low phase noise for home-built stretched pulse fiber lasers, but fell short of required specifications (Table 1.1) for soliton fiber-lasers, indicating additional noise sources in those systems.

Full photonic transceivers on-chip have been demonstrated using the MIT EPHI platform, operating at 6Gb/s, with a receiver consuming 460fJ/bit and a transmitter consuming 100fJ/bit [73]. CMOS-compatible whispering gallery germanium-on-silicon photodetectors have been demonstrated, with 32GHz bandwidth, 1.04A/W responsivity, and low dark current [74].

Perhaps one of the key achievements of MIT EPHI effort to date is integrated nanophotonic phased arrays. MIT's Photonic Microsystems Group has developed a technology which consist of 2D arrays of vertically emitting optical nano-antennae, with ability to balance optical power and phase in each component. This allowed for a complete control over the far-field pattern and 51° degrees of steering at 100kHz for the devices centered in the telecom C-band [40, 75]. Applications of this technology

include free space communications and LIDAR. Additionally, the team has recently demonstrated visible-wavelength (λ_0=635nm) phased array operation [76] with direct applications to 3D holography.

1.4 Direct-on-Chip Digital Optical Synthesizer

Optical frequency combs have been demonstrated in the 1980s [77, 78], and have since enabled numerous interesting applications (see Section 1.1), one of those being a synthesis of optical frequencies with high precision, followed by ultra-stable optical clocks. However, such systems are laboratory-scale, require numerous components that need precise alignment, and numerous expensive equipment pieces. This limits their potential applications in the field. To address those challenges, in April of 2014, DARPA solicited for proposals to create an optical frequency synthesizer, referenced to an external 10MHz oscillator.

1.4.1 DODOS: Goals/Objectives

DARPA's Direct-on-Chip Digital Optical Synthesizer (DODOS) program was launched to produce an optical ultra-stable frequency line, in the communications C-band, and reference it to an external 10MHz clock [5]. Major requirements of the program are listed in Table 1.2, and emphasize outstanding relative stability to the reference clock, precise tunability, under 1cm^3 volume, and under 1W total electrical power consumption.

With such aggressive size, and power requirements, integrated photonics with CMOS control electronics is the only realistic approach to demonstrate the final synthesizer. Therefore, the goal of the program is to leverage integrated photonics knowledge to miniaturize a known large physical system, keeping specifications very tight and drastically reducing the size. The program is structured in 3 Phases. Phase I demonstration should include photonics components only, with each major component working according to desired specifications independently, along with a full synthesizer demonstration that should include several photonic chips connected together with free

Metric	Goal
Tuning Resolution	<1 Hz
Relative Stability	$< 10^{-13}/\tau$, for $\tau \in \{1s, 10^5 s\}$
Central Output wavelength	1550nm
Output Wavelength Tuning Range	± 25nm
Input Reference Frequency	10MHz
Frequency Switching/Settling Time	1μs
Volume	1cm^3
Power Consumption	< 1 W
Operating Temperature Range	0° to 50°C

Table 1.2: DARPA DODOS program specifications. A complete list of specifications can be found in [5].

space optics / fibers / optical amplifiers, and bench-top control electronics. Phase II should demonstrate all integrated photonics components connected and working together on the same chip (co-integration), and bench-top electronics. Phase III demonstration should include the full photonics part of the synthesizer and CMOS control electronics integrated together.

1.4.2 DODOS: MIT Approach

The proposed solution, from the MIT team, to create a full DODOS synthesizer, centers around the stabilized on-chip frequency comb to be realized in a Silicon Photonics platform [79, 80]. A high level schematic of the MIT DODOS approach is shown in Figure 1-4. A mode-locked laser, centered around 1900nm, is directed to a supercontinuum generating silicon waveguide that creates the optical spectrum spanning from ∼1100nm to ∼2400nm. The 2400nm part of the spectrum is filtered out and is used in the on-chip silicon-based frequency-doubler device. The frequency-doubler device creates optical spectrum around ∼1100nm, which is then combined with the 1100nm spectrum from the supercontinuum device on the RF detector. The combined beat note allows for the f_{CEO} detection and locking. The repetition rate of the mode-locked laser is locked to a multiple of a 10MHz RF source. The 1900nm wavelength used for the comb generation is important because it allows for 1f-2f generation in silicon and

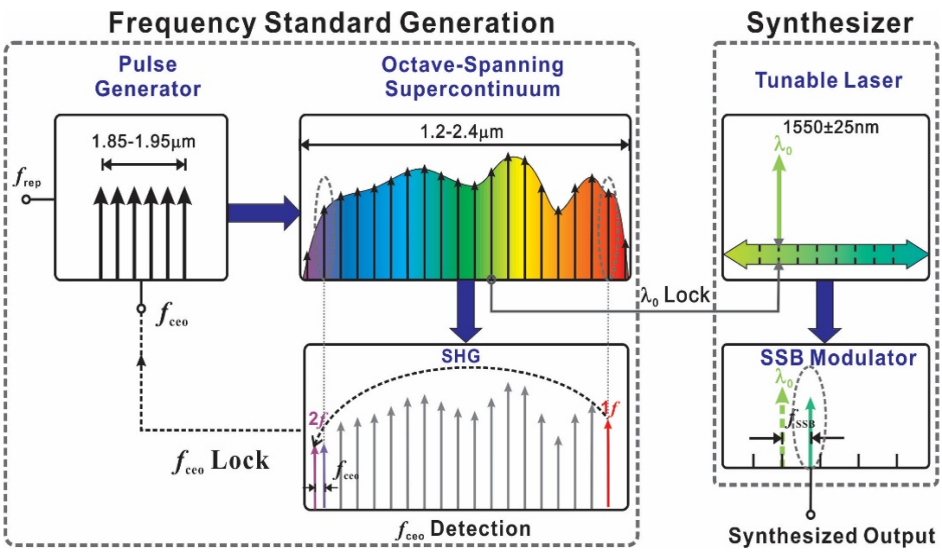

Figure 1-4: MIT DODOS high level architecture.

just falls into the bandwidth range where the 2f part (≈1100nm range) is outside of the silicon absorption spectrum, while the 1f part (2400nm) is in the region of low two-photon absorption in silicon. This setup produces a fully-stabilized comb referenced to an external oscillator. The 1550nm part of the comb is then filtered out and allowed to beat with a separate 1550nm tunable CW laser, fabricated on the same platform, locking the CW laser to the comb. This produces an ultra-stable CW laser signal, completely referenced to an external RF oscillator. The in-between comb-line optical frequencies for the final synthesizer are generated from the CW laser using an integrated modulator.

MIT has partnered with CNSE for CMOS electronics/photonics fabrication, with UC Berkeley for CMOS development, and with UC San Diego for supercontinuum work.

1.4.3 DODOS: Photonic Integration Approach

Fabrication for the DODOS program is done at SUNY CNSE on a 65nm CMOS 300mm wafer platform. Full 3D integration is achieved by wafer-bonding of a silicon photonics wafer to the CMOS wafer using through-oxide vias developed by MIT

during the EPHI program (Section 1.3.3). Our integration approach allows for fabrication of all the required devices using the same CMOS-compatible process and then for the 3D-integration of electronics and photonics together using through-oxide vias, thereby making a truly integrated fully-on-chip device. The full photonics layer stack is shown in Figure 1-5. It includes a silicon waveguide layer with optional ridge, three silicon nitride layers, a full suite of dopant implants, germanium photodetectors, and two metal layers. The designs of the mode-locked and CW lasers rely on stoichiometric silicon nitride(Si_3N_4) in SiO_2, which has low optical propagation losses. Individual layer thicknesses for silicon nitride FN and SN layers are 200nm each, and the thickness of silicon Si layer is 380nm. Although the common thickness of a silicon layer on Si-on-SiO_2wafers is 220nm, this layer height is inadequate for an octave-spanning supercontinuum-on-silicon generation, due to the very large normal dispersion of a 220nm-tall silicon waveguide. CNSE has developed a process to grow the Si layer to 380nm to produce low-loss Si waveguides, which enables operation in the anomalous dispersion regime for efficient supercontinuum generation. The three nitride layers are necessary for design flexibility, and for robust silicon-to-silicon nitride layer transition components. The final losses of our waveguides, fabricated using this platform,

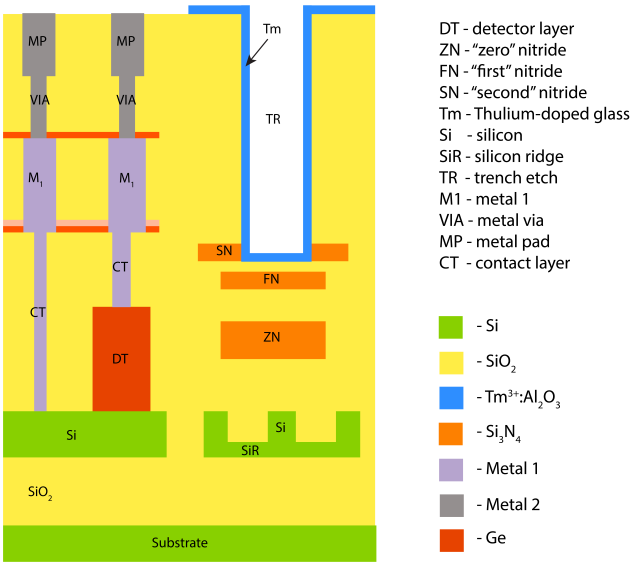

Figure 1-5: MIT DODOS full photonic layer stack.

are 0.6 dB/cm for Si_3N_4 waveguides, 0.74 dB/cm for passive gain waveguides with narrow trench, 0.4 dB/cm for passive gain waveguides with wide trench, and 1.2-1.5 dB/cm for silicon ridge waveguides.

Photonic layout for DODOS program is done using a PDK that was described in Section 1.3.3, and developed for EPHI program. Many components were added and modified and seamlessly integrated with an existing PDK at MIT.

The gain material for our Thulium and Erbium-based lasers is deposited at MITs Microsystems Technology Laboratories, with a single fabrication step, with no lithography required. The material is deposited into a predefined trench ("TR" layer in Figure 1-5, while the gain waveguide itself is defined by Si_3N_4 in SiO_2. Rare-earth-doped aluminum oxide glass (Al_2O_3) is deposited at high temperature using RF sputtering off Aluminum and Thulium (or Erbium) targets, with O_2 flowing separately into the chamber at a pre-defined rate. Erbium doping is used for 1550nm CW lasers, and Thulium doping is used for 1900nm lasers. While Al_2O_3:Er^{3+} has been demonstrated in the past as an excellent gain material for integrated photonics [64], Al_2O_3:Tm^{3+} was developed at MIT for the first time for DODOS program [6]. The gain materials are completely characterized spectroscopically, in order to optimize the active ion concentrations and to properly design the integrated lasers.

1.4.4 DODOS: Progress/Outcomes to-Date

By summer of 2017, MIT's DODOS development had been in full swing for a year and a half, and the program had just entered Phase II stage. Major accomplishments from Phase I are summarized below.

- **Al_2O_3:Tm^{3+} gain material development, Al_2O_3:Tm^{3+} CW laser.** MIT has developed Thulium-doped aluminum oxide glass as a gain platform for integrated photonics. Deposition conditions, such as temperature, pressure, O_2 flow rate, and RF power to sputtering targets have been optimized, and the first integrated CW DFB and DBR lasers were demonstrated using this platform. The maximum on-chip lasing power achieved for the DFB and DBR devices were

267mW and 387mW, with slope efficiencies of 14% and 23%, respectively [81].

- **Integrated mode-locked laser at 1900nm.** A fully-on-chip mode-locked laser (MLL) at 1900nm was demonstrated under the DODOS program, with sub-picosecond pulse duration [82]. The laser uses MIT's silicon photonics platform with Si_3N_4 in SiO_2photonic layers and uses Al_2O_3:Tm^{3+}, pumped at 1600nm, as the optical gain material. Two different mode-locking methods were investigated. First, semiconductor saturable absorbers were used for mode-locking. For those devices, Q-switched mode-locking was demonstrated. Second, a fully integrated on-chip artificial saturable absorber was designed for the DODOS program, therefore allowing us to make the laser with no off-chip components and no additional alignment steps. CW mode-locking and Q-switched mode-locking were demonstrated for the on-chip artificial saturable absorber lasers. Integrated MLLs are designed using three silicon nitride layers [FN, SN, ZN in Figure 1-5], along with a large trench, labeled "TS" in Figure 1-5, where the gain material is deposited. Design, development, and characterization of these mode-locked lasers are the main topics of this thesis, and are presented in detail in Chapter 3.

- **Integrated frequency doubler (2200nm→1100nm).** The first-ever fully-integrated frequency doubler in silicon has been developed and demonstrated by MIT for the DODOS program [83]. The device is based on the electric-field-induced second harmonic generation (EFISH) effect, where a DC field is used to break the symmetry of a silicon crystal, inducing a large $\chi^{(2)}$ in silicon, which is proportional to its large $\chi^{(3)}$. The device architecture is based on a ridge silicon waveguide, with quasi-phase-matched spatial p-i-n junctions, where the DC field is applied. Devices were demonstrated for several pump wavelengths (2μm region) and characterized using both CW and pulsed sources. The measured efficiency of the second harmonic, for a 1-mm long waveguide, is $P_{2\omega}/P_{\omega^2} = 12\%/W$, which corresponds to $\chi^{(2)}$=41pm/V.

- **Integrated octave-spanning supercontinuum device.** Octave-spanning

supercontinuum generation in silicon was demonstrated on the DODOS platform using a ridge silicon waveguide [84]. The device, which was measured using a 1900nm short-pulse source, spans 1.2-2.4μm range, and produces -20dBm of coherent supercontinuum. The coherence of the spectrum at the 1f and 2f spectral ranges was measured and verified. The strength of the supercontinuum signal at 1f and 2f was measured, and an signal-to-noise calculation was performed coupled with the frequency doubler device efficiency to verify an acceptable level of the f_{ceo} beat note.

- **Bench-top optical frequency synthesizer.** A bench-top synthesizer testbed with commercial-off-the-shelf (COTS) components was fully implemented. This testbed is based on a commercial 250MHz mode-locked laser in the optical C-band, that was passed through highly nonlinear fiber to generate spectrum from $1\mu m$ to $2.1\mu m$. f_{rep} and f_{ceo} of the comb were locked to different RF sources, both derived from a common 10MHz oscillator. A commercial tunable CW laser was locked to the stabilized comb, and the frequency stability, tuning range, and switching time were measured. Next, a bench-top synthesizer testbed with MIT DODOS silicon photonics components, instead of COTS devices, was demonstrated. In particular, the supercontinuum spectrum was generated using MIT's integrated silicon waveguide, the 1f-2f interferometry was performed using MIT's integrated frequency doubler, and the CW tunable laser used for final optical frequency generation was MIT's on-chip Erbium-based laser.

Other demonstrated integrated devices include a wide-band sharp roll-off WDM filter [85], that separates supercontinuum spectrum into 2000nm channel, 1000nm channel(to do 1f-2f interferometry), and 1550nm channel, to later lock the CW laser to this comb line and the 50nm tunable integrated C-band Erbium-based laser. An integrated pulse compressor has been designed and taped out, with a purpose of further shortening optical pulses coming out of the mode-locked in such a way as to generate the most supercontinuum. All the devices described in this section are fabricated using the same photonic layer stack, and therefore could be completely integrated

together on a single silicon chip.

MIT has successfully demonstrated most of the individual components required for the final optical frequency synthesizer and is strongly positioned to show a successful demonstration of all the photonic components integrated on the same chip by the end of Phase II. A diagram of our Phase II architecture is shown in Figure 1-6. All the photonic devices, except for 790nm pump for thulium lasers, and 980nm pump for erbium lasers, would be integrated on the same chip, and all the electronic control loops would remain as commercial off-the-shelf devices/setups, which could be integrated pending successful program continuation into Phase III. As of September 2017, MIT is in process of taping out the run schematically illustrated in Figure 1-6.

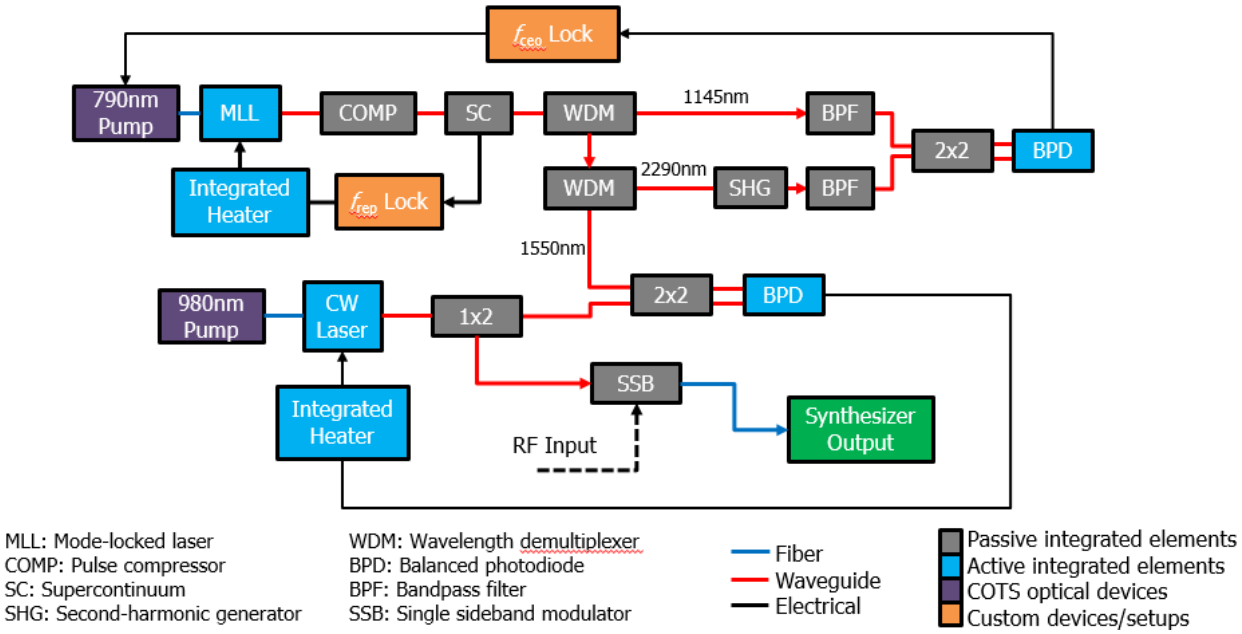

Figure 1-6: MIT DODOS Phase II synthesizer diagram

Thesis Contributions

The work in this thesis centers around the devices and systems made during the tenure of two major DARPA programs at MIT, as presented in Sections 1.4.1 and 1.3.1. Numerous graduate students, post-docs, and research scientist from Photonics

Microsystems Group, Optics and Quantum Electronics Group, and Ultrafast Optics and X-Rays Group have contributed to various parts of the general effort.

Since the main topic of this thesis centers on integrated artificial saturable absorbers and on-chip mode-locked lasers, below we list key contributors to this particular effort:

- **Gain Material Depositions** The deposition of active gain material for Erbium-based mode-locked lasers was done by Dr. Jonathan Bradley, Dr. Anna Baldycheva, Gary Riggott, E. Salih Magden, and Nanxi Li. Deposition of active material layers for Thulium-based mode-locked lasers was done by Gary Riggott, Nanxi Li, and E. Salih Magden.

- **Fabrication Facilities** All our devices were fabricated at SUNY CNSE, in Albany, NY.

- **Artificial Saturable Absorber work** This work was done fully and entirely by thesis author.

- **Mode-locked Laser Design and Development** The development of all integrated mode-locked lasers presented in this thesis was done by thesis author in collaboration with Patrick Callahan. While thesis author focused more on mode-locking devices, the physics of mode-locking, full system specifications, modeling, and complete characterization, Patrick Callahan focused on in-depth integrated photonics design of the individual laser elements (except for nonlinear interferometer). All mode-locked laser results and achievements presented in this work were possible because of this close continuous collaboration.

Chapter 2

CMOS-Compatible Artificial Saturable Absorber

Laser mode-locking methods and underlying physical mechanisms have been investigated and studied since late 1960-s [86, 87, 88, 89]. Today, several mature and well-understood mode-locking techniques are routinely used in scientific community and industry. The challenge, for integrated mode-locked lasers, is to implement some of those mode-locking methods in an integrated, CMOS-compatible way. Ideally, such mode-locking implementation would not use any external devices, and would not require any extra fabrication steps on top of the standard CMOS-compatible photonics process. To enable this, one needs to use known physical principles of mode-locking and apply them to engineer a new device architecture, according to CMOS process constrains and requirements.

There are two broad categories of mode-locking methods - active mode-locking and passive mode-locking. Active mode-locking uses an amplitude modulator inside of the laser cavity, to change the cavity loss with the rate equal to the laser round-trip frequency [90]. The modulator can be implemented in many different ways, such as, for example, electro-optic or acoustic-optic devices. Although it is relatively straightforward to design and implement, active mode-locking has several limitations. Apart from having a separate "driver" element in the cavity that needs to be controlled separately, the major limitation of active mode-locking is the difficulty is scaling

the pulse duration to below a few picoseconds. Therefore, active mode-locking is widely employed in applications where short pulse duration is not necessary. For femtosecond-level pulses, one needs to use passive mode-locking.

Passive mode-locking relies on the passive intensity-dependent loss element in the laser cavity. Such a device should have properties such that higher light intensities have decreased loss compared with lower intensities. When the loss of the cavity is decreased with increasing intensity, pulse formation and shaping follows. This method allows the pulse to shape itself after passing through the mode-locking element, and thus allows for much shorter optical pulses compared with active mode-locking.

This chapter briefly reviews some of the most common passive mode-locking techniques, discusses their potential implementation in CMOS-compatible integrated photonics, and presents a complete design and characterization of a CMOS-compatible artificial saturable absorber, based on one of the reviewed mode-locking techniques.

2.1 Passive Mode-Locking Methods

Two classes of devices used for passive mode-locking are real saturable absorbers and artificial saturable absorbers.

Real Saturable Absorbers

A physical mechanism known as "saturable absorption" results in an intensity-dependant loss property of a material or a device. A saturable absorber element would have a certain amount of optical absorption at low light intensities. However, for higher light intensities, the absorption would be bleached, or saturated, hence the device would have lower absorption, and would transmit more light. Some of the early work on saturable absorption for mode-locking of lasers was done using dye lasers, with organic dye acting as a saturable absorber element. Femtosecond pulses were demonstrated, and some of the early mode-locking theory was developed around those results [87, 91]. A different physical saturable absorption method has been developed in the early 1980s, based on a semiconductor saturable absorber mirror [92, 93]. This device is based on a quantum well structure, where the time

response of the excited carriers allows for a certain loss modulation in the cavity (see Section 2.1.1 for further details). Such devices have been designed to operate both in reflection and transmission regimes. Because semiconductor saturable absorber mirrors are much easier to maintain and operate, they quickly replaced dye-based methods. Recently, novel saturable-absorption materials have been demonstrated based on graphene, quantum-dots, and carbon nanotubes.

Artificial Saturable Absorbers

Further mode-locking methods have been developed using devices referred to as "artificial saturable absorbers". Such devices do not have a physical absorption element that saturates/bleaches; however, they do have an intensity-dependent loss element (usually based on Kerr-nonlinearity), that can initiate and sustain mode-locking.

A key advantage of artificial Kerr-nonlinearity-based saturable absorbers is their instantaneous response. Since Kerr nonlinearity is considered to act on the order of a few femtoseconds, such mode-locking elements are considered "fast". On the other hand, the response of a semiconductor saturable absorber is limited by its recovery time (see Section 2.1.1 for details)which ranges from hundreds of femtoseconds to tens of picoseconds - such saturable absorbers are considered "slow". Generally, a slow saturable absorber device has a response time that is larger than the pulse duration, while a fast saturable absorber has a response time that is faster than the actual pulse duration. With the proper balance of dispersion and nonlinearity in the laser cavity, fast saturable absorbers allow for much shorter pulse durations compared with slow saturable absorbers [94].

Section 2.1.1 describes semiconductor saturable absorbers in detail, while Section 2.1.2 describes common artificial saturable absorber implementations. The terminology and parameters to evaluate many types of real and artificial saturable absorber devices come directly from the physics and the structure of semiconductor saturable absorbers, as described in the next section.

2.1.1 Semiconductor Saturable Absorbers

Saturable absorber mirrors have been around since late 1980s, and are based on a semiconductor layer, deposited on top of a Bragg reflector [93, 92]. Depending on the research institution, geographical location, and exact structure of the saturable absorber, they have been given different abbreviation terms in scientific literature. Most common terms are SAM(Saturable Absorber Mirror), SBR(Saturable Bragg Reflector), and SESAM(Semiconductor Saturable Absorber). In this work, we shall use the term "SBR". The basic structure of such a device is shown in Figure 2-1 [a]. The Bragg reflector is typically made of 20 to 60 alternating refractive index layers designed to provide a high reflection for a particular wavelength. At low incident power, the reflection of the saturable absorber mirror is determined by the reflection profile of the Bragg stack minus the absorption of the semiconductor material (Figure 2-1 [c]). The semiconductor material has a bandgap corresponding to the desired central wavelength so that the incident light excites the carriers from the valence band to the conduction band. At low incident power levels, the amount of carrier excitation is small. However, as more photons are incident on the SBR, the available carriers temporarily move from the valence band to the conduction band, and the semiconductor cannot absorb as much light. In this case, the absorption of the semiconductor well becomes saturated, and it starts transmitting more light (hence the term "saturable absorption"). Since the semiconductor layer is directly on top of the Bragg reflector, the full SBR device now has reduced absorption, so it starts temporarily reflecting more light. Therefore, we have an energy-dependent reflection - the higher the incident energy - the higher the reflection of the SBR. This leads directly to pulse shaping, as higher intensities in the cavity (peak of the pulse) experience higher reflection, while lower intensities (edges of the pulse) experience more loss. The pulse is therefore shaped in time domain. Unlike with artificial saturable absorbers where the device reflection depends on the incident peak power, SBRs instead are saturated with numbers of photons, and hence with incident energy.

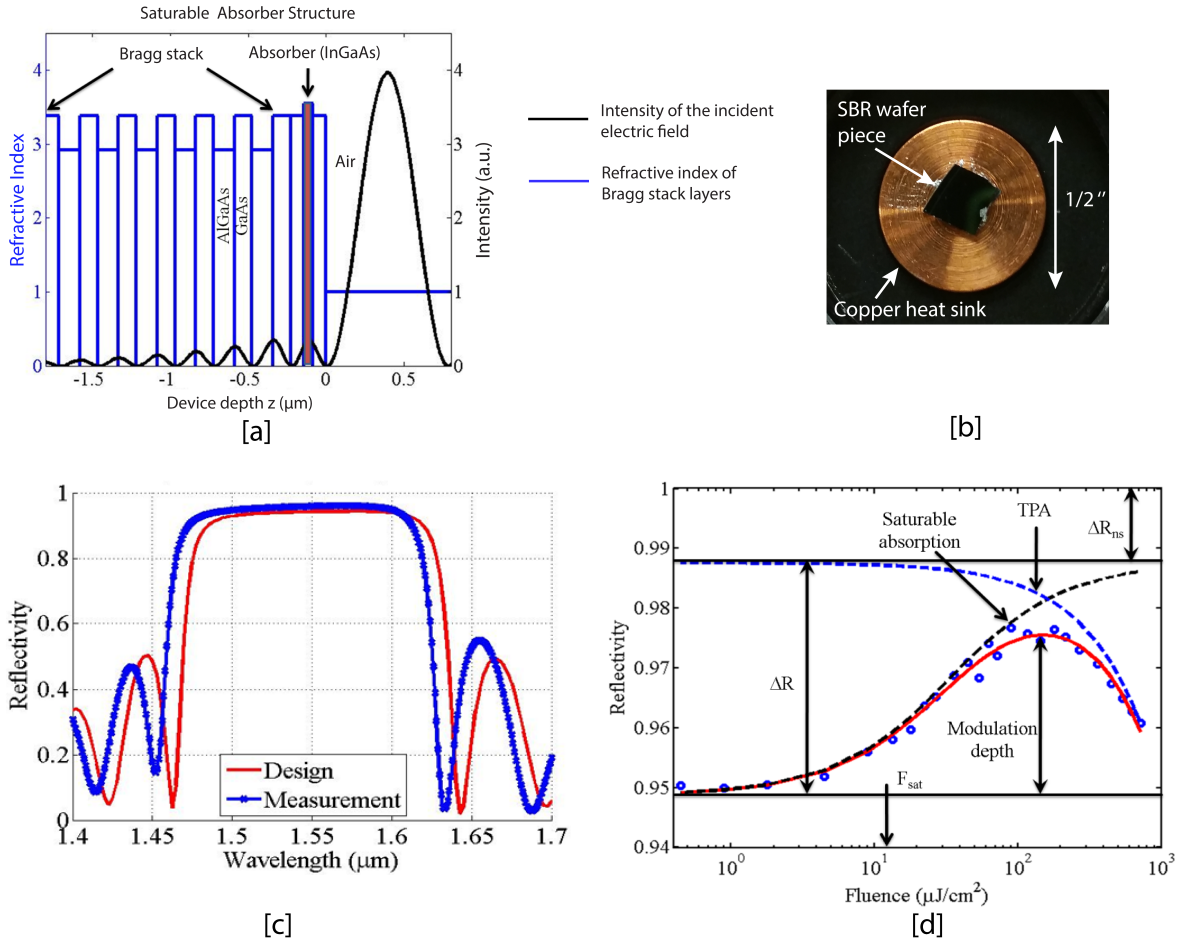

Figure 2-1: Semiconductor Saturable Absorbers: [a] Structure of the typical SBR, showing actual SBR design, courtesy of H. Shen [1]; [b] A photo of an SBR mounted on a heat sink; [c] CW reflection profile of an SBR device shown in part[a],courtesy of M. Sander [2]; [d] Saturation properties of a typical saturable absorber, courtesy of A. Motamedi [3].

The excited carriers within the quantum well eventually relax back to the ground state via a combination of thermalization and recombination processes [95]. This recombination time is called a "recovery time" of a saturable absorber. It effectively determines how fast an SBR can shape the pulse, and therefore the final pulse duration. The recovery time usually consists of two components - the fast and the slow recovery times, respectively, where the fast recovery time comes from the fast

carrier thermalization process, and slow recovery time results from carrier recombination. Typically, fast carrier recovery times are on the order of tens or hundreds of femtoseconds, while slow recovery times are on the order to several picoseconds. Generally, in the literature and vendor websites, unless otherwise noted, the term "recovery time" refers to slow recovery time. Because this recovery time is generally limited by intrinsic semiconductor carrier recombination times, most SBRs are classified as "slow saturable absorber".

Figure 2-1 [d] explains saturation properties of a typical SBR [3, 96]. The power-dependent reflection is characterized as a function of incident fluence on the saturable absorber. At low incident fluence, the device reflects a certain amount of light (95% in Figure 2-1 [d]). When the fluence is increased, the reflectivity goes up. Eventually, two-photon-absorption(TPA) properties in the semiconductor layer inhibit further increase in reflection, and the curve exhibits a reflection roll-off. Any SBR device, even when the absorption is perfectly bleached, has a certain amount of intrinsic loss, called non-saturable loss, or R_{ns}. Without the TPA, the reflection could increase up to the maximum value (1-R_{ns}). However, TPA lowers this maximum reflection value. The difference between the highest reflection point and the CW reflection is called **modulation depth**. It is a critical parameter pertaining to how strongly the device would favor the peak of the pulse as opposed to pulse wings. Higher modulation depth usually means it is easier to achieve stable mode-locking, however, it always comes at the expense of lower CW reflection. Another important parameter is the saturation fluence, which is defined as the incident fluence that reduces the saturable absorption to $1/e$ of its starting value. Saturation fluence is used to characterize and compare different saturable absorbers. For optimum mode-locking operation, the fluence on the SBR should be 2-3 times higher than the saturation fluence value. Table 2.1 lists relevant SBR parameters, corresponding units of measure, and typical values.

Saturable absorber mirrors have been studied for over twenty years [97]. Today, both the scientific community and industry have a good understanding of their operation, design, carrier dynamics, and the resulting pulse-shaping mechanism. SBRs are used in many university laboratories as well as many in industrial laser systems.

Parameter	Variable	Unit	Approximate value range
Non-saturable loss	R_{ns}	%	0.2 - 20
Saturable loss	ΔR_{sat}	%	0.2 - 50
Modulation depth	ΔR_M	%	0.1 - 50
Saturation Fluence	F_{sat}	$\mu J/cm^2$	10-100
Recovery time	τ_r	ps	0.2-10
Central wavelength	λ_0	μm	0.8, 1.1, 1.55, varies

Table 2.1: Semiconductor Saturable Absorber: parameters, units, and approximate values

The key advantage of using an SBR over other mode-locking methods is that the slope of the saturation fluence curve in Figure 2-1 is always positive, meaning the laser experiences higher reflection with increased CW power. This is not the case for many interference-based mode-locking methods, such as additive-pulse mode-locking, where the initial state may have lower reflection with higher CW power, which actually inhibits mode-locking, and the system needs to bee stabilized interferometrically in order to work properly (see Section 2.1.3 for details). SBRs don't need any such interferometric stabilization. Due to this property, lasers with SBRs in place typically self-start more easily. However, mode-locking methods based on Kerr nonlinearity are "fast", while SBRs are "slow". Therefore, SBRs have a self-starting advantage, but Kerr-based methods can produce much shorter pulses. To mediate this, SBRs are sometimes used together with Kerr-based mode-locking methods, to facilitate self-starting. For example, in a typical Titanium-sapphire pulsed systems, Kerr-lens mode-locking is used to shorten the pulses, but SBR or a fast dithering mirror are used to help the system self-start reliably [98]. If the system had just the SBR, it would produce much longer pulses. If it had just the Kerr lens, it would have difficulty self-starting.

Traditional SBRs are fabricated using semiconductor epitaxial growth, most commonly using Molecular Beam Epitaxy (MBE). Such methods allow for unprecedented control over individual layers, in terms of thickness, refractive index and strain. However, maintaining an MBE facility is very costly. Moreover, the growth process is

very time consuming, as it relies on careful fabrication of 20 to 60 individual material layers. In the past, few groups in the world were able to reliably produce SBRs with specific properties. This meant that general SBR and SBR-based mode-locked laser research was restricted to the groups that had MBE growth facilities, and their collaborators. For example, at MIT, in early 2000s, a collaboration between an MBE group and ultrafast lasers group had produced a wide variety of novel SBR structures, had investigated their properties, including ultrafast carrier dynamics, and had demonstrated many fiber-based and eventually waveguide-based lasers using in-house grown SBRs [99, 100, 101, 96]. This was made possible by a very close collaboration between several research groups, and an impressive in-house MBE growth facility. Today, a commercial company (BATOP Gmbh [102]) offers a variety of SBRs for purchase, for different wavelengths, modulation depths, bandwidths, and overall configurations. Commercially available SBRs allowed numerous research groups to demonstrate mode-locking by using, for example, their proprietary novel gain materials, and quickly purchasing an SBR from a commercial vendor. The drawback is that of course, although BATOP provides most of the SBR specifications listed in Table 2.1, they do not disclose the internal structure of the device, including semiconductors used, exact nature of the Bragg stack, etc. Nevertheless, BATOP has lowered the barrier of entry to mode-locked laser research for many groups and small companies that could not afford MBE growth facilities.

Although SBRs are a gold standard in many laser systems, they nevertheless have numerous limitations, which are particularly prohibitive for CMOS-compatible integrated mode-locked lasers.

Some of the limitations of semiconductor saturable absorbers are listed below.

- **Wavelength restrictions** The key element of a semiconductor saturable absorber is a direct gap semiconductor. The material used for this layer must have the electronic bandgap corresponding to the desired operating wavelength. Therefore, one is restricted to the available semiconductors and their respective bandgaps. Certain wavelengths (1550nm, 800nm) could be implemented using common materials (InGaAs, Si), other wavelength ranges are difficult, many

are not currently accessible.

- **Damage Threshold** A well-known problem with SBRs is their low damage threshold. High optical energy incident on the absorber heats it up locally and may produce thermal damage on the surface of the device. This becomes more prominent when a laser goes into Q-switching mode prior to mode-locking. Q-switched pulses have repetition rates on the order of several kHz, and therefore a much higher energy per pulse than CW-mode-locked pulses with a repetition rate in the multi-MHz or GHz range. Many lasers go into Q-switching prior to mode-locking, and thus SBRs become damaged prior to being able to mode-lock the laser. For many saturable absorbers, the incident fluence that induces a thermal damage is not far off from the saturation fluence, making it difficult to find a good operating regime for the laser. Several techniques exist for mitigating this problem, most of which rely on heat dissipation management methods. Typically, SBRs are mounted on copper heat sinks, moreover, SBR handle-wafer-substrate thinning has been demonstrated successfully, to increase the heat flow from the SBR to copper heat sink [96]. Additionally, pump-reflective coatings have been deposited on top of the SBRs to prevent the pump laser from damaging the absorber [3]. Although mitigating techniques exit, they further increase the complexity of SBR fabrication process and use, and thermal damage remains a frequent problem.

- **Slow recovery time** As explained in the beginning of this section, the recovery time of an SBR depends strongly on the intrinsic carrier dynamics in a semiconductor. Typically, such values are on the order of 1-20ps. This effectively limits the pulse duration to approximate that of the recovery time. Various techniques, usually based on induced defects in a semiconductor layer, exist to shorten the recovery time (compressive strain during the growth of the absorber, fast ion bombardment [103]). However, they always come at the expense of increasing the non-saturable loss. Kerr-lens mode-locking methods allow for much shorter pulse durations.

- **Alignment** Nearly all SBRs physically are small pieces of a wafer mounted on a heat sink. This small wafer piece needs to be carefully aligned to the laser cavity, making sure the SBR is exactly perpendicular to the structure. The reflection of the Bragg stack is very sensitive to the incident angle. Half-a-degree drift makes a difference, resulting in the loss of a mode-locked state. With modern nano-positioning equipment, such alignment is possible, but this is not a robust solution for long-term stability.

- **High incident losses** An SBR is typically "butt-coupled" to the laser cavity, where the light from the main laser section is incident upon the SBR, and then reflects from the SBR back into the laser. This means the light experiences the loss of entering/exiting the cavity, twice. For integrated waveguides, this means exiting and entering the chip, and thus experiencing the facet coupling loss twice, in addition to any SBR-internal losses. Typically, SBR-induced losses, including on/off chip or fiber coupling losses, are on the order of 1.5-5 dB total. While less of a problem for solid-state of fiber-based lasers with plenty of gain, this becomes problematic for the on-chip lasers with a smaller footprint/cavity length.

- **Fabrication and packaging** SBR is a device with an extensive sub-structure, that needs to be carefully grown in controlled conditions. For CMOS-compatible integrated lasers, this presents a challenge, since MBE growth of required materials is not a standard CMOS process, plus the device would need to be deposited on the facet of the chip, after all other layers have been fabricated. This calls for a different mode-locking method. Preferably, the mode-locking device would not require any special, additional fabrication steps, and could use an integrated photonics device, which is done in one of the standard material layers (for standard photonic CMOS-compatible layer stack in MIT process, see Figure 1-5).

Novel saturable absorber materials

Although semiconductor saturable absorbers have been the gold standard for over

20 years, new types of devices based on the physical saturable absorption effect have been demonstrated over the past 10 years, that offer significant advantages and new opportunities, compared to semiconductor-based SBRs. Saturable absorbers have been successfully demonstrated using quantum dots, carbon nanotubes, and graphene. Carbon nanotubes(CNTs) have sub-picosecond recovery times, and large bandwidth that can be tuned by varying nanotube diameter [104]. A combination of various diameters allows to make CNT films with over 200nm of bandwidth. In 2005, Schibli et al demonstrated a 68fs pulse duration Er/Yb glass laser, mode-locked using a film of CNTs deposited on a broadband dielectric mirror [105]. Later, Kieu and Wise demonstrated a thulium-holmium co-doped fiber laser, with 750fs pulse duration, with all-fiber components, mode-locked entirely using single-walled CNTs [106]. Quantum dots have also proven to be a good material for saturable absorbers - they cab be very broadband (a mixture of various diameter quantum dots exhibits inhomogeneous broadening), and the bandgap can be easily tuned by changing quantum dot diameter [107]. A structure of a quantum-dot-based saturable absorber is similar in that a broadband Bragg stack is used together with a saturable absorption layer, in this case made of quantum dots [108]. The advantages of quantum-dot-based saturable absorbers over traditional SBRs are significantly larger bandwidth, flexibility in engineering the bandgap and hence the central wavelength of the device, and fast recovery times. Mode-locked lasers with pulse durations under 200fs have been demonstrated using a semiconductor quantum-dots-based saturable absorber [109]. Graphene is another promising material that has been used for saturable absorbers over the last few years. With zero bandgap, it is extremely broadband and has saturation fluence that has been reported to be significantly lower than that of SBRs [110, 111]. Moreover, graphene thickness variation, for multi-layer graphene, results in changes in the modulation depth of the saturable absorber, allowing for greater flexibility in laser design. Single layer graphene is typically synthesized separately in a chemical vapor deposition system. It is then "transferred" to a desired location, and patterned to a desired shape. Similarly to SBRs, graphene has a certain thermal damage threshold that becomes apparent with high fluence levels. However, as a graphene layer is typi-

cally only 1 atom thick, it can be deposited anywhere in the laser cavity (and not just on the end-reflector). Evanescent field mode-locking, achieved with a graphene film in on top of a D-polished optical fiber, has been demonstrated. Instead of being directly focused onto a graphene film, the light interacts with it evanescently over a specific length, and thus thermal damage does not occur as easily [112]. Graphene-based waveguide modulators have been demonstrated in various configurations [113]. Therefore, this material could be used both as passive and active saturable absorber (the latter in modulator configuration). Overall, graphene offers interesting and unique opportunities as a novel saturable absorber material. Better and more efficient ways for transferring and patterning graphene are currently being investigated.

2.1.2 Artificial Saturable Absorber Implementations

In this section, we briefly review some of the well-established artificial saturable absorber mode-locking methods and their potential implementation in integrated photonics. Additive Pulse Mode-Locking is further explored in greater detail in Section 2.1.3.

1. **Kerr-Lens Mode-Locking (KLM)**. Kerr-lens mode-locking, discovered in the 1990s [114], is based on a Kerr nonlinear medium and the subsequent self-focusing effect [115]. The light, while propagating within a material with a Kerr nonlinearity, experiences self-phase modulation and also a self-lensing effect, where the central portion of the beam having higher intensity also has higher nonlinear refractive index. Gaussian beams have a spatial distribution profile such that light in the spatial center of the pulse has a much higher intensity compared to the edges. Since nonlinear refractive index is proportional to intensity, the central portion of the pulse will experience higher nonlinear index ($n = n_0 + \Delta n = n_0 + n_2 I$), and be delayed relative to the wings, as would happen with a lens (Figure 2-2[a]). As a result, there is intensity-dependent self-focusing of the beam. Soft-aperture KLM uses an internal effect to produce mode-locking, such as pump/signal overlap in the gain medium - higher intensity

increases the overlap between the pump and the signal, increasing gain. Hard aperture mode-locking uses a physical aperture that is placed inside the cavity. The aperture blocks the outer portion of the Gaussian beam, allowing only the more strongly self-focused part of the beam to go through. This produces increased transmission for increased power in the cavity, and achieves an artificial saturable absorption effect. KLM is a popular mode-locking method that is typically implemented in multi-mirror resonator laser configurations, with some type of glass or a crystal being used for the optical gain material. A major advantage of KLM is its bandwidth - it is the most broadband type of mode-locking. Together with the discovery of the titanium-sapphire lasing material (also very broadband), KLM allowed for generation of ultrafast pulses with 5-6fs duration, with only a few optical cycles underneath the pulse [116, 117]. One of the disadvantages of this method is difficulty with self-starting of the mode-locking. However, this has been successfully mitigated by adding a semiconductor saturable absorber into the cavity [98], or by having a small dithering mirror.

2. **Additive Pulse Mode-locking (APM)**. Additive pulse mode-locking, also called coupled-cavity mode-locking, is based on a nonlinearity-induced interference between the two pulses [118, 119, 120, 121]. The method is illustrated in Figure 2-3, and involves an auxiliary cavity, which is length-matched to the main lasing cavity. A portion of the pulse exits the main cavity and enters the auxiliary cavity (originally implemented in a single mode fiber), where a nonlinear phase shift is imparted on the pulse. When the pulse from the auxiliary cavity returns back to the main cavity, it interferes with the pulse from the main cavity in such a way that this interference is constructive at the central portion of the pulse, and destructive at the edges. Therefore, the edges experience higher loss in this laser, and the peak of the pulse gets favored. This leads to the pulse formation. Further details and calculations for additive pulse mode-locking are presented in Section 2.1.3. The interferometric stabilization required

to precisely match the lengths of the main and auxiliary cavities and to adjust the linear phase in the system limit the popularity of this mode-locking method in the industry. However, APM is generally a flexible technique because it can be used in many material systems and it could be designed for any wavelength, therefore, it could be potentially implemented in integrated photonics without major difficulties.

Integrated optical implementation of APM for CMOS-compatible process is presented with a complete design, simulations, and results, in Sections 2.2–2.4.3.

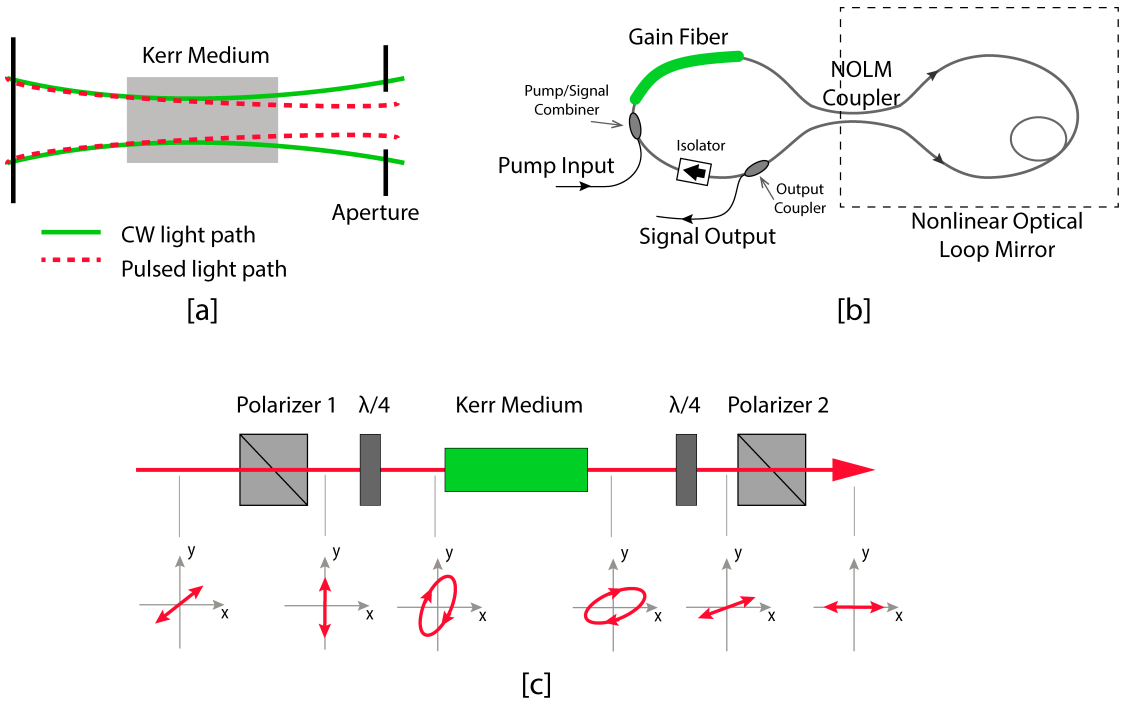

Figure 2-2: Passive Mode-Locking Methods: [a] Kerr Lens mode-locking illustration; [b] "Figure 8" laser, with NOLM used as a mode-locking device; [c] Nonlinear Polarization Rotation mode-locking illustration.

3. **Nonlinear Polarization Rotation (NPR)**. Nonlinear polarization rotation is a case of APM, and in fact uses the same physical principle [122, 118]. The technique, illustrated in Figure 2-2 [c], has been used mostly in fiber lasers. It relies on a birefringent element, a low linear birefringence Kerr medium, and a

polarization discriminator. A pulse passes through a birefringent element (typically, a combination of a quarter and half waveplates), and becomes elliptically polarized. It then enters a Kerr medium (typically a fiber with very low linear birefringence) with a certain nonlinear refractive index n_2. Because of the initial elliptical polarization, the x- and y- components of the electric field of the pulse are different, producing polarization ellipse. Those components pick up different nonlinear phases along the x and the y dimensions (but equal linear phase). This imparts a differential nonlinear phase shift between those x- and y- field components, and ends up rotating the polarization ellipse. By having a polarization discriminator at the end of the fiber, certain output polarization orientation is favored. Higher pulse intensities would rotate polarization ellipse further, hence, intensity-dependent transmission and the resulting pulse formation [123]. One drawback of NPR method is the need to manually adjust the initial polarization state of the system, usually by rotating a combination of waveplates [124]. Once this is done, the laser is very stable for long time periods. NPR is widely used in fiber lasers, and requires no interferometric stabilization. However, this method is limited to media with low linear birefringence.

An integrated version of an NPR-based device is theoretically possible to implement, especially because CMOS-compatible on-chip polarization rotators and splitters have been demonstrated recently [125, 126, 127, 128]. However, dielectric and semiconductor waveguides typical have 1 to 5% tolerances on their dimensions, meaning maintaining low linear birefringence over a required length of the device is challenging.

4. **Nonlinear Optical Loop Mirror (NOLM).** Nonlinear optical loop mirror, also called nonlinear Sagnac loop, is another a case of APM, usually implemented in the optical fiber [129, 130, 131]. The method is illustrated in Figure 2-2[b]. A fiber loop has an imbalanced coupler, with a splitting ratio different from 50/50. The pulse is split between the two arms, where the two arms later combine at the splitter. Each pulse is then traversing the same loop of fiber.

The pulses counter-propagate and interfere again at the coupler as they exit the device. The linear phase that counter-propagating pulses pick up is the same for both pulses, but the nonlinear phase is different, because it is proportional to optical power, and the power splitting ratio of the coupler is not 50/50. Therefore, the nonlinear phase difference between two counter-propagating pulses is $\Delta\phi_{NL} = \gamma L \Delta P$, where γ is the effective nonlinearity of the fiber, L is the effective fiber length, and ΔP is power difference between the two counter-propagating pulses. Thus the system exhibits a power-dependent nonlinear phase difference, which translates into output power modulation, which gives rise to optical pulses. NOLMs have been used extensively in fiber lasers due to their simplicity, and the fact that no additional elements are needed for their implementation. "Figure 8" laser is a common term used in a scientific community for a NOLM-based laser, for its double-loop appearance [132]. Frequently, one section of the "figure 8" contains the gain element, a pump/signal combiner, and an output coupler (which could all be fiber-based components - see Figure 2-2[b]), and the NOLM is another section of the "eight" in "figure 8". A gain section has also been incorporated into the NOLM itself on many occasions, in which case the device is called a NALM, for Nonlinear Amplifying Loop Mirror [133, 134]. A necessary component for all NOLM and NALM-based lasers is an isolator at the signal wavelength. If this isolator is lacking, and the laser has a "figure 8" configuration, it starts lasing in two counter-propagating directions, which leads to instabilities and irregular pulse trains.

Although it would be straightforward to implement a NOLM-like device using an integrated waveguide, the current lack of an integrated CMOS-compatible on-chip isolator would make stable lasing with consistent pulse trains impractical. Should such an isolator be developed in the future, NOLM-based integrated lasers could quickly become a reality.

2.1.3 Additive Pulse Mode-Locking

The basic theory and the main physical principle of our integrated saturable absorber relies on the additive pulse mode-locking method, that has been first described by Ippen et al in 1989 [118]. In this section we review the basic theory and relevant parameters of the conventional APM method, and later, in Section 2.3, we modify and refine this theory for our integrated approach.

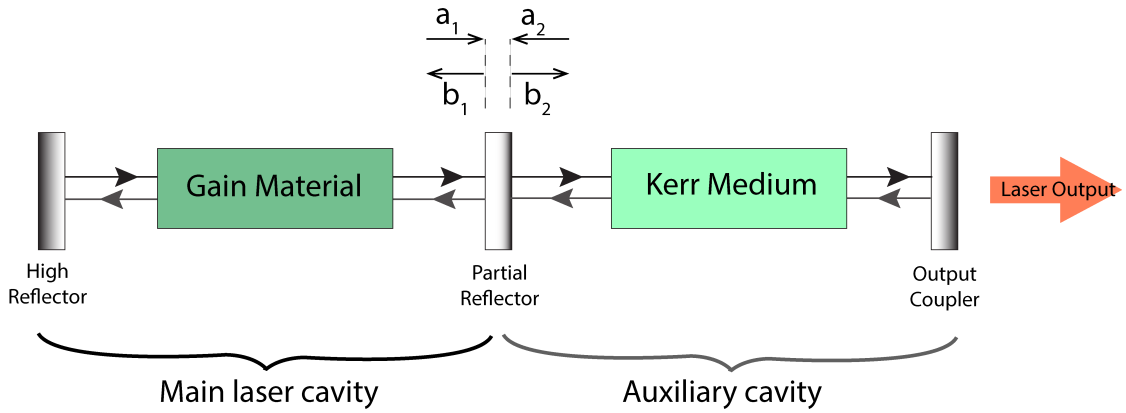

Figure 2-3: APM diagram.

Figure 2-3 illustrates the basic principle, where the main laser cavity contains the gain material, and the auxiliary cavity contains the Kerr medium. The light builds up in the main cavity, and the pulse, upon being incident on the partial reflector in the main cavity, is partially reflected back to the main cavity, and partially transmitted to the auxiliary cavity. The lengths of the two cavities should be identical. This way, the pulse that travels through auxiliary cavity and back to the main cavity will arrive to the partial reflector at the same time as the pulse that was reflected to the **main** cavity. The two pulses will therefore interfere at the partial reflector. If the linear and nonlinear phases imparted by the auxiliary cavity are properly adjusted, the pulses will interfere constructively at the center of the pulse, and destructively at the wings, therefore making the pulse shorter. Usually, linear phase between the cavities can be adjusted interferometrically in order to guarantee proper bias for pulse shortening.

Basic analytical theory of APM is presented below. It closely follows and elaborates on derivations in [118], [8], and [7].

The scattering matrix of the partial reflector in APM cavity, shown in Figure 2-3, is given by

$$\begin{pmatrix} b_1 \\ b_2 \end{pmatrix} = \begin{pmatrix} r & \sqrt{1-r^2} \\ \sqrt{1-r^2} & -r \end{pmatrix} \begin{pmatrix} a_1 \\ a_2 \end{pmatrix} \tag{2.1}$$

where r is a field reflection coefficient, and a_1, a_2, b_1, b_2 are field amplitudes in time domain, defined such that $|a|^2 = P$, where P is optical power. In the auxiliary cavity, the field a_2 should return to the partial reflector as b_2, after making one round-trip through this auxiliary cavity. Upon this round-trip, it picks up a linear transmission factor $\eta = e^{-\alpha L_{aux}}$ (where α is the linear power loss in [1/m], applied to the field amplitude as $\alpha/2$ field loss, over the length of $2L_{aux}$), and linear and non-linear phases ϕ_l and ϕ_{NL}:

$$a_2 = b_2 e^{-j(\phi_l + \phi_{\mathrm{NL}})} e^{-\alpha L_{aux}} = \eta e^{-j(\phi_l + \phi_{\mathrm{NL}})} b_2 \tag{2.2}$$

In the above equation, the linear phase is given by $\phi_l = \frac{2\pi}{\lambda} n L_{aux}$, where n is the effective refractive index of the auxiliary cavity; the nonlinear phase, over the round-trip of the auxiliary cavity, is

$$\begin{aligned} \phi_{\mathrm{NL}} &= \kappa |a_1|^2 \\ &= \frac{2\pi}{\lambda} n_2 \frac{\eta^2 (1-r^2) |a_1|^2}{A_{\mathrm{eff}}} 2L_{aux} \\ &= \left[\frac{4\pi}{\lambda} n_2 \frac{\eta^2 (1-r^2)}{A_{\mathrm{eff}}} L_{aux} \right] |a_1|^2 \\ &= \left[\gamma_{\mathrm{NL}}\, \eta^2 (1-r^2) 2L_{aux} \right] |a_1|^2 \end{aligned} \tag{2.3}$$

where λ is the central lasing wavelength, κ is a proportionality constant in units of W^{-1}, n_2 is the nonlinear refractive index of the auxiliary cavity, A_{eff} and L_{aux} are effective nonlinear area and length of the auxiliary cavity, respectively [135, 136]. The last line of the equation is the alternative notation, most commonly used in integrated waveguides, where an effective nonlinearity parameter γ_{NL}, in units of $(Wm)^{-1}$, is used instead of nonlinear index and effective area [135].

Next, we plug in Equation 2.2 in Equation 2.1, to find expressions of b_1 and a_1 as functions of a_2:

$$\begin{aligned} b_2 &= \sqrt{1-r^2}a_1 - ra_2 \\ &= \eta^{-1}e^{j(\phi_l+\phi_{\mathrm{NL}})}a_2 \\ a_1 &= \frac{1}{\sqrt{1-r^2}}\left[\eta^{-1}e^{j(\phi_l+\phi_{\mathrm{NL}})}\right]a_2 \end{aligned} \tag{2.4}$$

$$\begin{aligned} b_1 &= ra_1 + \sqrt{1-r^2}a_2 \\ &= r\left[\frac{1}{\sqrt{1-r^2}}\left[\eta^{-1}e^{j(\phi_l+\phi_{\mathrm{NL}})}\right]\right]a_2 + \sqrt{1-r^2}a_2 \\ b_1 &= \frac{1}{\sqrt{1-r^2}}\left[1 + r\eta^{-1}e^{j(\phi_l+\phi_{\mathrm{NL}})}\right]a_2 \end{aligned} \tag{2.5}$$

The field reflection coefficient back to the main cavity is obtained by dividing Equation 2.5 by Equation 2.4:

$$\begin{aligned} \Gamma &= \frac{b_1}{a_1} = \frac{1 + r\eta^{-1}e^{j(\phi_l+\phi_{\mathrm{NL}})}}{r + \eta^{-1}e^{j(\phi_l+\phi_{\mathrm{NL}})}} \\ \Gamma &= \frac{\eta + re^{j(\phi_l+\phi_{\mathrm{NL}})}}{\eta r + e^{j(\phi_l+\phi_{\mathrm{NL}})}} \end{aligned} \tag{2.6}$$

Equation 2.6 is the most general, exact field reflection expression, ignoring dispersion.

To make the result more intuitive, several assumptions are further made to the above model. Assuming small transmission factor, $\eta \ll 1$ and a Taylor expansion is used to approximate Γ near $\eta = 0$ as $\Gamma \approx \Gamma_{\eta=0} + \frac{\partial\Gamma/\partial\eta|_{\eta=0}}{1!}(\eta - 0) + ...$ Expanding to the first order, we get

$$\Gamma = r + \eta(1-r^2)e^{-j(\phi_l+\phi_{NL})} \tag{2.7}$$

Assuming small nonlinear phase ϕ_{NL}, we can make another approximation such that

$e^{-j\phi_{\mathrm{NL}}} \approx (1 - j\phi_{\mathrm{NL}})$:

$$
\begin{aligned}
\Gamma \approx\ & r + \eta(1-r^2)e^{-j\phi_l}(1 - j\phi_{\mathrm{NL}}) \\
=\ & r + \eta(1-r^2)\Big[\cos\phi_l - j\sin\phi_l - j\phi_{\mathrm{NL}}\cos\phi_l - \phi_{\mathrm{NL}}\sin\phi_l\Big] \\
=\ & r\ + \eta(1-r^2)\ \cos\phi_l \qquad\qquad \rightarrow \quad \text{term 1 – linear amplitude loss} \\
& - j\eta(1-r^2)\ \sin\phi_l \qquad\qquad \rightarrow \quad \text{term 2 – linear phase change} \\
& - j\eta(1-r^2)\phi_{\mathrm{NL}}\ \cos\phi_l \qquad \rightarrow \quad \text{term 3 – nonlinear phase change} \\
& - \eta(1-r^2)\phi_{\mathrm{NL}}\ \sin\phi_l \qquad \rightarrow \quad \text{term 4 – nonlinear amplitude change}
\end{aligned}
\tag{2.8}
$$

The result is four terms, corresponding to linear and nonlinear phase and amplitude changes. The nonlinear phase term ϕ_{NL} is proportional to the incident power through Equation 2.3. Therefore, terms 3 and 4 in the above equation are directly proportional to the incident power - hence we have power-dependent phase change and power-dependent amplitude change. The proportionality constants between field reflection coefficient and incident power, for phase and amplitude modulation terms, are called self-phase modulation (SPM), δ_{SPM}, and self-amplitude modulation (SAM), γ_{SAM} coefficients, respectively. Using the expression from Equation 2.3 in terms 3 and 4 of Equation 2.8, those coefficients are:

$$
\begin{aligned}
\gamma_{SAM} &= -\eta(1-r^2)\frac{\phi_{\mathrm{NL}}}{|a_1|^2}\ \sin\phi_l \\
&= -\left[\frac{4\pi}{\lambda}\eta^3(1-r^2)^2\frac{n_2}{A_{eff}}L_{aux}\right]\ \sin\phi_l \\
&= -\Big[2\gamma_{\mathrm{NL}}\ \eta^3(1-r^2)^2 L_{aux}\Big]\sin\phi_l
\end{aligned}
\tag{2.9}
$$

$$
\begin{aligned}
\delta_{SPM} &= -\eta(1-r^2)\frac{\phi_{\mathrm{NL}}}{|a_1|^2}\ \cos\phi_l \\
&= -\left[\frac{4\pi}{\lambda}\eta^3(1-r^2)^2\frac{n_2}{A_{eff}}L_{aux}\right]\ \cos\phi_l \\
&= -\Big[2\gamma_{\mathrm{NL}}\ \eta^3(1-r^2)^2 L_{aux}\Big]\cos\phi_l
\end{aligned}
\tag{2.10}
$$

It is instructive to note that in the absence of Kerr nonlinearity (i.e. $\phi_{\mathrm{NL}} = 0$), terms 3 and 4 of Equation 2.8 vanish, and we are left with linear interferometric equation for the field reflection. In this case, linear phase in the auxiliary cavity can be used to maximize the reflection $\Gamma = r + \eta(1-r^2)\cos\phi_l - j\eta(1-r^2)\sin\phi_l$, by setting $\phi_l = 0$: $\Gamma_{max} = r + \eta(1-r^2)$. However, keeping $\phi_l = 0$ and now adding Kerr nonlinearity also sets term 4 in Equation 2.8 to zero, and hence completely removes self-amplitude modulation - no pulse stabilization takes place. On the other hand, to maximize self-amplitude modulation and to get to increasing reflection for increasing pulse intensity, one needs to set $\phi_l = -\pi/2$.

Equations 2.8, 2.9, and 2.10 are valid only in a small transmission (and hence high loss) regime. In a low loss regime, on the other hand, the APM cavity behaves like a resonator where the reflection has characteristic resonance dips, while in a high loss / low transmission regime the reflection behaves more like a sinusoid. Exact definitions for γ_{SAM} and δ_{SPM}, with no approximations, are:

$$\begin{aligned} \gamma_{SAM} &= \frac{\partial\,|\Gamma|}{\partial |a_1|^2} \\ \delta_{SPM} &= \frac{\partial\,\angle(\Gamma)}{\partial |a_1|^2} \end{aligned} \tag{2.11}$$

where $\angle(\Gamma)$ is the phase of the field reflection, as in $\Gamma = |\Gamma| e^{j\phi}$, where $\phi = \angle(\Gamma) = \tan^{-1}\frac{\Im(\Gamma)}{\Re(\Gamma)}$.

As an example of characteristic behavior, we plot the power reflection of the APM cavity $R = |\Gamma|^2$, and associated SAM coefficient γ_{SAM}, for the following parameters: $\alpha_{lin} = 0.8$dB/cm, $L_{aux} = 10$cm (one way), $r = 0.85$, $\gamma_{NL} = 1.6$ (W m)$^{-1}$. Figure 2-4 [a] shows the absolute value squared of the field reflection coefficient Γ versus incident peak power ($P_{in} = |a_1(t=0)|^2$), where a large achievable modulation depth of over 50% is evident. The results are shown for three values of linear phase bias ϕ_l : $-\pi, -\pi/2,\ 0$. SAM coefficient γ_{SAM}, which is proportional to the slope of $|\Gamma|^2$ with respect to $|a_1|^2$, is shown in Figure 2-4 [b].

Figure 2-5 shows shortening of a pulse a single APM roundtrip, where the APM cavity has parameters as described above. Both input and output pulses are normal-

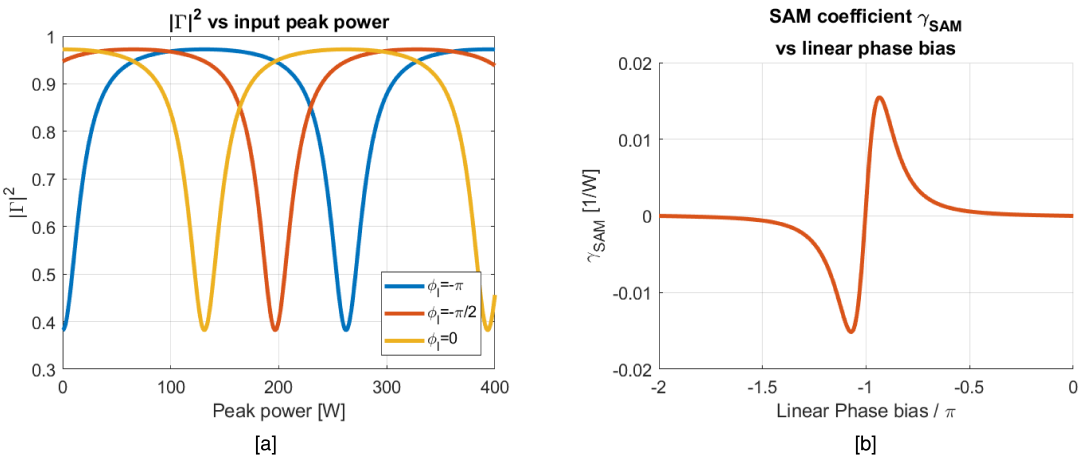

Figure 2-4: APM Response: [a] $|\Gamma|^2$ vs incident peak power, for three linear phase bias values; [b] Self-amplitude modulation coefficient γ_{SAM}, vs linear phase bias.

ized to their respective maximum power, in order to visualize the pulse shortening more clearly. The linear phase bias is set to -0.9π, which maximizes the SAM coefficient (according to Figure 2-4 [b]), and hence the pulse shortening. Figure 2-5 [b] shows percent pulse shortening, defined as $100\% \times \left[1 - \frac{FWHM(|b_1|^2)}{FWHM(|a_1|^2)}\right]$, versus peak input power $|a_1|^2$, for Gaussian and Sech^2 pulses, with 200fs input pulse duration. Pulse shortening over 6% is possible with proper adjustment of linear bias of APM cavity.

While field reflection coefficient Γ is the most straightforward to derive and directly relates to SAM coefficient, the physical measurable quantity is power reflection $R = |\Gamma|^2$, as optical power meters measure optical power, not the electric field. Experimental results should produce a figure similar to Figure 2-4[a], where one could extract modulation depth ΔR vs input pump power, as well as average power reflection value R. In order to be able to compare experiment and theory for APM-type saturable absorbers, we relate γ_{SAM} directly to ΔR and R:

$$\begin{aligned}\gamma_{SAM} &= \frac{\partial \Gamma}{\partial |a_1|^2} = \frac{\partial |\Gamma|^2}{\partial |a_1|^2}\frac{\partial \Gamma}{\partial |\Gamma|^2} = \frac{\partial |\Gamma|^2}{\partial |a_1|^2}\frac{1}{2|\Gamma|} \\ &= \frac{\partial R}{\partial |a_1|^2}\frac{1}{2\sqrt{R}}\end{aligned} \tag{2.12}$$

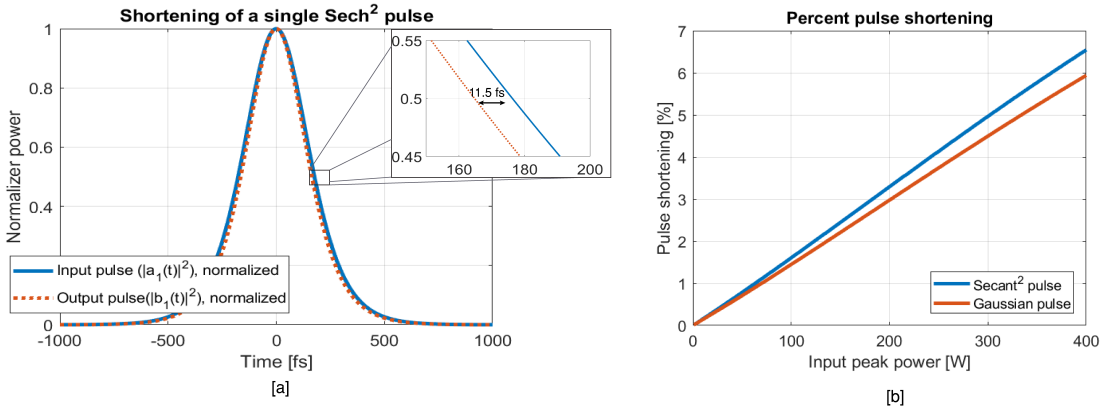

Figure 2-5: APM-induced pulse shortening: [a] Single pulse shortening with the APM cavity, corresponding to Figure 2-4, for fixed input power, linear phase bias of -0.9π, for secant squared 200fs input pulse duration; [b] Percent pulse shortening as a function of input power, for Gaussian and Sech^2 pulses, shown for linear phase bias of -0.9π and 200fs input pulse duration.

The definitions of the SPM and SAM coefficients as proportionality constants between field reflection coefficient and the incident power are standard in the literature, but exact formulas vary for a particular laser and mode-locking element geometries. A different example of calculating such coefficients, for a nonlinear Sagnac loop geometry, could be found in [7]. Both calculations (the one presented here, and in reference [7]) ignore dispersion, which could be easily incorporated, but makes the explanations less obvious. Moreover, an equivalent set of parameters could be derived for all Kerr-nonlinearity-based mode-locking methods described in Section 2.1.2. The strength of those parameters determines important mode-locking characteristics, such as stability of the pulses, possible pulse durations, and overall mode-locking regime, as described by the Haus Master Equation [137, 119] and presented in Section 3. Physical design of the mode-locked laser systems by carefully balancing gain, loss, SAM and SPM coefficients and dispersion should be the first step in designing any novel mode-locked laser.

The APM method has been used extensively in the scientific community, and some of the early demonstrations of solid state laser mode-locking have been implemented using this method. However, the requirement of interferometric stabilization of the

auxiliary cavity made it impractical for robust industrial applications. Instead, other mode-locking methods that essentially use APM but exploit a clever cavity geometry that does not require precise length stabilization, such as, for example, nonlinear optical loop mirror or NPR (described in Section 2.1.2), have become more popular. However, when applied to integrated photonics, one can easily design two waveguides of the same length, for any wavelength of interest. Moreover, effective Kerr nonlinearity of optical waveguides could be engineered to significantly exceed the values obtained with free space bulk materials [136, 135]. For this reason, APM is the most straightforward method to be implemented in integrated photonics. In the next section we show the design of a novel fully CMOS-compatible mode-locking element, which is fundamentally based on the APM pulse interference principle.

2.2 Operating Principle

A CMOS-compatible mode-locking element should ideally include only the materials that are already a part of the CMOS-compatible photonic layers within a particular fabrication platform. The Kerr-nonlinearity-based approach is a good choice for this task for several reasons. First, in integrated waveguides, device nonlinearity can be greatly enhanced by waveguide geometry [136], which enables over an order of magnitude increase in nonlinearity compared with a core material bulk value. Second, since the optical Kerr effect is considered instantaneous, proposed artificial saturable absorbers are "fast", meaning they are capable of supporting optical pulses on the order of a few femtoseconds, provided that a proper balance between dispersion and nonlinearity exist in the laser cavity. Finally, such devices could be designed for any operating wavelength, provided this wavelength is outside of the material's two-photon absorption range.

We propose a Kerr-nonlinearity-based artificial saturable absorber partially based on the APM principle. The schematic of the device is shown in Figure 2-6. The device acts as a linear reflector at low incident power and has a nonlinear reflection profile when incident peak power is high. Therefore, it acts as a saturable absorber,

and with proper laser cavity design it should be able to initiate and sustain short optical pulses. The device consists of an imbalanced coupler with power splitting ratio $\alpha/(1-\alpha)$, two long arms, and linear reflectors at the end of each arm. The light enters the device from the main laser cavity, gets split into two arms, propagates through each arm, reflects back, and exits the device through the imbalanced coupler. Part of the light is reflected back into the main laser (labeled as output 1 in Figure 2-6), and part of it exits the cavity through output 2. Desired nonlinear behavior of the device is caused by power-dependent pulse interference based on a difference between accumulated nonlinear phases in each arm. The accumulated nonlinear phase in each arm changes as a function of input intensity due to the Kerr nonlinearity: $\phi_{\mathrm{NL},i} = \frac{2\pi}{\lambda} n_{2,i} I_i L_i$, where I refers to intensity inside of the waveguide, λ is the central wavelength, n_2 is the nonlinear refractive index (responsible for the Kerr effect), and L is the length of the device. Subscript i stands for a particular arm of the device. Assuming identical lengths and cross-sections in both arms, with perfect end-reflectors, the nonlinear phase difference between the arms would be $\Delta\phi_{\mathrm{NL}} = \frac{2\pi}{\lambda}\frac{n_2}{A_{\mathrm{eff}}} L_{\mathrm{eff}}(P_1 - P_2) = \frac{2\pi}{\lambda}\frac{n_2}{A_{\mathrm{eff}}} L_{\mathrm{eff}}(2\alpha - 1)P_{in}$, where P_{in} is incident power. This power-dependent difference between the nonlinear phases in the two arms would give a power-dependent interference of the return signals at the coupler, which will result in a sinusoidal output power as a function of the input power of the NLI.

If the two arms of the device are identical (i.e. have the same length, width, and cross-section), and the end-reflectors at the end of each arm are identical as well, then the linear phase accumulated by the light beam in each arm is identical, and there is no *linear* phase difference. According to the theory presented is Section 2.2, with zero linear phase difference the device should not need any linear phase bias. However, for the case of integrated photonics implementation, small fabrication-induced differences on waveguide dimensions would almost certainly impart a small linear phase difference between the two arms of the device. Such linear phase difference is not power dependent, and could be mitigated by some form of linear phase bias in one of the arms.

Because of the interferometric principle and power-dependent nonlinearity, we

refer to the device in Figure 2-6 as Nonlinear Interferometer (NLI).

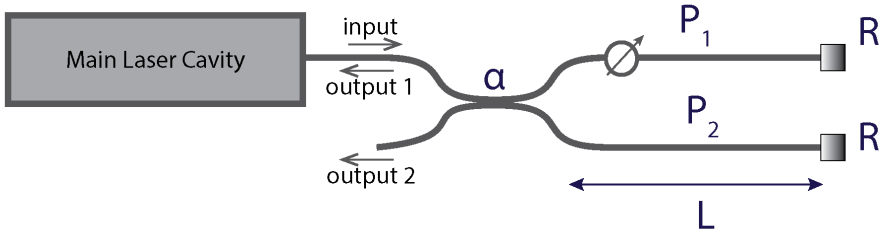

Figure 2-6: Schematic of a nonlinear interferometer.

If a nonlinear phase difference between the two arms is present, one of two situations is possible: 1) the reflection of the device, defined as fraction of input power that is reflected back into the laser, will increase as a function of the input power (this corresponds to positive SAM coefficient), 2) the reflection would decrease as a function of the input power (negative SAM coefficient). For the artificial saturable absorber effect, device output power should increase as a function of the input power. Thus, a proper phase bias should be used.

A nonlinear phase difference between the two arms (and thus artificial saturable absorption effect) can be achieved by any of the following methods:

1. Having the splitting ratio of the coupler that is different from 50/50. The nonlinear phase difference is maximized when $\alpha = 0.75$. However, this significantly lowers the overall reflection level of the device. We have designed and fabricated integrated splitters with splitting ratios of 96/4, 93/7, and 90/10.

2. Having two different end-reflectors. If one reflector has, for example, 10% reflection, and another reflector has 90% reflection, this will cause different intensities in the two arms of the device, and thus will lead to a nonlinear phase difference and artificial saturable absorption effect. However, this also introduces additional losses into the arms of the NLI.

3. Having two arms of different lengths. As the nonlinear phase in each arm is proportional to the length of that arm, the nonlinear phase difference between

the two arms could be achieved by having the arms be different lengths. In this case, care must be taken to account for differential group delay between the two arms, in order for optical pulses from each arm to arrive back to the coupler after traveling through the nonlinear interferometer, at the same time.

4. Having two arms of different cross-sectional geometries. The Kerr nonlinearity of the waveguide depends on both the materials used for the waveguide and the exact waveguide geometry. Having different cross sections will result in different effective nonlinearities in each interferometer arm, which will result in a different nonlinear phase shift. As in (3), care must be taken to match the group delays between the two arms. Having different arm lengths in order to compensate for the group-delay mismatch that is caused by different cross sections is one potential design option.

5. Any combination of methods (1)-(4) could be used together to achieve even greater nonlinear phase difference than what would be possible with just one method. For example, one could employ an unbalanced coupler, different end-reflectors, and different waveguide cross-sections/lengths in order to achieve the nonlinear phase difference desired.

For the devices demonstrated in this thesis, we chose to imbalance the nonlinear interferometer using the splitting ratio of the coupler only, as it is the most straightforward way to achieve SAM.

Although in this thesis we explore the NLI geometry presented in Figure 2-6, various other device configurations are possible. For example, instead of the end-reflectors, one may add another coupler at the left of the device, therefore making it a Mach-Zehnder-type device that works in transmission, as opposed to reflection. Another example of the same principle and different geometry would be using a multi-mode waveguide, where the two modes have different effective nonlinearities, and the power-dependent phase difference is achieved by coupling of the two modes together.

2.3 Theory

The theory for the NLI closely follows APM theory presented in Section 2.1.3, but includes important modifications for the particular geometry and device design. We start with the device schematic shown in Figure 2-7, where the a_i and b_i are field amplitudes defined such that $|a_i|^2$ is optical power. The coupler has a power splitting ratio $\alpha/(1-\alpha)$, or corresponding field splitting ratio of $r/\sqrt{1-r^2}$, where $r^2 = \alpha$.

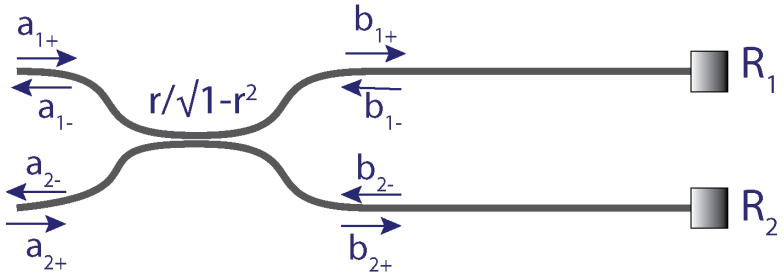

Figure 2-7: Nonlinear interferometer coupler

The fields right after the coupler are written in terms of the fields incident on the coupler as follows:

$$\begin{pmatrix} b_{1+} \\ b_{2+} \end{pmatrix} = \begin{pmatrix} r & -j\sqrt{1-r^2} \\ -j\sqrt{1-r^2} & r \end{pmatrix} \begin{pmatrix} a_{1+} \\ a_{2+} \end{pmatrix} = S \begin{pmatrix} a_{1+} \\ a_{2+} \end{pmatrix} \tag{2.13}$$

where S is the scattering matrix of the coupler. The light then propagates along each arm, reflects off the mirrors with power-reflections R_1 and R_2, and is incident upon the coupler again. For our particular device implementation, $R_1 = R_2 = R_m$, where m stands for "mirror", and both arms have identical cross-sections and length. With linear power-loss of the waveguide α_{loss}, one-way power transmission factor of the cavity is written as $\eta = e^{-\alpha_{\text{loss}} L}$. Before the fields enter the coupler for the second time, after round-trip propagation through the device, they could be written in terms

of the fields immediately after the coupler:

$$\begin{pmatrix} b_{1-} \\ b_{2-} \end{pmatrix} = \begin{pmatrix} e^{-\alpha_{\text{loss}}L}\sqrt{R_m}e^{-j\phi_1} & 0 \\ 0 & \sqrt{R_m}e^{-\alpha_{\text{loss}}L}\ e^{-j\phi_2} \end{pmatrix} \begin{pmatrix} b_{1+} \\ b_{2+} \end{pmatrix}$$
$$= \eta\sqrt{R_m} \begin{pmatrix} e^{-j\phi_1} & 0 \\ 0 & e^{-j\phi_2} \end{pmatrix} \begin{pmatrix} b_{1+} \\ b_{2+} \end{pmatrix} \tag{2.14}$$

where L is a one-way physical length of the interferometer arm, and ϕ_l and ϕ_2 are phases accumulated in arm 1 and arm 2 respectively during the round trip propagation. The phase accumulated in each arm can be written as a combination of linear and nonlinear phases:

$$\begin{aligned} \phi_1 &= \phi_{l_1} + \phi_{\text{NL}_1} \\ \phi_2 &= \phi_{l_2} + \phi_{\text{NL}_2} \end{aligned} \tag{2.15}$$

Linear phases in arm 1 and arm 2 are equal, provided the lengths and the cross-sections are equal: $\phi_{l_1} = \phi_{l_2} = \phi_l = \frac{2\pi}{\lambda}\ n_{\text{eff}}L$. Therefore, we re-write Equation 2.14:

$$\begin{pmatrix} b_{1-} \\ b_{2-} \end{pmatrix} = \eta\sqrt{R_m}\ e^{-j\phi_l}e^{-j\phi_{\text{NL}_2}} \begin{pmatrix} e^{-j(\phi_{\text{NL}_1}-\phi_{\text{NL}_2})} & 0 \\ 0 & 1 \end{pmatrix} \begin{pmatrix} b_{1+} \\ b_{2+} \end{pmatrix} \tag{2.16}$$

Then, the final output of the coupler, using the S matrix, is:

$$\begin{pmatrix} a_{1-} \\ a_{2-} \end{pmatrix} = \eta\sqrt{R_m}e^{-j\phi_l}e^{-j\phi_{\text{NL}_2}} \begin{pmatrix} r & -j\sqrt{1-r^2} \\ -j\sqrt{1-r^2} & r \end{pmatrix} \begin{pmatrix} e^{-j(\phi_{\text{NL}_1}-\phi_{\text{NL}_2})} & 0 \\ 0 & 1 \end{pmatrix} \times$$
$$\times \begin{pmatrix} r & -j\sqrt{1-r^2} \\ -j\sqrt{1-r^2} & r \end{pmatrix} \begin{pmatrix} a_{1+} \\ a_{2+} \end{pmatrix} \tag{2.17}$$

Finally, the input $a_{2+} = 0$, and we write the output fields from NLI as functions of

the input fields, from Equation 2.17:

$$
\begin{aligned}
a_{1-} &= (\eta\sqrt{R_m}\; e^{-j\phi_l} e^{-j\phi_{\mathrm{NL}_2}})\Big[r^2\; e^{-j\Delta\phi_{\mathrm{NL}}} - 1 + r^2\Big]\; a_{1+} \\
a_{2-} &= (\eta\sqrt{R_m}\; e^{-j\phi_l} e^{-j\phi_{\mathrm{NL}_2}})(-jr\sqrt{1-r^2})\Big[e^{-j\Delta\phi_{\mathrm{NL}}} + 1\Big]\; a_{1+}
\end{aligned}
\tag{2.18}
$$

where $\Delta\phi_{\mathrm{NL}} = \phi_{\mathrm{NL}_1} - \phi_{\mathrm{NL}_2}$. Nonlinear phase accumulated in each arm is a product of optical power in that arm [W], effective nonlinearity parameter γ_{NL} [1/ W$\cdot$ m], and effective length of that arm [m], where L_{eff} is the effective length of one arm, given by $L_{\mathrm{eff}} = \frac{1-e^{-\alpha_{loss}L}}{\alpha_{loss}}$, and $\gamma_{\mathrm{NL1}} = \gamma_{\mathrm{NL2}} = \gamma_{\mathrm{NL}}$, since the cross-sections of the waveguides in each arm are identical:

$$
\begin{aligned}
\phi_{\mathrm{NL}_1} &= \underbrace{r^2\gamma_{\mathrm{NL1}}L_{\mathrm{eff}}|a_1|^2}_{\text{forward path}} + \underbrace{r^2 R_m\,\eta\gamma_{\mathrm{NL1}}L_{\mathrm{eff}}|a_1|^2}_{\text{backward path}} \\
&= r^2\gamma_{\mathrm{NL}}L_{\mathrm{eff}}\Big[1 + R_m\eta\Big]\; |a_1|^2 \\
\phi_{\mathrm{NL}_2} &= \underbrace{(1-r^2)\gamma_{\mathrm{NL2}}L_{\mathrm{eff}}|a_1|^2}_{\text{forward path}} + \underbrace{(1-r^2)R_m\,\eta\,\gamma_{\mathrm{NL2}}L_{\mathrm{eff}}|a_1|^2}_{\text{backward path}} \\
&= (1-r^2)\gamma_{\mathrm{NL2}}L_{\mathrm{eff}}\Big[1 + R_m\eta\Big]\; |a_1|^2 \\
\Delta\phi_{\mathrm{NL}} &= \phi_{\mathrm{NL}_1} - \phi_{\mathrm{NL}_2} = \gamma_{\mathrm{NL}}L_{\mathrm{eff}}\,(1 + R_m\eta)(2r^2 - 1)\,|a_1|^2
\end{aligned}
\tag{2.19}
$$

From Equations 2.18 and 2.19 it is evident that the output fields have an oscillating term proportional to the input power and based on the nonlinear phase difference - the key in power-dependent behavior of the NLI.

Reflection R of the NLI is defined as a fraction of incident optical power that gets reflected back into the main laser cavity; similarly transmission T of the NLI, T, is a fraction of the input optical power that exits the NLI through the auxiliary output 2:

$$
\begin{aligned}
R &= \frac{|a_{1-}|^2}{|a_{1+}|^2} = \eta^2\; R_m\; \left[r^4 + (r^2-1)^2 + 2r^2(r^2-1)\cos\left(\Delta\phi_{\mathrm{NL}}\right)\right] \\
T &= \frac{|a_{2-}|^2}{|a_{1+}|^2} = \eta^2\; R_m\; \Big[2r^2(1-r^2)(1 + \cos\left(\Delta\phi_{\mathrm{NL}}\right))\Big]
\end{aligned}
\tag{2.20}
$$

To illustrate the power-dependent behavior of the NLI, we plot characteristic reflec-

tion and transmission curves for a set of input parameters given in Table 2.2. The results are shown in Figure 2-8. The modulation depth of this device, as seen from R and T curves, is around 15%, and the increase in input power initially increases R, which is the regime required for artificial saturable absorption (positive γ_{SAM}).

Parameter	α_{loss}	r	L (one way)	R_{mirror}	γ_{NL}
Value	0.8 dB/cm	0.95	2 cm	0.98	0.8 1/W m

Table 2.2: Parameters used for NLI simulations.

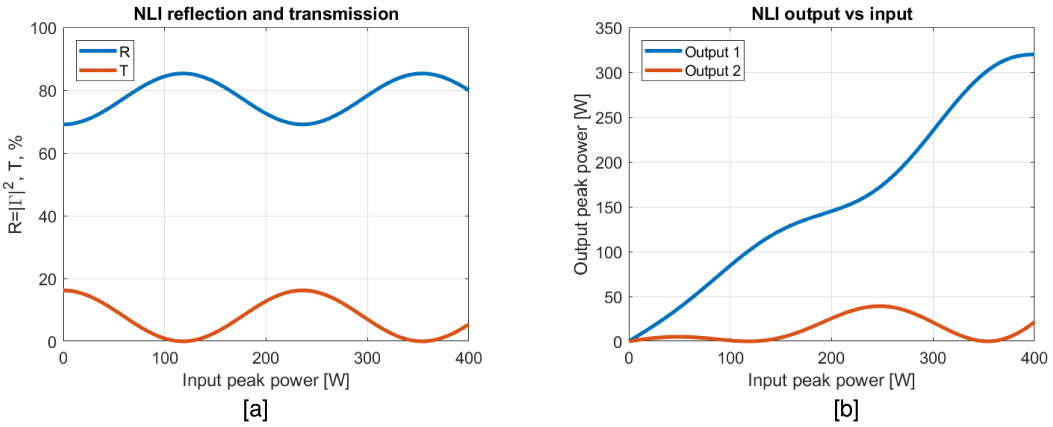

Figure 2-8: Nonlinear interferometer response vs input peak power. [a] Power reflection and transmission; [b] Power outputs.

The simulation above theory assumes ideal fabrication of the device, where the two arms of the NLI have identical waveguides, and therefore identical linear phase. In reality, normal fabrication-induced variations would introduce a small linear phase difference between the arms. Theoretically this would change the expression for $\Delta\phi_{\text{NL}}$, and make it

$$\Delta\phi_{\text{NL}} = \phi_{\text{NL}_1} - \phi_{\text{NL}_2} + \phi_b \tag{2.21}$$

where ϕ_b is power-independent phase bias. This phase bias will translate the curves in Figure 2-8[a] horizontally, and thus may put it in increased incident power - decreased reflection regime. Therefore, small phase bias might be necessary to compensate for such fabrication-induced variations.

Similarly to APM, we can calculate SAM coefficient γ_{SAM} from power reflection R, by substituting R from Equation 2.20 to Equation 2.12:

$$\begin{aligned}\gamma_{SAM} &= \frac{\partial R}{\partial |a_1|^2}\,\frac{1}{2\sqrt{R}} \\ &= \eta^2\, R_m\, 2r^2(r^2-1)\,\frac{\partial \cos\left(\Delta\phi_{\mathrm{NL}}\right)}{\partial |a_{1+}|^2}\,\frac{1}{2\sqrt{R}} \\ &= \frac{\eta\,\sqrt{R_m}(1+R_m\eta)\,r^2(1-r^2)(2r^2-1)\,\gamma L_{\mathrm{eff}}\sin\left(\Delta\phi_{\mathrm{NL}}\right)}{\left[r^4+(r^2-1)^2+2r^2(r^2-1)\cos\left(\Delta\phi_{\mathrm{NL}}\right)\right]^{0.5}}\end{aligned} \tag{2.22}$$

where $\Delta\phi_{\mathrm{NL}}$ is given by Equation 2.19. It is, however, much easier to obtain γ_{SAM} from power reflection data by numerical differentiation and normalization. Figure 2.3 shows SAM coefficient corresponding to parameters in Table 2.2. γ_{SAM} is maximum when the slope of R is maximum, and zero when the value of R is maximum and minimum. One can easily tune the linear phase of the NLI to bias it at the point of maximum SAM coefficient. Similarly to APM analysis, we next send a single

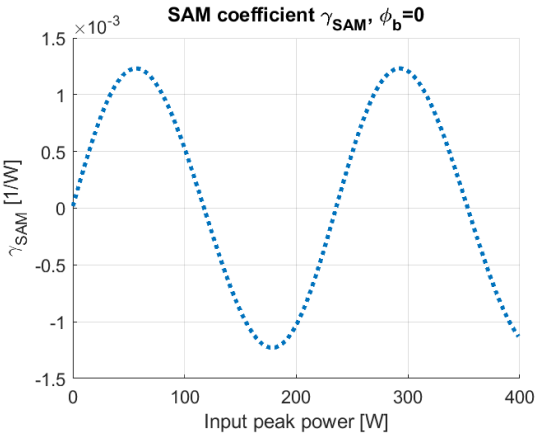

Figure 2-9: Self-amplitude modulation coefficient for nonlinear interferometer, corresponding to Figure 2-8, and data from Table 2.2.

secant squared pulse through the NLI (with FWHM pulse duration of 350fs), and look directly at the pulse shortening. The result, for an input peak power of 85W, is shown in Figure 2-10 [a]. Single pass pulse shortening by 28fs is evident. This pulse shortening depends on the input peak power. Secant squared and Gaussian pulses

of varied peak powers are next propagated through NLI, and the resulting percent pulse shortening, normalized to maximum power, is shown in Figure 2-10 [b]. For secant squared pulses and this particular NLI, up to 8% of undistorted single pass pulse shortening is possible.

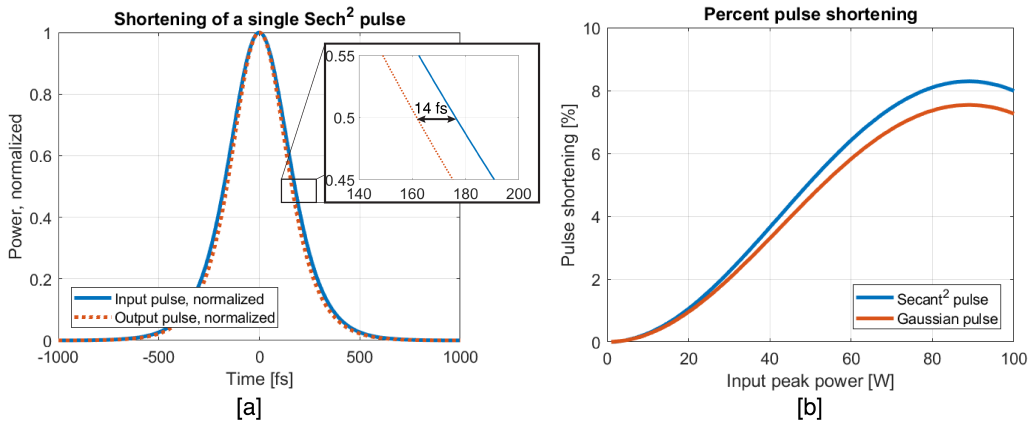

Figure 2-10: NLI-induced single pulse shortening: [a] Shortening of one sech^2 pulse; [b] Percent pulse shortening vs input peak power. Dispersion effects not included.

Device parameters optimization

In order to optimize the NLI, it is instructive to see how different device parameters affect NLI performance. The device coupling ratio, effective nonlinearity, length and dispersion could all be optimized in order to maximize the performance. In this section, for any particular simulation one parameter is varied, while the others take the values specified in Table 2.2). First, the performance of the NLI as a function of the coupler power splitting ratio $r^2/(1-r^2)$ is evaluated, where r is the field coupler transmission, and r^2 is therefore power transmission of the coupler. For r^2=0.5, both NLI arms get the same amount of power, hence there is no nonlinear phase difference, and no self-amplitude modulation (sine term in Equation 2.22 is zero). Reflection and Transmission of the NLI are then flat with respect to input power, and the device reflects minimum possible amount of light. Similar behavior happens for r^2=1, when all the light goes into one NLI arm, there is no nonlinear phase difference, and the

maximum possible amount of light is reflected back to the main laser cavity. Desired modulation range of R vs input power happens for r^2 between 0.5 and 1, where r^2 affects both the amplitude and phase of R in different ways. The results of the NLI response for $r^2 \in [0.5, 1]$ are shown in a 2D map in Figure 2-11 [a]. At r^2 values close to 0.5, the nonlinear phase difference between the two arms is small (but non-zero), and the device is close to its minimum reflection. Only with very high peak power can it reach high R values, and exploit full modulation depth. Theoretical modulation depth in this case is the highest, since the device reflection spans the range from its lowest to highest values. For r^2 values around 0.75, one can reach higher R values at much lower input peak power, however, the modulation depth of the device is reduced. The closer r^2 gets to 1, the less peak power is needed to reach the peak amplitude. Peak SAM coefficient and modulation depth for each r^2 value are plotted in Figure 2-11 [b]. The SAM coefficient (proportional to the slope of the sinusoid) increases with increased r^2, until its maximum at $r^2 = 0.75$. This would be a good point to operate the device if the modulation depth were also strong. However, the modulation depth, as shown in Figure 2-11 [b], appears to decrease significantly with higher r^2. This is somewhat deceptive, because with low r^2 values one needs very high peak power to reach full possible modulation depth. For example, from Figure 2-11[a], to reach 85% possible modulation depth at $r^2 = 0.55$, one needs over 1000W of peak power. Physical lasers systems usually have a certain operating region, and further power increase is impractical. If we assume, for example, that the maximum achievable peak power in the laser is 100W, we can define *available modulation depth*, which is the modulation depth that the laser would have IF the peak power could not go above 100W. In this case, as r^2 goes up, this modulation depth also goes up, as the slope of the cosine function increases. The point of highest SAM coefficient and modulation depth for this case is around r^2=0.85.

Next, the performance of the NLI is evaluated for a fixed coupler splitting ratio, but for varying effective nonlinearity parameter γ_{NL}. NLI reflection as a function of γ_{NL} is shown in Figure 2-12 [a]. Since γ_{NL} changes the phase of R only (Equation 2.20), increase in effective nonlinearity results directly in increase of oscillation frequency,

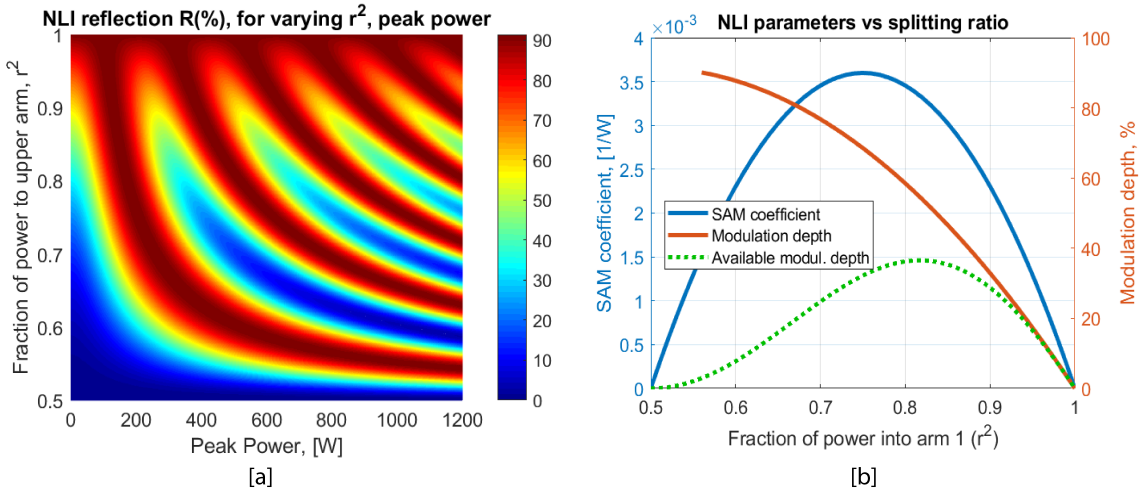

Figure 2-11: NLI splitting ratio optimization.[a] NLI Reflection as a function of coupler power splitting ratio and input peak power; [b] corresponding peak effective nonlinearity, modulation depth, and "available modulation depth", which assumes maximum 100W of incident peak power.

and hence the slope of the R vs peak power curve, with no changes to amplitude, or modulation depth. Peak SAM coefficient (proportional to maximum of the cosine slope) is directly proportional to effective nonlinearity, as shown in Figure 2-12[b]. Effective nonlinearity should be designed to be as large as possible for stable mode-locking with short pulses.

NLI performance vs device length is more complicated. Increasing length helps increase the nonlinearity of the device, but it also directly adds loss to the system. A 2D map of NLI reflection R vs peak power and one-way length L is plotted in Figure 2-13 [a]. For higher device lengths, significantly lower input powers are needed to reach maximum possible reflection. However, the overall value of reflection decreases significantly, as the overall loss is added to the system. Figure 2-13[b] plots peak SAM coefficient, modulation depth, and available modulation depth(with 100W maximum input peak power limit). There is an optimum value of length (≈25cm for this particular device) that maximized the SAM coefficient, with decreased modulation depth value. However, with this NLI length, the overall loss of the device is so high that the reflection of the NLI back to the main cavity is under 30% - meaning

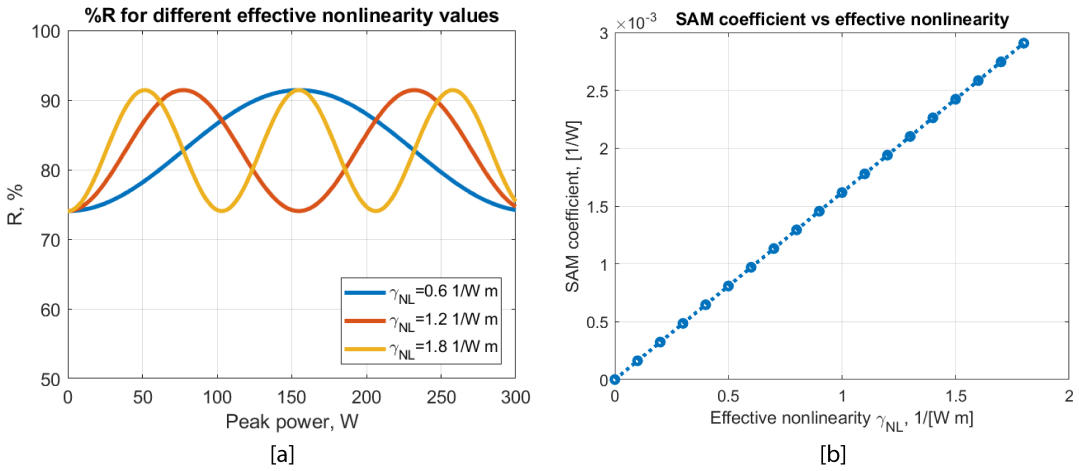

Figure 2-12: NLI effective nonlinearity optimization. [a] NLI Reflection as a function of effective nonlinearity of the waveguide; [b] corresponding peak SAM coefficient.

the NLI becomes a terrible reflector inside of a laser cavity. The length of the NLI should be optimized together with the rest of the laser - first, one should determine the maximum amount of additional loss the laser cavity could take from one of its reflectors, and still generate desired amount of power to drive nonlinearity and support ultrafast pulses; second, with this loss value, the proper NLI length should be picked out to maximize the SAM coefficient, with a sufficient value of modulation depth. Finally, overall effective nonlinearity of the NLI must also be considered. For most mode-locked lasers operating in a soliton regime, increase in overall nonlinearity on the laser cavity is beneficial to a certain limit - combined with net negative dispersion, larger nonlinearity creates shorter pulses. However, if the nonlinearity becomes too strong, the pulses become unstable. Therefore, the length of the NLI should also be considered, apart from its mode-locking properties, in terms of "additional laser cavity element" with a certain value of γ_{NL}.

In summary, all the derivations and optimizations in this section are calculated using realistic parameters, but they do not include dispersion, or dispersion-nonlinearity interplay during pulse propagation. Generally, channel waveguides would have normal dispersion. The effect of such normal dispersion on NLI performance would be to stretch the reflection vs peak power curve horizontally - the peak power of the pulse

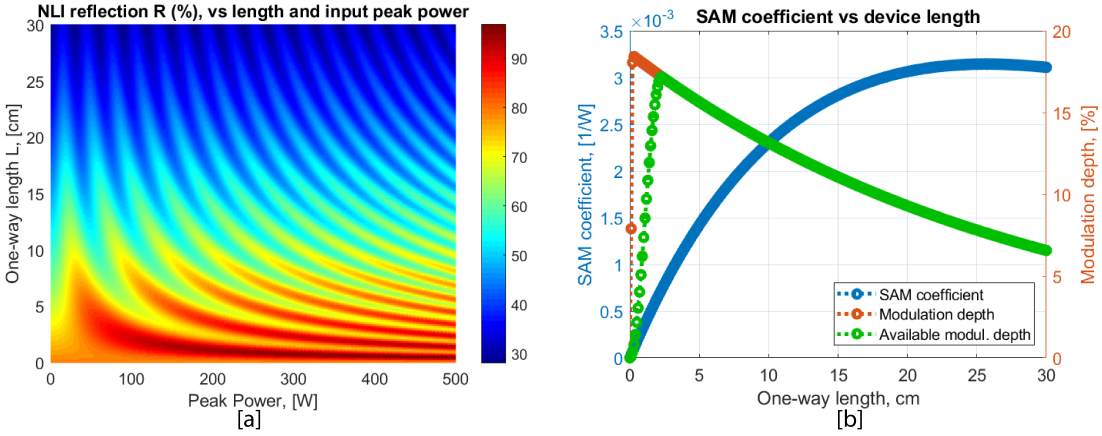

Figure 2-13: NLI length optimization.[a] NLI Reflection as a function of length and incident peak power; [b] corresponding peak SAM coefficient, modulation depth, and "available modulation depth", which assumes maximum 100W of incident peak power.

would be constantly lowered due to pulse spreading in time domain. This would result in lower SAM coefficient. To exactly model NLI performance with all effects included, one needs to run a complete split-step simulation for the device, which is done in Section 2.4.1. Nevertheless, the theory presented above gives excellent intuition into NLI parameter space and overall device performance.

2.4 Nonlinear Interferometer for 1900nm

2.4.1 Integrated Implementation

There are numerous potential implementations of the nonlinear interferometer architecture presented in Figure 2-6 using various integrated photonics structures. The main NLI coupler could be implemented using directional coupler, multi-mode interference coupler, or other more sophisticated devices. The end-reflectors at the end of each arm could be implemented as integrated loop mirrors or as integrated grating reflectors. Integrated grating reflectors could potentially reduce the footprint of the device, and add additional dispersion compensation if necessary.

Figure 2-14 shows one particular integrated implementation of the NLI device [138]

as designed for the DODOS project (shown is an actual layout of the device in Cadence Virtuoso). The unbalanced power splitter is implemented by using an integrated directional coupler. The end-reflectors are implemented using integrated loop mirrors. We choose to keep the NLI arms identical in terms of cross-section and length and achieve the nonlinear phase difference by the unbalanced coupler alone, in order not to deal with group velocity mismatch. Although the two NLI arms are designed to be identical, minor fabrication tolerances almost always impart a small linear phase difference between the arms, and thus we end up tuning the device in order to balance it properly. Integrated heaters are fabricated on top of the NLI arms in order to be able to tune the device.

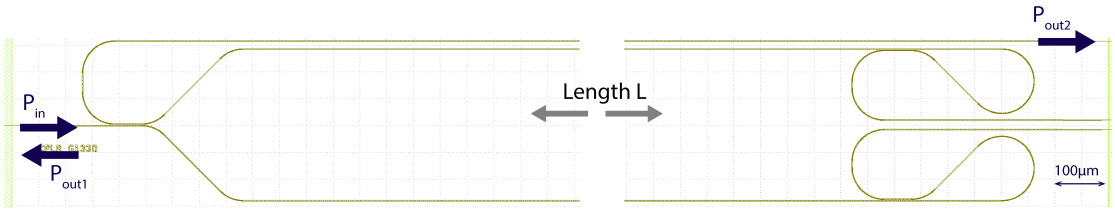

Figure 2-14: Nonlinear interferometer layout

The device was fabricated as part of DODOS project, and thus the photonic layer heights were restricted to DODOS fabrication platform, using CMOS-compatible photonics layers as shown in Figure 1-5. A more-detailed view of photonic layers with relevant names and dimensions is shown in Figure 2-15. Available layers for the NLI are the three silicon nitride layers (SN, FN, ZN), and a silicon layer. We avoid the silicon layer, because two-photon absorption at 1900nm , although significantly reduced from its' peak value at 1550nm [21], is still significant and will act as a power limiter in the cavity. Main NLI waveguides are therefore implemented in silicon nitride layers.

NLI Waveguide Design

In order to maximize NLI performance, it is important to design the main waveguide in order to maximize effective nonlinearity γ_{NL}, which in turn would maximize SAM

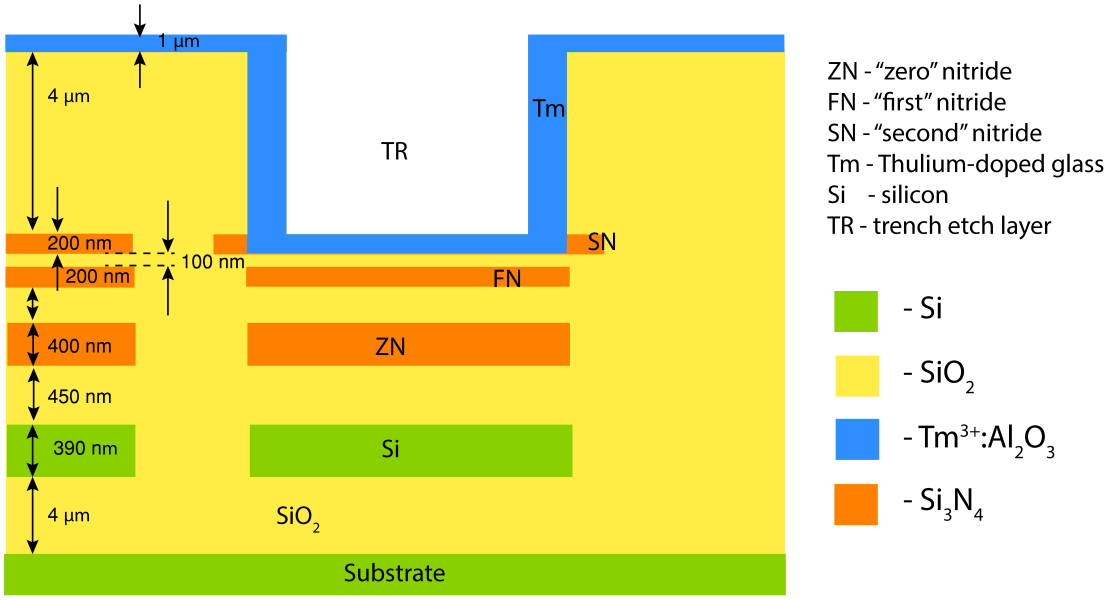

Figure 2-15: DODOS Photonic layers with relevant layer heights

coefficient. However, this should not come at the expense of significant increase in normal dispersion, which will have the opposite effect. We therefore choose the best Si_3N_4 material layer, within our fabrication platform, to achieve this. From Figure 2-15, NLI could be implemented in 400nm thick ZN Si_3N_4 layer, 200nm thick FN Si_3N_4 layer, or a combination of FN and SN layers together, termed "DN" for Double Nitride. We calculate effective nonlinearity and dispersion, at λ=1900nm, using finite difference eigenmode(FDE) solver, vs waveguide width, for FN, DN, and ZN layers, making sure the waveguide width is within a single mode operation regime only. The results are shown in Figure 2-16. The DN layer combination yields higher γ_{NL} over the SN layer. The ZN layer yields even higher effective nonlinearity, however, increased normal dispersion of ZN waveguides, together with higher linear loss due to larger nitride height spreads the pulse in time as it propagates within the waveguide, thus constantly reducing the peak power available to drive the nonlinearity. This, in turn significantly reduces the SAM coefficient and makes mode-locking prohibitively difficult. We therefore choose to implement NLI in the double-nitride layer, and pick the waveguide width of 1.5μm, which maximizes nonlinearity, minimizes dispersion,

and ensures single mode operation. γ_{NL} was calculated using the formalism presented in [135]. Final cross-section of the main NLI waveguide, optical mode profile, and the

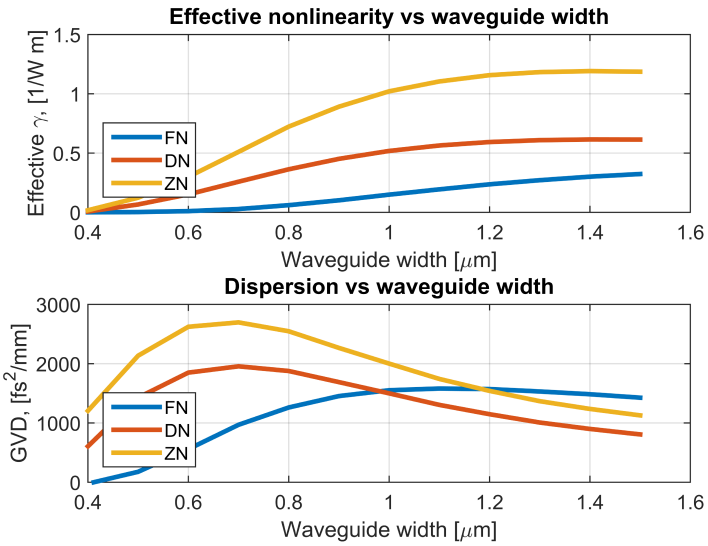

Figure 2-16: Effective nonlinearity and dispersion of different Si_3N_4 layers.

resulting nonlinearity and dispersion are shown in Figure 2-17.

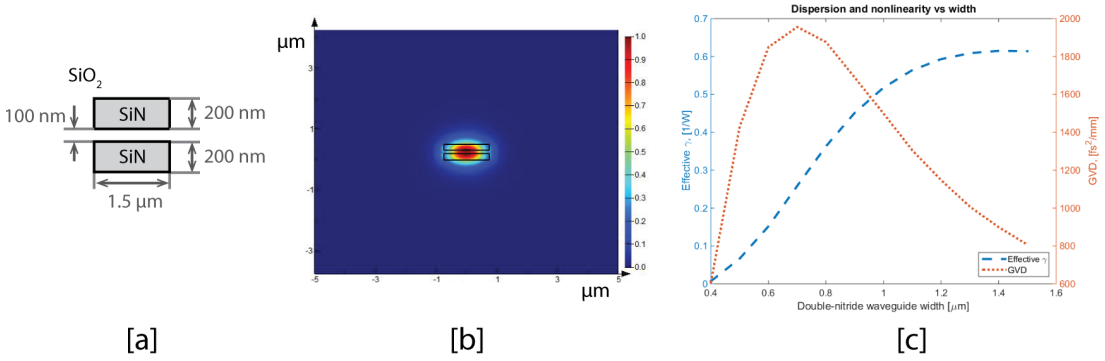

Figure 2-17: NLI waveguide design: [a] Cross-section of waveguide; [b] Mode profile; [c] Dispersion and nonlinearity optimization.

NLI Coupler Design

Once the design of the main waveguide is selected, other NLI components are designed using the waveguide geometry of the main waveguide. It is possible to implement the

loop mirror, coupler, and NLI arms all in different nitride layers, and then use layer-to-layer transition components in between. However, for simplicity, we choose to make all NLI components using the same waveguide cross-section, shown in Figure 2-17.

A directional coupler is used in order to implement both the power splitting coupler and the loop mirrors. The transfer matrix of the directional coupler is given by

$$S = \begin{pmatrix} t & -j\kappa \\ -j\kappa & t \end{pmatrix} \tag{2.23}$$

where $t^2 + \kappa^2 = 1 \longrightarrow \kappa = \sqrt{1-t^2}$, and t is the field transmission through the coupler. The output fields b_1 and b_2 are written as $b = Sa$, where $a = [a_1; a_2]$ are input fields. Given a_2=0, and assuming lossless coupler, the fraction of light power coupled into each arm is:

$$\begin{aligned} T_1 &= \frac{P_1}{P_{in}} = t^2 \\ T_2 &= \frac{P_2}{P_{in}} = \kappa^2 = 1 - t^2 \end{aligned} \tag{2.24}$$

The NLI coupler splitting ratio is a critical parameter, since it affects directly the SAM coefficient, the available modulation depth, and the loss of the NLI as an end-reflector in the laser cavity, as shown in Figure 2-11. Since the actual reflection value of the device is very important, we choose T_1/T_2 values to be 90/10, 93/7, and 97/3. The last two coupling gaps result in single digit modulation depth values (see Section 2.4.2 for simulations), which is still sufficient to sustain mode-locking action. For an integrated directional coupler, the t and κ coefficients obey the following relation [139]:

$$\begin{aligned} t^2 &= \cos^2(CL) \\ \kappa^2 &= \sin^2(CL) \end{aligned} \tag{2.25}$$

where L is the length of the coupler, and C is a coupling coefficient, proportional to

e^{-Ag}, where g is the size of the gap, and A is some constant. Therefore, the required splitting ratio can be obtained by varying either the coupling gap, or coupler length. We choose to keep the length of the coupler fixed, and vary the gap between the two waveguides. Coupled mode theory [140], together with an FDE solver are used to calculate the field coupling coefficients as the gap between the two waveguides is varied. The results for the top arm transmission T_1 vs the gap size are shown in Figure 2-18 [b], and are used to select the gap values corresponding to T_1=90%, 93%, and 97%. Full layout of the power splitter, with exact dimensions corresponding to T_1=90%, is shown in Figure 2-18 [a].

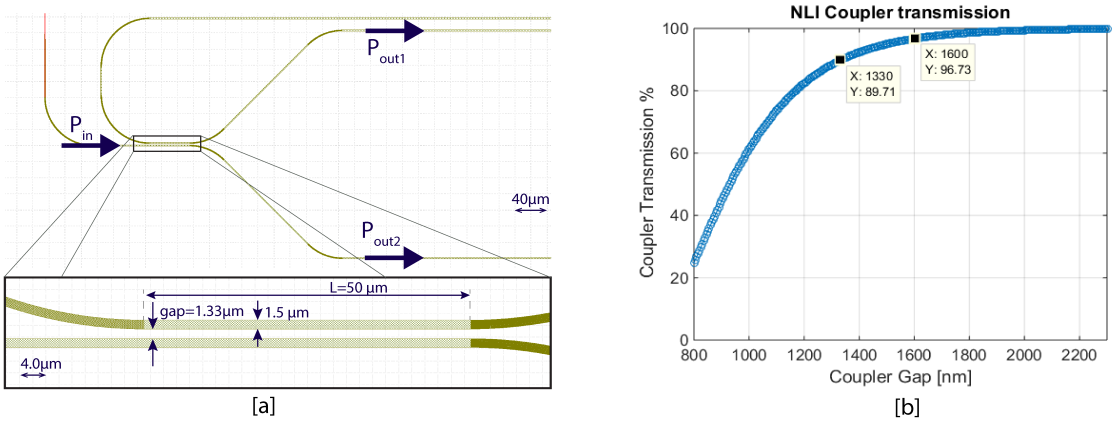

Figure 2-18: NLI coupler design: [a] Layout; [b] Transmission vs gap size.

Loop Mirrors Design

In the ideal case, the integrated mirrors at the end of each NLI arm would be 100% reflective. In this design iteration, we implement integrated reflectors using linear loop mirrors. Such a loop mirror consists of a directional coupler with 50/50 splitting ratio, with the arms connected together to form a loop, as shown in Figure 2-19 [a]. When the two outputs of the directional coupler described by transfer matrix in Equation 2.23, are connected to each other, the final transfer matrix of the loop

mirror becomes

$$S_{lm} = S \begin{pmatrix} 0 & 1 \\ 1 & 0 \end{pmatrix} S = \begin{pmatrix} -2j\kappa t & t^2 - \kappa^2 \\ t^2 - \kappa^2 & -2j\kappa t \end{pmatrix} \tag{2.26}$$

The power fraction R back into the laser, and T out of the cavity, are

$$\begin{aligned} R &= 4(1 - t^2)t^2 \\ T &= (2t^2 - 1)^2 \end{aligned} \tag{2.27}$$

Solving the above equation for t^2 when R=1 gives $t^2 = 1/2$. We therefore design the directional coupler in the loop mirror to have field transmission coefficient $t = \sqrt{2}/2$ to give maximum reflection back to the laser cavity. Using the same coupled mode theory-based directional coupler code as in the previous section, we sweep the gap size and calculate the resulting field transmission and corresponding power reflection R. The results are shown in Figure 2-19[b]. The gap size of 940nm corresponds to 100% reflection in a loop mirror configuration for our NLI waveguide geometry. The layout of the device with all relevant dimensions, is shown in Figure 2-19[a]. The bend-radius inside of the "loop" of the mirror is 60 μm, which was optimized for our particular cross-section.

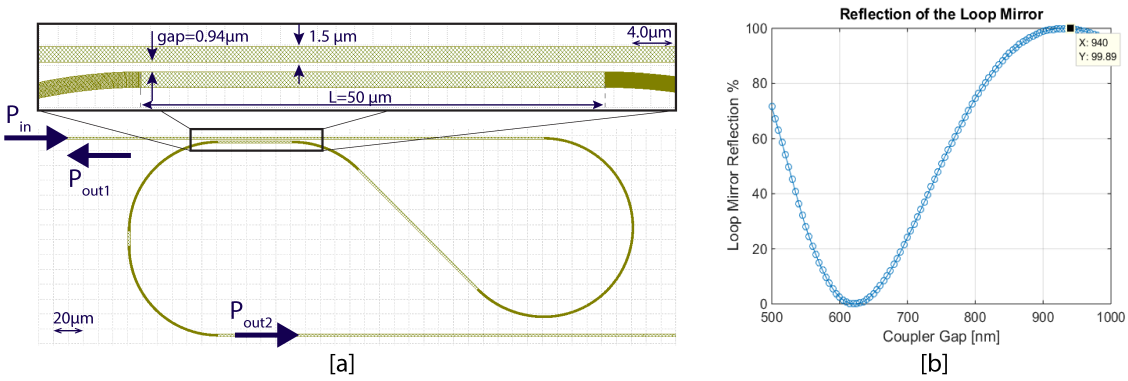

Figure 2-19: NLI Loop mirror design: [a] Layout; [b] Reflection vs gap size.

Bandwidth consideration

It is important for the NLI to be broadband in order to support ultrafast optical pulses. Therefore, the bandwidth of the device should be carefully evaluated. The loop mirror was designed to have 100% reflection at 1900nm, and the coupler was designed to have 90/10 splitting ratio exactly at 1900nm. With the design parameters fixed, we analyze the wavelength dependence of those components. Figure 2-20 [a] shows the wavelength dependence of the loop mirror and the coupler individually. Both appear to be broadband. Next, a combined wavelength response of the full NLI is calculated, taking linear loss into account. The full response (NLI reflection R, assuming no nonlinearity) is shown as a black curve in Figure 2-20 [a]. This combined response peaks at about 1850nm, and has less then 2.5%variation within 100nm bandwidth. However, this shows that the NLI prefers 1850nm wavelength over 1900nm, by 2.5%. If the rest of the mode-locked laser had no wavelength dependence (i.e. flat gain profile), the NLI would be the element picking the central wavelength of the device. However, the gain in fact is strongly wavelength dependent, with an effect that is much stronger than 2.5% (see Chapter 3). The gain profile of the laser would then pick the final operating wavelength, with the NLI playing a small additional effect.

It is possible to re-design the NLI to have a peak response at 1900nm, by, for example, shifting the peak loop mirror reflection to higher wavelengths. The result is shown in Figure 2-20 [b]. In this case, NLI will have the strongest reflection at 1900nm, which is also very broadband. However, this introduces small additional losses to the device - in the original case (Figure 2-20 [a]), the peak reflection value of the NLI is 62%, while in the wavelength-shifted case (Figure 2-20 [b]) this value is at 55%.

In both cases, the device has sufficient bandwidth to support femtosecond-level optical pulses - the reflectivity drop within 100nm around central wavelength value is only 2.5%. At most 40nm are needed to support 100fs-long secant square pulses according to time-bandwidth product, therefore, the NLI should not pose any band-

width limitations.

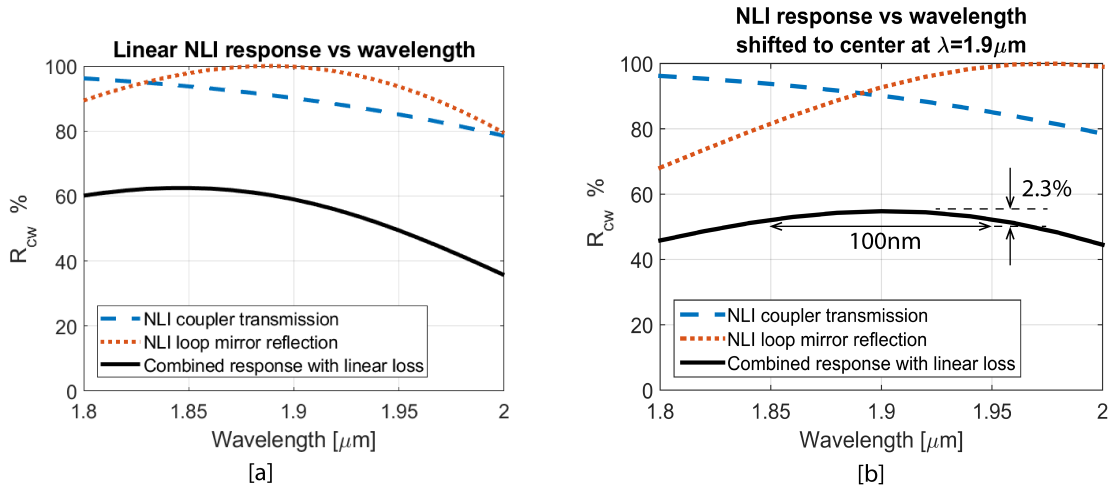

Figure 2-20: NLI bandwidth: [a] NLI reflection (no nonlinearity) vs wavelength; [b] NLI reflection (no nonlinearity), with peak response shifted to 1900nm.

2.4.2 Full Device Simulations

In order to fully model the NLI response, the effects of dispersion, nonlinearity, and all the associated losses must be taken into account. To do this, we numerically solve Nonlinear Schrodinger Equation (NLSE) using the symmetric split-step Fourier method [141], at each point along the NLI. The associated NLSE form is

$$\frac{\partial A(z,t)}{\partial z} = j\frac{\beta_2}{2}\frac{\partial^2 A(z,t)}{\partial t^2} - j\gamma_{\mathrm{NL}}|A(z,t)|^2 A(z,t) - lA(z) \tag{2.28}$$

where β_2 is group delay dispersion in fs^2/m, γ_{NL} is effective nonlinearity in $(Wm)^{-1}$, and l is linear field loss in m^{-1}. The algorithm for this model is:

1. Create a pulse (electric field), with a peak power P_{peak}
2. Apply NLI coupler transfer matrix
3. Propagate light forward, separately for each NLI arm, using NLSE
4. Apply loop-mirror reflections

5. Propagate light backward, separately for each NLI arm, using NLSE

6. Apply NLI coupler transfer matrix

7. Calculate R, T, other system outputs for this P_{peak}

8. Increment peak power value, repeat 1-7.

The devices were originally modeled using simulated values for nitride loss, the NLI coupler, and loop mirror reflection, however, the model was updated to use exact values for those parameters, as measured (see Section 2.4.3). The values for effective nonlinearity and dispersion are simulated, where the dispersion is calculated using the FDE solver with Sellmeier coefficients as extracted from the refractive index measurements of our materials, and effective nonlinearity is calculated using the same FDE solver based on the algorithm outlined in [135], and bulk material Kerr nonlinearity values taken from the literature. The parameters for the simulation are shown in Table 2.3.

Parameter	l (loss)	r^2	L (one way)	R_{mirror}	γ_{NL}	β_2
Unit	m^{-1}	-	m	-	$(\text{W m})^{-1}$	fs^2/m
Value	18.42	0.91	0.023	0.98	0.6	810×10^3

Table 2.3: Parameters used for full NLI propagation simulations.

The results of the simulated reflection and transmission of the device are plotted in Figure 2-21[b]. The reflection of the device varies between 28% and 40%, implying 12% possible modulation depth, if one could achieve the 500W peak power necessary to reach it. For an efficient CW laser, it is desirable to have a much higher end-reflector, ideally above 80%. However, linear loss of the NLI waveguide is the limiting factor, where the material loss of the Si_3N_4 is currently limited by fabrication capabilities. Making the NLI shorter would reduce the loss, but would also significantly reduce the SAM coefficient. Corresponding output power of the device is shown in Figure 2-21 [a]. Average as opposed to peak power is plotted here, because peak power is not clearly defined for an output pulse that has been stretched and modulated in

time domain due to dispersion effects. Peak power is defined for the input pulses - in this case, the peak-to-average power conversion is based on the simulation input parameters - secant squared pulse train, with 960MHz repetition rate, with FWHM pulse duration of 200fs.

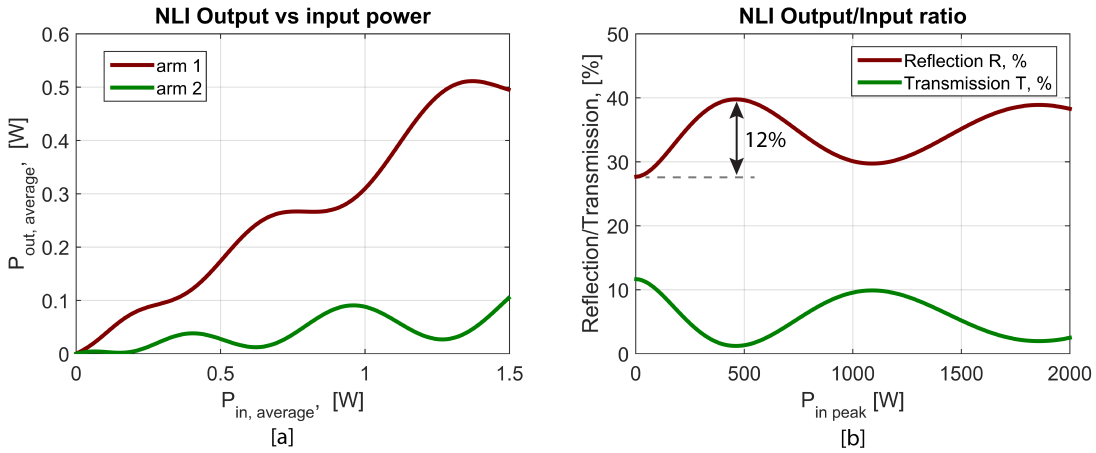

Figure 2-21: NLI simulation: [a] Average output power vs average input power, for both outputs. Peak-to-average power conversion is done based on 960MHz repetition rate laser with 200fs pulses; [b] Reflection and Transmission vs input peak power.

Corresponding SAM coefficient and modulation depth are shown in Figure 2-22. Mode-locking is only possible when R is increasing with increasing incident power, and hence with positive γ_{SAM} coefficient (shown shaded in Figure 2-22). Corresponding modulation depth is shown at each point, in regions where $\gamma_{\mathrm{SAM}} > 0$. The laser is likely to work only during the first region of positive SAM coefficient, where the input peak power is from 0 to 450 mW. The second region of increasing R and corresponding positive SAM coefficient (input peak power range from 980mW to 1620mW, from Figure 2-22 [b]) would impart oscillating power-dependent reflections to the wings of the pulse, breaking up the pulse. The device can be easily biased at the point of maximum γ_{SAM}, however, this reduces available modulation depth by 50%. The integrated mode-locked laser presented in this thesis has up to a 150W of peak power inside of the laser cavity. This allows using up to a third of available modulation depth (about 4%). Therefore, for the lasers described in Chapter 3, biasing the NLI at a maximum γ_{SAM} point doesn't sacrifice available modulation depth.

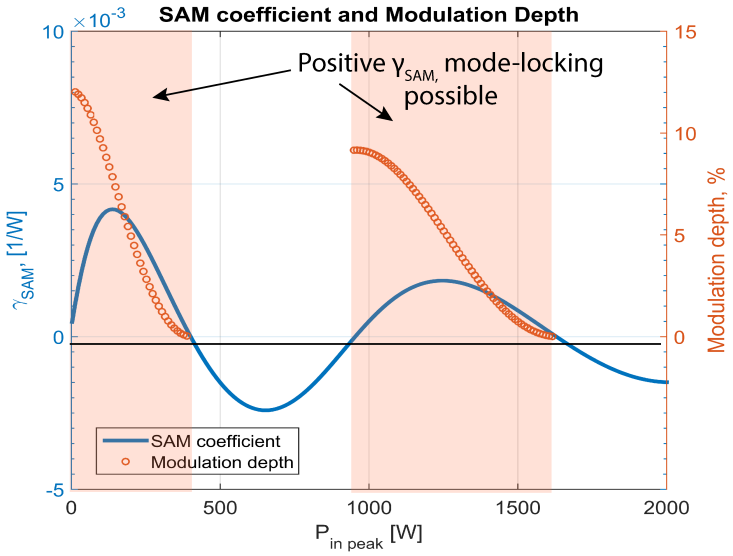

Figure 2-22: SAM coefficient γ_{SAM}, and corresponding available modulation depth, shown only in regions with $\gamma_{SAM} > 0$, where mode-locking is possible.

For comparison, we simulate three NLIs with as-designed coupler power splitting ratios (90/10, 93/7 and 97/3) and all other parameters as shown in the Table 2.3. The results for all three power splitting ratios are shown in Figure 2-23 [a], and corresponding SAM coefficients are plotted in Figure 2-23 [b]. While the NLI with a coupler with 97/3 splitting ratio has the lowest SAM coefficient and the lowest modulation depth, it also has the highest average reflection value, meaning if the laser is just above the threshold, this device is most likely to work. Further changing the coupler splitting ratio of the NLI, down from 97/3, increases the SAM coefficient, and would continue to increase it up until 75/25 splitting ratio, where γ_{SAM} is at its maximum.

The final full simulation illustrates the effects of the dispersion on the NLI response. Figure 2-24 [a] shows NLI reflection for one device with coupler power splitting ratio of 90/10 and all other parameters corresponding to Table 2.3, and another device with the same parameters, but with dispersion $\beta_2 = 0$. Figure 2-24 [b] shows the corresponding SAM coefficient. The effect of dispersion is the stretching of the R curve horizontally, reducing γ_{SAM}, and making higher reflection accessible at higher

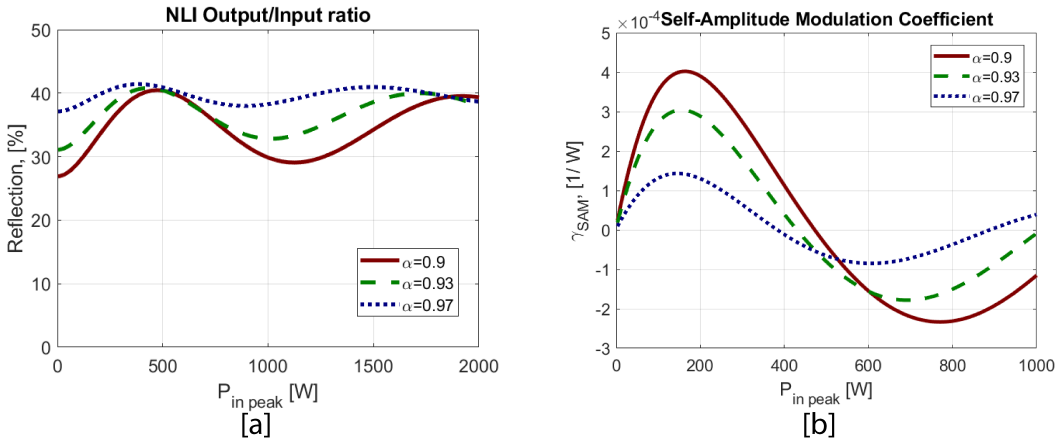

Figure 2-23: NLI response for three different power splitting ratios: [a] Reflection; [b] Corresponding SAM coefficients.

input power, compared with zero dispersion case. It is impractical to design an integrated waveguide with high nonlinearity and near-zero dispersion. A better approach would be to make sure that the dispersion compensation in the cavity is balanced in such a way that the pulse, upon entering the NLI, has negative chirp. The positive dispersion of the NLI will then shorten the pulse as it propagates through the device, which will drive nonlinearity with higher peak power, and would thus have a higher SAM coefficient. Another approach is to add dispersion-compensating gratings into the NLI itself.

2.4.3 Results

Linear characterization of the NLI was done to measure passive waveguide losses, loop mirror reflection/transmission, and NLI coupler reflection/transmission. Linear loss of the waveguide was measured using the cut-back method, by having straight waveguides of two different lengths, and by having paperclip structures with the same number of bends but different lengths of the straight sections in between those bends (Figure 2-25 [a]). The NLI coupler was characterized using a test structure corresponding to the directional coupler used. CW light was coupled into the input waveguide and collected through the two outputs of the coupler (Figure 2-25 [b]). This

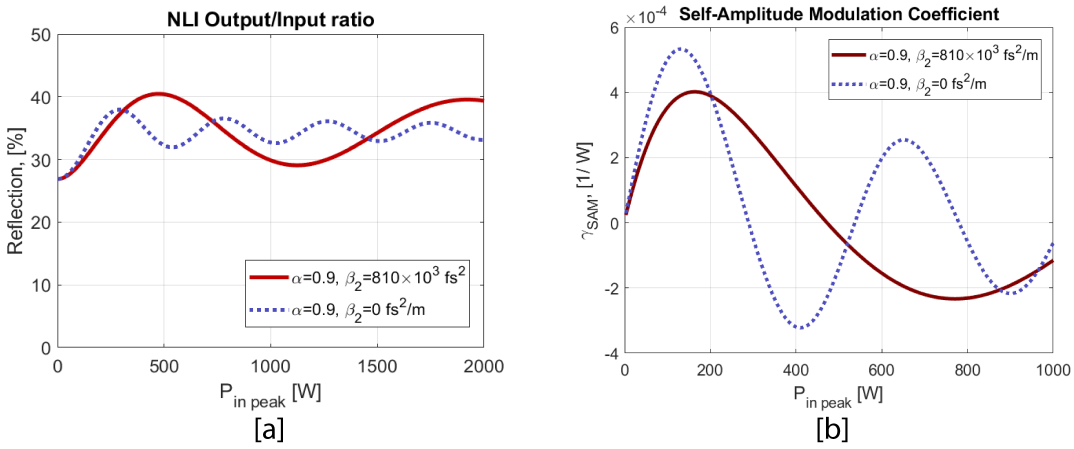

Figure 2-24: Dispersion effects on NLI performance: [a] NLI response with and with no dispersion; [b] Corresponding SAM coefficients.

allows to directly estimate the power splitting ratio of the coupler. Loop mirrors were measured in a similar way, by having a test structure for a directional coupler that was used inside of the loop mirrors(Figure 2-25 [c]), and calculating the actual response of the loop mirrors using Equation 2.27. The results of the linear measurements are summarized in Table 2.4. The slight discrepancy in power splitting ratio between design and measurement values is due to a slight fabrication-induced change in the Si_3N_4 refractive index, compared with initial expected values.

	Design Value	Measured Value
Linear Waveguide Loss	-	0.8 dB/cm
Loop Mirror Reflection	100%	98%
Splitter % Ratio 1	90/10	83/17
Splitter % Ratio 2	93/7	86/14
Splitter % Ratio 3	96/4	91/9

Table 2.4: NLI linear characterization summary, for 1900nm devices

Nonlinear characterization of the device was performed using an optical parametric oscillator (OPO) centered at 1.9μm, with an 80MHz pulse repetition rate, and a pulse duration of 200fs. In order not to pre-chirp the input pulses, light was coupled into the device using a free-space objective. Light was collected at the output of the waveguide using a lensed fiber. An optical chopper and lock-in amplifier were used

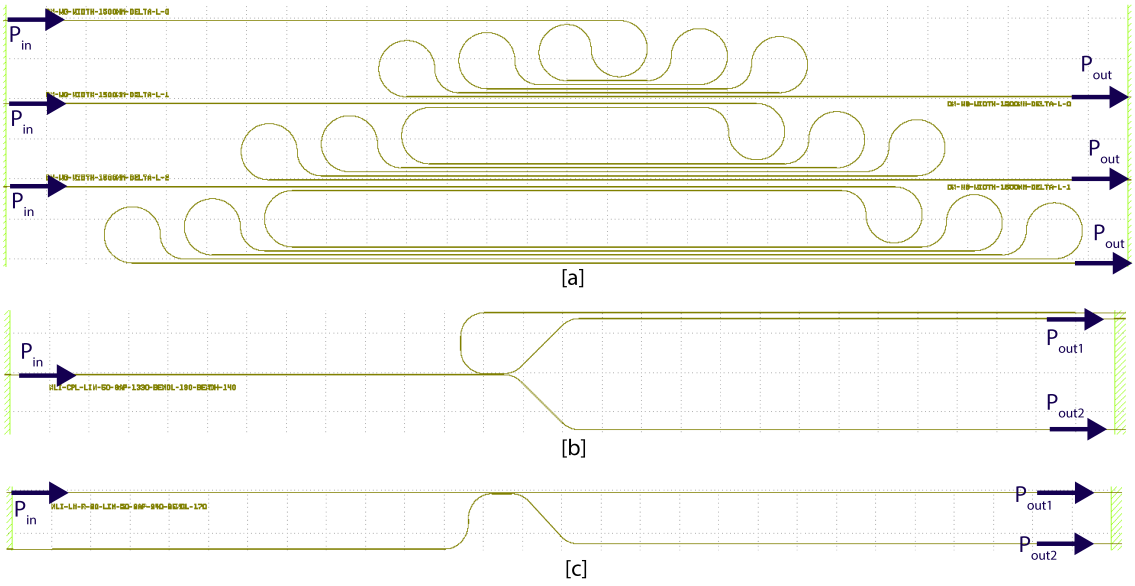

Figure 2-25: Test structures for linear characterization of the NLI: [a] Paperclip structures for linear loss measurements; [b] NLI coupler test structure; [c] Loop mirror coupler test structure

to detect small changes in the device output power. The setup diagram is shown in Figure 2-26.

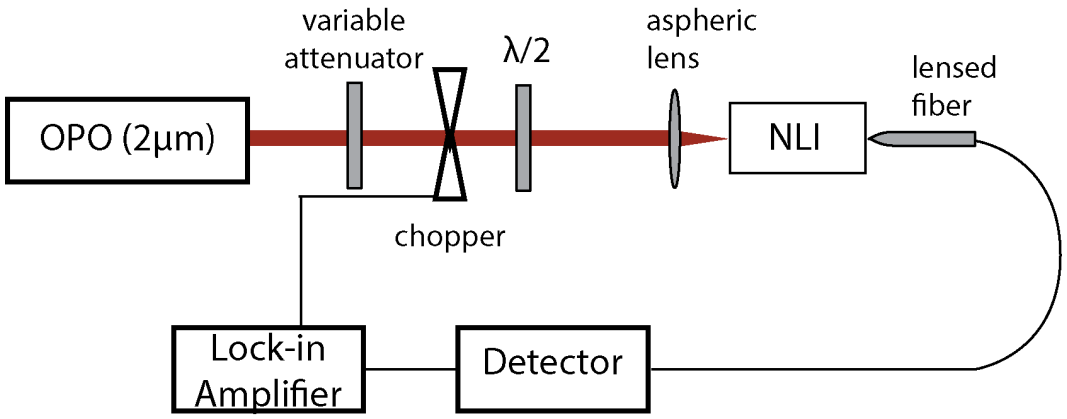

Figure 2-26: Setup used to measure NLI devices.

In the above setup, the output of the NLI was measured through "output 2", as shown in Figure 2-14. Therefore, the transmission of the device was measured, as opposed to the reflection. Reflection could be easily calculated from transmission measurement using Equation 2.20.

NLI output power as a function of the input power, measured using setup in Figure 2-26, is shown in Figure 2-27 [a]. On/off-chip coupling losses were calibrated out using separate measurements. The "transmission" of the device, calculated as the ratio of output power to the input power at the output of the NLI coupler, is shown in Figure 2-27 [b]. The nonlinear behavior of the device is immediately evident. We note that the peak power available for the experiment was limited by the peak power produced by the OPO. $1.9\mu m$-centered signal used was an idler OPO beam, with limited pulse energy. In order to properly calculate the modulation depth and the self-amplitude modulation coefficient, we fit the data to a sinusoid signal. Fitted data for NLI transmission, and corresponding NLI reflection (calculated from fitted transmission using Equation 2.20) are shown in Figure 2-28 [a]. The device exhibits 9% modulation depth, compared with the 12% design value. The data also shows a linear phase bias of about $-\pi$, as compared with simulation. For comparison, we plot simulation data with a linear bias of $-\pi$ in Figure 2-28 [b]. This shows a close simulation/measurement modulation depth correspondence; however, the period of the sinusoid (the peak power it takes the NLI to experience 2π nonlinear phase change) is about a factor of two larger in measured data (2-28 [a]) compared with simulation (2-28 [b]). The corresponding SAM coefficient would then be a factor of 2 smaller for measured data. This indicates that the simulation has either overestimated the value of effective nonlinearity, or underestimated the value of dispersion. While all other simulation parameters were measured experimentally, the dispersion and nonlinearity values come from separate simulations. Dispersion was calculated using an FDE solver with Sellmeier coefficients for the materials measured exactly, while effective nonlinearity was calculated using the formalism presented in [135, 136] using bulk Kerr nonlinearity values for Si_3N_4 and SiO_2 from the literature.

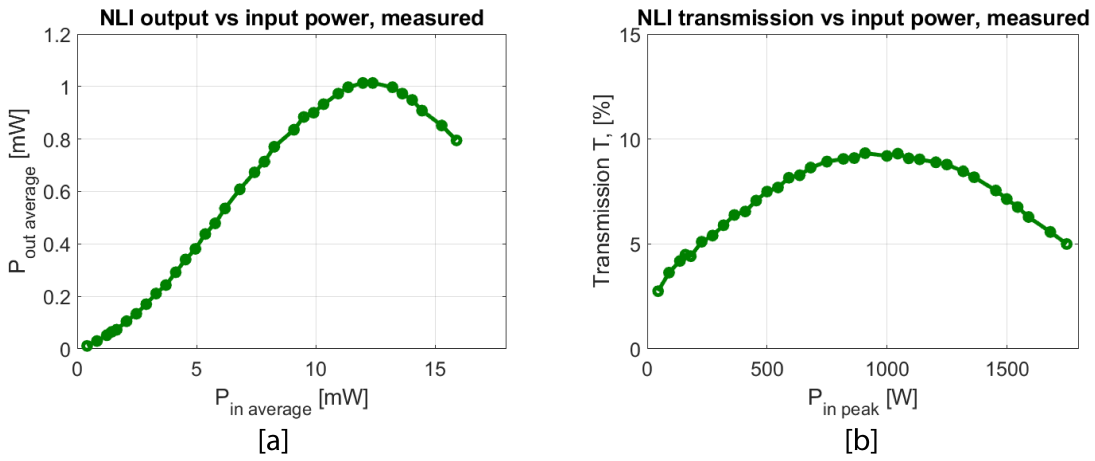

Figure 2-27: NLI results: [a] Measured output power vs input power. [b] Measured transmission vs input peak power.

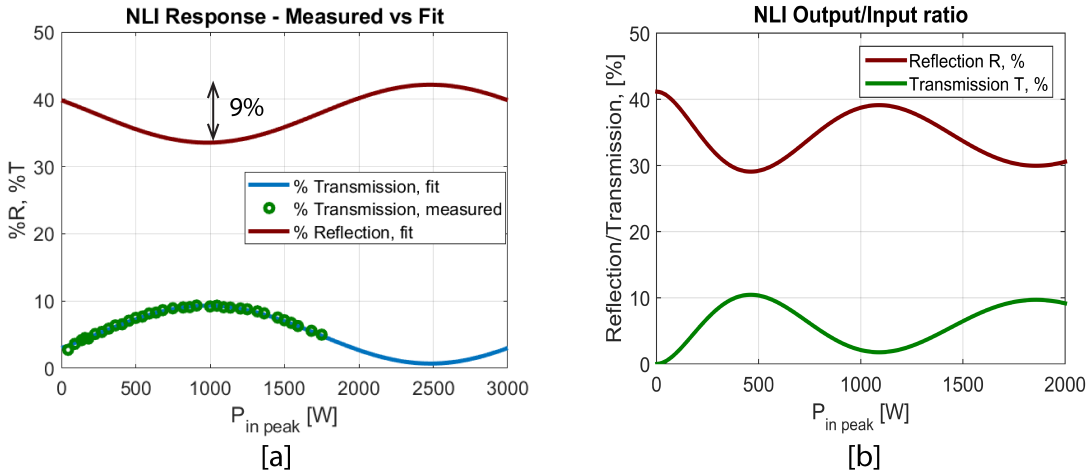

Figure 2-28: NLI fits to measured data: [a] Reflection and transmission fits to measurements; [b] Linear phase bias-shifted simulation of the reflection/transmission.

The MLLs presented in this thesis could have up to 150W of peak power, meaning they would be able to access about one sixth (1.5%) of measured modulation depth. According to full laser simulations presented in Chapter 3, this modulation depth and corresponding SAM coefficient are enough to mode-lock the lasers.

2.5 Nonlinear Interferometer for 1550nm

An integrated nonlinear interferometer for mode-locked lasers centered at 1550nm was designed similarly to the one for 1900nm, with the main architecture, layout, and optimization steps analogous to the previous section. First, the dimensions of a double-nitride Si_3N_4 waveguide were calculated to maximize effective nonlinearity γ_{NL} at 1550nm, and minimize dispersion at 1550nm. Next, the NLI coupler and integrated loop mirror were designed using this waveguide geometry, with parameters to maximize the reflection of the loop mirror and to optimize the NLI coupler for maximum SAM coefficient. The layout of the 1550nm NLI is identical to that of Figure 2-14, with waveguide dimensions adjusted for 1550nm design specifications. Next, full simulations of the NLI were done using the model described in Section 2.4.2, based on the 1550nm design parameters, and later adjusted based on the data from linear characterization. Finally, the devices were measured using a 1550nm-centered OPO with 180fs pulses at 80MHz. In this section, we show key simulations and results of the 1550nm NLI design/characterization.

Figure 2-29 shows the design of the main NLI waveguide, which consists of the two silicon nitride layers, where the height of each layer is 200nm, the oxide gap between the layers is 100nm, and the width of both Si_3N_4 waveguide layers is optimized for maximum effective nonlinearity and small normal dispersion. Table 2.5 shows the design and measured values for the NLI coupler splitting ratios, integrated loop mirror reflection, and linear waveguide loss. NLI coupler splitting ratios were designed to be 97/3, 96/4, and 90/10. Measured values are slightly lower, but close to the design specifications. Loop mirror reflectors are measured to be 98% reflective, which is close to a design value of 100%. Linear loss at 1550nm was measured using three different methods, all of which resulted in a value of about 1.4-1.6 dB/cm, which is considerably higher than expected. Upon further investigation, it was discovered that our fabrication facility had a problem with a nitride deposition tool during the wafer run, which resulted in much-higher-then expected losses for Si_3N_4 layer, for this particular tape-out. With 2.3 cm one-way NLI length, the net nitride-only NLI loss

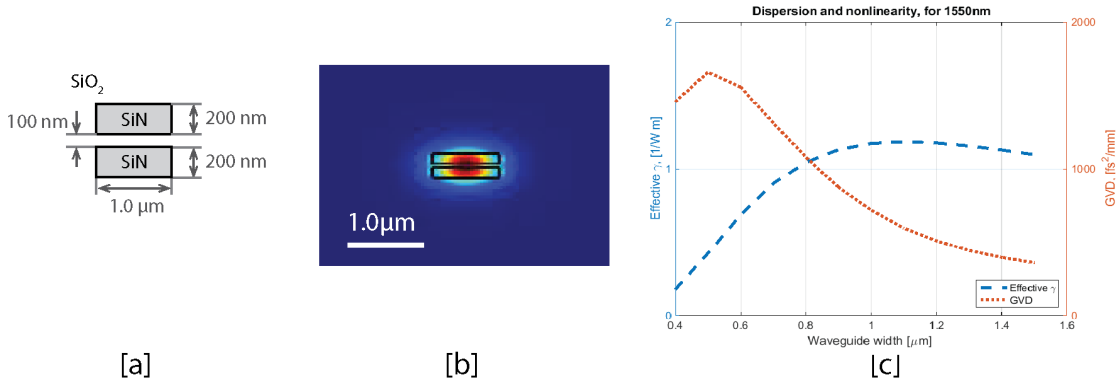

Figure 2-29: 1550nm NLI waveguide design: [a] Dimensions of the NLI waveguide cross-section, not-to-scale; [b] Intensity profile for optical mode in this waveguide; [c] Effective nonlinearity and dispersion optimization.

for this tape-out is 7.4dB, which drastically reduces NLI nonlinear performance, and makes it a poor reflector at the end of a laser.

	Design Value	Measured Value
Linear Waveguide Loss	-	1.5 dB/cm
Loop Mirror Reflection	100%	98%
Coupler Splitting Ratio 1, %	90/10	87/13
Coupler Splitting Ratio 2, %	96/4	91/9
Coupler Splitting Ratio 3, %	97/3	94/6

Table 2.5: NLI linear characterization summary, for 1550nm central wavelength devices

Full simulation of the NLI was done using the method described in Section 2.4.2, using data from Table 2.6. For linear loss, coupler power splitting ratios, and loop mirror reflectivity, measured data were used. For effective nonlinearity and dispersion, calculated data were used based on the FDE mode-solver, in-house measured values of Sellmeier coefficients for Si_3N_4 and SiO_2 materials, and literature-based Kerr nonlinearity values. The results of this simulation are shown in Figure 2-30, for three different values of the NLI coupler splitting ratios. The final modulation depths for 87/13, 91/9, and 94/6 modulation depths are 8%, 5.8%, and 4%, respectively. The device with an 87/13 power splitting ratio has the highest SAM coefficient, which is about a factor of two greater than that of 94/6 device. However, the reflection of

the NLI with the 87/13 coupler oscillates around a 14% value, which makes for an inefficient CW laser, and hence limits the amount of energy needed to form pulses and drive the NLI nonlinearity.

Parameter	l (loss)	r^2	L (one way)	R_{mirror}	γ_{NL}	β_2
Unit	m^{-1}	-	m	-	$(\text{W m})^{-1}$	fs^2/m
	34.9	0.94	0.023	0.98	1.12	717×10^3
	34.9	0.91	0.023	0.98	1.12	717×10^3
	34.9	0.87	0.023	0.98	1.12	717×10^3

Table 2.6: Parameters used for NLI (1550nm) simulations.

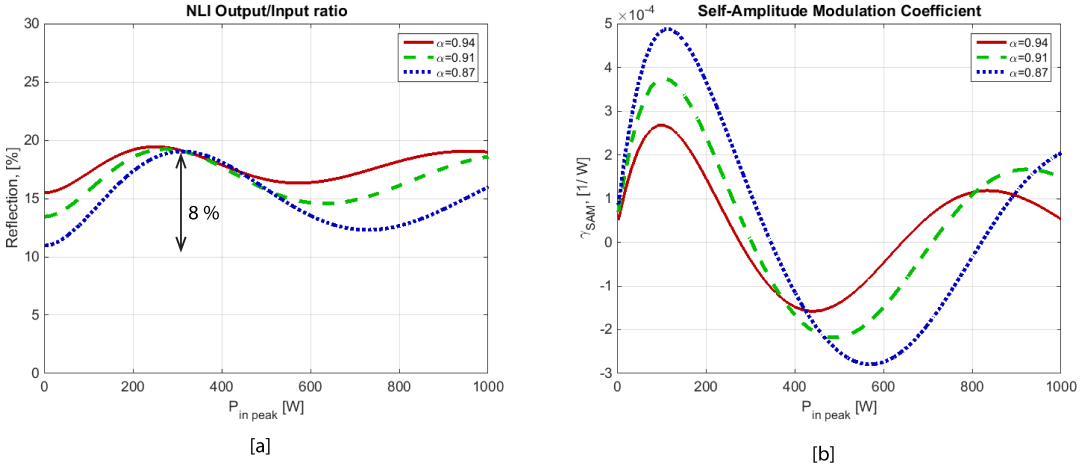

Figure 2-30: Full NLI simulations for 1550nm NLIs: [a] NLI Reflection for three measured values of NLI coupler power splitting ratio; [b] corresponding SAM coefficients.

Nonlinear interferometers were fabricated at the CNSE facility as a part of the EPHI project fabrication runs. Both stand-alone NLIs, and mode-locked lasers with the NLIs, were fabricated. The devices were tested using the setup similar to the one shown in Figure 2-26, but with an OPO that was centered at 1550nm, with 180fs transform-limited pulses at an 80MHz repetition rate.

In order to show that the NLI could be biased for increasing reflection at increasing incident peak power, integrated heaters were deposited over both arms of the NLI. The heaters are deposited on top of a 4μm of SiO_2 cladding layer, which is directly over the double-nitride structure (see Figure 2-31 [a]). The optical mode inside of a 1.0μm

double-nitride NLI waveguide is well-confined, therefore, the light doesn't interact with the metal heater deposited on top of the oxide. The thermo-optic coefficient of stoichiometric silicon nitride has been reported to be 2.45×10^{-5} REU/$^{\circ}C$ [142]. To arbitrarily tune the NLI phase bias, a maximum of 2π linear phase shift is needed (accumulated over the round-trip propagation): $\frac{2\pi}{\lambda}\Delta n(2L) = 2\pi \rightarrow \Delta n = \frac{dn}{dT}\Delta T = \lambda/2L = \frac{1.9\mu m}{2\times 2cm} \approx 4.75 \times 10^{-5}$, assuming a heater is deposited over the length of 2.0 cm (out of 2.3cm length of each NLI arm), directly over the Si_3N_4 waveguide, but away from NLI coupler and loop mirrors. This gives required temperature change at the Si_3N_4 waveguide $\Delta T = \frac{4.75\times 10^{-5}}{2.45\times 10^{-5}} = 1.94^{\circ}C$. Assuming a factor of 3 heat transfer loss from the surface of the heater to Si_3N_4 layers (conservative estimate, done without heat distribution simulation), this gives the required temperature of the heater to be $\Delta T = 1.94 \times 3 \approx 6^{\circ}C$, for a full 2π phase shift. This is a reasonable temperature to achieve in an integrated heater.

The heaters were fabricated at MIT's Microsystems Technology Laboratories, using standard photolithography process with lift-off, using chromium photomasks (Figure 2-31 [b]). The heaters are $20\mu m$ wide, 2cm long, and the thickness is made up of 150nm of titanium, followed by 100nm of gold. $100\times 100\mu m$ contact pads are deposited at each end of the heater. DC probes with are used to run current through the heaters (Figure 2-31 [c]). For this generation of heaters, the resistance of each heater was measured to be approximately 330Ω.

The results of the 1550 NLI measurements, for the device with 91/9 NLI coupler, with integrated heaters, are shown in Figure 2-32. Output vs input power measurement is shown in Figure 2-32 [a], with on/off-chip losses calibrated out using a separate measurement, for 4 applied heater voltages and corresponding currents. The output was measured through "output 2" - the transmission output of the device, as shown in Figure 2-14. NLI transmission can be directly calculated by dividing the transmission output power by the input power. The results for NLI transmission vs incident peak power are shown in Figure 2-32 [b]. From this data, ∼6mA of heater current is necessary to bias NLI by half-cycle. 6mA at 330Ω corresponds to 12mW of electrical power to the heater. Since accumulated linear phase is distributed along

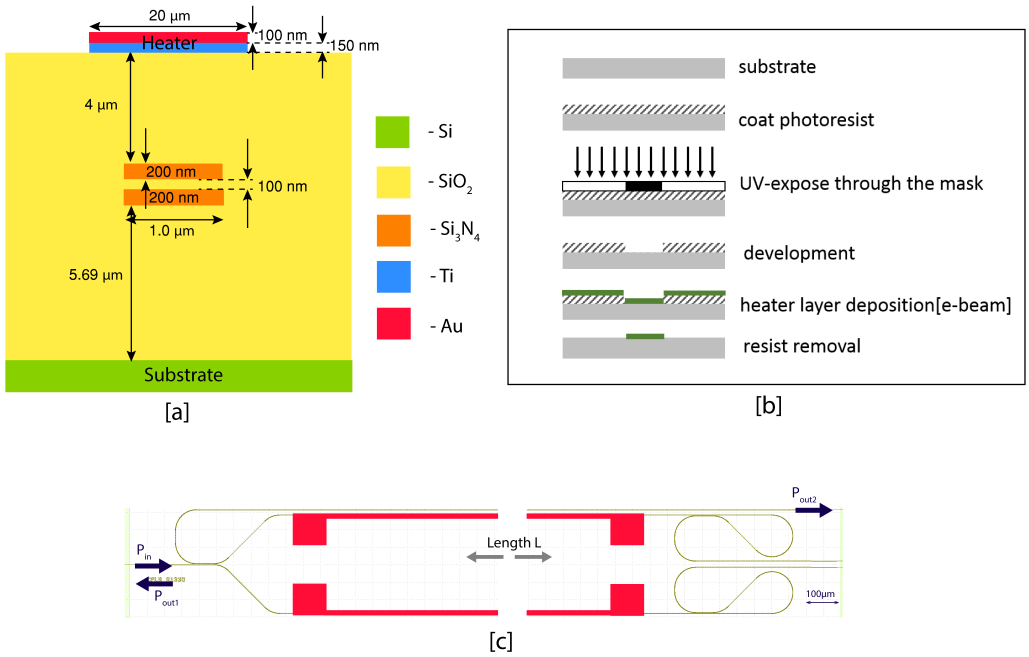

Figure 2-31: NLI heaters: [a] Cross-section of fabricated heaters (not-to-scale); [b] Heater deposition process; [c] Top view of the integrated heaters.

the 2cm length of the heater, the device is power-efficient. Further improvements in heater efficiency are possible with better heater designs and a more controlled heater fabrication. In addition, a p-n junction in silicon could be used as a Joule-heat-based heater, which would heat up NLI from underneath, as opposed to from above as done in this work. This result demonstrates that NLIs could be easily tuned to operate in a regime that favors mode-locking operation, with small electrical power consumption required for tuning. Chapter 3 shows the operation of such NLI heaters inside of the actual integrated MLLs, where heater tuning allows to turn the mode-locking on and off.

The reflection of the NLI is calculated from the transmission measurements using Equation 2.20. Corresponding reflection vs incident peak power are shown in Figure 2-32 [c]. The reflection oscillates around the central value of 14.5%, with the modulation depth of 2.5%. For the same device, full simulation predicts 5.8% modulation depth, with reflection average value of 16.5% (Figure 2-30 [a]). In addition, the pe-

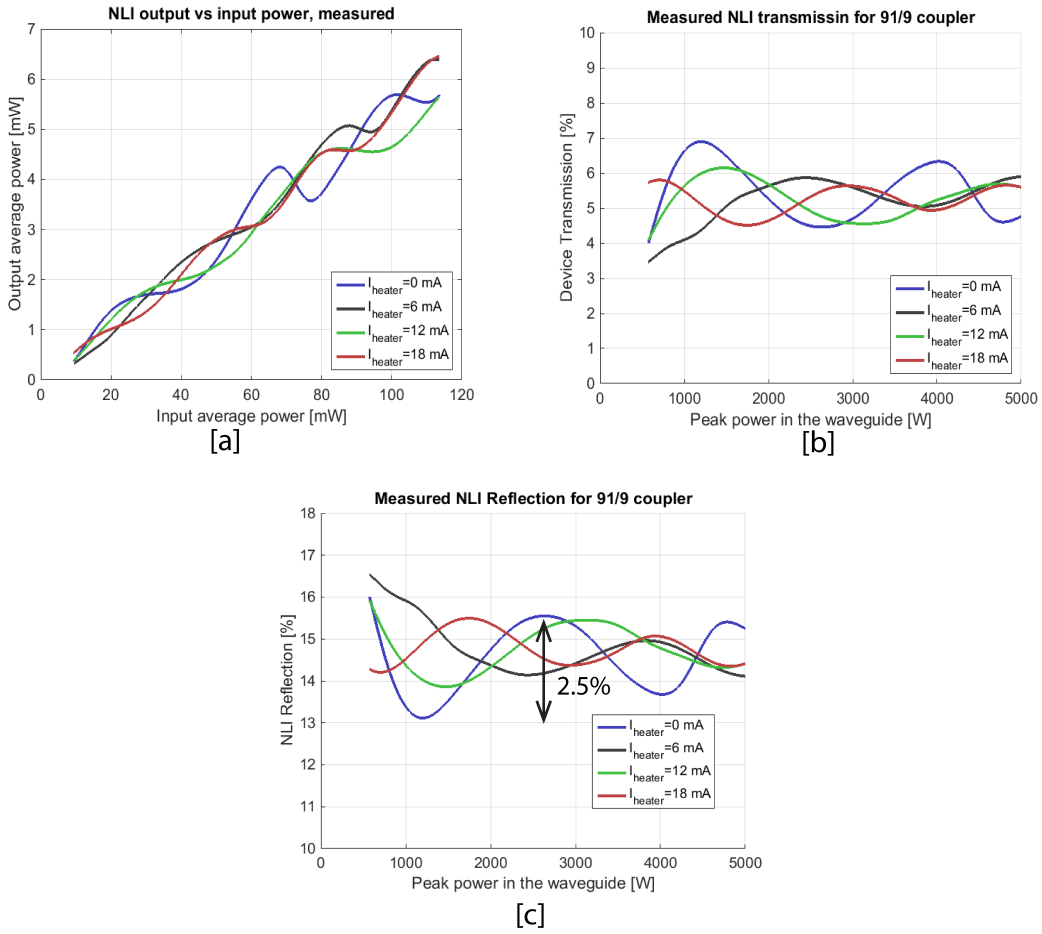

Figure 2-32: NLI (at 1550nm) measurement results: [a] NLI output power vs input power, for 91/9 coupling power splitting ratio NLI, for various heater-induced biases; [b] Corresponding transmission of the NLI; [c] Corresponding reflection of the NLI, calculated from measured transmission data.

riod of the sinusoidal oscillation is smaller by about a factor of two in simulation results, compared with measured results. This results in correspondingly larger SAM coefficient in simulation (it therefore overestimates it). The discrepancy between the simulation and measured data is likely in the value of the effective nonlinearity of the waveguide, which was calculated using full γ_{NL} as described in [135] using bulk n_2 values for $SiO_2$and Si_3N_4 from the literature. Because literature-reported values for Kerr nonlinearity of Si_3N_4 vary by more than a factor of 2, this discrepancy is likely causing the overestimation in effective nonlinearity of our devices. Similar discrepancy is found in our measurements of $2\mu m$-based NLI, as shown in Section 2.4.3, and Figure

2-28. Full NLI simulation uses all measured device/waveguide parameters, except for effective nonlinearity and dispersion, both of which are calculated separately.

In the above chapter, we have demonstrated fully-on chip integrated mode-locking devices, operating at 1550nm and 1900nm, to be used with integrated mode-locked lasers operating at corresponding wavelengths. Chapters 4 and 3 show the designs of such on-chip mode-locked lasers with the mode-locking devices being part of the laser cavity. Moreover, full mode-locked laser models are presented that highlight how NLI properties influence the behavior of the mode-locked laser, its stability, and pulse duration.

Chapter 3

1900nm Mode-Locked Lasers

This chapter presents several designs of integrated mode-locked lasers for 1900nm central wavelength operation. The main requirement of the lasers in this chapter is high peak power (and hence short pulse duration). The lasers were designed for the DODOS project, where they would drive an integrated supercontinuum generation device, where the resulting continuum would generate a frequency comb and which would be subsequently stabilized using the on-chip 1f-2f interferometry (see Section 1.4.2 for further details). In order to produce an octave of coherent supercontinuum signal in silicon waveguides, pulses on the order of 100-200fs are required [84]. Therefore, the starting point of the mode-locked laser design was selecting the laser architecture and mode-locking method that would enable and sustain such pulse durations.

This chapter is organized as follows: first, general physical guidelines for designing an on-chip mode-locked laser are discussed, and basic theoretical framework with general design parameter space for short pulse mode-locked lasers is presented. Next, Section 3.1 presents a complete design, numerical simulations, and results for an integrated MLL based on a spiral architecture. An improved MLL configuration, based on a segmented architecture, with corresponding design, simulations, and results, is presented in Section 3.2. Finally, novel MLL design variations are presented in Section 3.3, where full simulations and design improvements are investigated.

Design Principles

When designing integrated mode-locked lasers, both integrated photonics and laser physics should be considered together. The starting design point for such systems should always be the physics and operating regimes of mode-locked lasers, keeping in mind the constraints of state-of-the art silicon photonics (for example, the lack of an on-chip isolator makes certain laser systems challenging to implement on a chip)

Since active mode-locking generally produces pulses on the order of a few picoseconds, the approach in this work is to use passive mode-locking, which would allow pulse durations to go down to 100fs or below. In this case, the addition of a passive mode-locking element to the laser cavity is necessary. Passive mode-locking methods and associated devices, along with their potential implementation in integrated photonics, are discussed in details in Section 2.1. Regardless of the type of a passive mode-locking device used, such mode-locked lasers have several well-studied operating regimes based on their cavity configuration and net cavity group velocity dispersion (GVD). Figure 3-1 shows a map of various operating regimes, which are briefly discussed below:

- **Soliton operation regime** Soliton-like laser operation is possible in net anomalous dispersion regime [132, 143, 144]. To achieve shortest possible pulses, a careful balance of Kerr nonlinearity and dispersion in the laser cavity is needed. In particular, the cavity should operate in a net anomalous dispersion regime, with enough Kerr nonlinearity to allow for soliton effect to take place, which would facilitate further pulse shortening. However, too much Kerr nonlinearity in this operating regime would destabilize the pulses and make laser operation highly unstable. The soliton operating regime allows for shortest pulse durations at the output of the laser.

- **Stretched-pulse regime** The stretched pulse regime, also called "dispersion - managed" regime, relies on long sections of the laser with alternating normal and anomalous dispersion [145, 146]. Normal dispersion sections frequently contain optical gain. In such a case, the pulse is stretched in time domain, but is allowed

to accumulate energy. Anomalous dispersion laser cavity sections reverse the spreading stabilize the pulse. The pulses are usually strongly chirped at the output of the stretched pulse laser, and external dispersion compensators are frequently used to compress them.

- **All-normal dispersion regime** All-normal-dispersion regime fiber lasers avoid dispersion management altogether - rather, they rely on a bandpass filter with a well-defined bandwidth to shape optical pulses [147, 148, 149]. All-normal dispersion fiber is used for both gain and passive sections. The strongly up-chirped optical pulse is stretched in time. In the frequency domain, this manifests in more power at higher and lower frequencies within the pulse spectrum. The bandpass filter is then used to remove those higher and lower frequencies, and hence to stabilize pulse duration. The output pulses from all-normal dispersion-based lasers are usually up-chirped at the output and could be externally compressed.

- **Self-similar regime** Self-similar laser operation is characterized by optical pulses that have parabolic shape in both time and frequency domain, where nonlinear phase accumulation is translated into linear frequency chirp [150]. The pulse evolution takes place in an all-normal dispersion regime, where a parabolic pulse is strongly up-chirped. An optical filter with a carefully designed Gaussian transfer function shapes the pulses after one cavity round-trip propagation in such a way as to allow self-similar pulse evolution. Although the pulses exit the laser positively chirped, they could be compressed down to the appropriate transform-limit for parabolic pulse shape. Externally compressed pulses from self-similar lasers have been demonstrated with pulse durations under 100fs. One of the implementation drawbacks of this laser regime is its strong dependence on the exact parameters of the Gaussian filter used.

It is desirable to have the output of the integrated mode-locked laser to have the shortest pulse duration possible, without having to use an integrated pulse compressor. Although integrated pulse compressors have been demonstrated on a monolithic

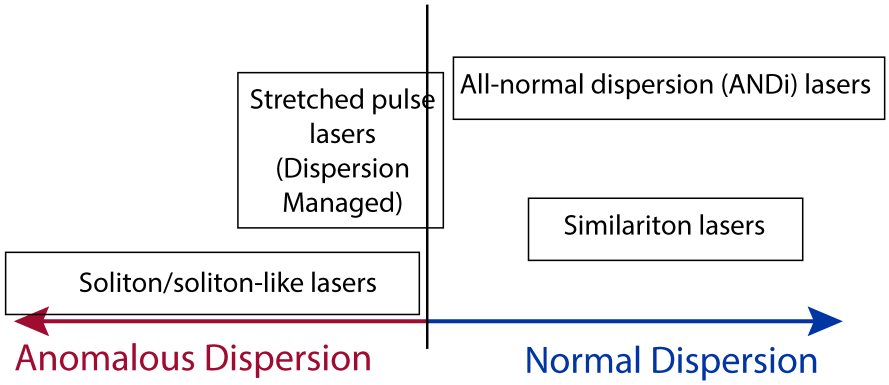

Figure 3-1: Mode-locked lasers operating regimes, based on net cavity dispersion.

on-chip platform [151], it would be an additional integrated photonics component inside of a DODOS on-chip synthesizer system, with possible insertion loss, and likely strong power and pulse duration sensitivity. As a general rule in integrated photonics sub-systems, it is good to avoid unnecessary additional devices. The pulse propagation scheme that provides the shortest pulse duration at the output of the MLL without any external pulse compression is a soliton, or soliton-like regime. Therefore, the MLL laser cavity should be designed with net anomalous dispersion and carefully controlled Kerr nonlinearity. While Kerr nonlinearity could be easily engineered, chromatic material dispersion of SiO_2 and Si_3N_4 is normal. Waveguide dispersion could be used to force net dispersion of a device to be in anomalous regime for the wavelengths of interest. A different approach would be to use the all-normal dispersion laser cavity with a discrete dispersion-compensating element.

To qualitatively look at the design parameter space of a soliton-like mode-locked laser, we look at general chirped secant squared solutions to Haus Master Equation [137, 119, 7], which assumes the effects of nonlinearity, dispersion, and self-amplitude modulation are small and additive within one cavity round-trip, assuming steady-state operation. The Master Equation is written as

$$\left\{(D_g + jD)\frac{d^2}{dt^2} + (g - l - j\psi) + (\gamma - j\delta)|a(t)|^2\right\} a(t) = 0 \tag{3.1}$$

where $D_g = \frac{g}{\Omega_g^2}$, g is optical (electric field) gain [1/m], Ω_g is gain bandwidth [1/m^2], D is dispersion parameter $[s^2/m]$ with D = GVD/2 where GVD is group velocity dispersion; l is field loss per round trip [1/m], ψ is accumulated linear phase, γ is SAM coefficient [1/W], and δ is SPM coefficient [1/W].

The solutions are plotted in terms of normalized parameters D_n and τ_n, where $D_n = D/D_g$, $\tau_n = \frac{W\tau_p}{2D_g}$, W represents the pulse energy, and τ_p represents the actual width of the pulse. Another parameter that is frequently calculated from solving the Master Equation is the stability S of the optical pulse, which is defined as net loss before and after the pulse. For stable mode-locking, optical pulse propagation should be favored and amplified over lower intensity noise, and thus $S = l - g > 0$. The net loss window must precede and follow each optical pulse. When stability S of the MLL is less then zero, the wings of the pulse get amplified more than the central part, which leads to pulse breakdown. Figure 3-2 shows pulse stability S, pulse duration, and chirp parameter versus normalized dispersion parameter D_n, for one particular value of SAM coefficient γ_{SAM}, but varying Kerr nonlinearity δ_{SPM} values. Soliton and soliton-like pulses are represented by curves at the upper left quadrant of each plot (negative D_n, anomalous dispersion regime). From the pulse duration plot it is evident that higher values of nonlinearity for a particular (low) value of anomalous dispersion allow for shorter pulse durations, which is exactly the soliton pulse shaping effect. For higher values of anomalous dispersion, the pulses become strongly negatively chirped, and nonlinearity can no longer shorten the pulse. Excessive Kerr nonlinearity (large δ_{SPM}) within anomalous dispersion could also drive the pulse into the unstable regime, looking at Figure 3-2 [c]. Net normal dispersion regime represents all-normal-dispersion laser solutions, which must be stabilized with bandwidth compensation. Generally, pulse durations in the normal dispersion regime are larger than those of the anomalous regime, given the same nonlinearity value and the same absolute value of dispersion.

Figure 3-3 [a], [b], and [c] show the solution curves for pulse duration, chirp, and stability, respectively, for a fixed value of δ_{SPM}, but varying values of self-amplitude modulation coefficient γ_{SAM}. From the chirp plot, in the net anomalous regime the

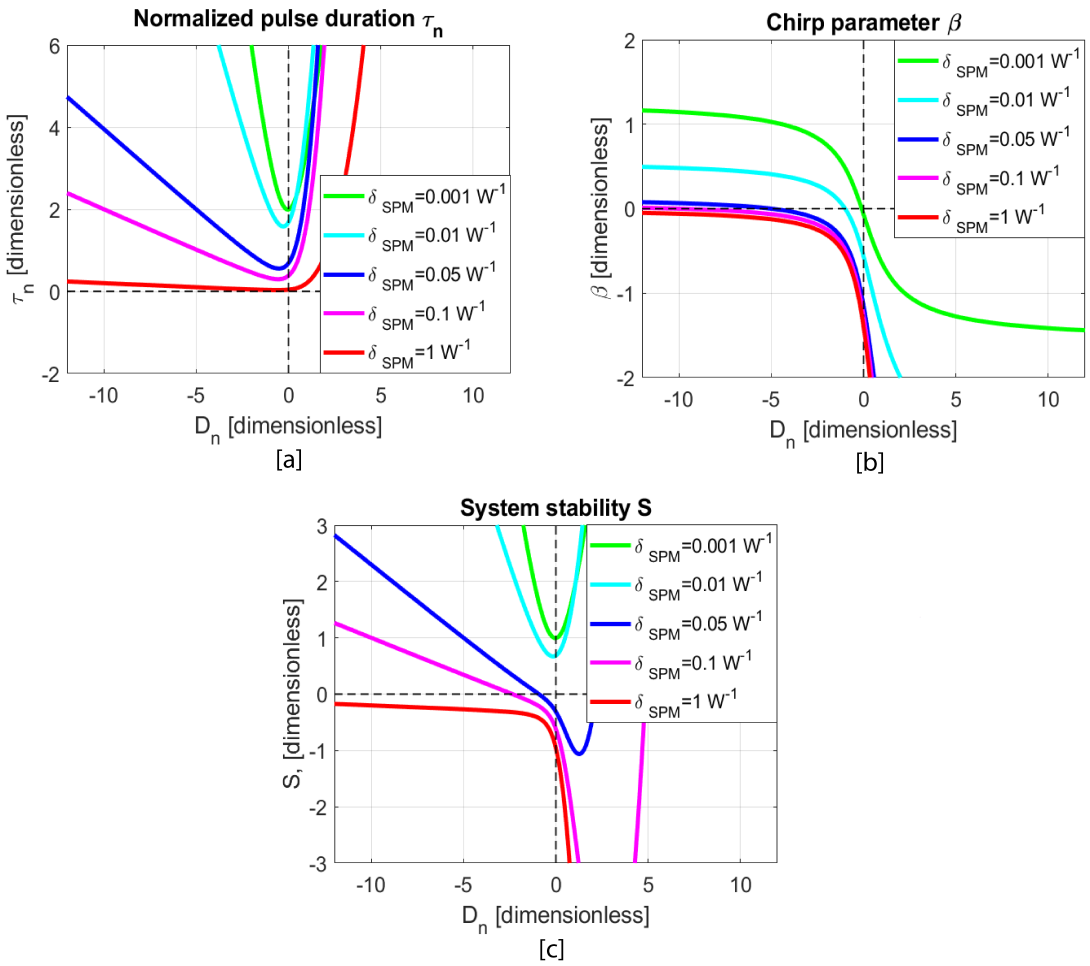

Figure 3-2: Haus Master Equation solution curves for a fixed value of $\gamma_{\mathrm{SAM}} = 0.01\ W^{-1}$, and varying nonlinearity δ_{SPM}. [a] Normalized pulse duration vs normalized dispersion; [b] Chirp vs normalized dispersion; [c] Stability parameter vs normalized dispersion.

SAM coefficient does not strongly affect the chirp or the pulse width. However, the stability of optical pulses strongly depends on the SAM coefficient. Larger SAM values allow for significantly more stable mode-locking solutions. If one is unable to increase the SAM coefficient in a particular laser system, potential solutions to bring the laser into a stable mode-locked operating regime might be to either decrease the nonlinearity of the system or make the net dispersion more anomalous, as proposed in Section 3.3. Chapter 2 focuses on design parameters of the integrated mode-locking device that would maximize the SAM coefficient and allow for a more stable mode-

locking operation.

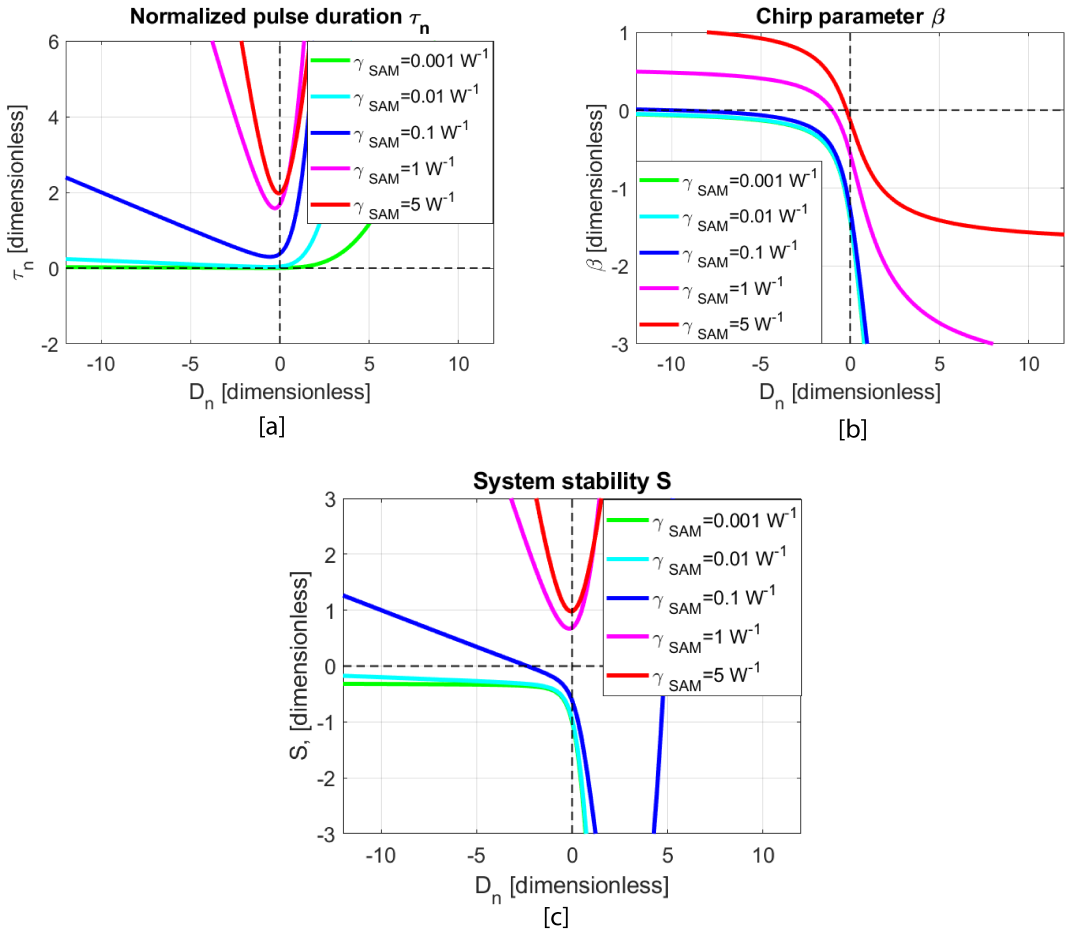

Figure 3-3: Haus Master Equation solution curves for a fixed value of $\delta_{\mathrm{SPM}} = 1\ W^{-1}$, and varying SAM coefficient γ_{SAM}. [a] Normalized pulse duration vs normalized dispersion; [b] Chirp vs normalized dispersion; [c] Stability parameter vs normalized dispersion.

For particular values of small signal gain coefficient, gain bandwidth, pulse energy, and dispersion / nonlinearity values, the Master Equation could be used to roughly estimate final pulse duration, chirp, and bandwidth. This formalism should be used only as general guidelines for initial laser design and a qualitative laser behavior indicator, to provide intuition and first look at the initial parameter space. The Master equation has analytical solutions only in the approximation of small-change-per-round-trip regime, where all laser cavity parameters could be linearly expanded to

the first order. This is generally inaccurate in many MLL systems (and particularly so in some of our integrated laser designs). Moreover, the formalism ignores many higher order effects. Nevertheless, this serves as an important first-order approximation design step.

Finally, we comment on possible laser resonator configurations. Free-space laser resonators have been constructed with linear, ring, sigma, and more-complicated multiple-mirror-assisted folded configurations. Only a linear configuration can produce stable pulses without some form of optical isolator in the cavity. Since the state-of-the-art CMOS-compatible integrated photonics community currently lacks integrated isolator approach, linear resonator configuration is the most straightforward choice. It does, however, have unique disadvantages, such as signal standing waves in the cavity, that could create spatial hole burning and prevent self-starting [152]. Once on-chip optical isolators become available, integrated mode-locked lasers will quickly move to ring-based resonator configurations, which should greatly simplify laser design and operation.

Once the physical design space of the laser has been established, integrated photonics is used to design laser components to create a cavity within the required parameter range. In the next few sections, we describe a comprehensive integrated photonics design process for on-chip MLLs with the following physical parameters, based on the discussion in this section:

- Linear laser cavity with 500MHz-1.5GHz repetition rate
- Net anomalous dispersion regime
- Sufficient Kerr nonlinearity to provide for soliton effect to shorten the pulses
- Artificial saturable absorber with strong γ_{SAM} to stabilize the pulses against laser noise

3.1 "Spiral" Mode-Locked Laser Design

Our first mode-locked laser architecture is based on a linear resonator spiral-shaped cavity configuration. The gain material is Thulium-doped Aluminum Oxide glass (Al_2O_3:Tm^{3+}) which is deposited using reactive ion sputtering on top of the entire chip. The laser is pumped with the 1614nm Erbium-doped Fiber Amplifier (EDFA), and lasing occurs around 1900nm, corresponding to $^3H_6$-$^3F_4$ atomic transition in Thulium. The total one-way length of the laser cavity is about 14cm, which corresponds to 680MHz repetition rate.

3.1.1 Architecture

The full laser architecture is shown schematically in Figure 3-4. The pump enters the MLL through a spot-size converter Si_3N_4 waveguide shown on the left in Figure 3-4. The pump light then further propagates through a pump/signal combiner, which is designed to let 1614nm pump light propagate straight through the coupler, and to let 1900nm signal light couple across, thereby separating the pump and the signal. Next, the pump light enters the gain waveguide through several waveguide transition components (which allow to transition between different photonic layers and eventually into the appropriate mode of the gain waveguide). In the gain waveguide, the pump mode is sufficiently expanded in order to have a large interaction region with the gain material. The trench, etched into the SiO_2 layer (shown in gray in Figure 3-4), contains the gain region where the pump and the signal modes overlap in the gain material over the length of the trench, establishing a sufficient interaction region to sustain steady-state lasing. The trench/gain waveguide bends in a spiral-like fashion and terminates via trench-to-Si_3N_4 waveguide transition components. The signal exits the trench and enters the Si_3N_4 waveguide that goes to either the saturable absorber spot-size converter, or to the integrated nonlinear mode-locking element (nonlinear interferometer), shown on the bottom right. Two laser configurations were investigated - the one that would work with a conventional semiconductor saturable absorber, and the one that would work with an integrated nonlinear mode-locking element. At

low average signal power levels, both the saturable absorber and the nonlinear mode-locking element act as linear reflectors. Thus, the signal is reflected back into the cavity, propagates through the gain region, exits the trench on the left, goes through the pump/signal combiner, and makes it into the dispersion-compensating grating. The grating is designed to both reflect the signal and to deliver a specific amount of dispersion onto the signal to put the gain cavity into the net anomalous regime, in order to properly mode-lock the laser. The laser cavity is therefore formed by two end-reflectors a dispersion-compensation grating (DCG) on one end, a nonlinear mode-locking element on the other end, and a gain region in between.

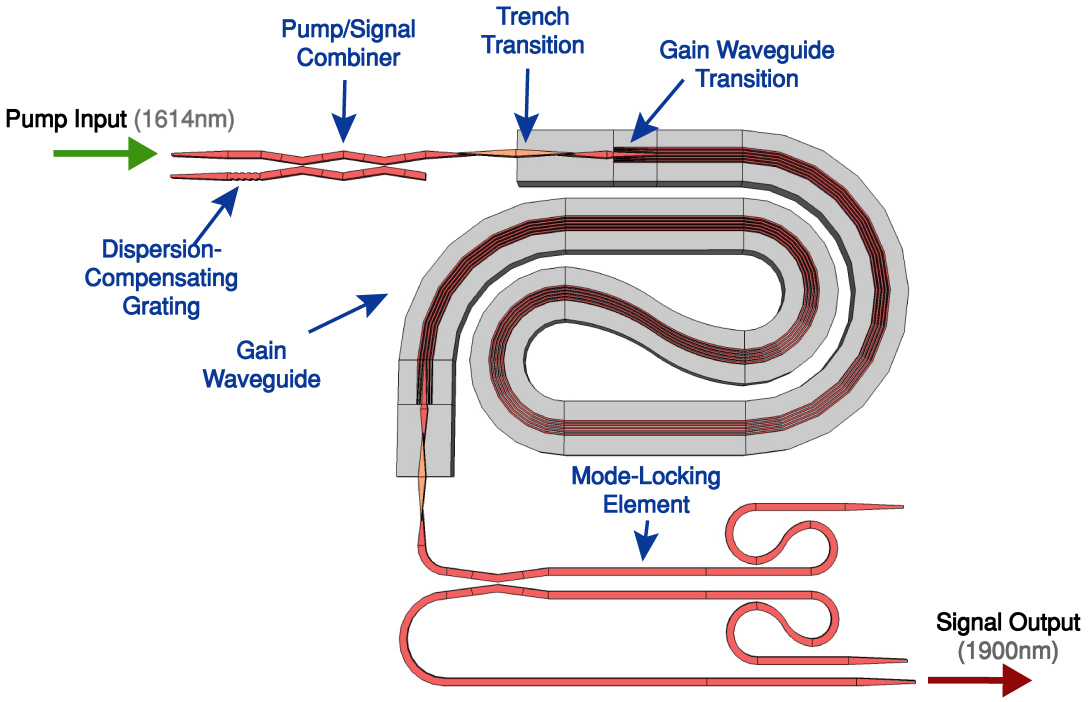

Figure 3-4: Schematic of the spiral mode-locked laser architecture, with key components shown (not-to-scale).

When designing integrated lasers, the gain cavity length should be sufficient to accumulate enough net gain to overcome all the component losses. Because the integrated chip size is small, the laser gain region should be folded. This folded

configuration depends strongly on the bend radius that allows the gain waveguide to have minimal bend radiation and bend mode mismatch losses. The MLL design presented in this section relies on a simple circular bend design, where almost no modifications were done to gain waveguide while bending it into a spiral. Therefore, the bend radius is large, and lasers have a large footprint that is determined primarily by the bend radius of the gain waveguide.

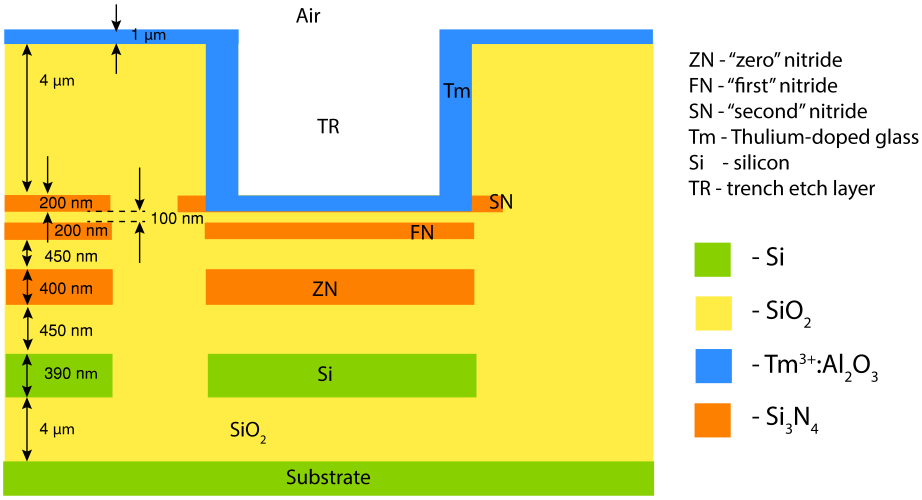

Figure 3-5: Photonic layers used for MLL design/fabrication.

Mode-locked lasers were designed using the photonic material and layer heights as determined by the DODOS project silicon photonics platform. Exact photonic layers with corresponding layer heights are shown in Figure 3-5. The silicon layer was not used in this design/tape-out. All $Si/SiO_2/Si_3N_4$ layers were fabricated at CNSE, while the gain material was deposited at MIT in the Microsystems Technology Laboratories. Over the gain region, a 70μm-wide and 4μm-deep trench was etched in SiO_2, and the gain material, deposited on top of the chip, partially filled in the trench. The trench allows to bring the first nitride layer (FN) within 200nm of the gain material. Therefore, when the pump/signal modes see the trench with Al_2O_3:Tm^{3+} in it, the modes expand and start interacting with the gain material. Although the gain material is physically present over the entire chip, the light doesn't interact with it outside of the trench region, as the four microns of SiO_2 that separates the Si_3N_4

layers from the Al_2O_3:Tm^{3+} layer is enough to have the optical mode confined in the nitride.

Due to various design requirements, different MLL components shown in Figure 3-4 were implemented using different available photonic layers from Figure 3-5. Layer-to-layer transition components were designed to facilitate low loss transitions between those layers. Table 3.1 lists MLL components and corresponding photonic layers that they were implemented in.

Component	Layer	Layer height
Input/Output spot size converters	FN/SN	200 nm
Pump/Signal Combiner	ZN	400 nm
Gain Waveguide	FN/TR/Tm	1.1μm for Al_2O_3:Tm^{3+}
Mode-locking element	FN/SN	200 nm
Dispersion-compensating grating	FN	200 nm

Table 3.1: Photonic material layers used for MLL components in spiral laser architecture.

3.1.2 Gain Material Properties

The gain material used for 1900nm lasers in Thulium doped aluminum oxide glass (Al_2O_3:Tm^{3+}), which is deposited in MIT's Microsystems Technology Laboratories as a back-end process on our MLL wafers.

Aluminum oxide glass has been shown to be a low loss host for various rare earth dopants [64, 67, 68, 153]. It is deposited using RF magnetron sputtering of Aluminum with Argon plasma and a controlled O_2 flow rate. The deposition is done under high vacuum, and at a substrate temperature of 550°C. The purity of the film is directly related to the substrate temperature. Film thickness is controlled by measuring the deposition rate at a fixed RF target power and running the deposition for a pre-calculated time period. Using a conventional quartz crystal monitor for deposition rate measurement is not practical in our case, due the high temperature in the chamber. Each film is characterized for background losses by coupling the light into the film using a prism, and measuring the decay of this guided light as a function

distance [154]. For active (gain) films, Thulium is co-sputtered with Aluminum at separate rates, corresponding to the desired active ion concentration in the film. Thulium has been widely used in industry and the scientific community to provide optical gain and lasing at 1900nm, due to its atomic $^3H_6$-$^3F_4$ transition [155, 156, 157]. A simplified energy level diagram for Thulium ion is shown in Figure 3-6. Two widely used pumping schemes are available for the $^3H_6$-$^3F_4$ transition, which is responsible for 1900nm lasing: 1. In-band pumping of the $^3H_6$-$^3F_4$ transition itself with 1600nm, and 2. out-of-band pumping the $^3H_6$-$^3H_4$ transition, with 790nm. The process for 790nm is quantum-mechanically more efficient, as it results in a cross-relaxation process, which generates two 1900nm photons for each absorbed 790nm photon [158, 159].

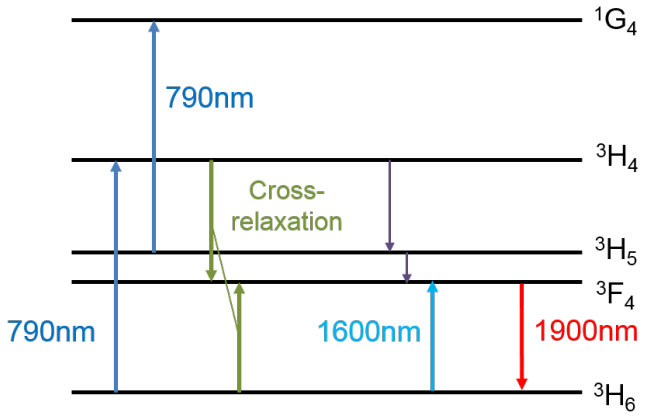

Figure 3-6: Thulium^{3+} ion energy level diagram (shown are only the most relevant energy levels).

Spectroscopic characterization of Al_2O_3:Tm^{3+}films was done by E. Salih Magden, and is described in detail in [6]. Here we briefly describe the film characterization, and list key measured parameters. Thulium ion concentration in the deposited Al_2O_3:Tm^{3+}films has been measured using a Rutherford back-scattering method for various levels of the RF power to Thulium target, and data obtained were fit to an analytical formula. This allows to determine the Thulium ion concentration versus applied power to the Thulium target. The absorption cross-section of Al_2O_3:Tm^{3+} was measured around 790nm and 1600nm, by using channel waveguides of known geometry with a tunable laser source of desired wavelength. Upper state life time of

the gain film was measured by characterizing the amplitude and phase response of the input pump light with a sinusoidally varying excitation, after it was sent through the waveguide where the majority of the mode was confined within the active film. Summary of spectroscopic parameters is shown in Table 3.2.

Upper state spontaneous emission lifetime	568 $\pm$48 μs
Thulium ion concentration at 16W Tm RF target power	2.3×10^{20} cm^{-3}
Absorption cross-section at 1614nm	2.75×10^{-21} cm^2
Absorption cross-section at 790nm	6.5×10^{-21} cm^2

Table 3.2: Spectroscopic properties on Al_2O_3:Tm^{3+} film, from [6].

We choose the in-band pumping scheme, because this greatly simplifies integrated photonics design. 1600nm pump and 1900nm signal wavelengths are close to each other, which allows to design various waveguides that are single mode for both the pump and signal wavelengths. Level-to-level layer transitions, pump/signal overlap, and waveguide bends are all much easier to implement with this pumping scheme. In contrast, 790nm pump is almost a factor of two and a half times smaller in wavelength that the 1900nm signal. This would necessitate a very different laser cavity architecture from the one presented in Figure 3-4. For all the 1900nm lasers presented in this thesis, 1600nm pumping scheme was used. However, since a key part of the DODOS program metrics is low electrical power consumption (see Table 1.2), 790nm-pumped mode-locked lasers will be designed at MIT in the near future.

3.1.3 Laser Components Design and Characterization

The following section describes the design and characterization results of all major MLL components in details. In addition to full mode-locked lasers, all individual components were fabricated as separate test structures with multiple parameter variations, in order to accurately characterize each individual component.

Pump/Signal Combiner

The pump-signal combiner component at the input of the MLL serves to couple the pump light into the cavity, and to direct the signal light to the dispersion compensating grating, and then back from the grating into the MLL cavity. The dispersion compensating grating acts both as a reflector and as a dispersion element. This component, which is shown in Figure 3-7 [a], is designed as a combination of two back-to-back directional couplers, each coupler having a 50/50 power splitting ratio at the signal wavelength (1900nm). This effectively makes the device a Mach-Zehnder interferometer for 1900nm with zero phase difference between the arms, with the 1900nm light always coupling across the device (ports 3↔2, 1↔4), as shown in Figure 3-7 [a]. The directional coupler parameters were designed in such a way as to transmit

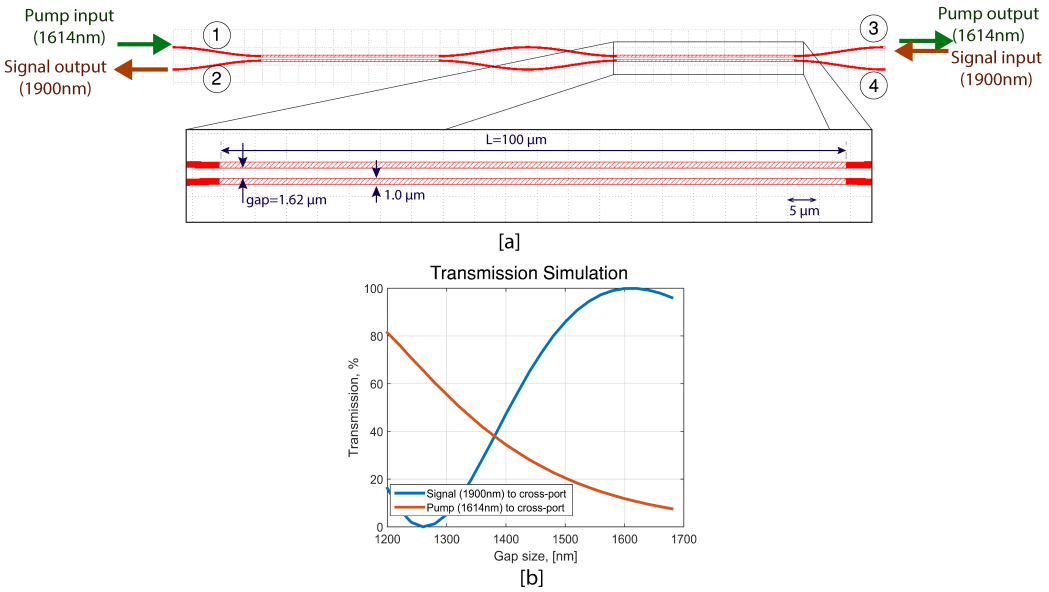

Figure 3-7: Spiral 1900nm MLL pump-signal combiner design: [a] Layout, with relevant ports and dimensions; [b] Cross-port transmission simulation.

the pump wavelength (1614nm) through the coupler with minimum loss. The large wavelength separation between the pump and the signal allows to easily pick the directional coupler parameters in such a way that shorter wavelengths (1614nm pump) do not see the directional coupler at all, and hence simply transmit through their waveguide unperturbed (ports 1↔3 and 2↔4). The device is implemented in the

"ZN" bottom 400nm thick nitride layer.

Coupled-mode-theory-based simulation of the full device transmission, for cross-port coupling, is shown in Figure 3-7 [b]. No pump signal should couple to the cross-port, and almost all the signal should couple through. The devices were characterized using a CW L-band laser for the pump, and a fiber-based 1900nm CW laser for the signal. The insertion loss for the signal, measured for signal path going across the device (ports 3↔2 in Figure 3-7 [b]), was measured to be 0.6 dB/cm. The insertion loss for the pump, measured for the pump through-path (ports 1↔3 in Figure 3-7 [b]), is 0.1 dB.

Gain Waveguide

The main MLL gain waveguide cross-section is shown in Figure 3-8 [a]. It consists of a 5-piece, 200nm tall segmented nitride waveguide, a 100nm oxide gap, and $\sim 1.1\mu m$ thick Al_2O_3:Tm^{3+} gain film. A 70μm-wide and 4μm-deep trench was etched into SiO_2 layer to allow the gain material to be within 100nm of the Si_3N_4 layer. The pump/signal modes are anchored to the structure by silicon nitride, but the majority of the mode is in the aluminum oxide film.

This specific waveguide geometry was chosen to optimize several parameters. First, both the pump and the signal modes must have a large overlap with the Al_2O_3:Tm^{3+} gain film. Second, the overlap of the pump and the signal modes together should be maximized inside of the gain film. Finally, the spiral laser architecture uses circular bends, so the bend radiation loss and the bend/straight waveguide mode overlap must be optimized by optimizing film height and the arrangement of the nitride pieces. The Si_3N_4 waveguide design was chosen to be segmented because this allows to reduce the effective index of the signal and pump modes, and thus to increase the mode fraction inside of the gain region. The width and separation of the Si_3N_4 segments was optimized for the pump/signal overlap in the gain region, and the film height was adjusted to minimize the mode mismatch with the circular bend mode (the size of the bend itself was limited by the chip reticle, the smallest gain waveguide bend radius used in this particular MLL cavity was 3.45mm). Thicker Al_2O_3:Tm^{3+}

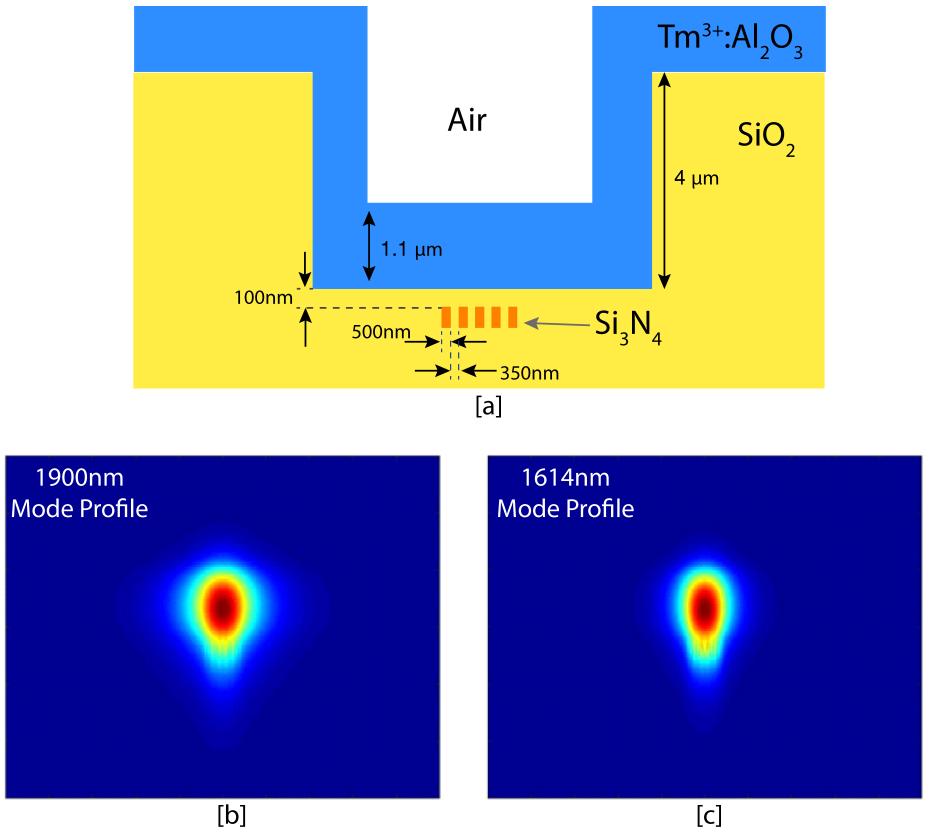

Figure 3-8: Spiral MLL (1900nm) gain waveguide geometry: [a] cross-section of the main gain waveguide; [b] Signal (1900nm) mode; [c] Pump (1614nm) mode.

film heights would increase the pump-signal overlap in the gain region, but would also increase the bend losses. Additionally, increasing film thickness also increases normal dispersion of the waveguide. We select the film height that allows to keep the bend-straight mode overlap to 99.8%, with a 60% of pump-signal mode overlap in the gain material. The final gain waveguide design was chosen to have a 5-piece segmented Si_3N_4 waveguide, with individual nitride pieces being 200nm tall and 500nm wide, with 300nm gap between the individual pieces. The optimum Al_2O_3:Tm^{3+} film height was calculated to be 1.1μm. We note however that active material deposition thickness could be accurately controlled to $\pm$50nm only. Signal and pump modes in the waveguide are shown in Figure 3-8 [b] and [c] respectively.

Passive losses of the gain waveguide, with a 1.1μm Al_2O_3film (no gain dopants) were measured to be 0.74 dB/cm using both the cut back method, and loss extraction

from Fabry-Perot-induced fringes. Exact bend losses were not measured for this chip, since the bend radius is too large, making large bend radius test structures impractical.

Trench Transition / Gain Waveguide Transition

Although our integrated mode-locked laser has numerous layer-to-layer and structure-to-structure transitions, in this section we discuss only the most relevant and challenging ones. In particular, prior to entering into the main gain waveguide, the light for both pump and signal wavelengths is confined inside of a Si_3N_4 ZN layer, which is 450nm below the FN layer, which is in close proximity to the gain trench. Therefore, there is a need for a vertical transition component, to couple both the pump and the signal from the confined ZN waveguide into the expanded trench mode, as shown in Figure 3-8 [b] and [c]. This component has two major parts. First, a transition component is designed to couple the light from ZN layer to a single nitride block in FN layer, underneath the gain trench. We refer to this component as a "trench transition" or an "escalator", due to its vertical layer change. After the escalator, the light is in the gain material, but it is held in place by a single piece of Si_3N_4 as opposed to the segmented nitride waveguide needed. Next, we slowly bring in additional nitride pieces and taper down the central silicon nitride block to get to the final gain waveguide architecture. We call the second component "gain waveguide transition".

The escalator component is shown schematically in Figure 3-9, which is not to scale but has all relevant dimensions and cross-sections along the transition. It is difficult to show the actual component layout, since it is much longer than it is wide, therefore it doesn't show up well in a single image. Part of the layout is shown in Figure 3-9 [b]. The ZN nitride layer is adiabatically tapered down, squeezing the optical mode out of the waveguide. At the same time, the FN nitride layer is adiabatically tapered up to the width of 2.0μm. As the mode is squeezed out of the ZN layer, it slowly transitions to the FN and active layers under the trench, over the length of the transition. The tapering profiles of both ZN and FN waveguides are slowly optimized to minimize

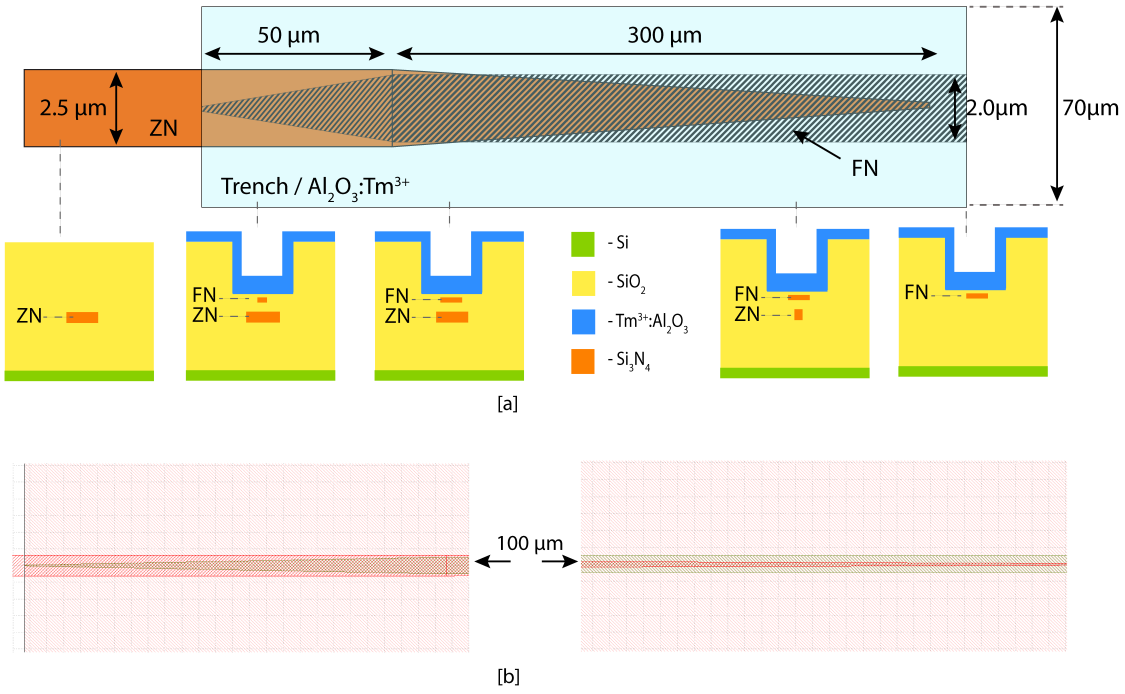

Figure 3-9: Spiral 1900nm MLL trench transition design:[a] Schematic of the ZN - FN escalator, with relevant dimensions, and cross-sections along the component; [b] Photonic layout of the transition (with middle part not shown).

optical losses through this transition for both the pump and signal wavelengths. The length of this transition component is 300μm. The insertion loss of the escalator transition was measured by a variation of the cut-back method, where test structures with progressively larger number of trench transitions stacked one after another were measured. In particular, 10, 20, 30 and 40 escalators were attached back-to-back in four different test structures, and the insertion loss of each such test structure was measured separately. The insertion loss of one escalator transition, at 1900nm, was measured to be 0.015dBs. The one-way spiral MLL cavity has two such escalator transitions. Therefore, the round-trip loss due to two escalators is 0.06 dB.

The next component is gain waveguide transition, where a single FN nitride piece underneath the gain trench is slowly transformed into the 5-piece gain waveguide, as shown in Figure 3-10. This waveguide transition was implemented using an adiabatic linear taper. Four extra four nitride pieces are slowly brought in from the sides

towards the main nitride block, while the width of the main nitride block is slowly tapered down. A single, 2μm long nitride piece is then adiabatically transitioned into a 5-piece waveguide, over 250μm long adiabatic transition. This waveguide transition ends with the gain waveguide as shown in Figure 3-8. It was measured in a similar way as the escalator transition, with a cut-back method variation, where an increasing number of back-to-back connected transitions were made as test structures. For this component, 28, 38, 48, and 58 waveguide transitions were made in a row, in order to accurately back-calculate the loss of one individual transition. Using a 1900nm CW laser, we measure the loss per single gain waveguide transition to be 0.02 dB/cm. For four such transitions per cavity round-trip, we get 0.08 dB net loss.

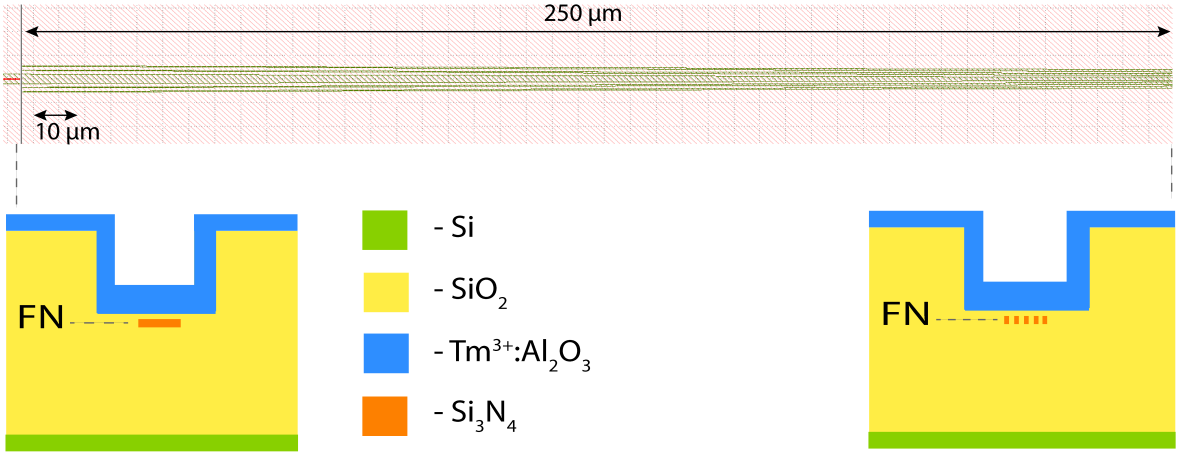

Figure 3-10: Gain waveguide transition for 1900nm MLL - a layout and relevant cross sections. The components transforms a single piece of nitride underneath the gain trench into a 5-piece waveguide needed for MLL operation.

Dispersion-Compensating Grating

Most of the MLL components presented so far in this section have normal dispersion (see Section 3.1.4 for the detailed dispersion map). For all constituent materials, chromatic dispersion is normal. Anomalous dispersion MLL components could potentially be achieved with waveguide dispersion, as has been done with optical fibers [160], however, since our material layer heights are fixed within the DODOS platform, this is

challenging for channel waveguides. Higher order waveguide modes could be used to achieve this task, however, they require adiabatic mode-converters to allow light to couple into the correct mode, which further increases the complexity of the system. Therefore, our laser cavity needs a dispersion-compensating component with a large anomalous dispersion in order to put the cavity back into the net anomalous regime, to facilitate soliton mode-locking. In fiber laser systems, anomalous dispersion could be added to the laser with a section of anomalous dispersion fiber or by using a chirped fiber Bragg grating. In free space and some fiber lasers, a prism pair [161] or a double-chirped mirror are used for dispersion compensation. [162, 163].

In this MLL design, we choose to implement an integrated double-chirped grating structure based on a double-chirped mirror theory developed in [162]. The layout, top view, and cross-section of the device are shown in Figure 3-11. The grating (designed by Purnawirman [164, 165] and characterized by P. Callahan) is implemented in the silicon nitride (FN layer), where the small side blocks are introduced next to the central waveguide to slowly perturb the effective index of the mode. By keeping the period of the side blocks constant (644nm for the central wavelength of 1900nm), but slowly varying the spacing between the side blocks and central waveguide, the reflection profile of the grating is changed slowly, avoiding strong oscillations in the dispersion profile of the device. This is analogous to slowly changing the duty cycle of the double-chirped mirror layer thicknesses. The central wavelength of the device is adjusted by tapering the width of the central waveguide block. The overall dispersion strength of the grating could be adjusted by varying the length of the grating. The gratings were designed to have over 90% reflection within 10nm bandwidth of the central 1900nm wavelength. Three separate designs, with three negative GDD values, were designed, in order to have several variations for more successful mode-locking. Gratings with higher GDD values are respectively longer. Table 3.3 shows the design values for the three gratings that were used in mode-locked lasers presented in this section. Figure 3-12 [a] shows the design-based simulations for the transmission, reflection, group delay, and group velocity dispersion for a grating with GDD value of -1.1×10^5 fs^2. The approximate bandwidth of the grating is 5-10nm, according to

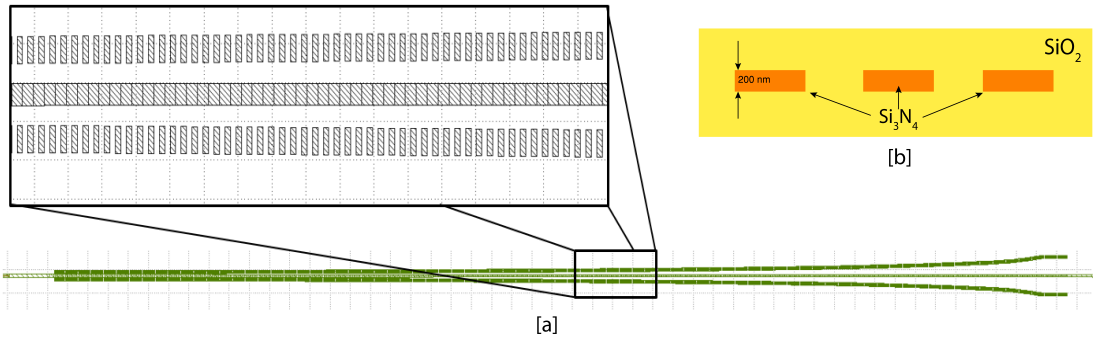

Figure 3-11: Integrated dispersion-compensating grating: [a] Layout and top view; [b] Cross-section.

design simulations.

Central Wavelength	Length	Period	GDD
1900 nm	360 μm	644 nm	-8.4×10^4 fs^2
1900 nm	500 μm	644 nm	-1.1×10^5 fs^2
1900 nm	760 μm	644 nm	-2.7×10^5 fs^2

Table 3.3: Dispersion compensating grating variations

Integrated gratings were fabricated and characterized for transmission/reflection bandwidth using a 1900nm CW laser. The result for the transmission measurement for the grating with GDD=-1.1×10^5 fs^2 is shown in Figure 3-12 [b]. The grating shows 90% reflection within 10nm bandwidth, centered around 1895nm. Because the 1900nm CW laser used for characterization of the devices didn't have enough wavelength resolution to actually measure the dispersion, the GDD values of the integrated gratings were not measured at 1900nm. However, separate gratings were fabricated for 1550nm-based lasers using the same theoretical formalism and software tools. The 1550nm-centered gratings were measured using an optical vector analyzer (LUNA Technologies), and the dispersion was within 10% of the simulated value. The results of the 1550nm characterization are presented in [165], and allow us to conclude that the general approach of the grating design works, and based on as-predicted transmission measurements at 1900nm, the GDD values for those gratings are within close agreement to design values.

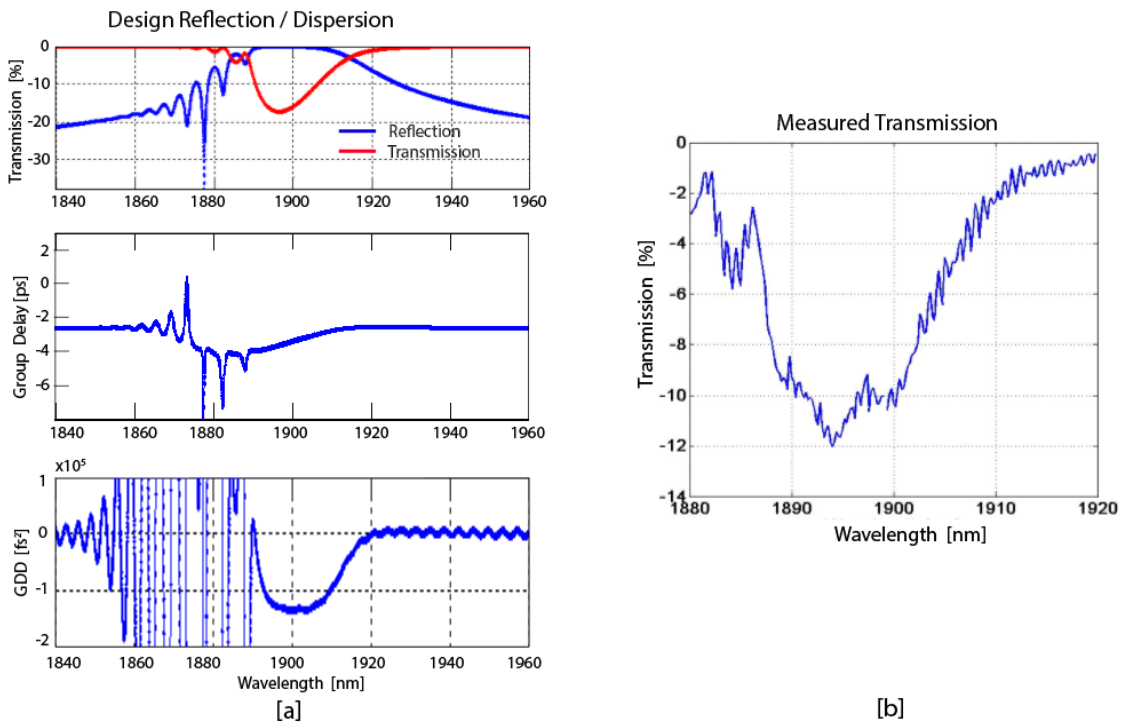

Figure 3-12: Design of the dispersion-compensating grating for 1900nm spiral MLL: [a] Simulations of reflection, transmission, group delay, and group delay dispersion. [b] Measured transmission for the respective grating.

Mode-Locking Element

We have designed the integrated MLL variations to be used with an on-chip integrated artificial mode-locking device, and with an off-chip commercial saturable absorber.

In case of a commercial saturable absorber, the light from the gain waveguide in Figure 3-4 is coupled into the FN/SN Si_3N_4 waveguide, which goes to the edge of the chip. The waveguide has a linear taper-based spot-size converter, which expands the optical mode incident onto the saturable absorber to provide enough saturation fluence to the device. The saturable absorber is then butt-coupled to the optical chip facet and acts as high reflector / saturable absorber. We have used the saturable absorbers from BATOP Gmbh [102], centered at 1900nm, with 60nm bandwidth, modulation depths from 4 to 30%, and 10 ps slow recovery time.

The on-chip integrated mode-locking device was a nonlinear interferometer, designed for the DODOS program, and described in detail in Chapter 2. The layout of

the device is shown in Figure 2-14, the exact device parameters are shown in Table 2.3, the nonlinear simulation of the device performance is shown in Figure 2-21, and the results are presented in Section 2.4.3. Based on the measured results, this device should have a reflection of around 35%, with 9% modulation depth.

Spot-Size Converters (pump/signal)

In order to maximize on/off chip coupling efficiency, edge couplers were designed for both the pump and the signal wavelengths. For all the experiments mentioned in this report, the pump (1614nm) was delivered to the chip using lensed SMF28 fiber, designed to have a spot diameter of $3\mu m$ (at 1550nm). The signal was picked up with a SM2000 lensed fiber, also designed for $3\mu m$ (at 2000nm). In order to standardize the components, one edge coupler device was designed and maximized for the pump wavelength. Although the edge coupler had higher losses at the signal wavelength, the losses were easily calibrated out to get the actual on-chip signal power. The edge couplers were designed in the double-nitride layers (FN and SN) as linear inverse tapers, where the mode, initially strongly confined in the Si_3N_4 layer, slowly expands to match the mode profile of the desired lensed fiber. The cross-section of the waveguide at the input (prior to tapering) of the linear taper along with corresponding electric field intensity profile is shown in Figure 3-13 [a]. This waveguide is then tapered down to a different width. We sweep the edge coupler width and calculate the overlap of the edge coupler mode profile with the Gaussian mode of the corresponding lensed fiber for both the pump and the signal (Figure 3-13 [b]) for each case. Next we optimize the length of the edge coupler in order to expand the mode adiabatically with minimum loss. Length optimization is shown in Figure 3-13 [c]. The final edge coupler is designed to taper down to 370nm width, using a $100\mu m$ long taper waveguide.

Edge couplers were characterized using separate test structures with a cut-back method. By having edge couplers with various straight waveguide sections in between, the losses of the straight waveguide and the edge couplers could be calculated. The loss of each edge coupler is measured in conjunction with the lensed fiber that is

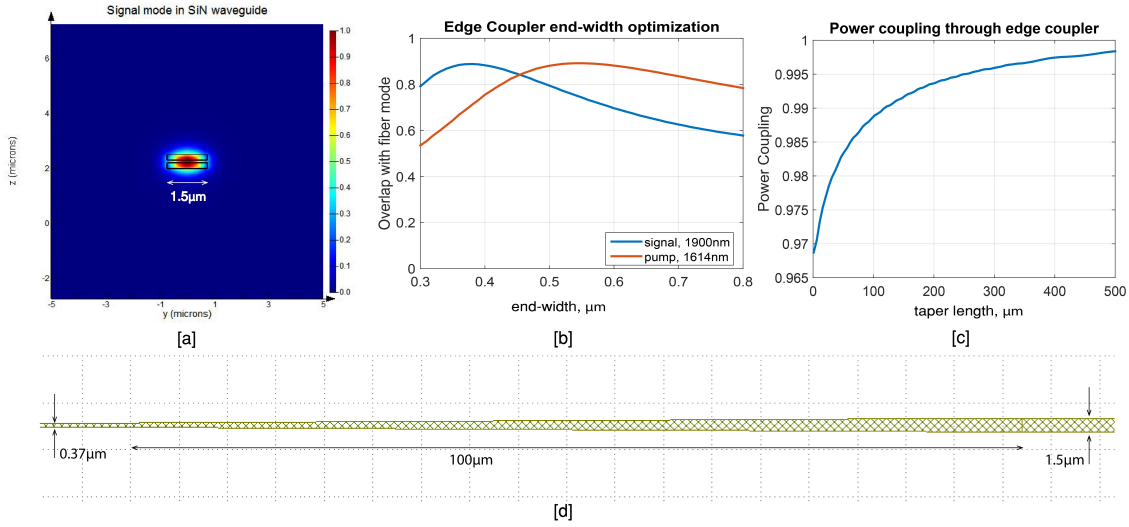

Figure 3-13: Edge coupler design: [a] Mode profile at the pump wavelength prior to the edge coupler; [b] Optimization of the final width of the edge coupler, for pump and signal wavelengths; [c] Optimization of the edge coupler length; [d] Layout of the device.

used to couple light into the device. The loss of the pump edge coupler, measured at 1614nm, was measured to be 1.6 dB/facet. The loss of the edge coupler for the signal wavelength of 1900nm was measured to be 2.1 dB/facet.

3.1.4 Dispersion/Nonlinearity Optimization

It is important to have net anomalous dispersion in the MLL cavity. Three GDD values for integrated grating designs were chosen to put the net laser GDD into the anomalous regime. Table 3.4 shows dispersion and effective nonlinearity values for each MLL component (without the integrated grating), along with their one-way lengths. Round trip contributions to nonlinearity and dispersion are also calculated. The net cavity dispersion, without any compensation or grating, is very strongly in the normal regime. The NLI contributes 1.5 times as much dispersion to net value as the gain waveguide, despite the fact that the gain waveguide is five times longer. The NLI also contributes larger nonlinear phase to the optical pulse. The last column in Table 3.4 can be used to roughly estimate the nonlinear phase accumulation in the

cavity. For example, given realistic parameters for our MLL, for average intracavity power of 20mW, with 500fs secant squared pulses at 600MHz repetition rate, the peak power is about 60W. The nonlinear phase accumulated during one cavity round-trip is then $0.05(W)^{-1} \times 60W = 3 \approx \pi$. This number is an estimate, because in reality loss, gain, and dispersion change the peak power of the pulse as it propagates, which all change the accumulated nonlinear phase. More accurate values could be estimated using full oscillator model as presented in Section 3.1.5.

	Layer	Width	Length	β_2	γ_{NL}	$\beta_2 \cdot 2L$	$\gamma_{NL} \cdot 2L$
		μm	mm	fs^2/mm	$(W\ m)^{-1}$	fs^2	$(W)^{-1}$
Pump/Signal Comb.	ZN	1.00	0.430	2001	0.78	1,721	6.7×10^{-4}
Gain Waveguide	FN/TR	-	120	100	0.088	24,000	0.021
NLI	FN/SN	1.5	23	820	0.6	37,720	0.028
					Total:	**63,441**	**0.05**

Table 3.4: Spiral MLL dispersion / nonlinearity component contributions. The last two columns show round-trip contribution of dispersion and nonlinearity, respectively. Dispersion compensating grating is not included.

Table 3.5 shows the net MLL cavity round-trip dispersion, with three available integrated grating GDD values. In each case, the net MLL cavity dispersion with grating compensation is strongly in the anomalous regime. Large nonlinear phase shift would be needed to make the pulse duration shorter than 1ps. We note that the bandwidth of our integrated gratings in this version of the MLL is at most 10nm. The reflection of the grating has a sharp roll-off outside of this 10nm bandwidth range. This restricts the pulse durations to above 400fs even with proper dispersion/nonlinearity balance. Section 3.2 shows a different MLL architecture, with novel integrated grating designs with 100nm bandwidth, which are able to support optical pulse with $<$ 100fs durations. Net GDD values from Table 3.5 and total accumulated nonlinearity could be used in the Soliton Area Theorem ($E_p = \frac{2|\beta_2|}{\gamma\tau}$) to estimate the lower bound on final pulse duration.

	unit	Design 1	Design 2	Design 3
Integrated Grating GDD	fs^2	$-84,000$	$-110,000$	$-270,000$
Round-trip MLL cavity GDD	fs^2	$+63,440$	$+63,440$	$+63,440$
Net GDD (MLL+Grating)	fs^2	$-20,560$	$-46,560$	$-206,560$

Table 3.5: Net cavity GDD, with three available integrated grating designs.

3.1.5 Numerical Pulse Propagation Model

Although the Haus Master Equation is an excellent tool for the first order MLL design, it is not very accurate for multi-component lasers with non-uniform distribution of dispersion and nonlinearity. A more rigorous approach to model mode-locked lasers is the numerical simulation of the laser based on the solutions of the Nonlinear Schrodinger Equation (NLSE). Such simulations allow to accurately account for the effects of the dispersion, nonlinearity, gain and loss interplay. Gain and saturable absorber saturation effects could be accurately modeled as well. Moreover, for bandwidth-sensitive devices, the exact wavelength-dependent response could be used inside of this model, to see, for example, how exactly the bandwidth of the grating affects the final pulse duration.

The following NLSE form is used for this simulation:

$$\frac{\partial A(z,t)}{\partial z} = \frac{\beta_2}{2}\frac{\partial^2 A(z,t)}{\partial t^2} - j\gamma_{\mathrm{NL}}|A(z,t)|^2 A(z,t) + gA(z,t) - lA(z,t) \tag{3.2}$$

where $A(z,t)$ is field amplitude, defined such that $|A(z,t)|^2$ is optical power, β_2 is dispersion in fs^2/m, γ_{NL} is effective nonlinearity in $(W\ m)^{-1}$, l is linear field loss in units of $1/m$, g is pulse energy-dependent (field) gain in units of $1/m$, where power gain is defined as $g = \frac{g_0}{1+E_{sat}/E}$ where E is pulse energy at any given time and g_0 is small signal gain. The small signal gain coefficient was calculated from a separate amplifier simulation, and E_{sat} was calculated from gain lifetime and emission and absorption cross-sections. Equation 3.2 is solved for each MLL cavity element using the symmetric split step method with adaptive step size. A full simulation schematic is shown in Figure 3-14 for the MLL cavity (the corresponding MLL cavity is shown in Figure 3-4), where the pulse is propagated through all successive MLL components

in the unfolded version of the MLL cavity (the unfolded version is needed to properly simulate the round-trip propagation, when the dispersion-compensating grating is applied only once per round-trip). Dispersion, nonlinearity, and length values for each MLL component in this simulation are taken from Tables 3.4 and 3.5. In addition, linear losses of each component, and gain in case of the gain waveguide, are taken into account. The pulse is then propagated through this simulation many times, until a steady-state solution is reached, meaning the pulse repeats itself exactly after each round trip. For unstable MLL cavities, the simulation should never converge. Once the steady state solution is found, the resulting pulse is then propagated through this MLL cavity one more time, and pulse duration is calculated at each step along the propagation. This allows to display the pulse dynamics inside the cavity and to determine the pulse duration at the output of the laser (which in our case is at the output of the NLI). dispersion quickly reduces the peak power.

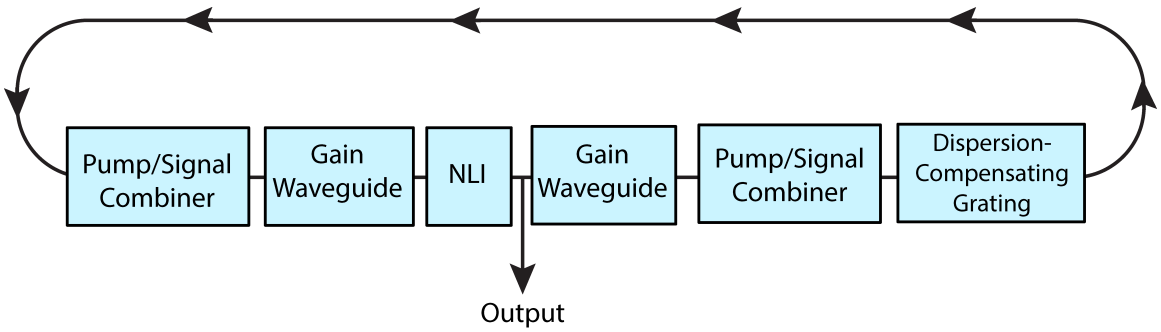

Figure 3-14: Schematic of a numerical propagation model structure for spiral MLL.

Figure 3-15 [a] and [b] show the convergence of a simulation for integrated grating #1 to a steady state solution. The pulse intensity in time and frequency domains are plotted in color vs time/frequency on x-axis, and the number of cavity round trips/10 on y-axis (the simulation saves the data every 10th round-trip in order to conserve memory during computation). The convergence is determined by looking at the final pulse shape in time and frequency domains to make sure it consistently reproduces itself over at least 10 round-trips. For both cavity design cases shown, about 2000 cavity round-trips are needed for the simulation to converge (this number would also highly depend on the gain and power inside of the cavity). Figure 3-15 [c] shows the

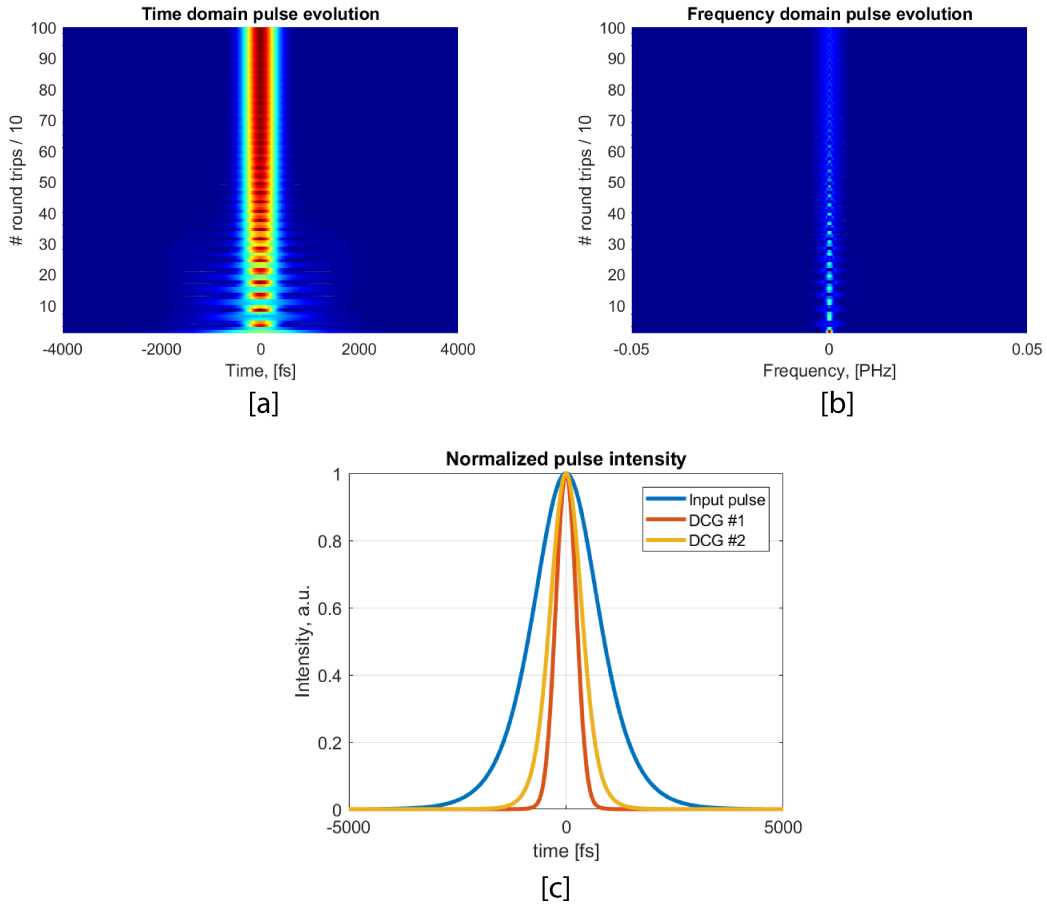

Figure 3-15: Numerical simulation results: [a] Pulse evolution to steady state in time domain, for grating GDD=$-8.4 \times 10^4\ fs^2$; [b] Pulse evolution to steady state in frequency domain, for grating GDD=$-8.4 \times 10^4\ fs^2$; [c] Normalized steady-state pulse duration for the input pulse, and the output pulses for two integrated grating dispersion values: DCG#1=$-8.4 \times 10^4\ fs^2$, DCG#2=$-1.1 \times 10^5\ fs^2$.

final pulse profile normalized to peak power, for integrated grating #1 and integrated grating #2, as specified in Table 3.5. For comparison, the pulse that was the input to the simulation is also shown. The cavity design that is closer to zero net GDD produces shorter pulses as expected. For the third integrated grating with GDD value of -2.7×10^5 fs^2, the simulation took a very long time to converge, the final pulses turned out to be 3.5ps long. Moreover, the simulation never reached a true steady state (but it didn't break apart the pulse either). For this reason, we do not show the simulation results for the third grating design. This design made the net MLL

GDD equal to $-206,000$ fs^2, which is a very large value. Likely there is not enough nonlinearity to stabilize the pulses, because such a large

Figure 3-16 [a] and [b] shows pulse evolution inside of the MLL cavity in steady state, for two GDD values of the integrated grating, corresponding to the pulses shown in Figure 3-15 [c]. In each case, the cavity is in the net anomalous regime. The pulse

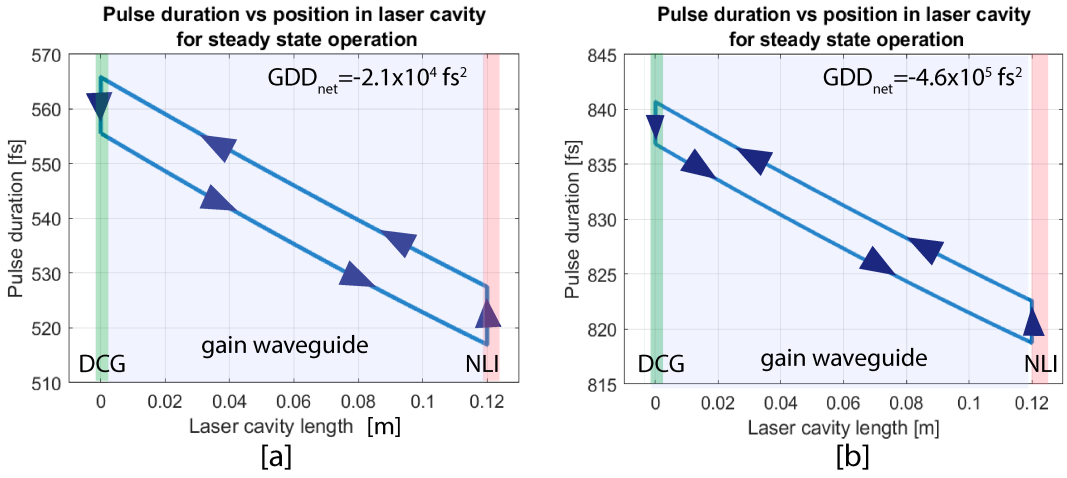

Figure 3-16: Steady-state pulse evolution inside of MLL cavity: [a] case with DCG#1, net cavity GDD$=-2.1\times10^4$ fs^2; [b] case with DCG#2, net cavity GDD$=-4.6\times10^4$ fs^2.

evolution is as follows: integrated grating adds a strong negative chirp on the pulse, making it longer than the transform-limited value. The pulse then propagates in the gain cavity towards the NLI, picking up normal dispersion, and partially un-doing the negative chirp. The pulse is the shortest in the NLI. NLI adds a large amount of normal dispersion, making the pulse longer at its output. The pulse then picks up more positive chirp as it propagates back in the gain waveguide towards integrated grating. The pulse is the longest at the input of the grating, but since the grating strongly overcompensates the GDD, the chirp of the pulse changes sign at the output of the grating. For a grating GDD of -8.4×10^4 fs^2, the pulse duration inside of the cavity varies from 518 fs to 565 fs. The pulse at the output of the laser is 526 fs long, according to this simulation. For a grating GDD of -1.1×10^5 fs^2, the pulse duration inside of the cavity varies from 819 fs to 841 fs. The pulse at the output of the laser

is 824 fs long.

Looking at both Figures 3-16 [a] and [b], the pulse duration evolves "counter-clockwise" with respect to the gain cavity, as shown with arrows. A more balanced dispersion compensation could make the pulse shorter at the output of the NLI, as opposed to on the input, thereby changing the "counterclockwise" pulse evolution to "clockwise" (see Section 3.2). Moreover, smaller net GDD value, together with larger grating bandwidth, should allow for much shorter pulses.

3.1.6 Layout and Fabrication

Figure 3-18 shows the final layout of our spiral MLL chip. Ten full spiral lasers are nested together to save space and form the main section of the chip. Separately, two chip columns (a wide column and a narrow column) with separate dicing trenches are made that include numerous test structures which allow us to measure and completely characterize all individual MLL components, and therefore verify their performance independently from the full laser. The layout was done in Cadence Virtuoso using in-house built PDK. We note that the structures inside of the MLL spirals in Figure 3-18 are not a part of the mode-locked laser or any related components.

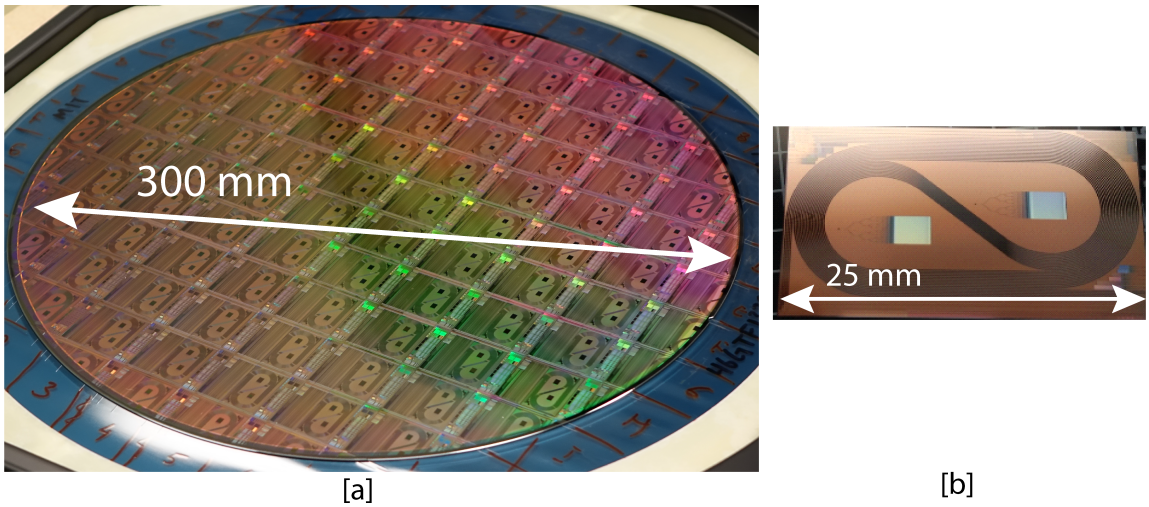

Figure 3-17: Fabricated device photos: [a] Full 300mm MLL wafer; [b] Individual MLL chip.

MLL devices were fabricated on 300mm wafers, using a 65nm CMOS-compatible fabrication facility at College of Nanoscale Science and Engineering at SUNY, Albany, NY. Photomasks and bulk silicon-on-isolator wafers were ordered separately. Fabricated wafers were diced into 2.4x2.5cm identical chips.

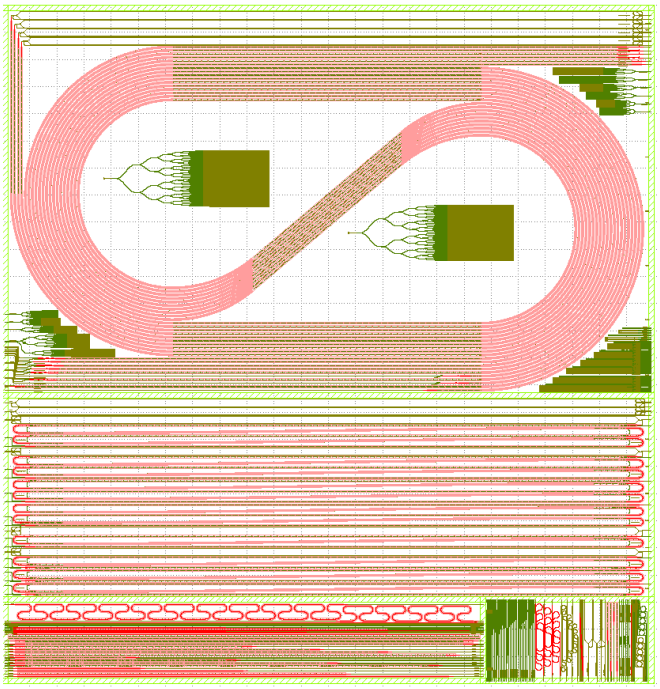

Figure 3-18: MLL chip layout, for spiral mode-locked lasers.

A photo of a diced wafer with MLL chips is shown in Figure 3-17 [a], and one individual MLL chip is shown in Figure 3-17 [b]. Active gain material was deposited on top of MLL chips at MIT's Microsystems Technology Laboratories. Following that, integrated heaters were deposited on top of NLIs (see Section 2.5) within each NLI-mode-locked laser, in order to tune the bias of the NLI for proper mode-locking regime.

3.1.7 Results

Full mode-locked lasers were characterized using the setup shown in Figure 3-19. The two different types of lasers measured were SBR-mode-locked lasers and NLI-mode-locked lasers. For both of those cases, the pump laser used was a 1614nm EDFA. It

was delivered to the optical chip through a fiber-based polarization controller. The

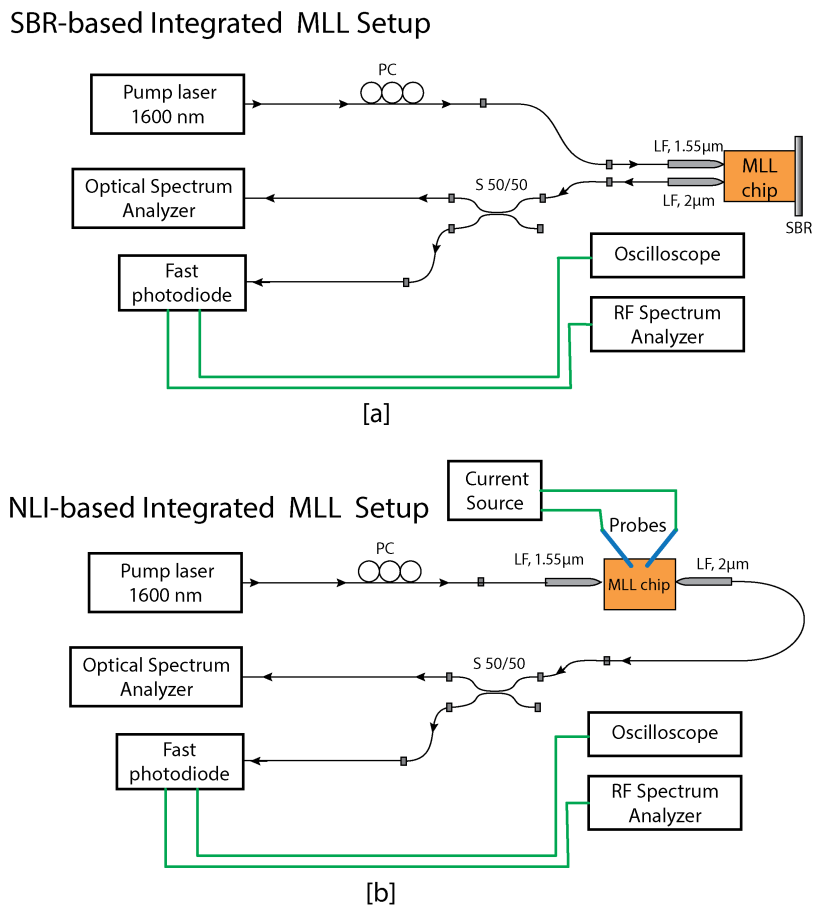

Figure 3-19: Experimental setup used for MLL characterization. [a] Setup used for SBR-based lasers; [b] Setup used for NLI-based lasers. Abbreviations: *LF* - lensed fiber, *PC* - polarization controller, *S 50/50* - 50/50 integrated power splitter.

pump light was coupled onto the laser using an SMF28 lensed fiber designed to have a spot size of 3 μm at 1550nm. The signal from the MLLs was collected using SM2000 lensed fiber, with the spot size of 3μm at 2μm wavelength. The output signal, once in SM2000 fiber, was split using an off-the-shelf broadband fiber-optic splitter, into two paths. One path was directed towards the Optical Spectrum Analyzer (Yokogawa, AQ6375, 1200-2400nm), and another path was directed onto a fast photodetector (EOT, ET-5000, 12.5 GHz electrical bandwidth). The electrical signal from the detector was split into two channels, going into the oscilloscope (4GHz sampling rate)

for time domain measurements, and into electrical spectrum analyzer for RF measurements (Agilent, PSA Series, 42 GHz).

SBR-mode-locked lasers look very similar in architecture to the device shown in Figure 3-4, having exactly the same integrated components design, with the difference that at the output of the gain cavity the double-layer silicon nitride waveguide goes directly to the edge of the chip (there is no integrated NLI). The waveguide has an appropriate spot-size converter edge coupler in order to deliver the correct amount of fluence onto the SBR, given simulated average seed power in the laser cavity. The end-facet was mechanically polished with diamond lapping paper to optical quality, in order to bring the SBR in full contact with the chip facet. After chip facet polishing, SBR, which was mounted on a copper heat sink, was coupled to the chip by 3-axis nano-positioning stages with additional tip/tilt adjustments. The experimental setup for SBR-based MLLs is shown in Figure 3-19 [a]. The output of the laser was taken from the integrated grating transmission side, which is on the input side of the chip. Since the grating has 90% reflection, and specifically 10% measured transmission, it can serve as an additional output from the laser cavity. The pulse duration through this output would often be higher than that from the NLI output, due to the distribution of dispersion in the laser. Since SBRs are always in increasing reflection for increasing input power regime, they do not need any additional tuning mechanisms in the laser cavity.

The experimental setup to measure the NLI-based mode-locked lasers is shown in Figure 3-19 [b]. This setup is very similar to the one used for SBR measurements, but the output is taken from auxiliary port of the NLI, on the chip side opposite from the pump input, as shown in Figure 3-4. This setup has an additional current source and DC probes, which are used to drive micro-heaters on top of the NLI to bias it in the right position.

The results of the SBR-mode-locked lasers are shown in Figure 3-20. The lasing threshold occurs at 40 mW of pump power in the cavity, when the laser starts operating in CW regime, with central wavelength around 1894nm (the corresponding optical spectrum is shown in blue in Figure 3-20 [b]).

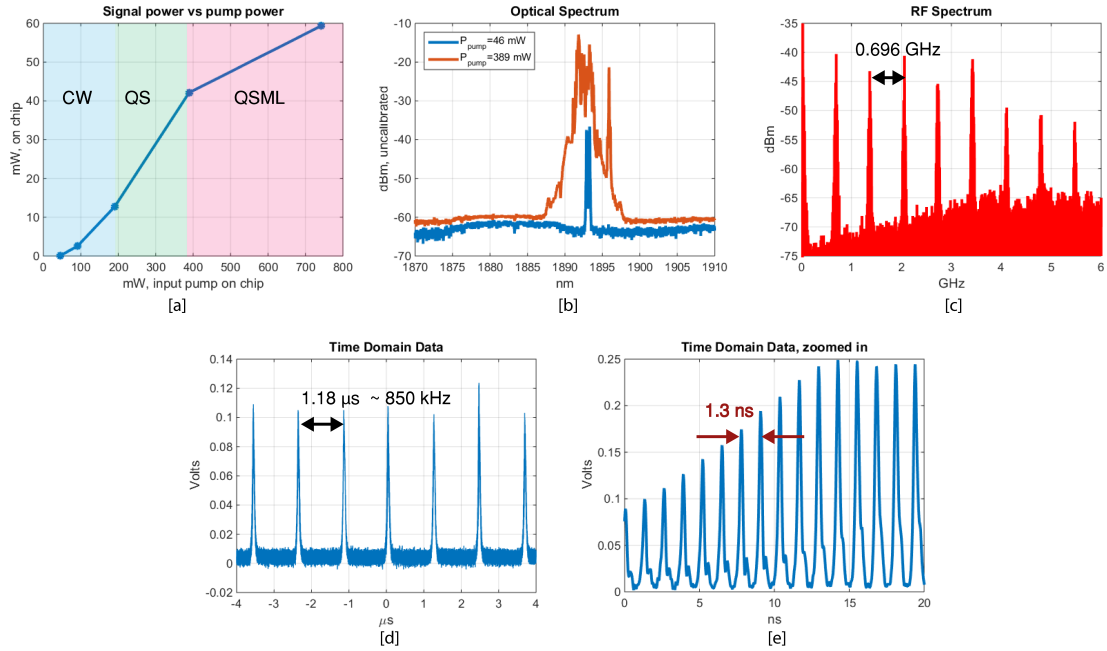

Figure 3-20: SBR-mode-locked laser results: [a] Signal power vs pump power; [b] Optical spectrum; [c] RF spectrum; [d] Time-domain spectrum; [e] Time-domain spectrum, zoomed in.

As the pump power is increased, the laser goes into a Q-switched regime. Time domain data the for Q-switched regime is shown in Figure 3-20 [d], which shows Q-switching at the rate of 850kHz. This rate can be varied by changing the amount of pump power. Finally, when the pump power is increased to 400mW on chip, the laser goes into a Q-switched mode-locked (QSML) state, where underneath the kHz pulses one can see individual mode-locked pulses with a time separation that matches the laser repetition rate (Figure 3-20 [e]). The spacing of the individual mode-locked pulses in time domain is ∼1.3ns, which corresponds to a repetition rate of ∼690MHz, visible in the RF domain (Figure 3-20 [c]). This matches with the ∼13cm one-way cavity length of this mode-locked laser. The optical spectrum in QSML regime (shown in red in Figure 3-20 [b]) shows considerable broadening and the spectral width of at least 3nm, indicating the phases of the individual modes starting to come together and forming pulses. We were unable to get the laser into true CW mode-locking regime

due to thermal damage to the SBR, as confirmed later by microscopic observations of saturable absorbers used. It is common for high energy Q-switched pulses to burn holes through saturable absorbers prior to obtaining true CW mode-locking. In order to get rid of this problem in the future, we plan to lower losses of the gain waveguide, which should allow us to reach CW mode-locking with lower intra-cavity power. In addition, using the nonlinear interferometer as a mode-locking device should get rid of the thermal energy-induced damage problem.

The results from measuring NLI-based mode-locked lasers, for an integrated grating with GDD of -8.4×10^4 fs^2, are shown in Figure 3-21. CW lasing threshold occurs with 70mW of pump power in the cavity. Similar to the SBR-mode-locked laser, with further increase of pump power this laser goes into Q-switching and then into a Q-switched mode-locking regime. NLI-based lasers, in this design, have both higher threshold and reduced on-chip CW signal power, compared with SBR-based lasers. Although SBR and NLI should have approximately similar insertion losses (for SBR, on-off-chip losses, for NLI silicon nitride propagation losses), the NLI may not be balanced properly due to fabrication-induced differences between the two arms. This would manifest in a different CW bias point, and increase the threshold of the laser. The results shown in Figure 3-21 were taken without using integrated heaters. Overall, with the current NLI MLL architecture, we are able to achieve up to 2mW of CW power on chip (outside of the laser cavity), and Q-switched mode-locking with a Q-switching rate tunable from 200kHz to 1 MHz. The 3nm spectral bandwidth indicates pulse durations on the order to 1.2ps. In this particular laser, the intracavity losses are likely the main factor in its low CW output power and above-picosecond-level pulse durations.

One of the issues with the above laser results was higher-than-expected loss of the gain waveguide. The gain waveguide, as described in Section 3.1.3, had a passive loss of 0.74 dB/cm. With less then 5% mode confinement in silicon nitride, this number should be significantly lower. Several reasons could contribute to this high loss. First, material loss of silicon nitride itself is high (this depends solely on our fabrication facility), second, the improper waveguide design could introduce additional

scattering losses from the side-walls, although silicon nitride layers in this fabrication run are already exposed to additional hydrogen thermal treatment to reduce Line Edge Roughness (LER). Third, the bends themselves may be lossy (the loss per bend

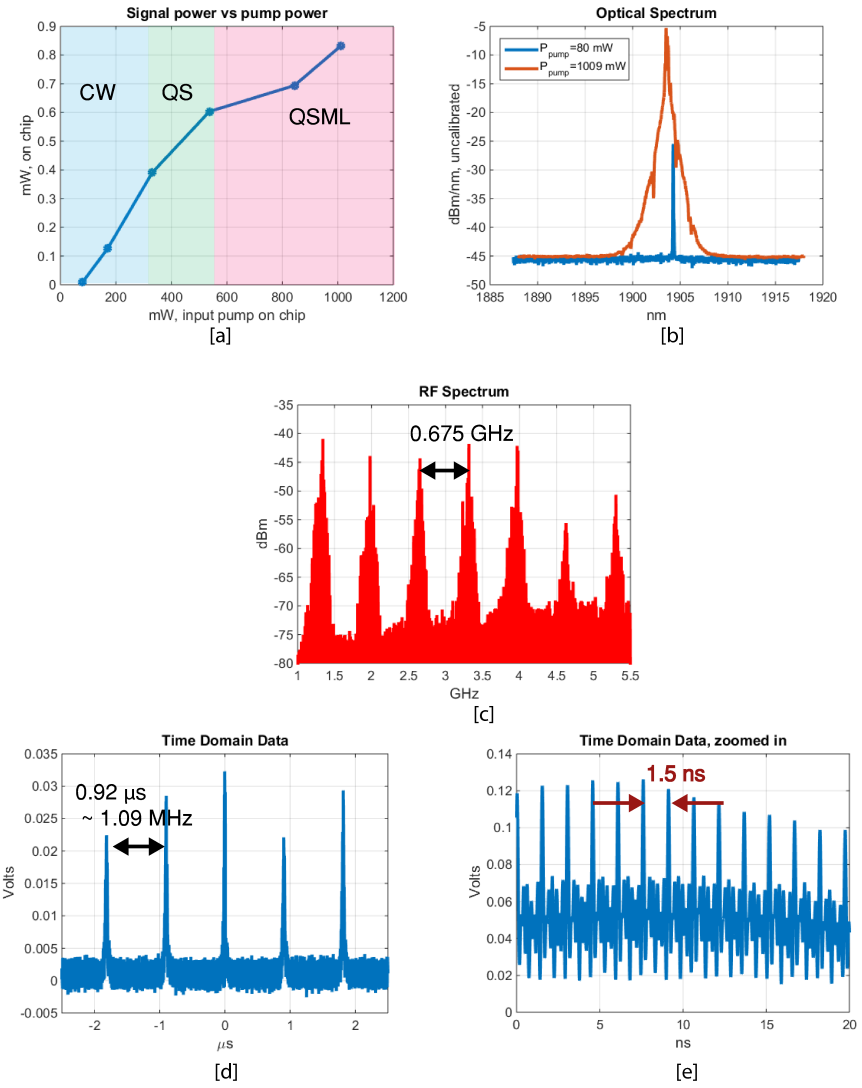

Figure 3-21: NLI-mode-locked laser results. [a] Signal power vs pump power; [b] Optical spectrum; [c] RF spectrum; [d] Time-domain spectrum; [e] Time-domain spectrum, zoomed in.

in a spiral laser is very difficult to measure). Finally, it is possible that the photonic trench itself introduces additional losses. Simulations reveal that such a trench, though necessary for the gain waveguide, introduced "trench mode" that contributed

to higher-then-expected loss of the gain waveguide. Although the photonic trench size is 70μm and thus the primary mode of the gain waveguide should not interact with the trench at all, additional modes could be guided by the trench itself. In order to mitigate this issue, we decided to partially eliminate the wide photonic trench. From Figures 3-5 and 3-8, the 4μm deep etch is necessary to bring the gain material close to the FN layer. However, it doesn't need to be 70μm wide - in fact, if it could be etched over the entire chip, this would be the best solution. However, over-entire-chip etch is not possible since some of our devices use FN/SN layer combination (the gain trench etch removes SN layer altogether); additionally, on-off chip spot-size converters depend on the large expanded mode size in FN/SN layers and the 4μm of oxide top cladding. Therefore, the best solution would be to etch a large area over all gain

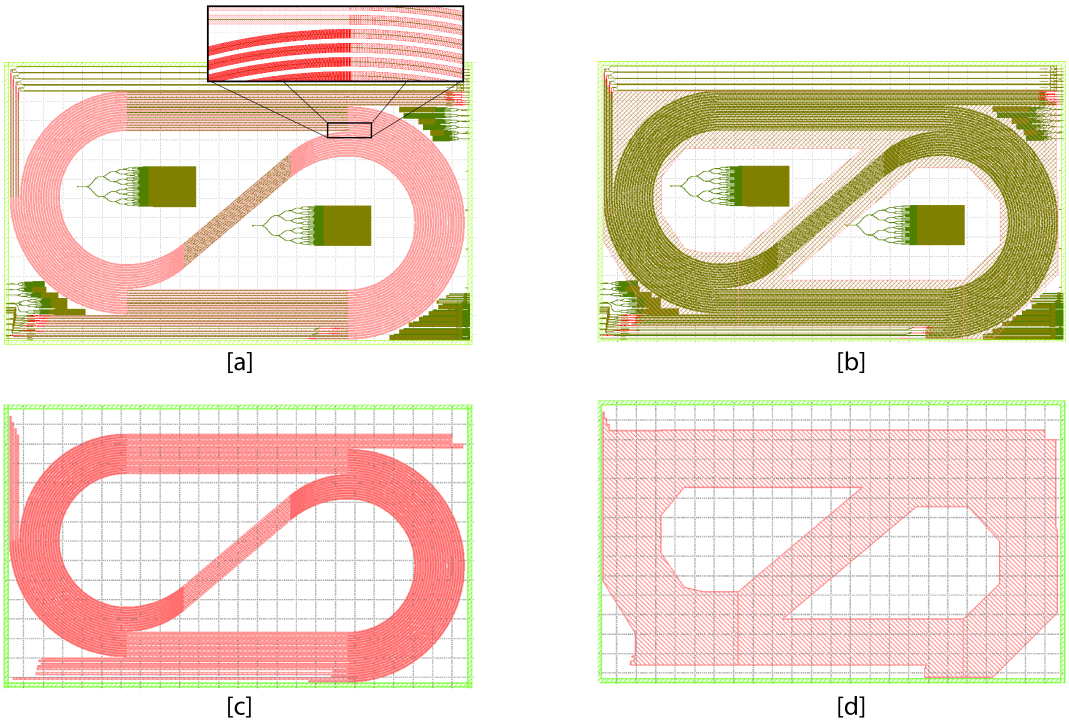

Figure 3-22: MLL chip layout with narrow and wide trenches. [a] Full chip layout with narrow trenches; [b] Full chip layout with one large trench; [c] Narrow trench layer only; [d] Large trench layer only.

waveguides, but leave all the components that require FN/SN layer combination and large oxide top cladding outside of this region. This is best explained looking at the

chip layouts, shown in Figure 3-22. Part [a] shows the original MLL chip layout, with gain trench layer (shown in red) following individual spiral waveguides. Part [b] shows the new layout, with one large trench etched over most of the chip area (new trench is also shown in red). For clarity, in Figures 3-22 [c] and [d] separate trench layers are shown without all other MLL layers.

New chips were fabricated with a large trench layer being the only modification to the laser design. The gain waveguides were tested with a passive Al_2O_3 film (no Thulium dopants), and the losses were measured by extracting data from Fabry-Perot effect-induced fringes. The passive loss of this new gain waveguide was measured to be 0.4 dB/cm, compared with 0.75 dB/cm for the previous design.

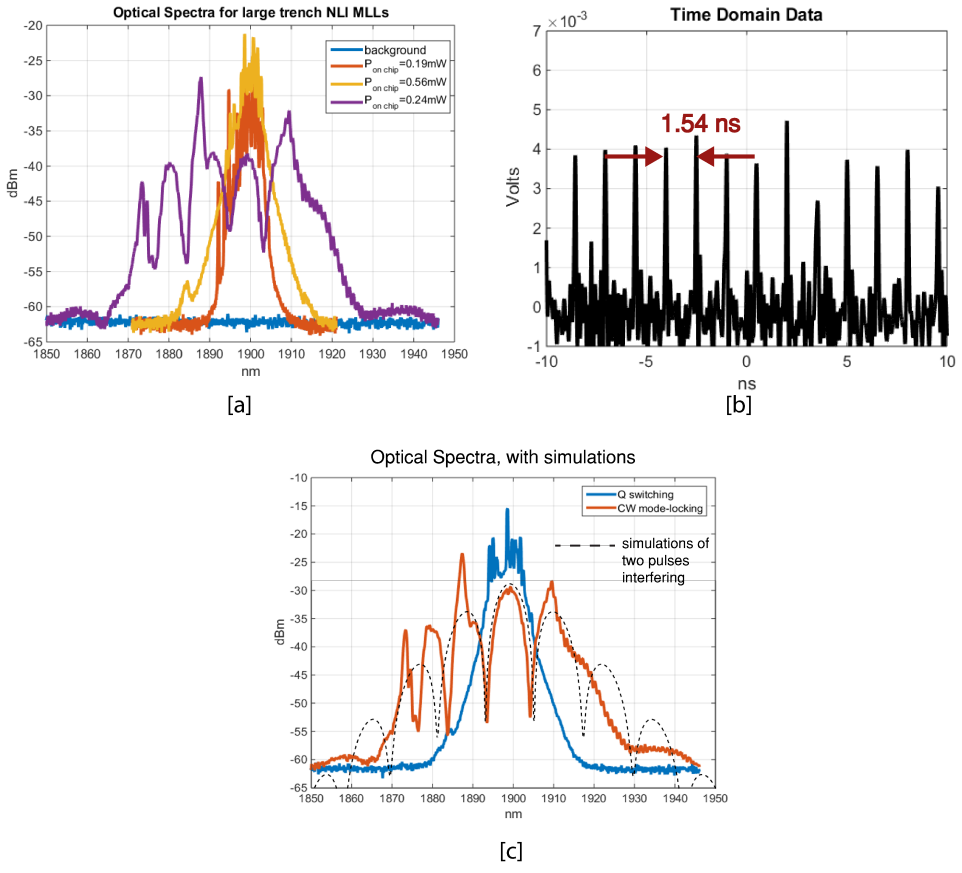

Figure 3-23: CW mode-locking results for large trench devices. [a] Optical spectra; [b] time domain spectra; [c] optical spectra with simulation fits.

The addition of one large trench dramatically improved the performance of MLLs. Our lasers go into true CW mode-locking with this modification. Figure 3-23 [a] and [b] show the measured results in optical and time domains respectively. Looking at the optical domain, when the laser goes from Q-switched state to a CW mode-locking state, the spectrum increases dramatically. Additional fringes in the optical domain indicate that the pulse is breaking into two separate pulses. Our simulations (Figure 3-23 [c]) indicate that the individual pulse durations are on the order of 800fs each. Therefore, we have achieved CW mode-locking, fully on-chip, with no saturable absorbers, at 680MHz repetition rate at 1.9μm central wavelength.

3.2 "Segmented" Mode-Locked Laser Design

A new, improved mode-locked laser architecture was designed after the spiral mode-locked lasers were fully characterized. In this section, we highlight key improvements and differences between the new segmented design and the previous spiral design, present new numerical models, and show improved results.

3.2.1 Architecture

The architecture of the re-designed mode-locked laser is shown in Figure 3-24. This laser consists of the three gain section segments, which are connected using parameterized Euler bends. The unique design of Euler bends, together with the laser architecture, allows for this significantly more compact design. One large photonic trench is etched over the entire gain region of the laser, as shown in Figure 3-24 with a large shaded region. This laser is pumped with the 1614nm EDFA via a pump/signal combiner which is identical to the one in the spiral laser. The pump then continues to the gain waveguide through a vertical escalator transition. In the gain waveguide, the pump and the signal propagate towards the so-called Euler bend on the opposite end of the cavity. Prior to entering the bend, the pump and signal modes are transitioned into the lower nitride layer (ZN), as shown in Figure 3-5, and propagate along the bend towards the second section of the gain waveguide, where

the modes are pulled back up into the gain material. This way, every time the gain waveguide bends, the light is coupled from the gain trench into one of the nitride. This allows to take advantage of a much smaller bending radius of the nitride. A nonlinear interferometer, similar to the one described in Chapter 2, is used as the end-reflector and as a mode-locking element in this laser. The other end-reflector - a dispersion-compensating grating - is located at the opposite end of the laser after the pump/signal combiner device. The cavity is then formed similarly to the spiral laser by the integrated grating on one side, an NLI on the other side, and three gain sections in between, connected with Euler bends.

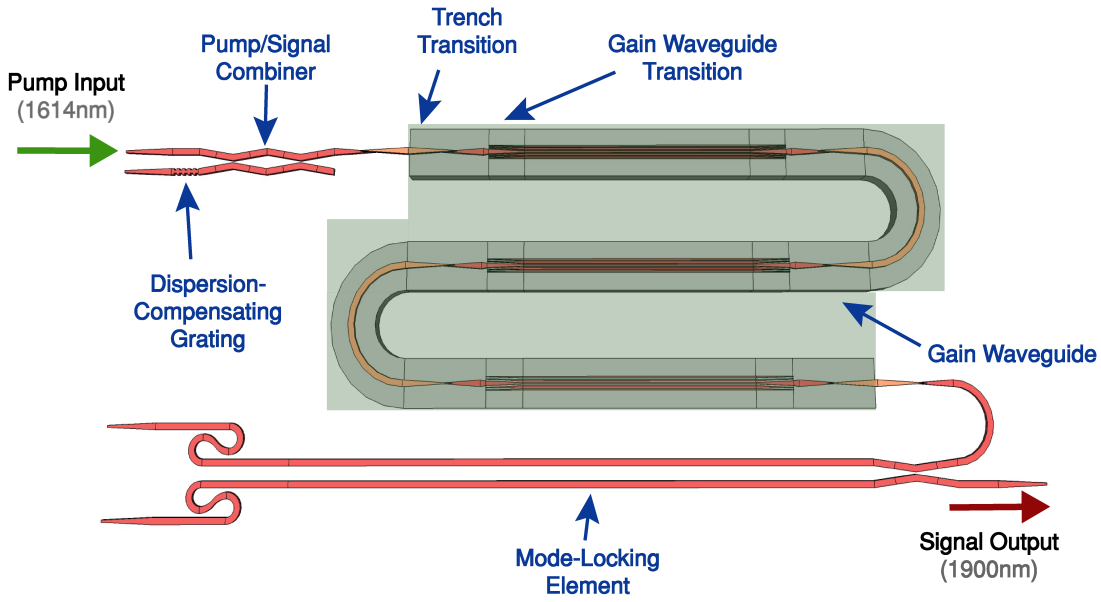

Figure 3-24: Schematic of the segmented 1900nm mode-locked laser architecture, with key components shown (not-to-scale).

The photonic material layers used for this laser are exactly the same as in the spiral MLL. The material layer stack is shown in Figure 3-5. The gain material is back-end-deposited Al_2O_3:Tm^{3+}, with the optimum film thickness of 1.1μm (see Section 3.1.2 for details on gain material fabrication and spectroscopic parameters). Table 3.6 shows photonic layers used for each of the new MLL components.

Component	Layer	Layer height
Input/Output spot size converters	FN/SN	200 nm
Pump/Signal combiner	ZN	400 nm
Gain Waveguide	FN/TR/Tm	1100nm for Al_2O_3:Tm^{3+}
Gain Waveguide bends	ZN	400 nm
Mode-locking element	FN/SN	200 nm
Dispersion-compensating grating	ZN	400 nm

Table 3.6: Photonic material layers used for MLL components in segmented 1900nm laser architecture.

A few key changes differentiate this segmented laser architecture from the previous design:

- **Compact bend design**. The new bend design allows to significantly reduce the footprint of the laser, making the final 3-dimensional footprint of one laser 23.6mm×0.78mm×0.6 mm.

- **Shorter gain section**. The one-way length of the full gain section is 6cm, which is about a factor of 2 less then the spiral laser version. This enables higher intracavity power at a particular value of pump power, since a shorter section of the waveguide needs to be pumped through.

- **New integrated grating design**. The new grating designs, described in Section 3.2.2, have over 100nm of optical bandwidth, meaning they can support optical pulses to below 100fs pulse duration.

- **Modified NLI design**. The NLI design was modified to reduce NLI losses, and hence make it a better intracavity reflector.

3.2.2 Laser Component Design and Characterization

The following MLL components remained identical to those of the spiral laser, presented in Section 3.1:

- Pump/Signal combiner

- Gain waveguide cross-section design
- Gain trench / gain waveguide transitions
- On/Off-chip spot size converters

The design/characterization for those components is described in Section 3.1.3, and will not be repeated here.

Although the gain waveguide cross-section remained identical to the one shown in Figure 3-8, the overall length of the gain waveguide is only 6cm (one way) in this design. With a fixed amount of pump power available, with shorter gain section we should be able to get significantly more signal power at a particular value of pump power (simulations show over a factor of 2 improvement). Figure 3-25 [a] shows measured gain as a function of wavelength for this waveguide, measured using segmented laser waveguide gain test-structure, for an optimum value of Thulium ion concentration in the film. Figure 3-25 [b] shows the gain as a function of pump power, at 1900nm. Maximum saturated gain was measured to be 0.8dB/cm at 1865nm. For comparison, for the same pump power the gain at 1900nm is 0.75dB/cm. The difference between the gain at 1865nm and 1900nm is only 0.05dB/cm, however, over the roundtrip propagation this difference becomes 0.05dB/cm×12cm=0.6dB.

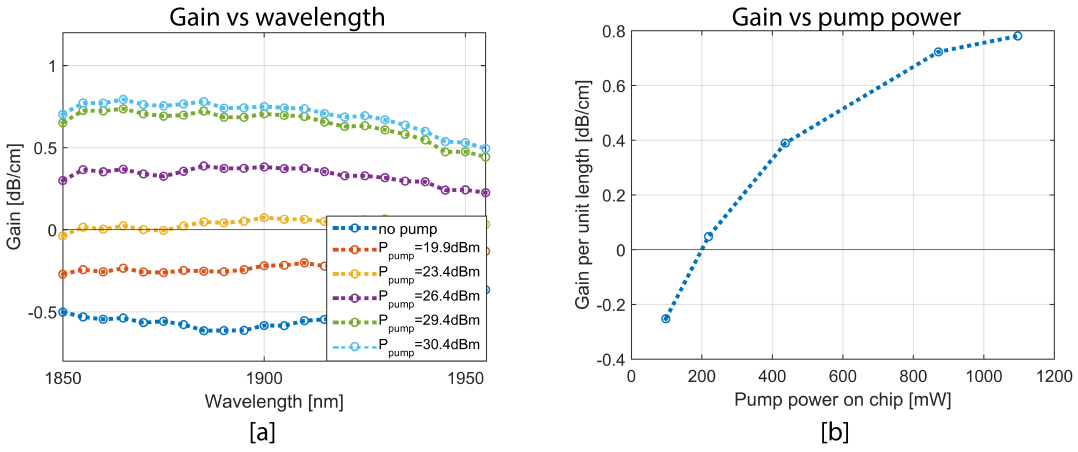

Figure 3-25: Gain measurement for segmented MLL for 1900nm: [a] Gain as a function of wavelength; [b] Gain as a function of pump power, for 1900nm.

As opposed to a large and possibly lossy circular bend, the new MLL design employs a novel low-loss bend design, implemented in a 2.5 μm-wide ZN Si_3N_4 layer. This bend type is called "Euler bend" because it is based on the Euler spiral. The basic principle is that the bend curvature changes linearly along the path length, so that $\frac{1}{R} = \frac{d\theta}{ds}$, where R is the bend curvature, θ is the angle, and s is the path length [166]. Before and after the bend, the escalator transition (see Section 3.1.3) is implemented to take the pump/signal out of the gain trench and into the ZN layer. The Euler bend layout is shown in Figure 3-26.

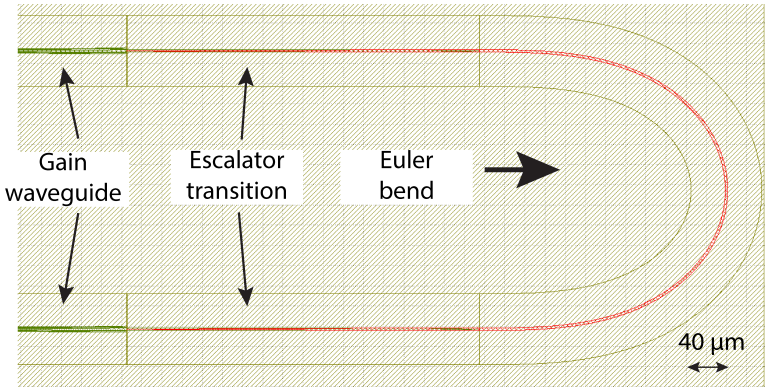

Figure 3-26: Euler bend layout.

Dispersion-Compensating Grating Design

A novel design for integrated dispersion-compensating gratings was implemented for this laser. The gratings were fabricated in the ZN Si_3N_4 layer, and the apodization profile was adjusted in order to both increase the bandwidth, and provide a smaller value of negative GDD, to put the net cavity GDD close to zero. The new integrated gratings were designed by Patrick Callahan, and the detailed design formalism is presented in [167].

Figure 3-27 shows the simulation values for group delay dispersion, central wavelength, and the overall grating reflection of each design. Five design variations were made, to provide successively larger values of negative GDD. The designs with progressively more negative dispersion are more narrow-band. Corresponding design

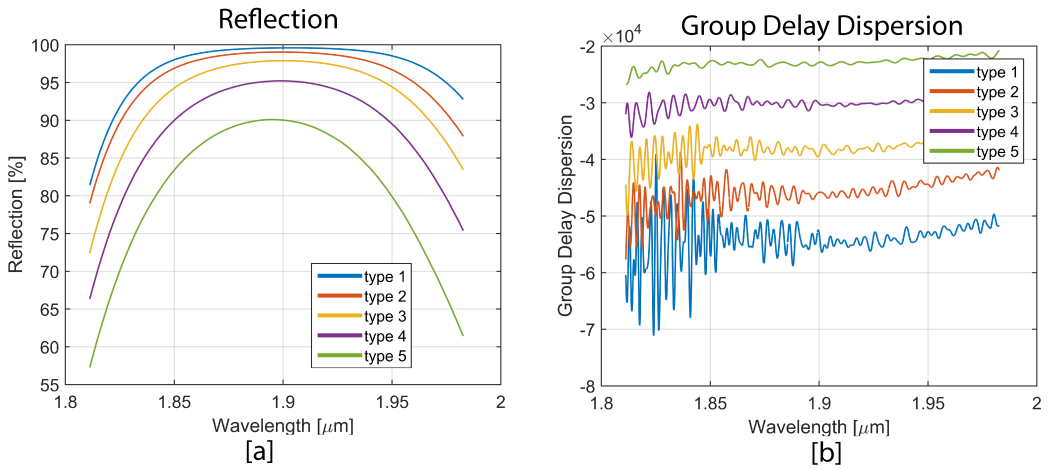

Figure 3-27: Broadband grating designs for 1900nm MLL: [a] Reflection values; [b] GDD values.

values for GDD are listed in Table 3.7.

	λ_c	Reflection	GDD
	nm	%	fs^2
Type 5	1900	99.6	$-24,000$
Type 4	1900	99	$-30,000$
Type 3	1900	98	$-40,000$
Type 2	1900	95	$-48,000$
Type 1	1894	90	$-55,000$

Table 3.7: Segmented 1900nm Laser: Integrated dispersion-compensating gratings GDD/reflection design values.

Figure 3-28 shows the layout for one of the new grating designs.

Mode-Locking Element Optimization

The nonlinear interferometer for the segmented laser design was modified from the one used in the spiral laser design. Spiral lasers had low intracavity power, possibly due to high NLI losses (0.8 dB/cm for 4.6cm net round-trip). One way to reduce NLI losses is to shorten the length of the NLI itself. This, however, also reduces effective nonlinearity available to shorten the pulses. Figure 3-29 shows simulations of the NLI reflection, for NLI parameters as listed in Table 2.2, and for two different NLI

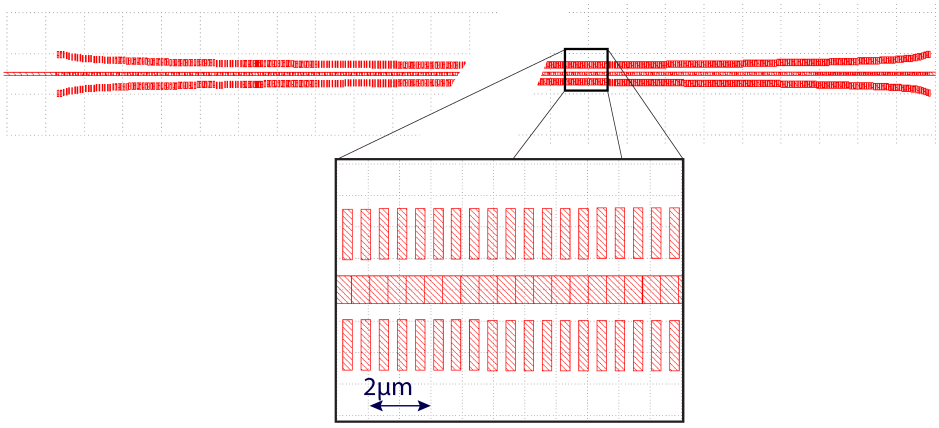

Figure 3-28: Broadband grating layout.

lengths. From this simulation, reducing the NLI length by about a half, increases the net NLI reflection by 10%. This in turn increases the intracavity power in the laser, and thus should allow to accumulate more nonlinear phase when propagating through the NLI. A separate CW laser oscillator simulation was done to calculate the effects of the 10% reflection increase in the laser. The results are summarized in Table 3.8. Reducing the NLI length in fact increases the net modulation depth. However, since we don't have unlimited pump power, the entire possible modulation depth is not available. Since the average power in the laser cavity is dramatically improved with the shorter NLI, we designed segmented lasers with a one-way NLI length of 9.4mm.

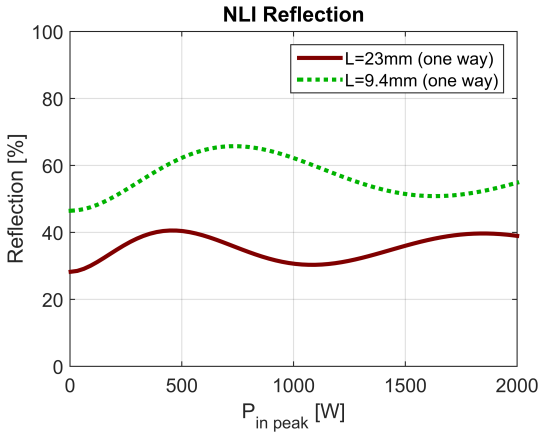

Figure 3-29: NLI reflection versus peak power, for two NLI lengths.

	ΔR	R	P_{av} (400mW pump)	P_{av} (600mW pump)
	%	%	mW	mW
L = 23mm	12.32	34.4	60.5	93
L= 9.4mm	19.2	56	100	152

Table 3.8: NLI length reduction effects on laser performance.

3.2.3 Dispersion/Nonlinearity Optimization

Effective nonlinearity and dispersion for each MLL component were calculated using an FDE solver with a full field-overlap-based nonlinearity calculation, where the bulk material kerr coefficients were taken from the literature. The results, for each successive component in the cavity, are shown in Table 3.9. The gain waveguide is shown three times because there are three gain waveguide sections in the final laser, with two Euler bends in between. The length of the middle gain segment is slightly different from the outer ones due to layout geometry. Table 3.9 is used to calculate the

	Layer	Width	Length	β_2	γ_{NL}	$\beta_2 \cdot 2L$	$\gamma_{NL} \cdot 2L$
		μm	mm	fs^2/mm	$(W\ m)^{-1}$	fs^2	$(W)^{-1}$
Pump/Signal Com.	ZN	1.00	0.430	2001	0.78	1,721	6.7×10^{-4}
Gain Wg. (part 1)	FN/TR	-	20.03	100	0.088	4006	3.5×10^{-3}
Bend 1	ZN	2.50	0.6	761	0.7	913	8.4×10^{-4}
Gain Wg. (part 2)	FN/TR	-	19.7	100	0.088	3,950	3.5×10^{-3}
Bend 2	ZN	2.50	0.6	761	0.7	913	8.4×10^{-4}
Gain Wg. (part 3)	FN/TR	-	20.03	100	0.088	4006	3.5×10^{-3}
ZN piece	ZN	1.00	0.26	2001	0.78	1035	4.0×10^{-4}
NLI	FN/SN	1.50	9.48	820	0.6	15,547	1.13×10^{-2}
					Total:	**32,090**	**0.025**

Table 3.9: Segmented 1900nm MLL dispersion / nonlinearity component contributions. The last two columns show round-trip contribution of the dispersion and nonlinearity, respectively. Dispersion compensating grating is not included.

net dispersion and potential additional nonlinearity needed to bring the MLL cavity into net anomalous regime and to ensure soliton pulse shortening. Table 3.10 shows the net MLL cavity group delay dispersion for four values of dispersion-compensating grating designs, as listed in Table 3.7. Three of such designs yield net anomalous dispersion, and one design results in a small net normal dispersion. For the same

value of accumulated nonlinear phase, shorter pulses should be achieved with net anomalous GDD value, which is closer to zero.

	unit	Type 1	Type 2	Type 3	Type 4
Grating GDD	fs^2	$-55,000$	$-48,000$	$-40,000$	$-30,000$
MLL cavity GDD (round-trip)	fs^2	$+32,090$	$+32,090$	$+32,090$	$+32,090$
Net GDD	fs^2	$-22,910$	$-15,910$	$7,910$	$2,090$

Table 3.10: Segmented 1900nm Laser: Net cavity GDD, with four available integrated grating designs.

3.2.4 Numerical Pulse Propagation Model

We simulate the full segmented MLL cavity using NLSE formalism as described in Section 3.1.5, by propagating an optical pulse through each MLL component at a time, with components exactly as listed in Table 3.9 plus the integrated grating, for a round-trip propagation. Small signal gain is calculated from a separate amplifier simulation for this particular gain cavity, and losses of each component are also added based on linear characterization measurements. Grating design values were applied to this simulation exactly, by loading simulated dispersion and reflection values to the numerical simulation, with corresponding bandwidth. We run the simulation for four cases of four integrated grating designs as summarized in Table 3.10. The simulation flow is shown in Figure 3-30, where the pulse is run over many simulation round-trips (typically over a thousand) until a steady state solution is reached.

The results of the simulation are shown in Figure 3-31, as pulse evolution along the cavity length. The three cases presented are: [a]. Net MLL GDD=-7.9×10^3 fs^2, Grating Type 3 with $GDD_{DCG} = -4.0 \times 10^4$ fs^2; [b]. Net MLL GDD=-15.9×10^4 fs^2, Grating Type 2 with $GDD_{DCG} = -4.8 \times 10^4$ fs^2; [c]. Net MLL GDD=-22.9×10^4 fs^2, Grating Type 1 with $GDD_{DCG} = -5.5 \times 10^4$ fs^2. In each plot, immediately after the grating, the pulse is strongly negatively chirped. As it propagates forward in the gain waveguide towards the NLI, normal dispersion of the gain waveguide reduces the negative chirp, making pulses shorter. The pulses are shortest in the NLI. The NLI contributes a significant amount of normal dispersion, which gives the pulse net

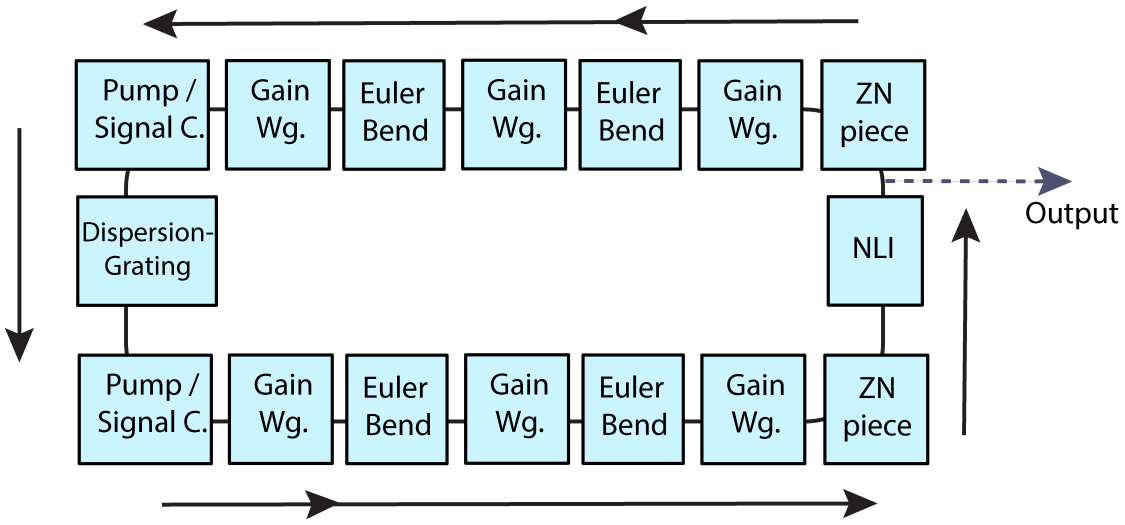

Figure 3-30: NLSE cavity simulation flow for a segmented laser.

positive chirp and makes at longer at the NLI output. The pulse then propagates back towards the grating through the gain waveguide, acquires more positive chirp and becomes longer, until it encounters the grating, which removes all the positive chirp, and adds a strongly negative chirp. In this manner the pulse circulates around the cavity, reproducing itself each round-trip. The "kinks" in pulse evolution curves are due to Euler bends and other ZN silicon nitride layer components, that add dispersion in large amount over their short length. As expected, the shortest pulse duration occurs for the design where the net dispersion is closest to zero on the anomalous side. For comparison, grating type 4 placed the MLL cavity into a net normal dispersion regime, with only slight normal dispersion, as shown in Table 3.10. Numerical simulation for that laser failed to converge.

Finally we note that the output of the laser can be taken at the output of the NLI (from Figure 3-31, the pulse is the shortest in the NLI, not the output), or at the input of the grating (measured through grating transmission). Figure 3-32 shows the pulse duration for each output versus the GDD of the gratings used. The shortest pulses, 293fs in duration, are obtained from the laser with an integrated grating type 3 (with GDD$=-4.0 \times 10^4$ fs^2), from the output of the NLI.

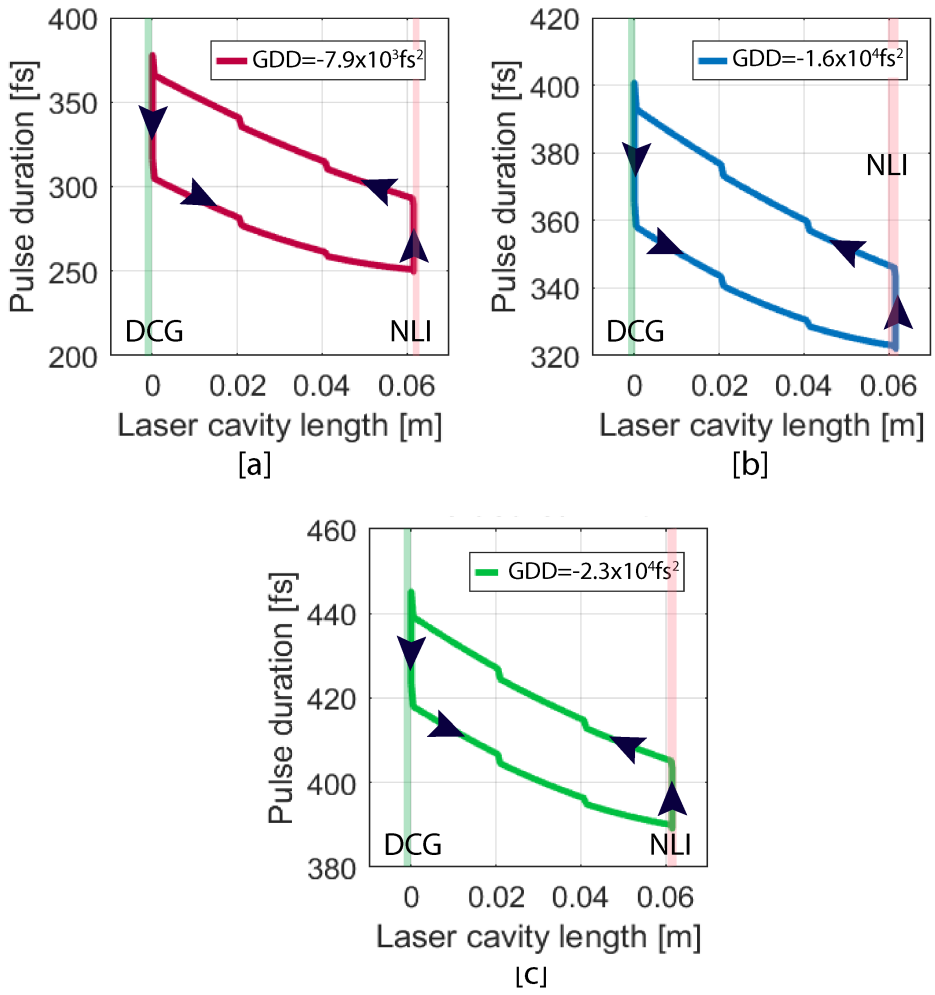

Figure 3-31: Results of numerical simulations for the 1900nm segmented laser for three values of integrated grating dispersion: [a] $GDD_{NET}=-7.9 \times 10^3$ fs^2; [b] $GDD_{NET}=-15.9 \times 10^4$ fs^2; [c] $GDD_{NET}=-22.9 \times 10^4$ fs^2

3.2.5 Layout and Fabrication

Segmented mode-locked lasers were fabricated using the same 300mm wafer 65nm CMOS-compatible process as the spiral lasers, as described in Section 3.1.6, and diced onto identical 25x24mm chiplets, which were additionally diced to separate various device columns. The layout of the chip, which contains 1900nm segmented lasers, 1550nm segmented lasers and several test structure columns, is shown in Figure 3-33 [a]. A photo of the diced 1900nm MLL part of the chip, with gold heaters deposited at MIT, is shown side by side with the layout in Figure 3-33 [b].

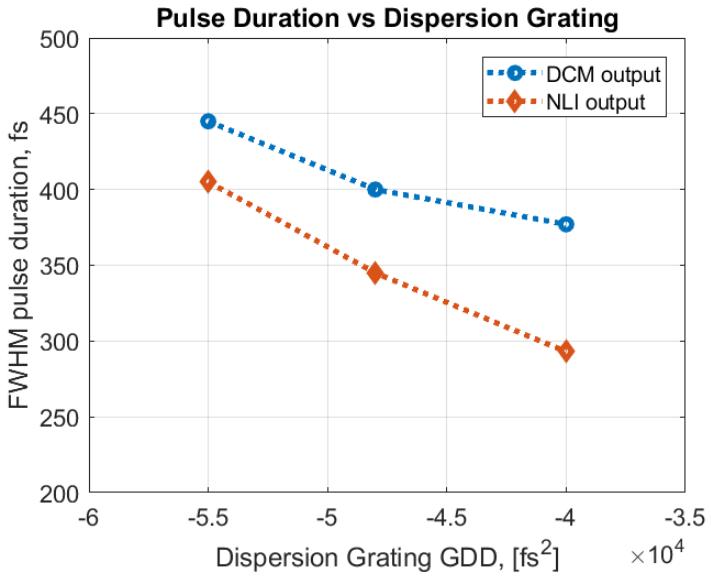

Figure 3-32: Numerical simulation results for 1900nm segmented MLL: pulse duration at various laser outputs vs grating dispersion used.

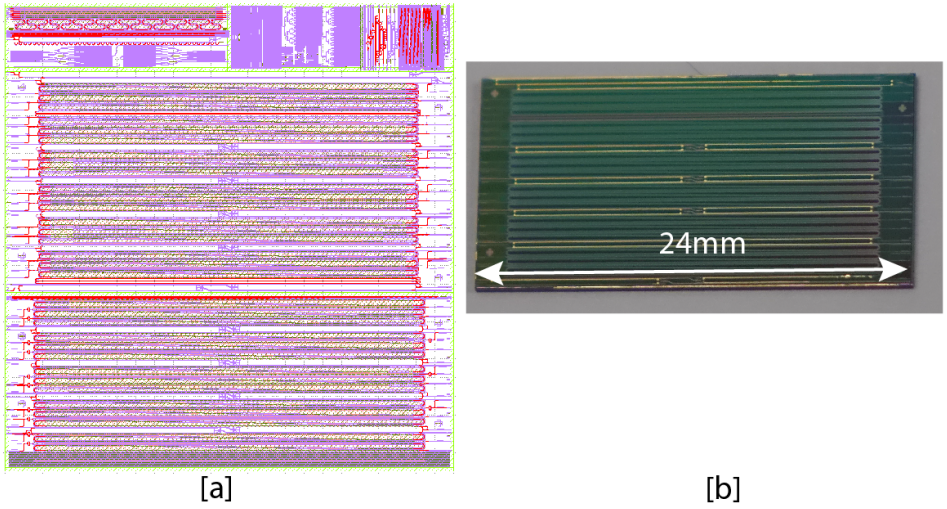

Figure 3-33: Segmented 1900nm lasers layout and chip photos: [a] Full layout of the chip; [b] A photo of diced 1900 MLL sub-chip.

3.2.6 Results

Segmented mode-locked lasers were measured using the setup shown in Figure 3-19. The results, for a laser in a strong anomalous regime, are shown in Figure 3-35. Integrated heaters are used with those lasers to tune them into proper operation regime. All segmented lasers have significantly lower threshold, and much higher intracavity power compared with spiral lasers (experimentally, the power increase is greater then factor of eight). The lasers operate in a Q-switched mode-locking regime within 2 dB power increase from threshold. We fit the optical spectrum in Figure 3-35 [a] to a Gaussian, to better estimate the pulse duration. The fit results in ≈ 460fs, as calculated from optical spectrum fit. Signal power on chip, outside of the

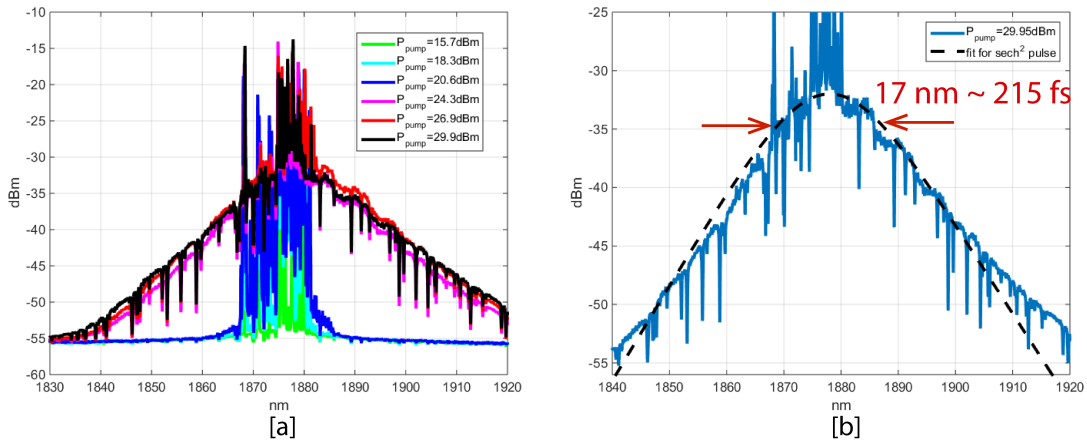

Figure 3-34: Segmented 1900nm laser results: [a] Optical spectrum for various on-chip power values; [b] optical spectrum, with a fit to the spectrum of a secant square pulse with 215fs pulse duration.

laser cavity, is plotted in Figure 3-35 [b]. The power inside the cavity is at least a factor of 10 higher. Time domain data, showing Q-switched operation at 720 kHz is shown in Figure 3-35 [c]. The Q-switching rate can be tuned with input pump-power to be from 500kHz to about 1 MHz. A close-up of a time domain data is shown in part [e], where the full Q-switched pulse envelope, and individual mode-locked pulses underneath are clearly visible. The mode-locked pulses are 0.8ns apart, which indicates cavity repetition rate of 1.2GHz. This repetition rate is also directly

observed in RF domain, in Figure 3-35 [d]. Figure 3-34 shows optical spectrum of

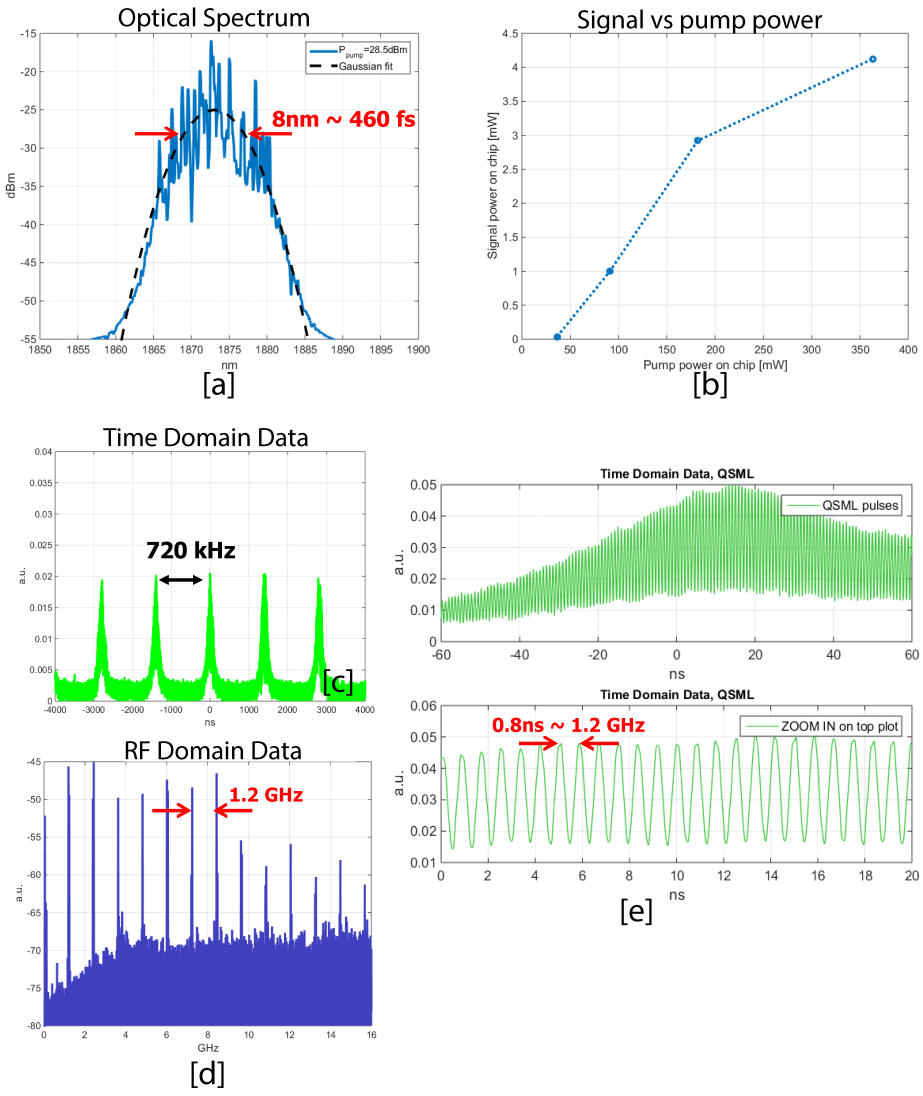

Figure 3-35: Segmented 1900nm laser results: [a] Optical spectrum; [b] Signal vs pump power on-chip; [c] Time domain data; [d] RF domain data; [e] Time domain data, close-up.

a different laser, with the net anomalous dispersion closest to zero. Figure 3-34 [a] shows optical spectrum for various input pump power levels. Figure 3-34 [b] shows a Q-switch mode-locked state, with optical pulses in time domain. This laser has on-chip power of about 8mW, and exhibits a very broad spectrum that indicated 215fs pulses. The laser goes into a Q-switched mode-locking regime similar to the

one shown on Figure 3-35 [e], but it always shows some CW laser spikes on top of a broad pulse in optical spectrum. Nevertheless the bandwidth of the laser is 17nm, which corresponds to 215fs pulse duration, in close agreement with our simulations.

3.3 Novel Mode-Locked Laser Designs

Although the lasers in the previous section have shown excellent Q-switched mode-locking, the Q-switching instabilities were very hard to get rid of, and the lasers often exhibited unstable operation. Therefore, we redesigned the lasers to improve the stability. The instabilities in soliton-like mode-locked lasers are most easily explained using Haus Master Equation theory. Looking at Figure 3-2, if the strength of the artificial saturable absorber is low in the net normal dispersion regime, the laser becomes unstable. One way to mitigate this issue is to ensure there is sufficient net anomalous dispersion in the MLL. This does not change the strength of the saturable absorption, but it does put the laser in a more stable mode-locking regime. Another option is to increase the strength of the saturable absorber itself. For this, we could either increase the length of the NLI, or change the NLI coupler splitting ratio from 90/10 to the value that gives the highest SAM coefficient, which is 75/25, or do both. Figure 3-36 shows full NLI simulations for the following four cases: 1. Long (23mm one way) NLI, with 90/10 coupler power splitting ratio ($\alpha = 0.9$, where α is the fraction of power into the upper arm; [2] Long NLI (23mm one way) for 75/25 coupler power splitting ratio ($\alpha = 0.75$); [3] Short (9.5mm one way) NLI with $\alpha = 0.9$; [4] Short NLI (9.5mm one way) for $\alpha = 0.75$. Figure 3-36 [a] shows NLI reflection, and Figure 3-36 [b] shows corresponding SAM coefficients. From these simulations, the highest SAM coefficient is obtained for NLI with α=0.75 and longer NLI length. However, corresponding reflection profile shows the reflection value for this device starting at 10% - this is due to increased linear loss due to extra silicon nitride length. This makes for a very poor end-reflector at the end of the laser cavity. A separate simulation shows that the laser will have a significantly higher threshold, and lower intracavity power. This means we might not have enough power to actually

drive the nonlinearity of the NLI to obtain maximum γ_{SAM}. A better option would be to use the device with longer length value, but with $\alpha = 0.9$, since the overall NLI reflection doesn't go below the 20% value. Short NLI variations display similar behavior - they are generally better reflectors than longer NLIs, due to lower nitride length and smaller linear losses, but they also have correspondingly smaller SAM coefficients due to smaller nonlinearity.

Separately, when NLI length is increased, this also increases the effective nonlinearity in the entire MLL, increases the loss in the laser (and hence decreases the available power in the cavity for a particular pump power value), and significantly increases cavity dispersion. Therefore, the lasers need to be carefully modeled in order to see the interplay of the loss, gain, average power, nonlinearity and dispersion, and how all those parameters affect the final pulse duration. We explore the following

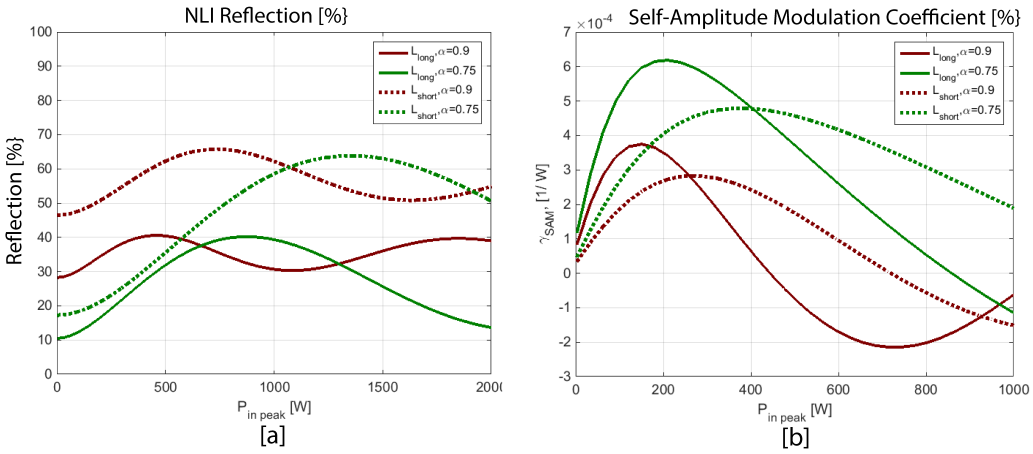

Figure 3-36: NLI strength (SAM coefficient) vs NLI length and coupler power splitting ratio: [a] Device reflection; [b] Corresponding SAM coefficient. L_{long}=23mm (one way), L_{short}=9.5mm (one way).

three options to increase the stability of the MLL:

1. Increase net intracavity anomalous dispersion (without changing the NLI).

2. Increase the SAM coefficient of the NLI by increasing the length of the NLI, keeping the NLI coupler with 90/10 splitting ratio.

3. Increase the SAM coefficient of the NLI by increasing the length of the NLI and changing the NLI coupler to 75/25 splitting ratio.

3.3.1 Modifications to Laser Architecture

When the NLI length is increased from 9.5mm one way to 23mm one way (which is the maximum length supported by the physical dimensions of the chip, provided no extra bends are used inside of the NLI), with segmented MLL design as presented is Section 3.2, this puts the net MLL group delay dispersion into normal regime, even with the strongest dispersion-compensating grating used. To put the laser back into net anomalous regime, further dispersion compensation is needed. We choose to add additional anomalous dispersion into MLL cavity by inserting additional dispersion compensating gratings into the NLI arms (replacing the loop mirror end-reflectors with the grating reflectors), as shown in Figure 3-37. The MLL cavity will then have integrated gratings on both ends of the cavity - one grating on the left, and gratings at the ends of both arms of NLI on the right. The rest of the laser would be exactly as shown in Figure 3-24.

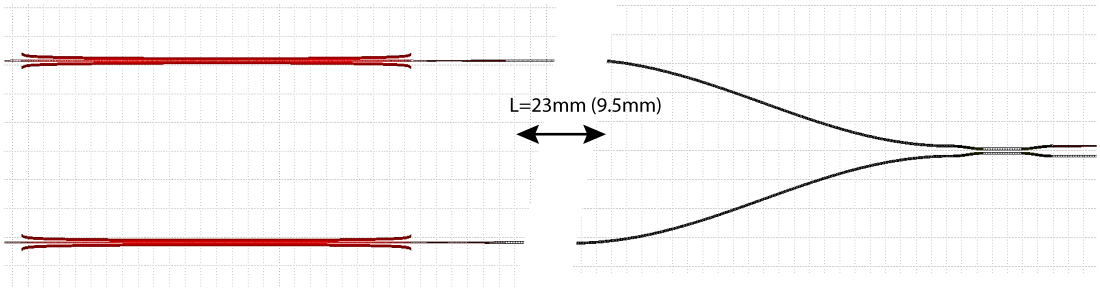

Figure 3-37: NLI layout with integrated gratings inside (not to scale).

3.3.2 Dispersion/Nonlinearity Optimization, Numerical Pulse Propagation Model

The net cavity GDD and nonlinearity are calculated for the three MLL modification cases discussed above. For each case, a full pulse propagation simulation is done, and

the results are presented and compared.

Case 1. Increasing anomalous intracavity dispersion (and keeping NLI length to 9.5mm).

Available values of GDD for the high bandwidth integrated grating designs are shown in Table 3.7. To keep the pulses below 1ps, we choose to have the total grating-contributed GDD to be around $-60,000$ fs^2. The nonlinearity / dispersion parameters for the MLL cavity without the grating compensation are identical to the segmented laser presented earlier, and are shown in Table 3.9. Table 3.11 shows the available grating combinations that would add additional anomalous dispersion to the cavity, keeping the pulse duration below 1ps (for longer pulse durations, even more negative dispersion could be added).

	unit	Case 1.1	Case 1.2	Case 1.3
Left Grating GDD	fs^2	$-40,000$	$-24,000$	$-30,000$
Right (NLI) Grating GDD	fs^2	$-24,000$	$-40,000$	$-30,000$
MLL cavity GDD (round-trip)	fs^2	$+32,090$	$+32,090$	$+32,090$
Net GDD	fs^2	$-31,910$	$-31,910$	$-27,910$

Table 3.11: Dispersion calculations for 1900nm laser: Available grating GDD combinations.

The distribution of dispersion in the laser cavity should be such that the pulse at the NLI output is shorter than, or close to, pulse duration at the input (since the laser output is at the output port of the NLI, and we want the shortest pulses at the output of the laser). A more balanced dispersion distribution within the MLL cavity achieves this task well. We simulate the **Case 1.1** and **Case 1.3** laser cavity designs from Table 3.11. We skip Case 1.2, since it will likely result in a pulse that is shortest at the DCG site. Full numerical simulation of the laser is performed as explained in Section 3.2.4, with changes to the NLI simulation to include the addition of the DCG instead of the loop mirrors. The wavelength-dependent grating response is loaded into the NLI simulation in the frequency domain. The simulations for both cases converge to a steady state solution, and the results for pulse evolution inside of the MLL cavity are shown in Figure 3-38. For an MLL design with a more unequal dispersion distribution (Case 1.1), the pulse duration evolves between 622fs at the

output of the NLI and 637fs at the output of the grating. This is a more balanced dispersion distribution compared to the case in the previous Section (Figure 3-31), and the pulse duration here is in fact shorter at the NLI output (i.e. the pulse evolves in a clockwise direction along the curve in Figure 3-38 [b]). For an even better dispersion distribution, as shown in Figure 3-38 [a] (corresponding to Case 1.3 MLL design), the pulse duration evolves between 440fs at the output of the NLI and 464fs at the output of the DCG. For this MLL, the net GDD is slightly less anomalous than for Case 1.1.

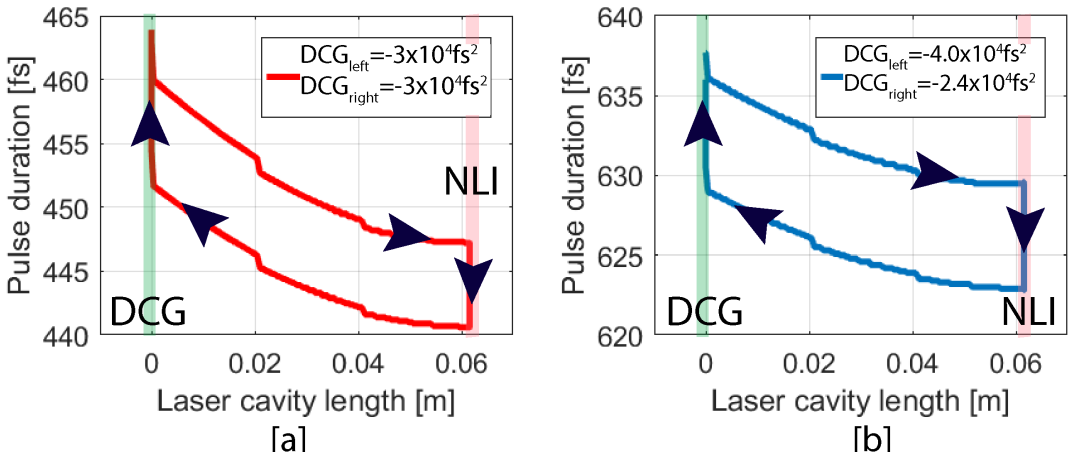

Figure 3-38: Pulse evolution simulation inside of strongly anomalous dispersion regime MLL: [a] Two identical gratings are used at both ends of the cavity (Case 1.3 in Table 3.11); [b] Two different gratings are used (Case 1.1 in Table 3.11).

Case 2. Increasing NLI strength by increasing its length (and keeping NLI coupler 90/10)

To increase the SAM coefficient of the NLI, we increase its' length from 9.5mm one way to 23mm one way. Increasing the NLI length changes the effective nonlinearity of the MLL and adds normal dispersion and a significant amount of linear loss. This additional 13.5mm of NLI length contributes about $15,500\text{fs}^2$ normal group delay dispersion to the MLL over the round-trip propagation. Table 3.12 shows the full MLL cavity dispersion with no integrated grating, and the two studied dispersion-compensation cases. Both cases were simulated using our numerical pulse propagation model. The results for pulse evolution inside of the cavity are shown in Figure 3-39.

	unit	Case 2.1	Case 2.2
Left Grating GDD	fs^2	$-40,000$	$-30,000$
Right (NLI) Grating GDD	fs^2	$-24,000$	$-30,000$
MLL cavity GDD (round-trip)	fs^2	$+54,260$	$+54,260$
Net GDD	fs^2	$-9,740$	$-5,740$

Table 3.12: Dispersion calculations for 1900nm laser (changing NLI length): Available grating GDD combinations.

From this figure, a more balanced and slightly less anomalous dispersion distribution in a mode-locked laser cavity results in shorter pulses (Figure 3-39 [a]), where the pulse duration varies from 225fs to 300fs. For this case, the net GDD of the cavity is $-5,740$ fs^2, which is the closest to zero net dispersion out of the two simulations, and therefore results in shorter pulses.

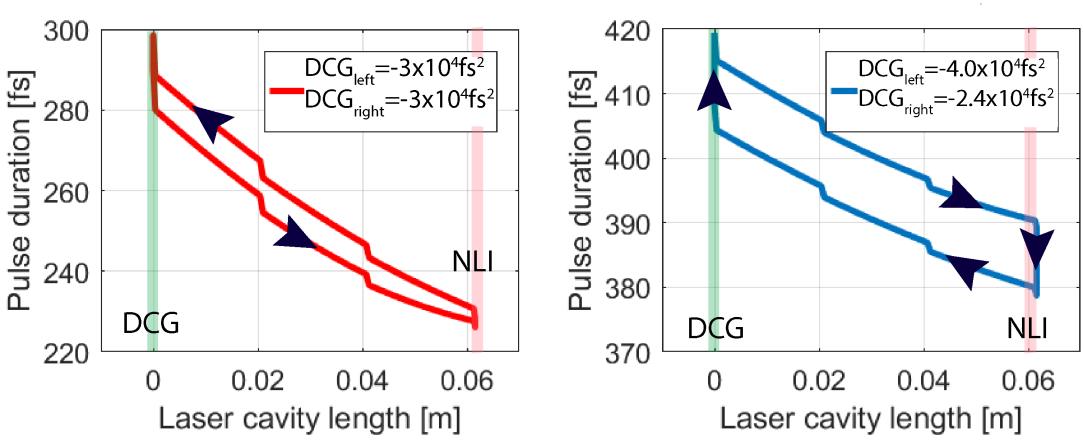

Figure 3-39: Pulse evolution simulation for segmented laser with L_{NLI}=23mm, and α_{NLI}=0.9: [a] Two identical gratings are used at both ends of the cavity (Case 2.2 in Table 3.12); [b] Two different gratings are used (Case 2.1 in Table 3.12).

Case 3. Increasing NLI strength by increasing its length and changing NLI coupler value to 75/25.

According to Figure 3-36, increasing NLI length and changing the NLI coupler ratio to 75/25 results in the highest effective SAM coefficient, and thus potentially has a good chance to mode-lock. Although this configuration adds a significant amount of loss to the cavity, with all other MLL elements optimized for low loss, this laser could

operate and potentially have enough power to drive the nonlinearity. The dispersion in the MLL cavity in this case is identical to the values listed in Table 3.12, since dispersion is not power-dependent. The results of a full numerical pulse propagation through this MLL are shown in Figure 3-40. Similarly to the previous case, the pulse duration is shorter for two identical gratings used in the MLL, compared with two different gratings. However, the pulse duration here is longer than that of Case 2, where the NLI coupler had 90/10 splitting ratio (Figure 3-39). Although NLI strength is higher for Case 3 presented here, this MLL configuration has less net nonlinearity, and thus will have longer pulse duration (smaller soliton effect). However, it is still worth implementing since it may be more stable.

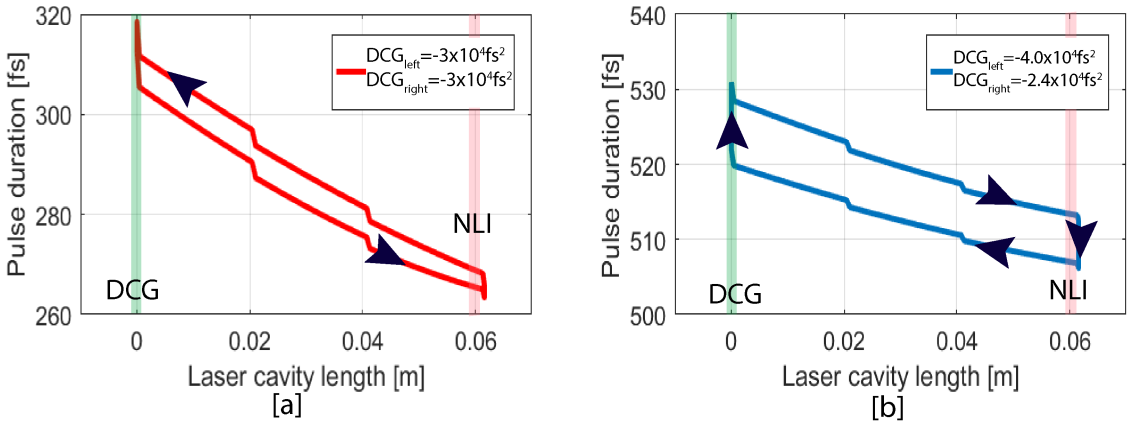

Figure 3-40: Pulse evolution simulation inside of strongly anomalous dispersion regime MLL: [a] Two identical gratings are used at both ends of the cavity (Case 2.1 in Table 3.11); [b] Two different gratings are used (Case 2.1 in Table 3.11).

We summarize the results of all three cases by plotting the pulse duration versus net cavity group delay dispersion in Figure 3-41. This plot agrees with the Haus Master Equation formalism (see Figure 3-2), in that for larger net dispersion, pulse durations are longer. For the same value of net dispersion but for two different values of net nonlinearity contribution, higher nonlinearity results in shorter pulse durations.

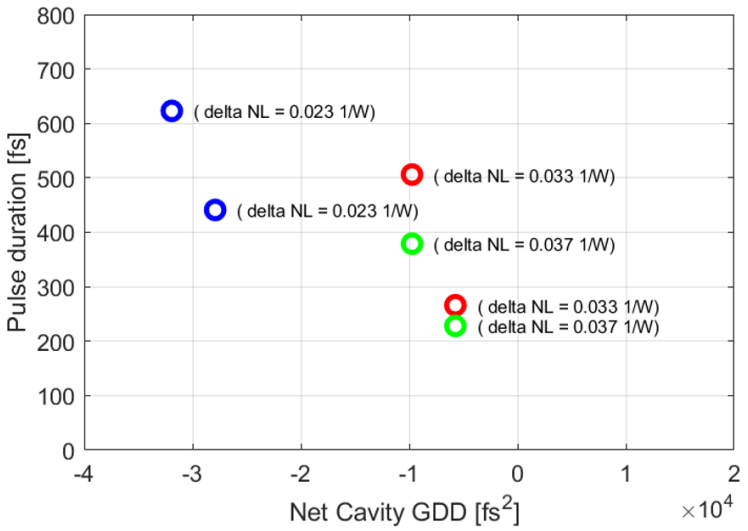

Figure 3-41: Summary of different MLL numerical simulations for future laser designs.

A more distributed dispersion within the MLL cavity results in shorter pulse durations, and that increasing NLI length generally helps making pulses shorter (though it also increases the loss and laser threshold). Therefore, for future MLL runs, design variations from Cases 1, 2, and 3 with the same dispersion compensating grating ($\text{GDD}_{DCG} = -30,000\text{fs}^2$) on each side of the MLL cavity would be used.

Chapter 4

1550nm Mode-Locked Lasers

In this chapter we review the 1550nm MLL laser development. One of the original goals of the MIT EPHI approach was developing a fully-on-chip mode-locked laser at 1550nm to be used in a low phase noise oscillator synthesizer, as shown in Figure 1-1.

The gain material for 1550nm-centered mode-locked lasers is Erbium-doped aluminum oxide glass (Al_2O_3:Er^{3+}). MIT began developing such lasers shortly after demonstrating the low loss doped aluminum oxide gain material platform [68, 69]. The material is deposited as a back-end process on top of the MLL chip. While the gain film covers the entire chip, the optical mode only interacts with the gain material in carefully engineered gain waveguide region. Erbium ions are used as dopants to the Al_2O_3 film in order to provide optical gain at 1550nm. Al_2O_3:Er^{3+} is deposited using RF co-sputtering of Aluminum and Erbium at high vacuum and 550° substrate temperature, with controlled oxygen flow [68]. Erbium lasers have been extensively used in the fiber laser community in both EDFA systems and many CW and pulsed fiber laser designs [168]. Integrated waveguide lasers based on Erbium have also been recently demonstrated [2, 67, 169].

In this section we present two different architectures for 1550nm MLLs. The first architecture relies on the spiral laser and a semiconductor saturable absorber as a mode-locking element. These lasers were developed in 2012-2013, when our group had little experience with integrated MLL design, and therefore present a less rigorous approach than the one used with 1900nm lasers and presented in Chapter

3. The second architecture relies on a segmented laser cavity structure, an integrated dispersion-compensating grating centered at 1550nm, and an integrated mode-locking element in the cavity.

Both laser designs use the ${}^4I_{13/2} \rightarrow {}^4 I_{15/2}$ atomic transition in Erbium for the lasing wavelength in the optical C-band, and in-band pumping at 1480nm. Although Erbium can also be pumped with 980nm, the integrated photonics design for 980nm pump and 1550nm signal is more challenging than that for 1480nm pump and 1550nm signal. When the pump and the signal are not too far apart in the wavelength domain, the waveguides could be designed to be single mode for both wavelengths, the pump and the signal modes in the gain waveguide could have a large overlap, and transition components that need to work at both wavelengths are easier to implement. Therefore, to simplify the integrated photonics design process, we choose the in-band pumping of Erbium at 1480nm.

4.1 "Spiral" Mode-Locked Laser Design

4.1.1 Architecture

The spiral laser architecture for a 1550nm mode-locked laser is shown in Figure 4-1. The laser resonator cavity is formed with an integrated optical loop mirror on the left side of the cavity, an SBR at the opposite end of the cavity, and a gain waveguide in between the two end-reflectors. The laser is pumped through the integrated loop mirror, as explained in Section 4.1.2. The gain waveguide has a large circular bend design that minimizes the straight-bend waveguide modes mismatch. The mode-locking device used is an in-house grown saturable absorber mirror centered at 1550nm. The output of the cavity is taken from the input of the loop mirror.

The lasers were fabricated using the MIT EPHI program photonics fabrication platform [71], at SUNY CNSE in Albany, NY. The photonic layers used are shown in Figure 1-2, where the height of each Si_3N_4 layer is 200nm, and the gap between the first and second nitride layers 100nm. Table 4.1 shows the MLL components and the

layers where those components were implemented.

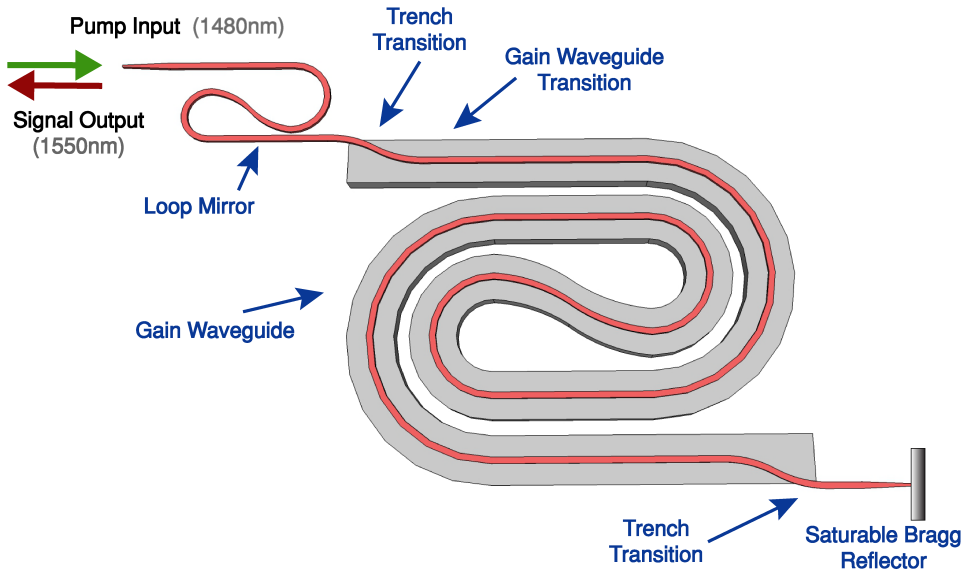

Figure 4-1: 1550nm MLL spiral laser architecture.

Component	Layer	Layer height
Input/Output spot size converters	FN/SN	200 nm
Loop Mirror	FN/SN	200 nm
Gain Waveguide	FN/TR/Tm	1.3μm for Al_2O_3:Er^{3+}

Table 4.1: Photonic material layers used for 1550nm MLL components in a spiral laser architecture.

4.1.2 Integrated Components Design/Characterization.

Gain Waveguide

The gain waveguide cross-section is shown in Figure 4-2 [a]. A 5-piece segmented Si_3N_4 waveguide is separated from a large gain trench by 100nm of SiO_2layer. The gain material is deposited into the gain trench to form a film with 1.3μm thickness (the final thickness can be adjusted on a per-deposition basis, and was optimized for low bend losses). The optical mode (for either pump or signal wavelengths) expands from the 5-piece nitride waveguide into the gain film in such a way that only 1.8% of

the mode is confined in the nitride pieces, and over 80% is confined in the Al_2O_3:Er^{3+} film. The dimensions of the nitride pieces were optimized to increase the overlap of the pump mode with the gain film, the signal mode with the gain film, and the overlap of both the pump and signal together in the gain material. Film height was optimized to lower the losses of a circular gain waveguide bend. The final pump-signal mode overlap in the gain material was calculated to be 80%.

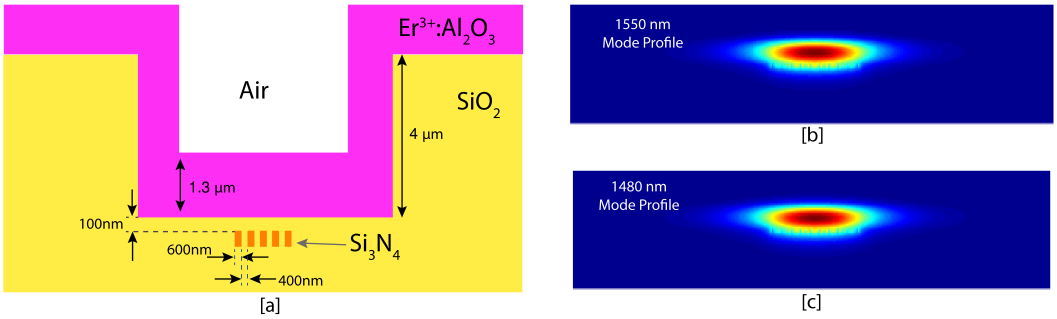

Figure 4-2: 1550nm spiral laser gain waveguide: [a] Schematic and relevant dimensions; [b] 1550nm mode profile; [c] 1480nm mode profile.

In the earlier version of this laser, a multi-mode beating was observed in frequency domain when measuring the gain waveguide response with a tunable laser. The likely reason for this beating was higher order trench modes, guided by the trench itself. To get rid of this problem, the so-called "trench roughness" was added to the side-walls of the trench, with a minimum defined feature size of 5-7 μm and a non-periodic variation along the gain waveguide. Figure 4-3 [a] shows the top view of the gain waveguide with and without the side-wall roughness. The gain waveguide transmission measurement, for various roughness minimum feature sizes, is shown in Figure 4-3 [b]. Although the roughness eliminates higher order modes, it also introduced additional losses into the gain waveguide. We note, three years after this design iteration, that the roughness was likely an erroneous design change, as the trench itself introduced significant losses, as shown in Section 2.4.3 for 1900nm laser. None of the 1900nm gain waveguide designs have exhibited multi-mode trench-induced beating with or without the trench. Therefore, higher order modes are likely the artifact of the improper gain waveguide design. With proper gain waveguide and

trench design, and specifically with a large over-the-entire-gain-area trench (Section 3.2, higher order trench modes could be eliminated, and passive gain waveguide losses could be significantly reduced.

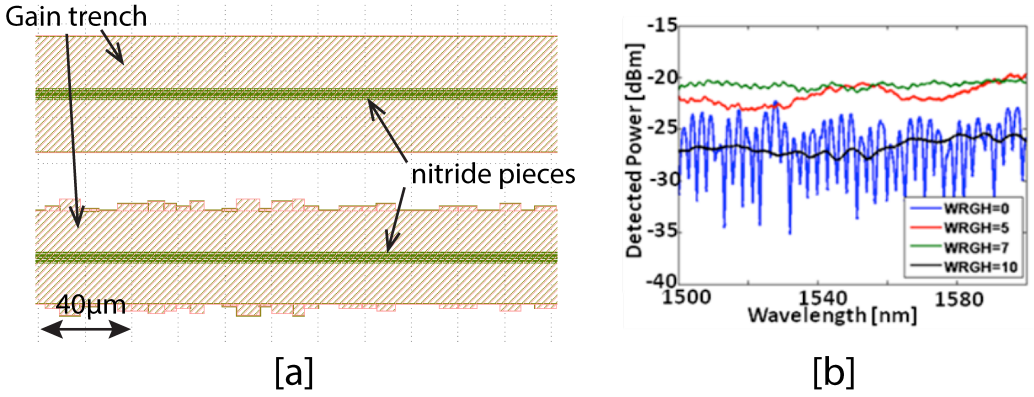

Figure 4-3: Trench sidewall roughness: [a] Top view of the gain waveguide layout view, with and without roughness; [b] Gain waveguide transmission measurement for devices with various sidewall roughness minimum feature size.

Laser variations with 10cm and 20cm one-way gain section lengths were fabricated. We measure the net gain of this gain waveguide by sending a small amount of seed light through the gain waveguide test structure, and monitor its amplification with increasing pump value. Figure 4-4 [a] shows measured gain as a function of wavelength, for increased pump power. The zero pump power case indicated gain waveguide loss and the signal absorption profile. The values for various powers are labeled as follows: the value specified as $P_{\text{on-chip}}$ refers to pump power on chip, at the input of the gain waveguide. The value labeled as P_{laser} refers to the power value as set on the pump laser, and is provided as a reference. Figure 4-4 [b] shows the net saturated gain vs on-chip pump power. The maximum saturated gain was measured to be 0.6 dB/cm at 1560nm.

Mode-Locking Element

The mode-locking element for this spiral laser configuration was an in-house-grown Saturable Bragg Reflector. The SBR was grown using the MBE method, and consisted of 22 pairs of alternating 155nm GaAs and 133nm $Al_{0.95}Ga_{0.05}As$ layers, with a

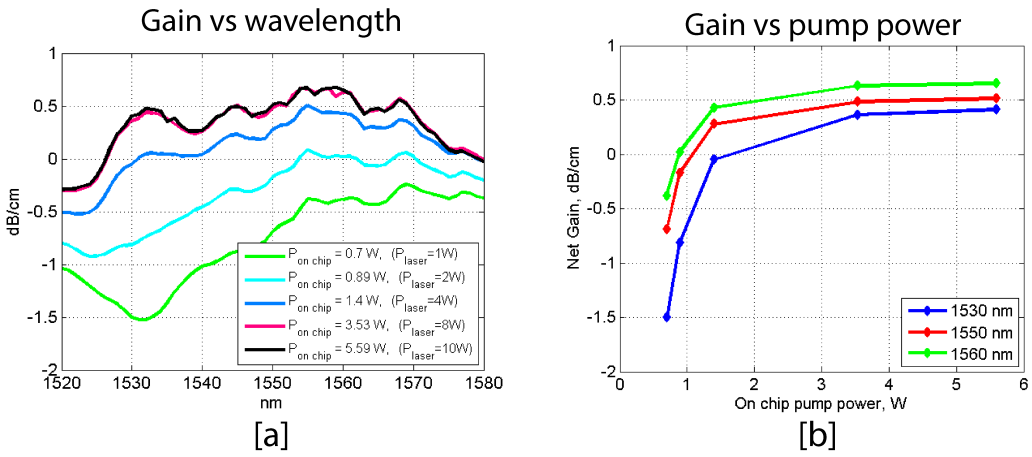

Figure 4-4: Measured gain for 1550nm spiral lasers: [a] Gain vs wavelength; [b] Gain vs pump power, for three wavelengths.

60nm $In_{0.537}Ga_{0.463}As$ absorber layer [2, 3] The saturation fluence on this SBR is 12 $\mu mJ/cm^2$, the modulation depth is 3.9%, the non-saturable loss is 1.1%, and the slow recovery time is 10 ps. The SBR was coupled to the laser chip by using three-axis nano-stages with additional tip/tilt adjustments.

The Si_3N_4 waveguide was linearly tapered down at the edge of the chip, to expand the beam spot size so that the energy incident on the SBR is 2-3 times the value of saturation fluence. The pulse energy was estimated from predicted intra-cavity power values and knowing the repetition rate of the laser. 2-4dB of net to-and-from SBR on/off chip losses were measured by using SBR as an end-reflector with a passive gain film waveguide.

Integrated Loop Mirror

The integrated loop mirror was designed to act as a high reflector at 1550nm (layout is shown in Figure 4-5 [a]). It was designed by using a directional coupler with close-to 50/50 power splitting ratio, where the two outputs are connected, as described in Section 2.4.1. For a shorter wavelength of 1480 nm, the coupler will have smaller cross-coupling and thus higher transmission - hence we can pump the gain waveguide through the loop mirror. because 1480nm wavelength is close to 1550nm wavelength,

the loop mirror will also have some reflection at 1480nm, which means that a portion of the pump would be reflected back by the loop mirror, towards the pump laser. Two different isolators on the pump path prevent the pump laser from this back-reflection-induced damage. Since our pump laser goes up to 10W of optical power as delivered by the output fiber, a significant amount of pump power could still be delivered into the gain waveguide. In the future, a more robust device should be designed, ideally in a way that allows for efficient pump coupling, strong signal reflection, and a loss-prone way to combine the pump and the signal. The loop mirror was simulated using coupled mode theory code, and test structures for the loop mirrors with different mirror gaps were implemented. The simulation and measurements of the loop mirror response are shown in Figure 4-5 [b].

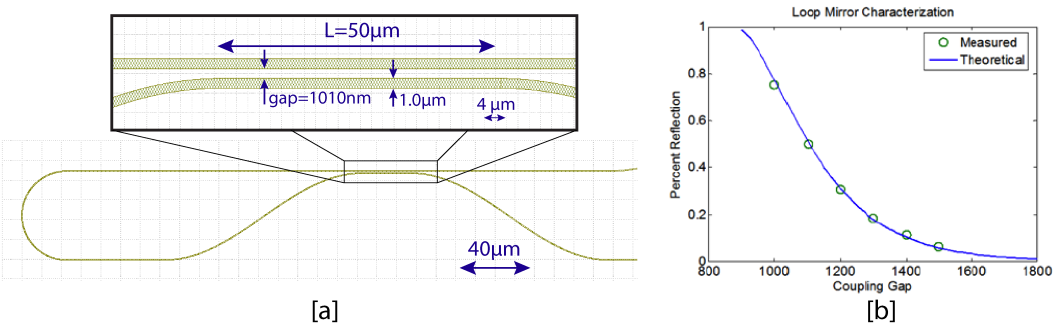

Figure 4-5: Loop mirror design for 1550nm spiral laser: [a] Layout with relevant dimensions; [b] Simulation and measurements of the response for various coupler gap sizes.

Trench Transition / Gain Waveguide Transition

Similarly to 1900nm lasers, the light prior to entering the gain material region is confined in a silicon nitride waveguide. In this MLL design, the loop mirror and the subsequent nitride waveguide are made of an FN and SN layer combination, as shown in Figure 4-6 [c]. Therefore, a transition component is needed to couple the light from this SN/FN layer combination to the gain waveguide. Although in 1900nm lasers this problem was solved with a very robust and low loss vertical layer change escalator transition (see Section 3.1.3) implemented in the ZN layer, at the time of this spiral

1550nm laser development (which was three years prior to the 1900nm lasers work), the ZN layer was not available, and this transition was done horizontally, as shown in Figure 4-6. The second nitride layer was slowly tapered down, transferring the optical mode to the FN waveguide alone. Next, this FN waveguide was brought close to, and ultimately under the photonic trench. This is shown in Figure 4-6, where in part [a] part of the transition photonic layout is shown, in [b] the top view of the intensity in the waveguide is shown along the length of the transition, in [c] and [d] the cross-sections of the waveguide at the beginning and close to the end of the transition are shown (FIMMWAVE^{TM} simulation). The length of this transition was chosen to be 1.2 μm, in order to adiabatically change the waveguide dimensions and therefore reduce mode mismatch losses.

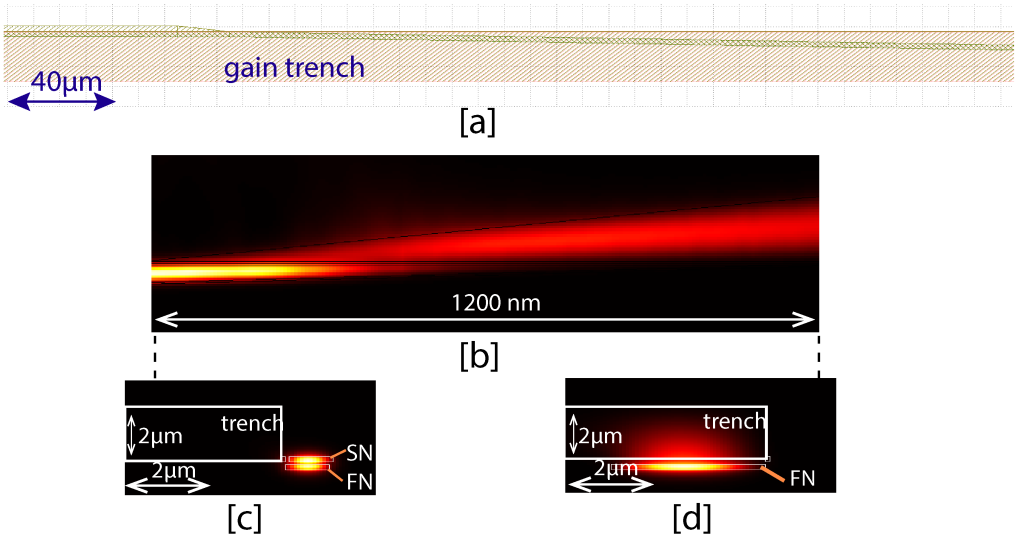

Figure 4-6: Gain trench transition design for 1550nm spiral laser: [a] Photonic layout of the transition; [b] Top view of the light intensity along the transition; [c] Optical mode profile cross-section at the beginning of the transition; [d] Optical mode profile cross-section close to the end of the transition

After the trench transition, the light was in the gain trench, but anchored by a single piece FN layer, as opposed to the desired 5-piece nitride waveguide. The single piece FN waveguide was then transitioned into a 5-piece waveguide by a simple linear taper, shown in Figure 4-7, with the length optimized for low loss transmission.

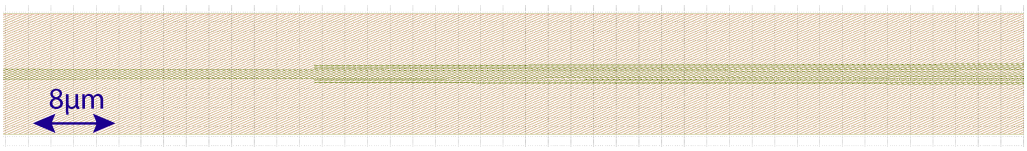

Figure 4-7: Gain waveguide transition for a single piece to 5-piece nitride, for 1550nm spiral MLL.

Combined loss of the trench transition and the subsequent gain waveguide transition together was measured to be 0.5-0.7 dB at 1550nm. Since the laser cavity has two of those transitions, the light encounters four of them in a round-trip propagation, making the net transition-induced loss 2-2.8 dB. This is a significant loss that reduced the net gain at a particular pump power, raising the threshold, and reduced the amount of signal power in the cavity. This design is not robust, and was the group's first attempt to design this component. An ideal photonic transition would be adiabatic. In this case, the trench wall is brought next to FN waveguide suddenly, likely causing extra reflections at that point. For comparison, the escalator transition, presented in Section 3.1.3, has 0.01 dB/transition loss.

4.1.3 Photonic Layout

The layout of the full MLL chip is shown in Figure 4-8. Eight variations of the 10cm-long (one way) laser and either variations of 20-cm long laser were fabricated, along with all relevant test-structures. The chips were fabricated in 300mm SOI wafers, and dices into individual 26mm x 24 mm chiplets.

4.1.4 Results

The spiral 1550nm mode-locked lasers presented in this section were characterized using a setup shown in Figure 4-9. A high average power 1480nm laser (IPG Photonics) was used as a pump source. The pump light was fiber-coupled, sent through a fiber-based isolator and a circulator (to measure the output of the laser), and subsequently coupled onto the chip using a lensed SMF28 fiber. A semiconductor saturable

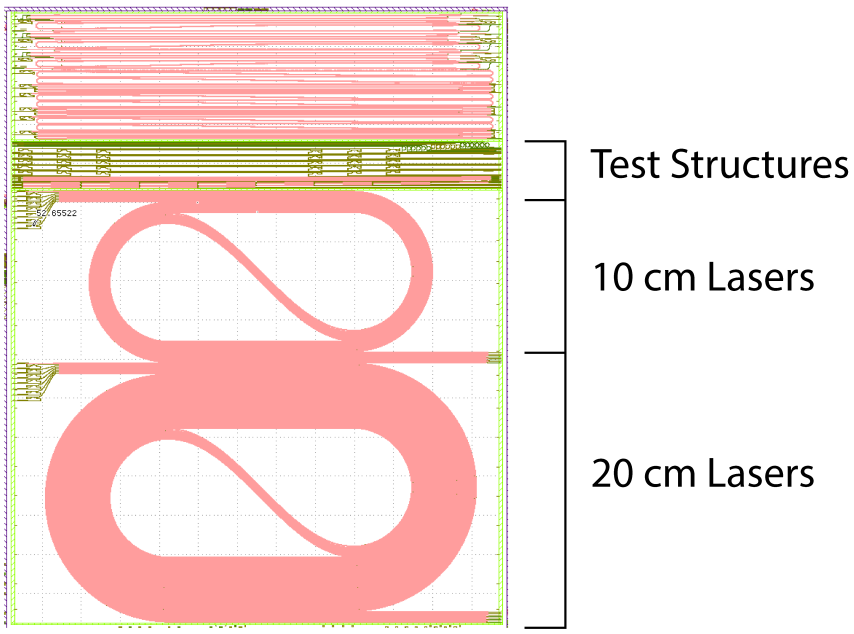

Figure 4-8: Full photonic layout of the 1550nm MLL chip.

absorber was aligned to the output facet of the laser. The output of the laser was measured at the output of the circulator, and was split to go to Optical Spectrum Analyzer (Yokogawa) and a fast photodetector (EOT, ET-3500F, 15 GHz electric bandwidth). The photodetector output was monitored on the oscilloscope and the RF analyzer. Figure 4-10 shows the characteristic green fluorescence (due to energy transfer upconversion processes) for single (10cm) and double (20cm) spiral lasers, when pumped with 1480nm laser. Figure 4-11 shows the optical spectra [a] and the

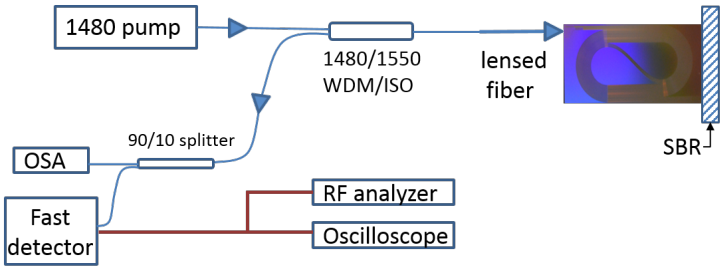

Figure 4-9: Experimental setup for characterization of 1550nm spiral-based MLLs.

corresponding signal vs pump power ([b]) results for 20cm-long lasers. The central

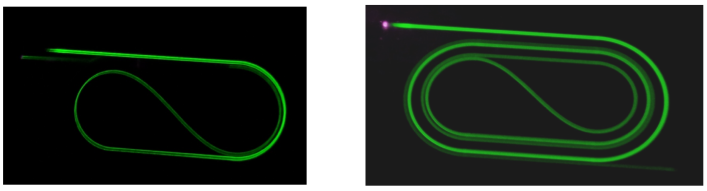

Figure 4-10: Green upconversion-based fluorescence, observed while pumping 1550nm MLLs.

wavelength is around 1560nm (corresponding to the peak of the gain), and the spectra appear very narrow band. The threshold for this laser is around 1.4W of pump power on chip, which is unusually high, but expected due to numerous loss sources within the laser cavity. We are able to achieve over 15mW of average signal power on chip, outside of the MLL cavity, though with over 2W of on-chip pump power. At on-chip pump power levels above 2W, the laser goes into a Q-switched, and even-

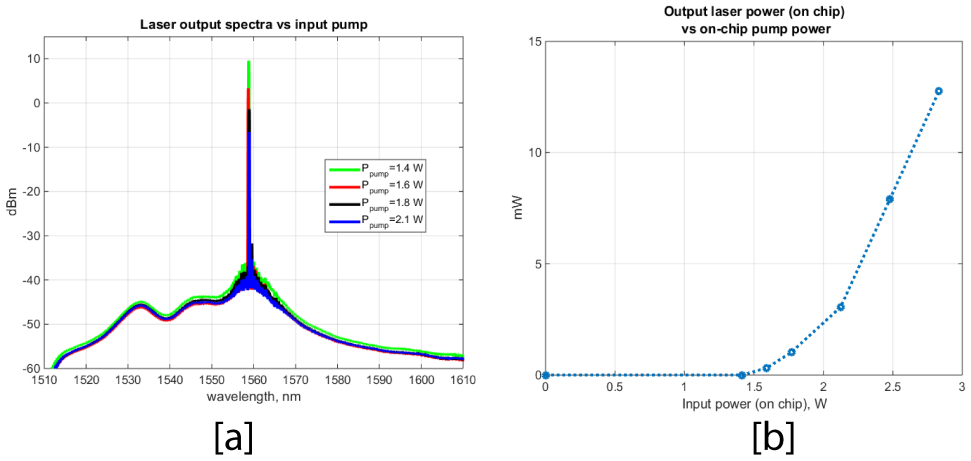

Figure 4-11: 1550nm MLL results: [a] Optical spectra for various pump power levels; [b] Output power on-chip vs input pump power on-chip.

tually a Q-switch-mode-locked, regime. Figure 4-12 [a] shows Q-switching it a rate of 1.1MHz, which could be varied by changing the pump power coupled onto the chip. Figure 4-12 [c] shows a close-up view of one Q-switched pulse, where individual mode-locked pulses are visible underneath the Q-switching envelope. Zooming in further in this plot, Figure 4-12 [d] shows an even closer look at the pulses underneath

the Q-switched envelope, with the pulse period of 2.1ns. Figure 4-12 [b] shows the corresponding RF spectra at the 470 MHz repetition rate, which corresponds to a 2.1ns pulse spacing. 470MHz also corresponds to the laser cavity repetition rate for a 20cm long laser.

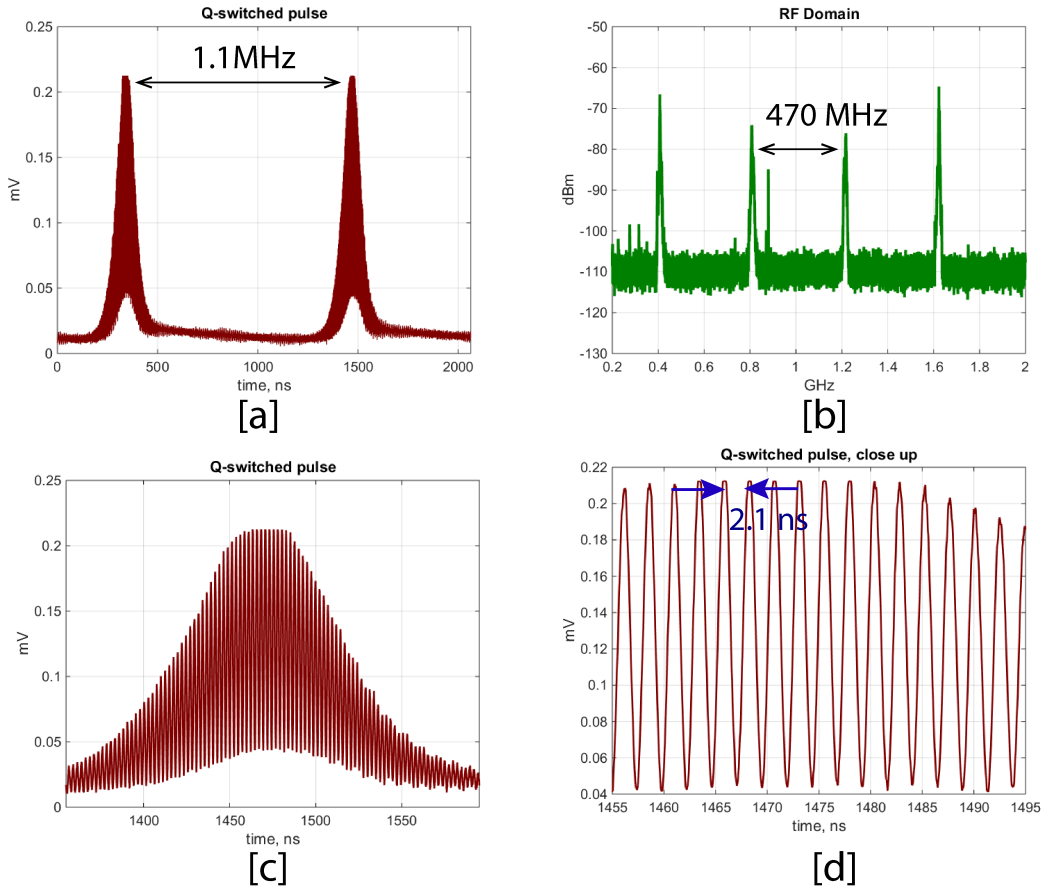

Figure 4-12: 1550nm MLL results: [a] Q-switched pulses in time domain; [b] RF spectrum of the pulse train; [c] Close up of an individual Q-switched pulse; [d] Further close up of an individual Q-switched pulse.

The laser in this section represents our group's earliest attempt to design an on-chip MLL. Therefore, some components are not very robust, with 1900nm lasers which were developed over the next three years having much better component design and overall MLL design methodology. Moreover, at the time when this laser was designed, the group did not have numerical pulse propagation simulation capabilities, and approached the MLL design from a purely integrated photonics point of view.

Over the next few years the design approach has evolved into having a complete gain model, looking at the dispersion/nonlinearity budget at the first-order design stage, and performing accurate numerical simulations of each MLL cavity designed prior to the tape-out.

The results in this section demonstrate a Q-switch mode-locked on-chip mode-locked laser at a 470MHz repetition rate, centered at 1560nm, with over 10mW on-chip power, and mode-locked using a semiconductor saturable absorber. The next section will outline a better laser configuration, with improved components and having an integrated mode-locking element.

4.2 "Segmented" Mode-Locked Laser Design

The architecture of an integrated segmented mode-locked laser for 1550nm central wavelength operation is shown in Figure 4-13. The laser is very similar to the 1900nm segmented laser design as presented in Section 3.2, and was designed using the same methodology, but for different pump/signal wavelengths. The laser is pumped with a

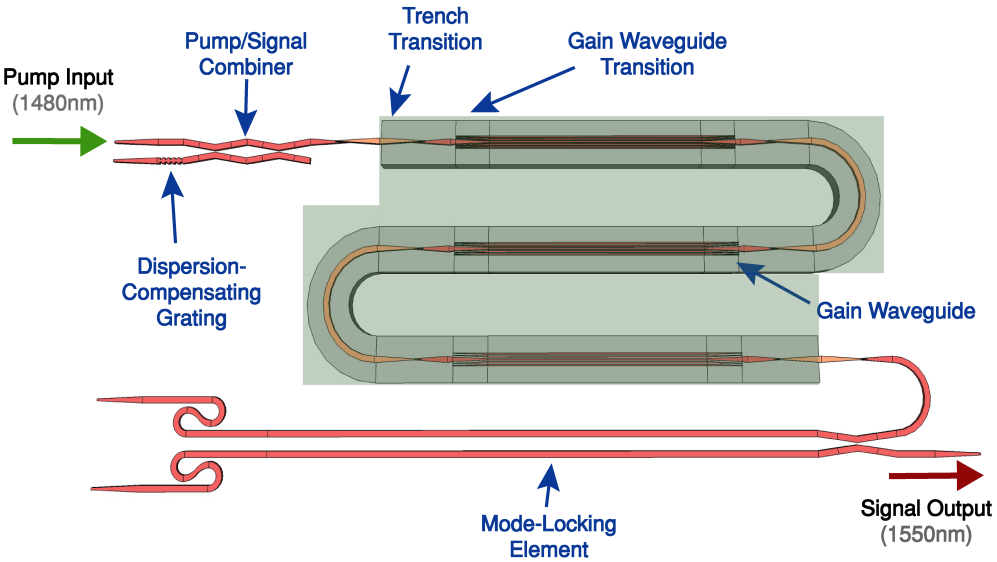

Figure 4-13: 1550nm MLL segmented laser architecture.

1480nm CW laser, and the pump goes through an imbalanced Mach-Zehnder interfer-

ometer component, which acts as a pump/signal combiner. The pump then enters the gain waveguide through the vertical escalator transition (see Section 3.1.3, redesigned to work at 1480nm and 1550nm. The gain waveguide is similar to the design presented for 1900nm lasers, but the dimensions of the silicon nitride pieces are adjusted for the 1480/1550nm wavelengths. Euler bends are also used to provide compact low loss bends inside of this laser cavity. The mode-locking element is the nonlinear interferometer, designed for 1550nm operation, and discussed in detail in Section 2.5. The laser resonator cavity is formed by the nonlinear interferometer on the right of the cavity and the dispersion-compensating grating on the other end of the cavity. The overall one-way length of the gain section is about 6mm, which should result in about a GHz repetition rate. The dispersion compensating grating was designed to be centered at 1550nm, and to deliver enough anomalous group delay dispersion to compensate for the all-normal dispersion of the rest of this laser. A large trench is etched over the entire gain region of the chip, as indicated by the gray shaped area in Figure 4-13. As of October 2017, these lasers have been fabricated, and initial characterization was in progress. Since most of the components of this laser architecture have been demonstrated in 1900nm laser (when designed for 1900nm wavelength), and the methodology for each component is well understood, there is a good chance the full lasers will work according to the design specifications.

Chapter 5

Conclusion

DARPA strategic initiatives targeting the US integrated photonics capabilities have enabled key developments in areas of photonic communications, electronic-photonic integration, photonic LIDAR, on-chip analog-to-digital converters, and many others. CMOS-compatible on-chip mode-locked lasers presented in this thesis are key enabling elements for several integrated photonics systems, specifically for precision low noise optical frequency synthesis and for low phase noise microwave generation. The lasers in this thesis were designed to be used in such sub-systems in conjunction with other components that are being simultaneously developed at MIT. While a full on-chip mode-locked laser-based microwave synthesizer is currently under development, a nearer-term goal is a fully stabilized on-chip optical frequency comb, with an integrated mode-locked laser being the master pulse generator for the comb.

Integrated CMOS-compatible mode-locked lasers at 1550nm and 1900nm with no off-chip components except for the pump source are presented in this work. 1900nm mode-locked lasers were demonstrated at 680 MHz and 1.2 GHz repetition rate, with pulse durations from 800fs to 215fs. Q-switching, Q-switched mode-locking, and CW mode-locking have been demonstrated, with over 10mW of on-chip average power. 1550nm-based mode-locked lasers have also been achieved with over 10mW on-chip average power and 470 MHz repetition rate, with Q-switching and Q-switch-mode-locking regimes demonstrated as well. The lasers are based on rare earth ion doped aluminum glass as a gain material in a stoichiometric silicon nitride in silicon dioxide

core photonic material platform. Thulium is used as a gain dopant for 1900nm laser operation, and Erbium is used for the 1550nm wavelength regime. The footprint of our compact laser design is 23.6x0.76x0.6mm. Although several lasers presented here rely on semiconductor saturable absorbers, the majority of the work in this thesis focuses on mode-locking with integrated on-chip CMOS-compatible devices.

The first fully-on-chip CMOS-compatible "fast passive mode-locking devices, referred to as artificial saturable absorbers, have been demonstrated in this thesis. These devices are based on Kerr nonlinearity-induced nonlinear reflection, and therefore are fast, meaning they can support pulses to below 100fs. Artificial saturable absorbers at 1550nm and 1900nm are demonstrated using a stoichiometric silicon nitride in SiO2 material platform, to be used with integrated mode-locked lasers of corresponding central wavelengths. 1550nm-based mode-locking devices have a modulation depth of 2.5%, while 1900nm-based mode-locking devices have a modulation depth of 9%. Integrated mode-locked lasers with these artificial saturable absorbers have been designed, fabricated, and characterized. By adjusting the linear phase bias of our artificial saturable absorbers, the mode-locking in the lasers could be turned on or off. Novel designs of the artificial saturable absorbers, with dispersion compensating gratings inside the mode-locking elements, are also presented. Such devices should allow for enhanced pulse shortening in a mode-locked laser cavity.

General theory and design optimization for the artificial saturable absorbers is presented, which allows to select and design parameters such as modulation depth, reflection/transmission of the device, and self-amplitude modulation coefficient. These devices could be designed for any wavelength provided it is outside of linear or nonlinear absorption of the constituent materials. They don't require any alignment, do not suffer from energy-related thermal damage threshold (like, for example, semiconductor saturable absorbers), have a few femtoseconds-long response time (hence they are considered "fast), and don't require any additional materials or packaging since they are part of a standard CMOS process.

Future work on improving the integrated artificial saturable absorbers should focus on reducing linear losses of the constituent materials and further improving effective

nonlinearity of the devices. However, the true performance of such artificial saturable absorbers should be fully evaluated together with the rest of the mode-locked laser cavity design parameters because the rest of the cavity affects the optical pulse characteristics incident onto the artificial saturable absorber. Moreover, the mode-locking devices should be designed specifically for a particular laser cavity. Additionally, different overall schemes of Kerr-nonlinearity-based artificial saturable absorbers should be explored. For example, nonlinear polarization rotation and Kerr lens mode-locking-based schemes could be explored using an integrated silicon photonics platform.

Future work on integrated mode-locked laser design should focus on reducing Q-switching instabilities, on improving the average power in the mode-locked laser cavity, and on adjusting the cavity parameters to shorten the pulse duration to below 200fs. Further, slope efficiency of the lasers should be improved to increase the overall power efficiency of the system. To do this, one could use more efficient pumping schemes, improve the pump coupling losses, and reduce the overall material and device-induced losses of all mode-locked laser components.

A key missing component in the integrated photonics CMOS-compatible platform is an on-chip isolator. Such a device is necessary to reduce many spurious back-reflections in a photonic system and to enable unidirectional laser operation. The material symmetry breaking necessary to realize this component is challenging to implement using CMOS-compatible processes. Several research groups are looking into potential solution options. These efforts should continue, and if they result in a CMOS-compatible on-chip isolator, numerous other on-chip mode-locked laser configurations would become possible. Ring-based lasers could be implemented with different established mode-locking schemes.

More generally, the scientific community and industry should put significant efforts into scalable co-packaging of the optical pump sources onto the CMOS platform itself. This is an engineering problem which could be solved for a particular CMOS 3D integrated platform using either available III-V or other novel integrated light sources. With co-integrated pumps, integrated mode-locked lasers, subsequent on-chip stabilized frequency combs, and further mode-locked-laser-based systems would

become truly portable.

CMOS-compatible integrated photonics-based mode-locked lasers could one day replace their bulk optics counterparts with devices that are at least two orders of magnitude smaller, significantly less expensive, more power-efficient, alignment-free, and easily mass-produced. This will revolutionize mode locked laser based systems for use in communications, medical devices and imaging, spectroscopy, and defense and military platforms. Additionally, on-chip mode locked lasers enable compact low noise microwave signal generation for numerous scientific and military applications. Mode-locked lasers presented in this thesis are key enablers of such compact systems. With the help of DARPA and the recently launched AIM photonics initiative, these and many other integrated photonic systems could be quickly on their way to commercial products and real defense solutions, positioning US as a global leader in the integrated photonics industry.

Bibliography

[1] H. M. Shen, *Novel broadband light sources and pulse generation techniques at 1.5μm.* PhD thesis, Massachusetts Institute of Technology, 2009.

[2] M. Y.-L. Sander, *High repetition rate fiber and integrated waveguide femtosecond lasers.* PhD thesis, Massachusetts Institute of Technology, 2012.

[3] A. R. Motamedi, *Ultrafast nonlinear optical properties of passive and active semiconductor devices.* PhD thesis, Massachusetts Institute of Technology, 2011.

[4] DARPA MTO, DARPA-BAA-11-45, April, 2011.

[5] DARPA MTO, DARPA-BAA-14-31, April, 2017.

[6] E. S. Magden, *Optical signal generation, stabilization, and manipulation in broadband silicon photonics.* PhD thesis, Massachusetts Institute of Technology, 2017.

[7] F. X. Kärtner, "Ultrafast optics, MIT OCW lecture notes," 2005. `https://ocw.mit.edu/courses/electrical-engineering-and-computer-science/6-977-ultrafast-optics-spring-2005/`.

[8] A. Weiner, *Ultrafast Optics*, John Wiley and Sons, Inc, Hoboken, New Jersey, USA, 2009.

[9] J.-C. Diels and W. Rudolph, *Ultrashort Laser Pulse Phenomena*, Elsevier, Inc, Burlington, Massachusetts, USA, 2nd ed., 2006.

[10] R. Walden, *Analog-to-digital conversion in the early twenty-first century*, John Wiley and Sons, Inc, 2008. Wiley Encyclopedia of Computer Science and Engineering.

[11] H. Byun, D. Pudo, S. Frolov, A. Hanjani, J. Shmulovich, E. P. Ippen, and F. X. Kärtner, "Integrated low-jitter 400-MHz femtosecond waveguide laser," *IEEE Photonics Technology Letters* **21**(12), pp. 763–765, 2009.

[12] A. Khilo, S. J. Spector, M. Grein, A. Nejadmalayeri, C. W. Holzwarth, M. Sander, M. Dahlem, M. Peng, M. Geis, N. A. DiLello, J. U. Yoon, A.Motamedi, J. Orcutt, J. Wang, C. M. Sorace-Agaskar, M. A. Popovic, J. Sun, G. Zhou, H. Byun, J. Chen, J. L. Hoyt, H. I. Smith, R. J. Ram, M. Perrott,

T. M. L. E. P. Ippen, and F. X. Kärtner, "Photonic ADC: overcoming the bottleneck of electronic jitter," *Optics Express* **20**, pp. 4454–4469, 2012.

[13] S. T. Cundiff and A. M. Weiner, "Optical arbitrary waveform generation," *Nature Photonics* **4**, pp. 760–766, 2010.

[14] I. Coddington, W. C. Swann, L. Nenadovic, and N. R. Newbury, "Rapid and precise absolute distance measurements at long range," *Nature Photonics* **3**, pp. 351–356, 2009.

[15] P. A. Roos, R. Reibel, T.Berg, B.Kaylor, Z. W. Barber, and W. Babbitt, "Ultrabroadband optical chirp linearization for precision metrology applications," *Optics Letters* **34**, pp. 3692–3694, 2009.

[16] E. Ippen, A. Benedick, J. Birge, H. Byun, L.Chen, G. Chang, D. Chao, J. Morse, A. Motamedi, M. Sander, G. Petrich, L. Kolodziejski, and F. X. Kärtner, "Optical arbitrary waveform generation," *Conference on Lasers and Electro-Optics 2010*, (San Jose, CA, USA), 2010.

[17] R. A. McCracken, J. M. Charsley, and D. T. Reid, "A decade of astrocombs: recent advances in frequency combs for astronomy," *Optics Express* **25**, pp. 15058–15078, 2017.

[18] G. Chang, C. Li, D. F. Phillips, A. Szentgyorgyi, R. L. Walsworth, and F. X. Kärtner, "Optimization of filtering schemes for broadband astro-combs," *Optics Express* **20**, pp. 24987–25013, 2012.

[19] R. Soref, "The past, present, and future of silicon photonics," *IEEE Journal of Selected Topics in Quantum Electronics* **12**(6), pp. 1678–1687, 2006.

[20] B. Jalali and S. Fathpour, "Silicon photonics," *Journal of Lightwave Technology* **24**(12), pp. 4600–4615, 2006.

[21] A. D. Bristow, N. Rotenberg, and H. M. van Driel, "Two-photon absorption and Kerr coefficients of silicon for $850 - 2200$nm," *Applied Physics Letters* **90**(19), p. 191104, 2007.

[22] R. J. Baker, *CMOS Circuit Design, Layout, and Simulation*, IEEE Press, John Wiley and Sons, Inc, Hoboken, New Jersey, USA, 2010.

[23] Global Foundries, "CMOS Capabilities." `https://www.globalfoundries.com/technology-solutions/cmos`, 2017. Accessed: 2017-08-01.

[24] Global Foundries, "65nm and 55nm LPe-RF foundry technologies." `https://www.globalfoundries.com/sites/default/files/product-briefs/55-65nm-lpe-rf-technology.pdf`, 2015. Accessed: 2017-08-01.

[25] S. Bogdanov, M. Y. Shalaginov, A. Boltasseva, and V. M. Shalaev, "Material platforms for integrated quantum photonics," *Optical Materials Express* **7**(1), pp. 111–132, 2017.

[26] K. Shtyrkova, C. Evans, O. Reshef, J. Bradley, M. G. Moebius, E. Mazur, and E. Ippen, "Third harmonic generation in polycrystalline anatase titanium dioxide nanowaveguides," *Conference of Lasers and Electro-Optics, 2014*, p. SW3I.6, (San Jose, CA, USA), 2014.

[27] C. C. Evans, K. Shtyrkova, J. D. B. Bradley, O. Reshef, E. Ippen, and E. Mazur, "Spectral broadening in anatase titanium dioxide waveguides at telecommunication and near-visible wavelengths," *Optics Express* **21**(15), pp. 18582–18591, 2013.

[28] O. Reshef, K. Shtyrkova, M. G. Moebius, S. Griesse-Nascimento, S. Spector, C. C. Evans, E. Ippen, and E. Mazur, "Polycrystalline anatase titanium dioxide microring resonators with negative thermo-optic coefficient," *Journal of Optical Society of America B* **32**(11), pp. 2288–2293, 2015.

[29] C. Sun, M. T. Wade, Y. Lee, J. S. Orcutt, L. Alloatti, M. S. Georgas, A. S. Waterman, J. M. Shainline, R. Avizienis, S. Lin, B. R. Moss, R. Kumar, F. Pavanello, A. H. Atabaki, H. M. Cook, A. J. Ou, J. C. Leu, Y. Chen, K. Asanovic, R. J. Ram, M. A. Popovic, and V. M. Stojanovic, "Single-chip microprocessor that communicates directly using light," *Nature* **528**, pp. 534–538, 2015.

[30] J. Cardenas, C. B. Poitras, J. T. Robinson, K. Preston, L. Chen, and M. Lipson, "Low loss etchless silicon photonic waveguides," *Optics Express* **17**, pp. 4752–4757, 2009.

[31] Y. A. Vlasov and S. J. McNab, "Losses in single-mode silicon-on-insulator strip waveguides and bends," *Optics Express* **12**, pp. 1622–1631, 2004.

[32] M. A. Popovic, T. Barwicz, M. R. Watts, P. T. Rakich, L. Socci, E. P. Ippen, F. X. Kärtner, and H. I. Smith, "Multistage high-order microring-resonator add-drop filters," *Optics Letters* **31**(17), pp. 2571–2573, 2006.

[33] Q. Xu, B. Schmidt, S. Pradhan, and M. Lipson, "Micrometre-scale silicon electro-optic modulator," *Nature* **435**(03569), pp. 325–327, 2005.

[34] C. Gunn, "CMOS photonics for high-speed interconnects," *IEEE Micro* **26**(2), pp. 58–66, 2006.

[35] E. Timurdogan, C. M. Sorace-Agaskar, J. Sun, E. S. Hosseini, A. Biberman, and M. R. Watts, "An ultralow power athermal silicon modulator," *Nature* **5**, 2014.

[36] T. Barwicz, H. Byun, F. Gan, C. W. Holzwarth, M. A. Popovic, P. T. Rakich, M. R. Watts, E. P. Ippen, F. X. Kärtner, H. I. Smith, J. S. Orcutt, R. J. Ram,

V. Stojanovic, O. O. Olubuyide, J. L. Hoyt, S. Spector, M. Geis, M. Grein, T. Lyszczarz, and J. U. Yoon, "Silicon photonics for compact, energy-efficient interconnects," *Journal of Optical Networking* **6**(1), pp. 63–73, 2007.

[37] V. Stojanovic, A. Joshi, C. Batten, Y. Kwon, S. Beamer, S. Chen, and K. Asanovic, "Design-space exploration for CMOS photonic processor networks," *Optical Fiber Communication Conference*, (San Diego, California, USA), March 2010.

[38] D. A. B. Miller, "Rationale and challenges for optical interconnects to electronic chips," *Proceedings of the IEEE* **88**(6), pp. 728–749, 2000.

[39] C. Batten, A. Joshi, J. Orcutt, A. Khilo, B. Moss, C. W. Holzwarth, M. A. Popovic, H. Li, H. I. Smith, J. L. Hoyt, F. X. Kärtner, R. J. Ram, V. Stojanovic, and K. Asanovic, "Building Many-Core Processor-to-DRAM networks with monolithic CMOS silicon photonics," *IEEE Micro* **29**(4), pp. 8–21, 2009.

[40] J. Sun, E. Timurdogan, A. Yaacobi, E. Hosseini, and M. R. Watts, "Large-scale nanophotonic phased array," *Nature* **493**, pp. 195–199, 2013.

[41] C. V. Poulton, A. Yaccobi, Z. Su, M. J. Byrd, and M. R. Watts, "Optical phased array with small spot size, high steering range and grouped cascaded phase shifters," *Advanced Photonics 2016 (IPR, NOMA, Sensors, Networks, SPPCom, SOF)*, p. IW1B.2, (Vancouver, Canada), 2016.

[42] N. D. Heidel, N. G. Usechak, C. L. Dohrman, and J. A. Conway, "A review of electronic-photonic heterogeneous integration at DARPA," *IEEE Journal of Selected Topics in Quantum Electronics* **22**, 2016.

[43] J. Shah, "DARPA'S EPIC program: electronic and photonic integrated circuits on Si," *IEEE International Conference on Group IV Photonics, 2005. 2nd*, (Antwerp, Belgium), 2005.

[44] J. Shah, "Moore's law for photonics and beyond." `http://archive.darpa.mil/DARPATech2005/presentations/mto/shah.pdf`, 2005. DARPA Technology Report.

[45] DARPA, "POEM program description." `https://www.darpa.mil/program/photonically-optimized-embedded-microprocessors`, 2015. Accessed: 08-01-2017.

[46] H. D. Thacker, X. Zheng, J. Lexau, R. Shafiiha, I. Shubin, S. Lin, S. Djordjevic, P. Amberg, E. Chang, F. Liu, J. Simons, J.-H. Lee, A. Abed, H. Liang, Y. Luo, J. Yao, D. Feng, M. Asghari, R. Ho, K. Raj, J. E. Cunningham, and A. V. Krishnamoorthy, "An all-solid-state, WDM silicon photonic digital link for chip-to-chip communications," *Optics Express* **23**(10), pp. 12808–12822, 2015.

[47] "A competition for the integrated photonics manufacturing institute." https://obamawhitehouse.archives.gov/the-press-office/2014/10/03/fact-sheet-president-obama-announces-new-manufacturing-innovation-instit, 2014. Accessed: 08-01-2017.

[48] "American Institute for Manufacturing Photonics." http://www.aimphotonics.com/, 2017. Accessed: 08-01-2017.

[49] J. J. McFerran, E. N. Ivanov, A. Bartels, G. Wilpers, C. W. Oates, S. A. Diddams, and L. Hollberg, "Low-noise synthesis of microwave signals from an optical source," *Electronics Letters* **41**(11), pp. 650–6, 2005.

[50] S. A. Diddams, A. Bartels, T. M. Ramond, C. W. Oates, S. Bize, E. A. Curtis, J. C. Bergquist, and L. Hollberg, "Design and control of femtosecond lasers for optical clocks and the synthesis of low-noise optical and microwave signals," *IEEE Journal of Selected Topics in Quantum Electronics* **9**(4), pp. 1072–1080, 2003.

[51] S. Hakobyan, V. J. Wittwer, P. Brochard, K. Gurel, S. Schilt, A. S. Mayer, U. Keller, and T. Sudmeyer, "Full stabilization and characterization of an optical frequency comb from a diode-pumped solid-state laser with GHz repetition rate," *Optics Express* **25**(17), pp. 20437–20453, 2017.

[52] T. Komljenovic, M. Davenport, J. Hulme, A. Y. Liu, C. T. Santis, A. Spott, S. Srinivasan, E. J. Stanton, C. Zhang, and J. E. Bowers, "Heterogeneous silicon photonic integrated circuits," *Journal of Lightwave Technology* **34**, pp. 20–35, 2016.

[53] T. Komljenovic, S. Srinivasan, E. Norberg, M. Davenport, G. Fish, and J. E. Bowers, "Widely tunable narrow-linewidth monolithically integrated external-cavity semiconductor lasers," *IEEE Jouranl of Selected Topics in Quantum Electronics* **21**, pp. 214–222, 2015.

[54] X. Xie, Q. Zhou, E. Norberg, M. Jacob-Mitos, Y. Chen, A. Ramaswamy, G. Fish, J. E. Bowers, J. Campbell, and A. Beling, "Heterogeneously integrated waveguide-coupled photodiodes on SOI with 12 dBm output power at 40 GHz," *2015 Optical Fiber Communications Conference and Exhibition*, (Los Angeles, CA, USA), 2015.

[55] F. Y. Liu, D. Patil, J. Lexau, P. Amberg, M. Dayringer, J. Gainsley, H. F. Moghadam, X. Zheng, J. E. Cunningham, A. V. Krishnamoorthy, E. Alon, and R. Ho, "10-Gbps, 5.3-mW optical transmitter and receiver circuits in 40-nm CMOS," *IEEE Journal of Solid-State Circuits* **47**(9), pp. 2049–2067, 2012.

[56] A. H. B. Yousuf, N. M. Hossain, and M. H. Chowdhury, "Performance analysis of through silicon via (TSV) and through glass via (TGV) for different materials," *2015 IEEE International Symposium on Circuits and Systems (ISCAS)*, 2015.

[57] Y. Jeong, C. Alegria, J. K. Sahu, L. Fu, M. Ibsen, C. Codemard, M. R. Mokhtar, and J. Nilsson, "A 43-W C-band tunable narrow-linewidth erbium-ytterbium codoped large-core fiber laser," *IEEE Photonics Technology Letters* **16**(3), pp. 756–758, 2004.

[58] A. L. Schawlow and C. H. Townes, "Infrared and optical masers," *Physical Review* **112**, pp. 1940–1949, 1958.

[59] K. Numata, A. Kemery, and J. Camp, "Thermal-noise limit in the frequency stabilization of lasers with rigid cavities," *Physics Review Letters* **93**(250602), pp. 97–105, 2004.

[60] P. Drever, J. L. Hall, F. V. Kowalski, J. Hough, G. M. Ford, A. J. Munley, and H. Ward, "Laser phase and frequency stabilization using an optical resonator," *Applied Physics B* **31**, pp. 97–105, 1983.

[61] D. Li, *Attosecond timing jitter modelocked lasers and ultralow phase noise photonic microwave oscillators*. PhD thesis, Massachusetts Institute of Technology, 2014.

[62] E. Timurdogan, Z. Su, K. Settaluri, S. Lin, S. Moazeni, C. Sun, G. Leake, D. D. Coolbaugh, B. R. Moss, M. Moresco, V. Stojanovic, and M. R. Watts, "An ultra low power 3D integrated intra-chip silicon electronic-photonic link," *2015 Optical Fiber Communications Conference and Exhibition (OFC)*, (Los Angeles, CA, USA), 2015.

[63] C. McDonough, D. L. Tulipe, D. Pascual, P. Tariello, J. Mucci, M. Smalley, A. Nguyen, T. Vo, C. Johnson, P. Nguyen, J. Hebding, G. Leake, M. Moresco, E. Timurdogan, V. Stojanovic, M. R. Watts, and D. Coolbaugh, "Heterogeneous integration of a 300mm silicon photonics-CMOS wafer stack by direct oxide bonding and via-last 3D interconnection," *International Symposium on Microelectronics*, pp. 621–626, 2015.

[64] J. Bradley, $Al_2O_3 : Er^{3+}$ *as a gain platform for integrated optics*. PhD thesis, University of Twente, 2009.

[65] K. Worhoff, J. D. B. Bradley, F. Ay, D. Geskus, T. P. Blauwendraat, and M. Pollnau, "Reliable low-cost fabrication of low-loss Al_2O_3:Er^{3+} waveguides with 5.4 dB optical gain," *IEEE Journal of Quantum Electronics* **45**(5), pp. 454–461, 2009.

[66] E. S. Magden, Purnawirman, N. Li, G. Singh, J. D. B. Bradley, G. S. Petrich, G. Leake, D. Coolbaugh, M. Watts, and L. A. Kolodziejski, "Fully CMOS-compatible integrated distributed feedback laser with 250°C fabricated Al_2O_3:Er^{3+} gain medium," *Conference on Lasers and Electro-Optics*, p. SM1G.2, 2016.

[67] J. D. B. Bradley and M. Pollnau, "Erbium-doped integrated waveguide amplifiers and lasers," *Laser and Photonics Reviews* **5**(3), pp. 368–403, 2010.

[68] Purnawirman, J. Sun, T. N. Adam, G. Leake, D. Coolbaugh, J. D. B. Bradley, E. S. Hosseini, and M. R. Watts, "C- and L-band erbium-doped waveguide lasers with wafer-scale silicon nitride cavities," *Optics Letters* **38**(11), pp. 1760–1762, 2013.

[69] E. S. Magden, N. Li, Purnawirman, J. D. B. Bradley, N. Singh, A. Ruocco, G. S. Petrich, G. Leake, D. D. Coolbaugh, E. P. Ippen, M. R. Watts, and L. A. Kolodziejski, "Monolithically-integrated distributed feedback laser compatible with CMOS processing," *Optics Express* **25**(15), pp. 18058–18065, 2017.

[70] E. S. Magden, M. Y. Peng, J. D. B. Bradley, G. Leake, D. D. Coolbaugh, L. A. Kolodziejski, F. X. Kärtner, and M. R. Watts, "Laser frequency stabilization using pound-drever-hall technique with an integrated TiO2 athermal resonator," *2016 Conference on Lasers and Electro-Optics (CLEO)*, (San Jose, CA, USA), 2016.

[71] C. M. Sorace-Agaskar, P. T. Callahan, K. Shtyrkova, A. Baldycheva, M. Moresco, J. Bradley, M. Y. Peng, N. Li, E. S. Magden, P. Purnawirman, M. Y. Sander, G. Leake, D. D. Coolbaugh, M. R. Watts, and F. X. Kärtner, "Integrated mode-locked lasers in a CMOS-compatible silicon photonic platform," *2015 Conference on Lasers and Electro-Optics (CLEO)*, p. SM2I.5, (San Jose, CA, USA), 2015.

[72] D. Li, M. Y. Peng, H. W. Chen, J. Lim, M. R. Watts, and F. X. Kärtner, "Fiber-optic demonstration of optical frequency division for erbium silicon photonics integrated oscillator," *Conference on Lasers and Electro-Optics*, (San Jose, CA, USA), 2014.

[73] E. Timurdogan, Z. Su, K. Settaluri, S. Lin, S. Moazeni, C. Sun, G. Leake, D. D. Coolbaugh, B. R. Moss, M. Moresco, V. Stojanovic, and M. R. Watts, "An ultra low power 3D integrated intra-chip silicon electronic-photonic link," *Optical Fiber Communications Conference and Exhibition*, (Los Angeles, CA, USA), 2015.

[74] Z. Su, E. S. Hosseini, E. Timurdogan, J. Sun, M. Moresco, G. Leake, T. N. Adam, D. D. Coolbaugh, and M. R. Watts, "Whispering gallery germanium-on-silicon photodetector," *Optics Letters* **42**(15), pp. 2878–2881, 2017.

[75] A. Yaacobi, J. Sun, M. Moresco, G. Leake, D. Coolbaugh, and M. R. Watts, "Integrated phased array for wide-angle beam steering," *Optics Letters* **39**(15), pp. 4575–4578, 2014.

[76] M. Raval, A. Yaacobi, D. Coleman, N. M. Fahrenkopf, C. Baiocco, G. Leake, T. N. Adam, D. Coolbaugh, and M. R. Watts, "Nanophotonic phased array

for visible light image projection," *2016 IEEE Photonics Conference (IPC)*, pp. 206–207, (Waikoloa, HI, USA), 2016.

[77] J. N. Eckstein, A. I. Ferguson, and T. W. Hänsch, "High-resolution two-photon spectroscopy with picosecond light pulses," *Physical Review Letters* **40**, pp. 847–850, Mar 1978.

[78] T. Udem, J. Reichert, R. Holzwarth, and T. W. Hänsch, "Absolute optical frequency measurement of the cesium d_1 line with a mode-locked laser," *Physical Review Letters* **82**, pp. 3568–3571, 1999.

[79] F. X. Kärtner, D. Vermeulen, Z. Su, N. Li, K. Shtyrkova, P. T. Callahan, M. Xin, E. S. Magden, P. Purnawirman, E. Timurdogan, J. D. B. Bradley, E. P. Ippen, and M. R. Watts, "Electronic-photonic integration platform enabling a chip-scale optical synthesizer," *IFCS*, (New Orleans, LA, USA), 2016.

[80] T. R. Schibli, K. Minoshima, F. L. Hong, H. Inaba, Y. Bitou, A. Onae, and H. Matsumoto, "Phase-locked widely tunable optical single-frequency generator based on a femtosecond comb," *Optics Letters* **30**, pp. 2323–2325, May 2005.

[81] N. Li, P. Purnawirman, E. S. Magden, Z. Su, P. T. Callahan, K. Shtyrkova, M. Xin, A. Ruocco, C. Baiocco, E. P. Ippen, F. X. K. J. D. B. Bradley, D. Vermeulen, and M. R. Watts, "High-power thulium lasers on a silicon photonics platform," *Optics Letters* **42**, pp. 1181–1184, 2017.

[82] P. T. Callahan, K. Shtyrkova, N. Li, E. S. Magden, C. Baiocco, D. Coolbaugh, E. P. Ippen, M. R. Watts, and F. X. Kärtner, "Fully-integrated CMOS-compatible Q-switched laser at 1.9μm using thulium-doped Al_2O_3," *Conference on Lasers and Electro-Optics*, (San Jose, CA, USA), 2017.

[83] E. Timurdogan, C. V. Poulton, M. J. Byrd, and M. R. Watts, "Electric field-induced second-order nonlinear optical effects in silicon waveguides," *Nature Photonics* **11**, pp. 200–206, 2017.

[84] N. Singh, M. Xin, D. Vermeulen, K. Shtyrkova, S. E. Magden, P. T. Callahan, N. Li, A. Ruocco, G. Leake, D. D. Coolbaugh, E. P. Ippen, F. X. Kärtner, and M. R. Watts, "Octave spanning supercontinuum generation in silicon from 1.1μm to beyond 2.4μm," *Conference on Lasers and Electro-Optics*, (San Jose, CA, USA), 2017.

[85] S. E. Magden, C. V. Poulton, N. Li, D. Vermeulen, A. Ruocco, N. Singh, G. Leake, D. Coolbaugh, L. Kolodziejski, and M. R. Watts, "Mode-evolution-based, broadband 1x2 port high-pass/low-pass filter for silicon photonics," *Conference on Lasers and Electro-Optics*, (San Jose, CA, USA), 2017.

[86] A. J. DeMaria, D. A. Stetser, and H. Heynau, "Self modelocking of lasers with saturable absorbers," *Applied Physics Letters* **8**(7), pp. 174–176, 1966.

[87] E. Ippen and C. Shank, "Sub-picosecond, kilowatt pulses from a mode-locked CW dye laser," *IEEE Journal of Quantum Electronics* **10**(9), pp. 722–722, 1974.

[88] H. Haus, "Parameter ranges for CW passive mode locking," *IEEE Journal of Quantum Electronics* **12**(3), pp. 169–176, 1976.

[89] J. Herrmann and F. Weidner, "Theory of passively mode-locked cw dye lasers," *Applied Physics B* **27**(2), pp. 105–113, 1982.

[90] H. Haus, "A theory of forced mode locking," *IEEE Journal of Quantum Electronics* **11**(7), pp. 323–330, 1975.

[91] R. L. Fork, B. I. Greene, and C. V. Shank, "Generation of optical pulses shorter than 0.1 psec by colliding pulse mode locking," *Applied Physics Letters* **38**(9), pp. 671–672, 1981.

[92] S. Tsuda, W. H. Knox, E. A. de Souza, W. Y. Jan, and J. E. Cunningham, "Low-loss intracavity AlAs/AlGaAs saturable Bragg reflector for femtosecond mode locking in solid-state lasers," *Optics Letters* **20**(12), pp. 1406–1408, 1995.

[93] U. Keller, K. J. Weingarten, F. X. Kärtner, D. Kopf, B. Braun, I. D. Jung, R. Fluck, C. Honninger, N. Matuschek, and J. A. der Au, "Semiconductor saturable absorber mirrors (SESAM's) for femtosecond to nanosecond pulse generation in solid-state lasers," *IEEE Journal of Selected Topics in Quantum Electronics* **2**(3), pp. 435–453, 1996.

[94] F. X. Kärtner, J. A. der Au, and U. Keller, "Mode-locking with slow and fast saturable absorbers - what's the difference?," *IEEE Journal of Selected Topics in Quantum Electronics* **4**(2), pp. 159–168, 1998.

[95] A. Othonos, "Probing ultrafast carrier and phonon dynamics in semiconductors," *Journal of Applied Physics* **83**(4), pp. 1789–1830, 1998.

[96] H. Byun, M. Y. Sander, A. Motamedi, H. Shen, G. S. Petrich, L. A. Kolodziejski, E. P. Ippen, and F. X. Kärtner, "Compact, stable 1 GHz femtosecond Er-doped fiber lasers," *Applied Optics* **49**(29), pp. 5577–5582, 2010.

[97] U. Keller, "Ultrafast solid-state laser oscillators: a success story for the last 20 years with no end in sight," *Applied Physics B* **100**(1), pp. 15–28, 2010.

[98] D. H. Sutter, G. Steinmeyer, L. Gallmann, N. Matuschek, F. Morier-Genoud, U. Keller, V. Scheuer, G. Angelow, and T. Tschudi, "Semiconductor saturable-absorber mirror–assisted Kerr-lens mode-locked Ti:sapphire laser producing pulses in the two-cycle regime," *Optics Letters* **24**(9), pp. 631–633, 1999.

[99] H. Sotobayashi, J. T. Gopinath, E. M. Koontz, L. A. Kolodziejski, and E. P. Ippen, "Wavelength tunable passively mode-locked bismuth oxide-based erbium-doped fiber laser," *Optics Communications* **237**(4), pp. 399 – 403, 2004.

[100] S. N. Tandon, J. T. Gopinath, T. R. Schibli, G. S. Petrich, L. A. Kolodziejski, F. X. Kärtner, and E. P. Ippen, "Saturable absorbers with large area broadband Bragg reflectors for femtosecond pulse generation," *Conference on Lasers and Electro-Optics/Quantum Electronics and Laser Science Conference*, p. CWM5, 2003.

[101] D. Chao, M. Y. Sander, G. Chang, J. L. Morse, J. A. Cox, G. S. Petrich, L. A. Kolodziejski, F. X. Kärtner, and E. P. Ippen, "Self-referenced Erbium fiber laser frequency comb at a GHz repetition rate," *Optical Fiber Communication Conference and Exposition (OFC/NFOEC), 2012, and the National Fiber Optic Engineers Conference*, (Los Angeles, CA, USA), 2012.

[102] BATOP Gmbh. `http://www.batop.com/products/saturable-absorber/saturable-absorber.html`, 2017. Accessed: 08-01-2017.

[103] J. T. Gopinath, E. R. Thoen, E. M. Koontz, M. E. Grein, L. A. Kolodziejski, E. P. Ippen, and J. P. Donnelly, "Recovery dynamics in proton-bombarded semiconductor saturable absorber mirrors," *Applied Physics Letters* **78**(22), pp. 3409–3411, 2001.

[104] M. S. Dresselhaus, G. Dresselhaus, and P. Avouris, eds., *Carbon Nanotubes: Synthesis, Structure, Properties, and Application*, vol. 80 of *Topics in Applied Physics*. Springer-Verlag, Berlin, 2001.

[105] T. R. Schibli, K. Minoshima, H. Kataura, E. Itoga, N. Minami, S. Kazaoui, K. Miyashita, M. Tokumoto, and Y. Sakakibara, "Ultrashort pulse-generation by saturable absorber mirrors based on polymer-embedded carbon nanotubes," *Optics Express* **13**(20), pp. 8025–8031, 2005.

[106] K. Kieu and F. W. Wise, "Soliton thulium-doped fiber laser with carbon nanotube saturable absorber," *IEEE photonics technology letters* **21**(3), pp. 128–130, 2009.

[107] D. Bera, L. Qian, T.-K. Tseng, and P. H. Holloway, "Quantum dots and their multimodal applications: a review," *Materials* **3**(4), pp. 2260–2345, 2010.

[108] E. U. Rafailov, S. J. White, A. A. Lagatsky, A. Miller, W. Sibbett, D. A. Livshits, A. E. Zhukov, and V. M. Ustinov, "Fast quantum-dot saturable absorber for passive mode-locking of solid-state lasers," *IEEE Photonics Technology Letters* **16**(11), pp. 2439–2441, 2004.

[109] A. A. Lagatsky, F. M. Bain, C. T. A. Brown, W. Sibbett, D. A. Livshits, G. Erbert, and E. U. Rafailov, "Low-loss quantum-dot-based saturable absorber for efficient femtosecond pulse generation," *Applied Physics Letters* **91**(23), p. 231111, 2007.

[110] Q. Bao, H. Zhang, Y. Wang, Z. Ni, Y. Yan, Z. X. Shen, K. P. Loh, and D. Y. Tang, "Atomic-layer graphene as a saturable absorber for ultrafast pulsed lasers," *Advanced Functional Materials* **19**(19), pp. 3077–3083, 2009.

[111] C.-C. Lee, J. M. Miller, and T. R. Schibli, "Doping-induced changes in the saturable absorption of monolayer graphene," *Applied Physics B* **108**(1), pp. 129–135, 2012.

[112] N. H. Park, H. Jeong, S. Y. Choi, M. H. Kim, F. Rotermund, and D.-I. Yeom, "Monolayer graphene saturable absorbers with strongly enhanced evanescent-field interaction for ultrafast fiber laser mode-locking," *Optics Express* **23**(15), pp. 19806–19812, 2015.

[113] M. Liu, X. Yin, and X. Zhang, "Double-layer graphene optical modulator," *Nano Letters* **12**(3), pp. 1482–1485, 2012.

[114] D. E. Spence, P. N. Kean, and W. Sibbett, "60-fsec pulse generation from a self-mode-locked Ti:sapphire laser," *Optics Letters* **16**(1), pp. 42–44, 1991.

[115] T. Brabec, C. Spielmann, P. F. Curley, and F. Krausz, "Kerr lens mode locking," *Optics Letters* **17**(18), pp. 1292–1294, 1992.

[116] I. D. Jung, F. X. Kärtner, N. Matuschek, D. H. Sutter, F. Morier-Genoud, G. Zhang, U. Keller, V. Scheuer, M. Tilsch, and T. Tschudi, "Self-starting 6.5-fs pulses from a Ti:sapphire laser," *Optics Letters* **22**(13), pp. 1009–1011, 1997.

[117] R. Ell, U. Morgner, F. X. Kärtner, J. G. Fujimoto, E. P. Ippen, V. Scheuer, G. Angelow, T. Tschudi, M. J. Lederer, A. Boiko, and B. Luther-Davies, "Generation of 5-fs pulses and octave-spanning spectra directly from a Ti:sapphire laser," *Optics Letters* **26**(6), pp. 373–375, 2001.

[118] E. P. Ippen, H. A. Haus, and L. Y. Liu, "Additive pulse mode locking," *Journal of Optical Society of America, B* **6**(9), pp. 1736–1745, 1989.

[119] H. A. Haus, J. G. Fujimoto, and E. P. Ippen, "Structures for additive pulse mode locking," *Journal of Optical Society of America B* **8**(10), pp. 2068–2076, 1991.

[120] L. Y. Liu, J. M. Huxley, E. P. Ippen, and H. A. Haus, "Self-starting additive-pulse mode locking of a Nd:YAG laser," *Optics Letters* **15**, pp. 553–555, May 1990.

[121] E. P. Ippen, L. Y. Liu, and H. A. Haus, "Self-starting condition for additive-pulse mode-locked lasers," *Optics Letters* **15**(3), pp. 183–185, 1990.

[122] M. Hofer, M. E. Fermann, F. Haberl, M. H. Ober, and A. J. Schmidt, "Mode locking with cross-phase and self-phase modulation," *Optics Letters* **16**(7), pp. 502–504, 1991.

[123] K. Tamura, H. A. Haus, and E. P. Ippen, "Self-starting additive pulse mode-locked erbium fibre ring laser," *Electronics Letters* **28**(24), pp. 2226–2228, 1992.

[124] M. Olivier, M.-D. Gagnon, and M. Piché, "Automated mode locking in nonlinear polarization rotation fiber lasers by detection of a discontinuous jump in the polarization state," *Optics Express* **23**(5), pp. 6738–6746, 2015.

[125] L. Chen, C. R. Doerr, and Y.-K. Chen, "Compact polarization rotator on silicon for polarization-diversified circuits," *Optics Letters* **36**(4), pp. 469–471, 2011.

[126] Y. Ding, H. Ou, and C. Peucheret, "Wideband polarization splitter and rotator with large fabrication tolerance and simple fabrication process," *Optics Letters* **38**(8), pp. 1227–1229, 2013.

[127] M. R. Watts and H. A. Haus, "Integrated mode-evolution-based polarization rotators," *Optics Letters* **30**(2), pp. 138–140, 2005.

[128] Z. Su, E. Timurdogan, E. S. Hosseini, J. Sun, G. Leake, D. D. Coolbaugh, and M. R. Watts, "Four-port integrated polarizing beam splitter," *Optics Letters* **39**(4), pp. 965–968, 2014.

[129] N. J. Doran and D. Wood, "Nonlinear-optical loop mirror," *Optics Letters* **13**(1), pp. 56–58, 1988.

[130] I. N. Duling, C. J. Chen, P. K. A. Wai, and C. R. Menyuk, "Operation of a nonlinear loop mirror in a laser cavity," *IEEE Journal of Quantum Electronics* **30**(1), pp. 194–199, 1994.

[131] K. Smith, P. G. J. Wigley, and N. J. Doran, "Pulse shaping, compression, and pedestal suppression employing a nonlinear-optical loop mirror," *Optics Letters* **15**(22), pp. 1294–1296, 1990.

[132] I. N. Duling, "All-fiber ring soliton laser mode locked with a nonlinear mirror," *Optics Letters* **16**(8), pp. 539–541, 1991.

[133] M. E. Fermann, F. Haberl, M. Hofer, and H. Hochreiter, "Nonlinear amplifying loop mirror," *Optics Letters* **15**(13), pp. 752–754, 1990.

[134] K. Smith, E. J. Greer, N. J. Doran, D. M. Bird, and K. H. Cameron, "Pulse amplification and shaping using a nonlinear loop mirror that incorporates a saturable gain," *Optics Letters* **17**(6), pp. 408–410, 1992.

[135] V. S. Afshar, T. M. Monro, and C. M. de Sterke, "Understanding the contribution of mode area and slow light to the effective Kerr nonlinearity of waveguides," *Optics Express* **21**(15), pp. 18558–18571, 2013.

[136] C. Koos, L. Jacome, C. Poulton, J. Leuthold, and W. Freude, "Nonlinear silicon-on-insulator waveguides for all-optical signal processing," *Optics Express* **15**, pp. 5976–5990, May 2007.

[137] H. A. Haus, "Mode-locking of lasers," *IEEE Journal of Selected Topics in Quantum Electronics* **6**(6), pp. 1173–1185, 2000.

[138] K. Shtyrkova, P. Callahan, E. Ippen, M. Watts, and F. X. Kärtner, "Methods and apparatus for mode-locking on-chip lasers. US/PCT patent application, US 15/592, 905; PCT/US2017/032088," 2017.

[139] L. Chrostowski, *Silicon Photonics Design: From Devices to Systems*, Cambridge University Press, Cambridge, UK, 2015.

[140] A. Yariv, "Coupled-mode theory for guided-wave optics," *IEEE Journal of Quantum Electronics* **9**(9), pp. 919–933, 1973.

[141] G. Agrawal, *Nonlinear Fiber Optics*, Elsevier, fifth ed., 2013.

[142] A. Arbabi and L. L. Goddard, "Measurements of the refractive indices and thermo-optic coefficients of Si_3N_4 and $SiOx$ using microring resonances," *Optics Letters* **38**, pp. 3878–3881, Oct 2013.

[143] F. X. Kärtner, I. D. Jung, and U. Keller, "Soliton mode-locking with saturable absorbers," *IEEE Journal of Selected Topics in Quantum Electronics* **2**(3), pp. 540–556, 1996.

[144] R. Paschotta and U. Keller, "Passive mode locking with slow saturable absorber," *Applied Physics B* **73**(7), pp. 653–662, 2001.

[145] K. Tamura, E. P. Ippen, H. A. Haus, and L. E. Nelson, "77-fs pulse generation from a stretched-pulse mode-locked all-fiberring laser," *Optics Letters* **18**(13), pp. 1080–1082, 1993.

[146] K. Tamura, E. P. Ippen, and H. A. Haus, "Pulse dynamics in stretched−pulse fiber lasers," *Applied Physics Letters* **67**(2), pp. 158–160, 1995.

[147] A. Chong, W. H. Renninger, and F. W. Wise, "Properties of normal-dispersion femtosecond fiber lasers," *Journal of Optical Society of America B* **25**(2), pp. 140–148, 2008.

[148] J. R. Buckley, F. W. Wise, F. O. Ilday, and T. Sosnowski, "Femtosecond fiber lasers with pulse energies above 10n J," *Optics Letters* **30**(14), pp. 1888–1890, 2005.

[149] K. Kieu and F. W. Wise, "All-fiber normal-dispersion femtosecond laser," *Optics Express* **16**(15), pp. 11453–11458, 2008.

[150] W. H. Renninger, A. Chong, and F. W. Wise, "Self-similar pulse evolution in an all-normal-dispersion laser," *Physics Review A* **82**, p. 021805, 2010.

[151] D. T. H. Tan, P. C. Sun, and Y. Fainman, "Monolithic nonlinear pulse compressor on a silicon chip," *Nature Communications* **1**(116), 2010.

[152] K. Tamura, J. Jacobson, E. P. Ippen, H. A. Haus, and J. G. Fujimoto, "Unidirectional ring resonators for self-starting passively mode-locked lasers," *Optics Letters* **18**(3), pp. 220–222, 1993.

[153] K. Worhoff, J. D. B. Bradley, L. Agazzi, and M. Pollnau, "Rare-earth-ion-doped Al_2O_3 for integrated optical amplification," *Proc.SPIE* **7604**, 2010.

[154] H. P. Weber, F. A. Dunn, and W. N. Leibolt, "Loss measurements in thin-film optical waveguides," *Applied Optics* **12**(4), pp. 755–757, 1973.

[155] S. W. Henderson, P. J. M. Suni, C. P. Hale, S. M. Hannon, J. R. Magee, D. L. Bruns, and E. H. Yuen, "Coherent laser radar at 2 μm using solid-state lasers," *IEEE Transactions on Geoscience and Remote Sensing* **31**(1), pp. 4–15, 1993.

[156] L. Esterowitz, "Diode pumped holmium, thulium and erbium lasers between 2 and 3 micrometers operating cw at room temperature," *Optical Engineering* **29**, 1990.

[157] J. Geng, J. Wu, S. Jiang, and J. Yu, "Efficient operation of diode-pumped single-frequency thulium-doped fiber lasers near 2 μm," *Optics Letters* **32**(4), pp. 355–357, 2007.

[158] R. C. Stoneman and L. Esterowitz, "Efficient, broadly tunable, laser-pumped Tm:YAG and Tm:YSGG cw lasers," *Optics Letters* **15**(9), pp. 486–488, 1990.

[159] M. Tao, Q. Huang, T. Yu, P. Yang, W. Chen, and X. Ye, "Cross relaxation in Tm-doped fiber lasers," *Proc.SPIE* **8796**, 2013.

[160] B. Ainslie and C. Day, "A review of single-mode fibers with modified dispersion characteristics," *Journal of Lightwave Technology* **4**(8), pp. 967–979, 1986.

[161] R. L. Fork, O. E. Martinez, and J. P. Gordon, "Negative dispersion using pairs of prisms," *Optics Letters* **9**(5), pp. 150–152, 1984.

[162] F. X. Kärtner, N. Matuschek, T. Schibli, U. Keller, H. A. Haus, C. Heine, R. Morf, V. Scheuer, M. Tilsch, and T. Tschudi, "Design and fabrication of double-chirped mirrors," *Optics Letters* **22**(11), pp. 831–833, 1997.

[163] F. X. Kärtner, U. Morgner, R. Ell, T. Schibli, J. G. Fujimoto, E. P. Ippen, V. Scheuer, G. Angelow, and T. Tschudi, "Ultrabroadband double-chirped mirror pairs for generation of octave spectra," *Journal of Optical Society of America B* **18**(6), pp. 882–885, 2001.

[164] Purnawirman, *Integrated Erbium Lasers in Silicon Photonics*. PhD thesis, Massachusetts Institute of Technology, 2017.

[165] P. T. Callahan, P. Purnawirman, T. N. Adam, G. Leake, D. Coolbaugh, M. Watts, and F. X. Kärtner, "Double-chirped Bragg gratings in a silicon nitride waveguide," *Conference on Lasers and Electro-Optics*, p. SF1E.7, 2016.

[166] M. Cherchi, S. Ylinen, M. Harjanne, M. Kapulainen, and T. Aalto, "Dramatic size reduction of waveguide bends on a micron-scale silicon photonic platform," *Optics Express* **21**(15), pp. 17814–17823, 2013.

[167] P. T. Callahan, *Exact title to be determined..* PhD thesis, Massachusetts Institute of Technology, 2018.

[168] B. J. Ainslie, "A review of the fabrication and properties of erbium-doped fibers for optical amplifiers," *Journal of Lightwave Technology* **9**(2), pp. 220–227, 1991.

[169] D. Pudo, H. Byun, J. Chen, J. Sickler, F. X. Kärtner, and E. P. Ippen, "Scaling of passively mode-locked soliton erbium waveguide lasers based on slow saturable absorbers," *Optics Express* **16**(23), pp. 19221–19231, 2008.